

UNIVERSITY OF CALIFORNIA
RIVERSIDE

Measurement of Identified Charged Hadron Anisotropic Flow in d+Au Collisions

A Dissertation submitted in partial satisfaction
of the requirements for the degree of

Doctor of Philosophy

in

Physics

by

Matthew Mendoza

October 2016

Dissertation Committee:

Dr. Richard Seto, Chairperson
Dr. Kenneth Barish
Dr. John Ellison

Copyright by
Matthew Mendoza
2016

The Dissertation of Matthew Mendoza is approved:

Committee Chairperson

University of California, Riverside

Acknowledgments

I am grateful to my advisor, without whose help, I would not have been here.

To my parents for all the support.

ABSTRACT OF THE DISSERTATION

Measurement of Identified Charged Hadron Anisotropic Flow in d+Au Collisions

by

Matthew Mendoza

Doctor of Philosophy, Graduate Program in Physics

University of California, Riverside, October 2016

Dr. Richard Seto, Chairperson

Collective flow has historically been an indicator that nuclear matter created in heavy ion collisions has undergone a phase change to a novel state where its constituent particles are deconfined. This phase, called a *Quark-Gluon Plasma* (QGP), has many characteristics that are signature of its creation. Chief among these is the collective behavior of the nuclear matter indicated by its anisotropic flow, as well as high p_T particle suppression, baryon enhancement at mid- p_T , and the enhancement of strange quark containing particles above binary scaling expectations. Recent results from the Large Hadron Collider (LHC) show evidence of collective flow in the simpler p+Pb system, implying that a QGP may be formed in smaller systems than previously thought. An elliptic flow measurement with identified particles in d+Au collisions could reveal more about the nuclear matter created in these simpler systems. The Pioneering High Energy Nuclear Ion Experiment, or PHENIX, Time of Flight detector used in conjunction with its Aerogel Cherenkov Counter can provide particle identification with good proton/kaon/pion separation for $p_T < 7$ GeV/c. Measurements of particle identified elliptic flow using these detectors are presented and could help to elucidate the underlying physics of the baryon excess and strangeness enhancement anomalies that may be evidence of new physics in the d+Au system.

Contents

List of Figures	x
List of Tables	xiv
1 Introduction	1
1.1 Introduction	1
1.2 Early Experiments: An Overview	4
2 Nuclear Matter: Hot and Cold	7
2.1 Hot Versus Cold Nuclear Matter	7
2.2 The Cronin Effect	8
2.2.1 Initial State Multiple Scattering	10
2.2.2 Final State Multiple Scattering	12
2.3 Hot Nuclear Matter: Quark Gluon Plasma	16
2.3.1 Collective Flow	16
2.3.2 Baryon Enhancement	18
2.3.3 Theoretical Models of the QGP Hadron Interaction	21
Relativistic Hydrodynamics	21
Recombination and Fragmentation	23
2.4 Collective Flow at the LHC	26
2.5 Recombination and Fragmentation for All?	27
2.6 The Big(ger) Picture	29
2.6.1 The Glauber Model	29
2.6.2 Color-Glass Condensate	31
2.6.3 Glasma	35
2.6.4 Strangeness Enhancement	37
2.7 Moving Forward	38
3 Experimental Apparatus	39
3.1 The Relativistic Heavy Ion Collider	39
3.2 The Particle Acceleration Process	40
3.3 The PHENIX Detector	42

3.3.1	Central Arm	44
	Drift and Pad Chambers	45
	TOF: Time Of Flight Detectors	49
	ACC: Aerogel Cherenkov Counter	54
	EMCal and RICH: Electromagnetic Calorimeter and Ring Imaging Cherenkov Counter	56
3.3.2	Forward and Global Detectors	60
	BBC: Beam-Beam Counter	61
	ZDC/SMD: Zero Degree Calorimeter and Shower Max Detectors . .	63
	MPC: Muon Piston Calorimeter	64
	RXNP: Reaction Plane Detector	64
3.4	The DAQ	65
4	Heavy Ion Collisions in PHENIX: A Primer	70
4.1	Measurable Quantities	70
4.2	Event Characterization	71
4.2.1	Centrality	72
4.2.2	Event Vertex and Timing	75
4.3	Track Reconstruction	77
4.3.1	Variables for Track Selection	77
	Track Matching: DC and PC1	78
	Track Matching: TOF and PC3	79
4.3.2	Particle Identification	80
5	Anisotropic Flow	85
5.1	Flow from Geometry of Initial Conditions	85
5.2	Flow from Fluctuations	91
6	Event Plane	93
6.1	Determination of Event Plane	93
6.2	Q-vector Re-centering	95
6.3	Event Plane “Flattening”	96
6.4	Event Plane Resolution Correction	98
7	Results	100
7.1	Charged Track v_2	100
7.2	Separating Particle Signals	101
7.2.1	Single Gaussians	103
7.2.2	Multiple Gaussians	106
7.2.3	ACC as a Particle Discriminator	107
7.2.4	High p_T : Fixed Width and Mean	109
7.3	Identified Particle v_2	109

8 Error Analysis	111
8.1 Event Plane Resolution Correction	112
8.2 Centrality Resolution	114
8.3 Particle Identification Methods	115
8.3.1 Momentum Uncertainty	116
8.3.2 TOF Timing	117
8.3.3 Uncertainties from Gaussian Models	120
Single and Mixed Gaussians, no ACC, $p_T \leq 2.1 \text{ GeV}/c$	120
ACC Meson Separation and Gaussian Tail Cross Contamination, $2.1 \leq p_T \leq 2.9$	121
Fixed Width/Mean Gaussians and Background Effects	121
8.4 Detector Acceptance	122
8.5 Summary	123
9 Conclusions	127
9.1 Discussion	128
9.1.1 Hadronization	128
9.1.2 Comparison to Flow Models	130
9.1.3 Strangeness and Initial Conditions	132
9.2 Comparison to Other Results	135
9.3 Other Signatures of an Equilibrated Phase	137
9.4 Summary	139
A PHENIX Coordinate System	141
B Nuclear Modification Factor	143
C Analysis Data and Plots	145
C.1 Particle Identification: TOFW	145
C.1.1 Single Gaussian fits, $p_T=0.5\text{-}1.3 \text{ GeV}/c$, TOF.W, negative charged tracks	146
C.1.2 Single Gaussian fits, $p_T=0.5\text{-}1.3 \text{ GeV}/c$, TOF.W, positive charged tracks	150
C.1.3 Mixed Gaussian fits, $p_T=1.3\text{-}2.1 \text{ GeV}/c$, TOF.W, negative charged tracks	154
Mixed Gaussian fits, $p_T=1.3\text{-}2.1 \text{ GeV}/c$, TOF.W, positive charged tracks	158
C.1.4 TOF.W and ACC, $p_T=2.1\text{-}3.5 \text{ GeV}$, negative charged tracks	162
C.1.5 TOF.W and ACC, $p_T=2.1\text{-}3.5 \text{ GeV}$, positive charged tracks	183

List of Figures

2.1	Proton vs pion yield ratio from the Cronin paper	9
2.2	Illustration of Initial State Multiple Scattering	11
2.3	Feynman and Cartoon diagrams of Jet Formation	13
2.4	Planarity of jets created with protons incident on Pb targets vs H targets. .	14
2.5	Illustration of Final State Multiple Scattering	15
2.6	Central vs Peripheral collisions, geometry of initial conditions	17
2.7	Identified particle elliptic flow vs centrality in 200 GeV Au+Au collisions .	18
2.8	Evidence of Baryon Enhancement in Au+Au collisions	19
2.9	Quark Scaled Elliptic Flow Results from PHENIX and STAR in Au+Au $\sqrt{s_{NN}} = 200\text{GeV}$ collisions	22
2.10	Recombination model compared with Au+Au data	24
2.11	Illustration of an example hard scatter resulting in fragmentation to two pions	25
2.12	Elliptic Flow in p+Pb at the LHC	27
2.13	p/ π ratios compared for central d+Au and peripheral Au+Au	28
2.14	A diagram of QGP hydrodynamic evolution.	30
2.15	A cartoon of the Glauber Model	31
2.16	34
2.17	The Formation of Glasma from the collision of Color Glass Sheets.	36
3.1	An Aerial view of BNL	39
3.2	Illustration of all the accelerators used to boost ions to relativistic speeds at RHIC	40
3.3	PHENIX Detector Configuration for RHIC Run 8 (2008)	43
3.4	PHENIX Central Magnet Field Strengths.	44
3.5	Diagrams of DC wire configurations.	48
3.6	Pad Chamber 1 on top of the Drift Chamber.	50
3.7	A schematic of the slat layout in the TOFE.	51
3.8	An illustration of a single slat in the TOFE	52
3.9	Diagram of a basic RPC	53
3.10	Cross sectional diagram of the MRPCs used in the TOFW	54
3.12	A diagram of the RICH	58

3.13	Schematics of EMCal components	59
3.14	The Beam Beam Counter	61
3.15	The ZDC and SMD.	62
3.16	Schematic of the MPC	65
3.17	Diagram and picture of the RXNP detector	66
3.18	A diagram of the data flow of PHENIX data through the DAQ	69
4.1	Central versus peripheral ion collisions, BBC vs ZDC determination of	75
4.2	Diagram of BBC and ZDC event characterization	76
4.3	Event Vertex Distribution	77
4.4	Hits in the DC matched to tracks using a Hough transform	79
4.5	Diagram of track reconstruction by the DC/PC1 projected linearly onto the TOF/PC3	81
4.6	Particle separation in the TOF	82
4.7	m^2 vs p_T showing clear constant separation of particle signatures.	84
5.1	A cartoon showing pressure gradients in central versus peripheral collisions.	86
5.2	Reaction plane coordinates.	89
5.3	Plots of the first four harmonics of a cosine series.	90
5.4	Triangular Flow from Fluctuations.	92
6.1	Illustrations of the event plane in heavy ion collisions	94
6.2	Cartoon of Event Plane determination with forward detectors	95
6.3	Flattened event plane distributions in the BBC, MPC, and RXNP	97
7.1	Track p_T vs m^2 determined by the TOF.W showing separation of π , k , and proton particle signals.	102
7.2	Example single Gaussian fits of m^2 for $p_T \leq 1.3$ GeV/c in 6 bins of $\Delta\phi$	104
7.3	Particle distribution fit mean and width QA. π , K , p yield vs $\Delta\phi$ and corresponding Fourier fits for $p_T \leq 1.3$ GeV/c.	105
7.4	Example mixed Gaussian fits of m^2 for $1.3 \leq p_T \leq 2.1$ GeV/c in 6 bins of $\Delta\phi$	106
7.5	Number of ACC photoelectrons vs m^2 in bins of p_T	108
7.6	π^\pm , K^\pm , p/\bar{p} elliptic flow, $\sqrt{s_{NN}} = 200$ GeV d+Au collisions	110
8.1	Centrality uncertainty contribution to Systematic Error	116
8.2	Timing QA in the TOF.W	118
8.3	Systematic Offset in TOF.W	119
8.4	Effects of Systematic Shifts in Yield on v_2	125
9.1	Elliptic Flow vs Transverse Momentum, 200 GeV d+Au, 0-5% centrality	127
9.2	Quark Scaled Elliptic Flow (π^\pm and p/\bar{p}) vs Transverse Momentum, 200 GeV d+Au	129
9.3	π^\pm and p/\bar{p} Elliptic Flow compared to hydrodynamic models.	130

9.4	Elliptic flow of all charged hadrons compared to hydrodynamic models.	131
9.5	Meson Elliptic Flow plots	133
9.6	Results compared to previous PHENIX d+Au results.	136
9.7	Results compared to ALICE p+Pb results.	137
A.1	PHENIX coordinate system	141
C.1	PID fits and Yield vs $d\phi$ for $p_T=0.5\text{-}0.7 \text{ GeV}/c$, TOF.W, negative particles	146
C.2	PID fits and Yield vs $d\phi$ for $p_T=0.7\text{-}0.9 \text{ GeV}/c$, TOF.W, negative particles	147
C.3	PID fits and Yield vs $d\phi$ for $p_T=0.9\text{-}1.1 \text{ GeV}/c$, TOF.W, negative particles	148
C.4	PID fits and Yield vs $d\phi$ for $p_T=1.1\text{-}1.3 \text{ GeV}/c$, TOF.W, negative particles	149
C.5	PID fits and Yield vs $d\phi$ for $p_T=0.5\text{-}0.7 \text{ GeV}/c$, TOF.W, positive particles	150
C.6	PID fits and Yield vs $d\phi$ for $p_T=0.7\text{-}0.9 \text{ GeV}/c$, TOF.W, positive particles	151
C.7	PID fits and Yield vs $d\phi$ for $p_T=0.9\text{-}1.1 \text{ GeV}/c$, TOF.W, positive particles	152
C.8	PID fits and Yield vs $d\phi$ for $p_T=1.1\text{-}1.3 \text{ GeV}/c$, TOF.W, positive particles	153
C.9	PID fits and Yield vs $d\phi$ for $p_T=1.3\text{-}1.5 \text{ GeV}/c$, TOF.W, negative particles	154
C.10	PID fits and Yield vs $d\phi$ for $p_T=1.5\text{-}1.7 \text{ GeV}/c$, TOF.W, negative particles	155
C.11	PID fits and Yield vs $d\phi$ for $p_T=1.7\text{-}1.9 \text{ GeV}/c$, TOF.W, negative particles	156
C.12	PID fits and Yield vs $d\phi$ for $p_T=1.9\text{-}2.1 \text{ GeV}/c$, TOF.W, negative particles	157
C.13	PID fits and Yield vs $d\phi$ for $p_T=1.3\text{-}1.5 \text{ GeV}/c$, TOF.W, positive particles	158
C.14	PID fits and Yield vs $d\phi$ for $p_T=1.5\text{-}1.7 \text{ GeV}/c$, TOF.W, positive particles	159
C.15	PID fits and Yield vs $d\phi$ for $p_T=1.7\text{-}1.9 \text{ GeV}/c$, TOF.W, positive particles	160
C.16	PID fits and Yield vs $d\phi$ for $p_T=1.9\text{-}2.1 \text{ GeV}/c$, TOF.W, positive particles	161
C.17	ACC $N_{p.e.}$ vs m_2 , PID fits, and Yield vs $d\phi$ for $p_T=2.1\text{-}2.3 \text{ GeV}/c$, TOF.W, negative particles	164
C.18	ACC $N_{p.e.}$ vs m_2 , PID fits, and Yield vs $d\phi$ for $p_T=2.3\text{-}2.5 \text{ GeV}/c$, TOF.W, negative particles	167
C.19	ACC $N_{p.e.}$ vs m_2 , PID fits, and Yield vs $d\phi$ for $p_T=2.5\text{-}2.7 \text{ GeV}/c$, TOF.W, negative particles	170
C.20	ACC $N_{p.e.}$ vs m_2 , PID fits, and Yield vs $d\phi$ for $p_T=2.7\text{-}2.9 \text{ GeV}/c$, TOF.W, negative particles	173
C.21	ACC $N_{p.e.}$ vs m_2 , PID fits, and Yield vs $d\phi$ for $p_T=3.0\text{-}3.5 \text{ GeV}/c$, TOF.W, negative particles	176
C.22	ACC $N_{p.e.}$ vs m_2 , PID fits, and Yield vs $d\phi$ for $p_T=3.5\text{-}4.0 \text{ GeV}/c$, TOF.W, negative particles	179
C.23	ACC $N_{p.e.}$ vs m_2 , PID fits, and Yield vs $d\phi$ for $p_T=4.0\text{-}4.5 \text{ GeV}/c$, TOF.W, negative particles	182
C.24	ACC $N_{p.e.}$ vs m_2 , PID fits, and Yield vs $d\phi$ for $p_T=2.1\text{-}2.3 \text{ GeV}/c$, TOF.W, positive particles	185
C.25	ACC $N_{p.e.}$ vs m_2 , PID fits, and Yield vs $d\phi$ for $p_T=2.3\text{-}2.5 \text{ GeV}/c$, TOF.W, positive particles	188

C.26 ACC $N_{p.e.}$ vs m_2 , PID fits, and Yield vs $d\phi$ for $p_T=2.5\text{-}2.7 \text{ GeV}/c$, TOF.W, negative particles	191
C.27 ACC $N_{p.e.}$ vs m_2 , PID fits, and Yield vs $d\phi$ for $p_T=2.7\text{-}2.9 \text{ GeV}/c$, TOF.W, positive particles	194
C.28 ACC $N_{p.e.}$ vs m_2 , PID fits, and Yield vs $d\phi$ for $p_T=3.0\text{-}3.5 \text{ GeV}/c$, TOF.W, positive particles	197
C.29 ACC $N_{p.e.}$ vs m_2 , PID fits, and Yield vs $d\phi$ for $p_T=3.5\text{-}4.0 \text{ GeV}/c$, TOF.W, positive particles	200
C.30 ACC $N_{p.e.}$ vs m_2 , PID fits, and Yield vs $d\phi$ for $p_T=4.0\text{-}4.5 \text{ GeV}/c$, TOF.W, positive particles	203

List of Tables

8.1	Event Plane Resolution Corrections for MPC, 0-5% centrality	113
8.2	Table of Systematic Errors in each bin of p_T	126

Chapter 1

Introduction

1.1 Introduction

Humanity is set apart from the rest of creation by its tenacity to explore and discover, and it's no surprise that the driving force for this discovery is our constant desire to better understand the universe around us. From the deepest distances of outer space to the infinitesimally small structures of the atoms that comprise the matter we interact with every day, our growing understanding of the intricacies of our world has revealed such amazing complexities we never could have thought possible. Over the last century, one such exploration that has uncovered many unforeseen phenomena is the that of the building blocks of matter and the forces that hold it all together. From Planck's discovery that the world of the incredibly small is not smooth and continuous but rather comprised of discrete quanta, to Bohr's model of the atom showing that even the orbits of electrons

were quantized, a new quantum world changed the very way we approached physics. This was further solidified with the discovery of the neutron, which pointed the way to the discovery of new fundamental forces of nature, field theories with which to describe them, and eventually the venerable Standard Model of particle physics. At every turn, our ever-increasing understanding of the workings of the atom revealed many new surprises. In the last few decades, one such investigation into the makings of the atomic nucleus aims to study the properties of this nuclear material under extremes of temperature and energy density. As we now know, the proton and neutron were not the proverbial “end-of-the-line” for physicists seeking the fundamental components of matter. We discovered that they, too, are comprised of smaller particles called *quarks*, which are held together with a new fundamental force of nature called the *strong force*, which is mediated by the exchange of force carrier particles called *gluons*.

This binding of quarks into confined states such as protons and neutrons made physicists wonder about the nature of this confinement, namely whether or not it was possible to deconfine particles into free quarks. This culminated with Gross, Wilczek [1], and Politzer’s [2] 1973 discovery of this quark *deconfinement*, a property they called *asymptotic freedom* in the quantum field theory of the strong nuclear force, Quantum Chromodynamics (QCD). They discovered that the strength of the strong force became asymptotically weaker as energy increased and distance decreased. Collins and Perry [3] continued this idea to the nuclear matter extremes that exist in the centers of neutron stars and exploding black holes, noting that, due to the extreme pressures in these systems resulting in small distances

between quarks, the QCD coupling constant would decrease, resulting in asymptotically free quarks. Though their inferences pertained to low temperature, high density systems, they noted that similar phenomena could occur in high temperature systems like that of the early universe. The first to coin the term “Quark-Gluon Plasma” (QGP) was Shuryak in 1980 [4] who wrote:

“When the energy density, ϵ , exceeds some typical hadronic value ($\sim 1 \text{ GeV/fm}^3$)¹, matter no longer consists of separate hadrons (protons, neutrons, etc.), but as their fundamental constituents, quarks and gluons. Because of the apparent analogy with similar phenomena in atomic physics, we may call this phase of matter: the QGP (or quark gluon) plasma.”

It is with this theoretical framework that we have set out to develop an understanding of this quark/gluon deconfinement. But what of this Quark-Gluon Plasma? How is it created, and what are its properties? Historically, new physics discoveries have led to new frontiers of science. Could this search for the QGP deepen our understanding of nuclear forces beyond small system interactions to that of larger systems? And could a better understanding of these larger systems point to ever stranger new phenomena? It was questions such as these that have led us to a new era of physics discovery.

¹This energy density was later found to be $\epsilon \approx 2 \text{ GeV/fm}^3$ [5]

1.2 Early Experiments: An Overview

The earliest experiments that utilized the collisions of two ions to study nuclear matter were largely done by re-purposing existing accelerators that were used for elementary particle physics. The general goal of an accelerator setup to study elementary particle physics is to observe the production of new particles by the collision of small nucleons or leptons, which result in a small number of detected particle tracks. In contrast, an accelerator used for Heavy Ion Physics is used to study larger nuclear matter systems created by colliding large nuclei, which result in higher track multiplicity consisting of particles created by more common QCD processes.

Examples of this include the re-purposing of the weak focusing proton synchrotron, the Bevatron, at Lawrence Berkeley National Laboratory, when it was joined with the SuperHiLac, a linear accelerator capable of accelerating ions to relativistic energies of up to 2 GeV per nucleon. It became the only machine in the world at the time capable of accelerating all of the elements in the periodic table to relativistic speeds. This capability allowed researchers to pioneer the study of *quark matter* [6]; the major achievement of this epoch being the discovery that nuclear matter could be compressed to high temperatures [7]. This property was made evident by the observation of collective flow in niobium + niobium collisions that were accelerated to energies of 400 MeV/nucleon [8], paving the way for the search for other phases of nuclear matter, namely the Quark Gluon Plasma.

The first step into the “ultra-relativistic” energy regime (> 10 GeV/nucleon) took place at Brookhaven National Lab (BNL) in the mid-1980’s with the *Alternating Gradient*

Synchrotron (AGS), which initially was able to reach 14 GeV per nucleon with silicon ions. Concurrently, across the ocean, the European Organization for Nuclear Research (Conseil Européen pour la Recherche Nucléaire, CERN) had the *Super Proton Synchrotron* (SPS) which accelerated oxygen and sulfur ions up to 200 GeV per nucleon. By the mid 1990's both had seen upgrades that allowed them to create larger systems with the use of so called "heavy" ions. At the AGS, gold ions were accelerated to 11 GeV per nucleon; at the SPS, lead ions were accelerated to 158 GeV per nucleon [9]. Though both accelerators set the stage for the *Relativistic Heavy Ion Collider*, each had their own periods of discovery.

The first sign that quark matter behaved collectively was the observation that it "flowed" like a fluid would. This phenomena, called *collective flow*, was observed in 11.5 GeV Au + Au collisions at the AGS by the E877 collaboration [10]. This quark matter was indeed a new state of matter as it did not behave simply as a conglomerate of independent nuclei. The E802 collaboration compared the production of charged kaons to the production of charged pions in 14.6 GeV Si + Au collisions and saw that the production of kaons was enhanced compared to proton + proton collisions showing that the behavior of this quark matter produced a different spectrum of particles than the simpler proton+proton (p+p) collisions [11].

At the SPS, the increased production of hadrons² containing heavier quarks called *strange* quarks was studied in heavy ion collisions. This so-called *strangeness enhancement* was observed by the NA49 [12] and WA97 collaborations through the measurement of the

²Compared to the production of the same in p+p collisions. Increased production of particles compared to p+p is called *enhancement*, conversely decreased production is called *suppression*.

charged kaon to pion ratio and the production of multi-strange baryons (Λ , $\bar{\Lambda}$, Ξ^\pm , and Ω^\pm).

Meanwhile, the NA50 collaboration was finding not enhancement, but rather suppression of *charm quark*³ containing J/Ψ mesons in heavy ion collisions compared to the known production of them in p+p collisions [13]. This was caused by free quarks and gluons at high temperature weakening the strength of the coupling force between charmed quark pairs that comprise J/Ψ by screening the color charge. This color charge screening effectively breaks up the J/Ψ , resulting in the suppression of its production.

Concurrently, the teams at both accelerators used two particle correlations to study the evolving collision volume and two things. First, the energy density of the quark matter was a factor of 10 greater than naturally stable laboratory nuclei [14]. Second, the lower boundary of QGP formation by finding the conditions (energy density $\leq 100 \text{ MeV/fm}^3$) for thermal *freeze-out* [15], i.e., the point of re-confinement for quarks and gluons into hadronic states, a process called *hadronization*.

These various phenomena were signatures of new physics that could not be explained solely by scaling up p+p collisions. They were signs that new, undiscovered mechanisms were at work when large numbers of nucleons came together such as in a nucleus, or in extreme conditions, such as those in the early universe and inside of ultra-dense astrophysical objects.

³The second generation partner of the strange quark.

Chapter 2

Nuclear Matter: Hot and Cold

2.1 Hot Versus Cold Nuclear Matter

Since the deconfinement of quarks corresponds to a condition where the temperature of the system is above some critical value, it is often called “Hot Nuclear Matter.” Therefore, the region of the nuclear matter phase diagram where quarks and gluons are confined or “frozen” into hadronic states is often called “Cold Nuclear Matter.” Historically, “Hot” QGP systems were created by colliding two large nuclei, such as in Au+Au collisions. In contrast, “Cold Nuclear Matter” systems were studied by colliding smaller nuclei with large ones, such as in d+Au collisions, because it was believed that a large number of interacting quarks was needed in order to describe a thermal system undergoing a phase transition, and that small systems of few interacting quarks had an insufficient number of particles needed to describe such a system.

2.2 The Cronin Effect

The seminal paper titled *Production of hadrons at large transverse momentum at 200, 300, and 400 GeV* by J.W. Cronin, et al. detailed a fixed target experiment that collided protons with a tungsten target and observed a phenomenon which typified cold nuclear matter systems. Later dubbed the *Cronin Effect* after the paper's first author, the experiment found that the production of protons at mid p_T ¹ ($2 \leq p_T \leq 4$) was enhanced when compared to the production of pions [16]. Figure 2.1 shows the production ratio of protons to pions over a range of transverse momentum. In order to measure how nuclear matter affects particle production compared to small systems, they defined a quantity called the *number of effective nucleons*:

$$A_{eff} = \frac{\sigma_{absorption}}{\sigma_{pp}}, \quad A_{eff}^W = \frac{1635 \text{ mb}}{40 \text{ mb}} = 40.9, \quad (2.1)$$

where $\sigma_{absorption}$ is the absorption cross section of the target nuclei, σ_{pp} is the total p+p cross section, and A_{eff}^W is the number of effective nucleons with a tungsten target. In practice, the number of effective nucleons described the number of nucleons that interacted in the collision, with the limiting case of $A=1$ meaning p+p like collisions. The closed circle markers in Figure 2.1 show the data from 23.7 GeV proton collisions on a fixed tungsten target; the open circles show the same data extrapolated to the lower limit of p+p like collisions.

¹Transverse momentum. Scalar quantity of momentum that is perpendicular to beam axis.

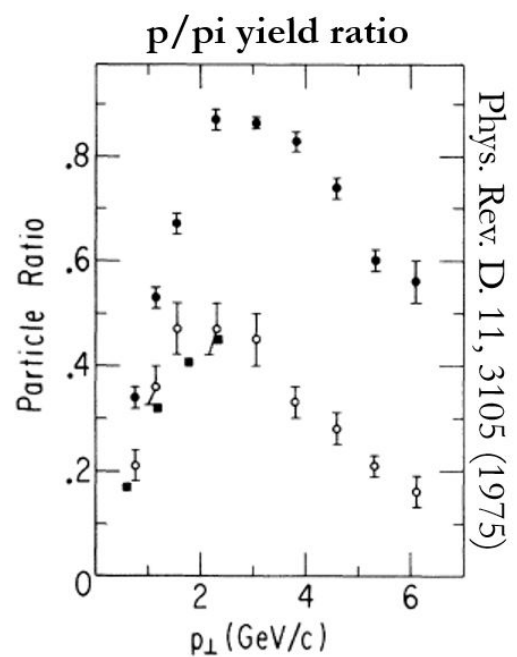


Figure 2.1: Proton vs pion yield ratio from the Cronin paper. Closed circles are the ratio obtained by colliding 23.7 GeV protons on tungsten ($A_{eff} = 40.9$). Open circles are the same data scaled to the low limit of single nucleon-nucleon interaction ($A = 1$).

After the observation of this baryon enhancement in mid- p_T , many set out to come up with theoretical mechanisms that could explain this baryon production preference. The focus of these models was to describe the effect of the nuclear medium on incoming partons². Specifically, the models differentiated between *soft*, *elastic* interactions and *hard*, *inelastic* collisions of partons inside nucleons, and whether soft interactions happened before or after hard collisions. These mechanisms can then largely be categorized into two types, as follows: those where the incoming partons interact with the nuclear medium and those where outgoing partons, created after an incoming nucleon hard scatters, interact with the nuclear medium. These two categories are called *Initial State Interactions* and *Final State Interactions*, respectively.

2.2.1 Initial State Multiple Scattering

The first attempts at explaining the Cronin Effect were made using initial state interactions. Kühn, in 1975, described a mechanism where incoming partons scatter on nuclear partons, randomizing the direction of the incoming parton, before finally colliding with a nuclear quark to produce an event similar to a proton+proton collision [17] (see Figure. 2.2). Since it is unclear how many “soft scatters” happen before the final hard scatter, the p_T spectrum is broadened, which could account for the increase of particle production for the mid p_T range. Furthermore, multiple soft scatters are unlikely to produce pions due to the high p_T required to break color confinement, possibly explaining the mid

²The point-like objects that comprise hadrons described in a model proposed by Richard Feynman to analyze high energy collisions. We now know these *partons* are quarks and gluons but the simplicity of the model lends itself well to describing these collisions and the terminology is still used today.

p_T baryon preference.

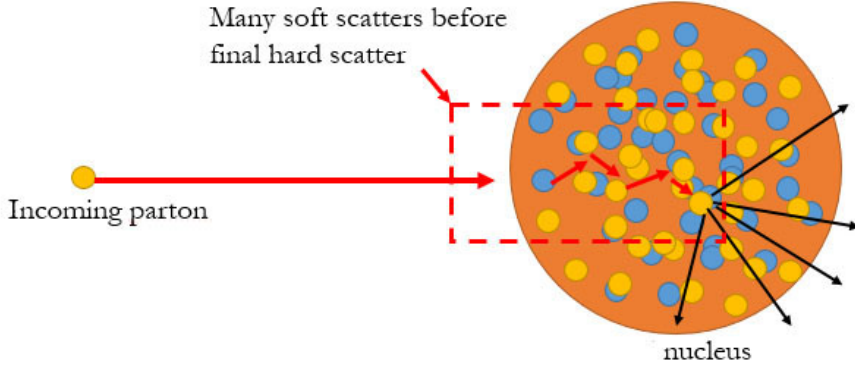


Figure 2.2: Illustration of Initial State Multiple Scattering.

The NA10 collaboration at CERN set out to use back to back lepton probes to study the effect of the nucleus on outgoing parton showers created by hard scattering called *jets*. They collided 140 GeV and 258 GeV negative pions on tungsten targets of various thicknesses and looked for muon pairs produced by quark-antiquark annihilation, also known as a *Drell-Yan Process*. They found the mean squared p_T of the muon pair did not vary substantially as a function of target thickness, which implies that incident partons are not affected by the thickness of the target and, therefore, the path length of soft scatters that would broaden the p_T spectrum is very short. Furthermore, the E772 collaboration, with an experiment colliding 800 GeV protons on H₂, C, Ca, Fe, and W targets, showed that Drell-Yan produced dileptons mean squared p_T did not vary much between the nuclear targets of varying nucleon number [18], i.e., increasing the number of nucleons does not substantially change the net p_T , further showing that initial state contributions to p_T broadening are

minimal.

2.2.2 Final State Multiple Scattering

In 1991, the E609 collaboration at Fermilab studied phenomena in experiments that collided 400 GeV/c protons with hydrogen and lead targets [21]. The conditions of interest were the creation of two back-to-back jets (dijets) produced after an incoming parton hard scattered with a target nucleon³. Since the dijets are produced back to back, they start with the same momentum. Any difference between two jets' momentum could therefore be attributed to a final state interaction. They defined a quantity called *planarity* which measured how back-to-back two jets are. In their words:

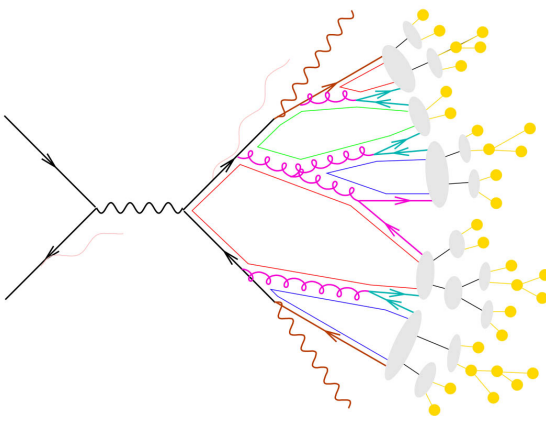
“An axis is found which maximizes the sum of the squares of all momentum components (b_{max}) along that axis while minimizing the sum of the squares of momentum components perpendicular to that axis (b_{min}). Planarity is then defined as:

$$P = \frac{b_{max} - b_{min}}{b_{max} + b_{min}}. \quad (2.2)$$

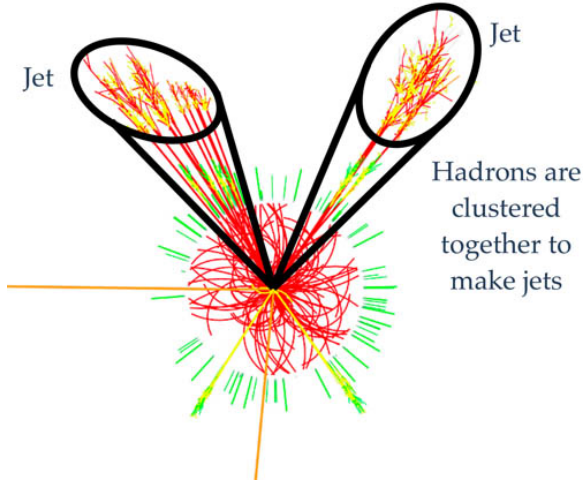
For two narrow back-to-back jets, P approaches 1, while for a circularly symmetric event P is 0.”

The E609 measurement (Figure 2.4) compared the planarity of dijets created from protons colliding with a hydrogen target with the planarity of those created with collisions

³Figure 2.3 describes the formation of dijets.



(a) A Feynman diagram[19] depicting the annihilation of two quarks creating a force carrying boson which creates a quark-antiquark pair. By the rules of QCD confinement, single particles that have a color charge cannot exist by themselves. As they travel away from the vertex where they were formed they create other colored objects around them in a manner that the net color charge of all particles in the group is colorless. Each group of colorless particles is called a jet. Since one jet forming quark is created going one direction, often another is formed going the opposite direction in order to conserve quantum numbers and momentum. This other quark in turn goes on to form its own jet in the same manner. This pair of jets is often referred to as a dijet.



(b) A cartoon illustration[20] of how this process might appear in an experiment.

Figure 2.3: Two illustrations of how jets are formed in particle collisions.

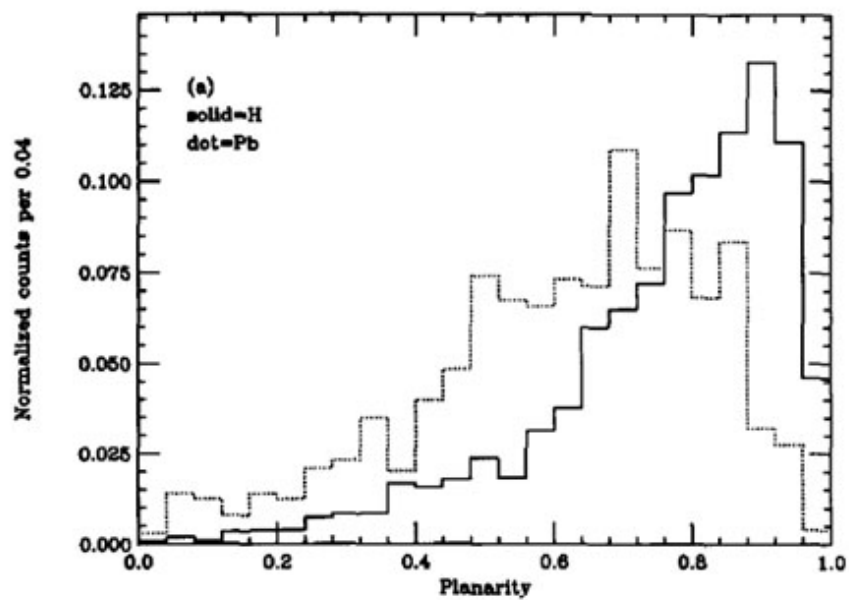


Figure 2.4: Planarity of jets created with protons incident on Pb targets vs H targets.

on a lead target. They noticed a downward shift in planarity and broadening of the spectrum for Pb dijets compared to H although both had very similar jet widths. This measurement led to a paper in 1993 where they concluded that “parton hard scatterings within nuclei involve very little nuclear scattering of the incident parton, but that there is substantial nuclear rescattering of outgoing hard scattered partons.” [22] Because of this, we call this type of mechanism a *Final State Interaction* (for example, see Figure 2.5). While it is true that this could account for the increase in particle production, it does not effectively explain why the effect is stronger for baryons than for mesons and why this preference disappears for at high p_T .

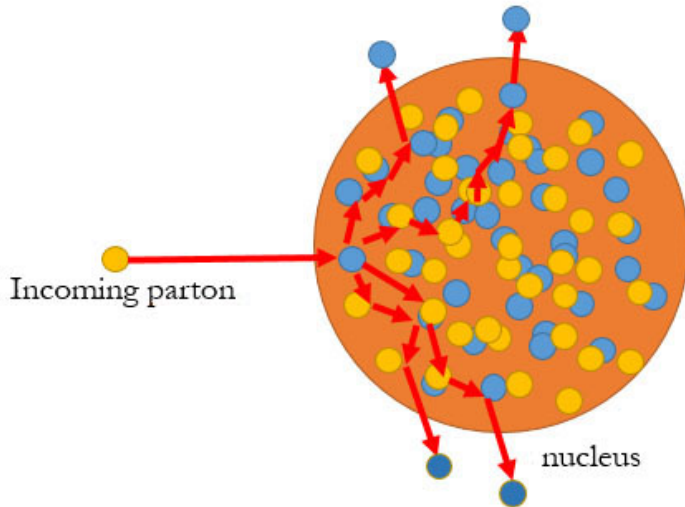


Figure 2.5: Illustration of Final State Multiple Scattering.

2.3 Hot Nuclear Matter: Quark Gluon Plasma

So far, this discussion has stayed within the temperature regime where quarks and gluons are confined to hadronic states. As summarized in the previous chapter, physicists had already seen enough hints that new physics was taking place when the energy density reached some critical value, and consequently RHIC was commissioned to study this phase change.

2.3.1 Collective Flow

As mentioned, one of the signatures of this phase change was that the medium behaved collectively and that, like a fluid, it flowed. *Collective flow* of the medium could be measured by the varying distribution of particles produced about the azimuth, or the *azimuthal anisotropy*. This anisotropy is a measure of how a pressure anisotropy caused by the initial conditions of an ion-ion collision can be correlated to a momentum anisotropy of outgoing particles about the azimuth of the collision. The details of this pressure anisotropy scale with a parameter called collision *centrality*, which is discussed in detail in Section 4.2.1, but for simplicity we can think of centrality as how “head-on” the collision of two ions is, i.e., if they collide with a large overlap or a small one. A large overlap creates a circular shaped pressure gradient whereas a small overlap creates an elliptic shaped pressure gradient as shown in Figure 2.6.

It follows, then, that mid-peripheral collisions create the largest azimuthal pressure

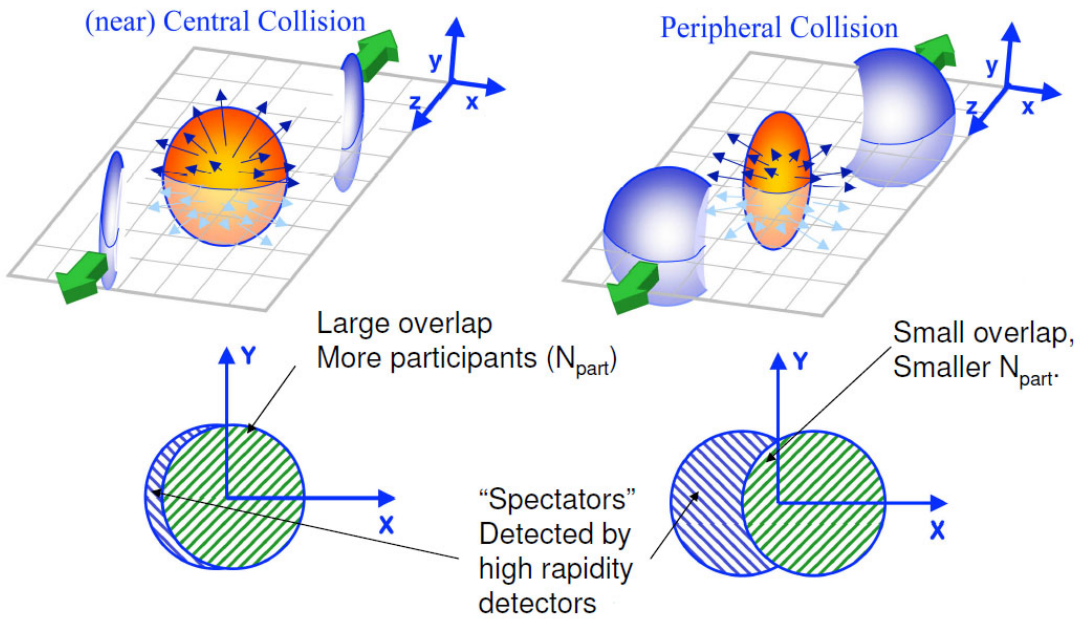


Figure 2.6: An illustration of central vs peripheral heavy ion collisions, geometry of initial conditions. The beam axis goes into and out of the page for the lower diagrams.

anisotropy, and therefore would result in the largest momentum anisotropy of outgoing particles. This pressure anisotropy is largest around the waist of the collision region and weakest at the poles, meaning that the collective flow of the QGP would happen with an elliptical shape, also called *elliptic flow* (see Figure 2.7), measured by the quantity v_2 . There are other types of flow which will be discussed further in Chapter 5.

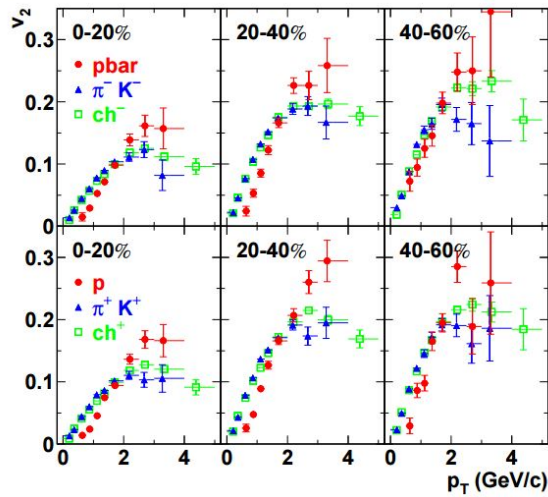
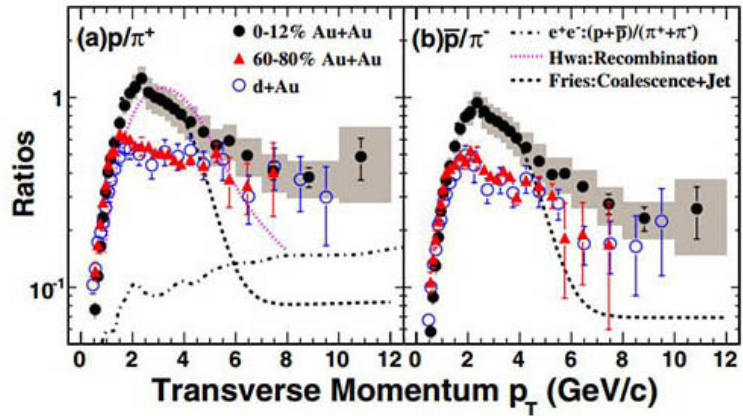


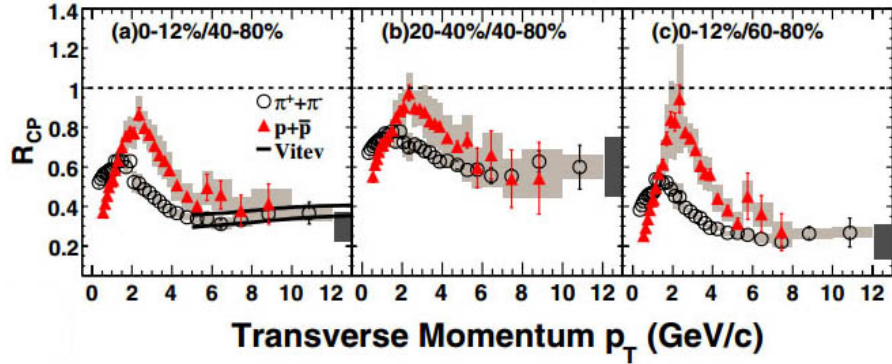
Figure 2.7: Identified particle elliptic flow vs centrality in 200 GeV Au+Au collisions. Flow is strongest for peripheral collisions due to initial pressure anisotropy indicative of QGP collective behavior. [23]

2.3.2 Baryon Enhancement

Another surprising feature of this new phase of matter was the way particles were created from the QGP, namely how it differed from simpler p+p collisions. Particle production in p+p collisions is statistically well-understood for common particles such as



(a) p/π^+ and \bar{p}/π^- ratios for central and peripheral 200 GeV $Au+Au$ collisions. Two leading models are compared to the data as well as the same ratio for 200 GeV $d+Au$ collisions.



(b) Nuclear modification factor, R_{CP} , comparing nuclear effects on particle production in central versus peripheral $Au+Au$ collisions compared to production in binary scaled $p+p$ collisions (see appendix B for a summary on nuclear modification factors)

Figure 2.8: p/π production ratio and R_{CP} as evidence of Baryon Enhancement in central $Au+Au$

pions and protons, and so the particle yields of these were compared to the particle yields of the same in heavy ion systems. If ion collisions behaved no differently than p+p collisions, then one would expect these yields to simply scale by some value proportional to the number of nucleon-nucleon collisions. That is, if two ions each containing N nucleons collided, then we would expect the yields to increase by a factor proportional to N, since a system of N colliding nucleons describes the number of p+p-like collisions. An indication that heavy ion systems were different was that the particle yields were different from those expected from scaling p+p collisions, specifically that particles containing three quarks (baryons) were produced in greater abundance compared to those containing two quarks (mesons) in peripheral Au+Au collisions [24]. This result is shown in Figure 2.8a and shows the comparative yield between protons and pions in bins of p_T . The phenomenon of interest is the apparent baryon excess, or *baryon enhancement*, in the central collision data set for the mid p_T range, which is strongest at around $p_T \approx 2$ GeV/c and disappears at around $p_T \approx 4$ GeV/c. Similarly, the *Nuclear Modification Factor*⁴ for central and peripheral collisions also shows this enhancement in the same range (shown in figure 2.8b). Though this enhancement is similar to the Cronin effect in cold systems, the Cronin effect had already been attributed to multiple scattering effects of partons on “frozen” hadronic states, whereas the asymptotic freedom of quarks in the QGP would not cause the same scattering effects since the whole system was outwardly expanding.

⁴See Appendix B.

2.3.3 Theoretical Models of the QGP Hadron Interaction

Though many have proposed models to describe this baryon enhancement, this discussion will focus on a handful of leading models. They each describe the following various parts of the collision evolution: the description of the nuclei before collision, the moments directly after a collision when the system equilibrates, the behavior of the equilibrated phase, and the freeze-out mechanism.

Relativistic Hydrodynamics

Luzum and Romatschke [25] proposed treating the collective flow of the equilibrated QGP as a *hydrodynamic* problem. That is, they sought to treat the QGP as a *relativistic viscous fluid* since it flowed like a fluid composed of strongly interacting particles traveling at relativistic speeds. Following the relativistic energy-momentum equations for a fluid with shear viscosity, they found that the strength of QGP elliptic flow depended on the ratio of the medium's shear viscosity and the entropy density. Furthermore, they made an important distinction between the rapidly evolving period just after the collision and the time described by the collective behavior of an equilibrated phase. The process of equilibration between the moment of collision and the equilibrated QGP is called *thermalization* and describes the conversion of relativistic ion kinetic energy before collision into deconfined quark matter thermal energy after collision. Their distinction was that this thermalization phase was not required to be very small⁵, and that many details could be

⁵ $\tau_0 < 1 \text{ fm/c}$ ($\sim 3 \times 10^{-24} \text{ sec}$), a.k.a. “early thermalization”.

garnered from the duration and mechanism of this thermalization process such as the eccentricity of the elliptic flow. Since the QGP consists of deconfined quarks, the hydrodynamic model suggests that baryon excess in flow could be attributed to the number of constituent quarks in the hadron. That is, mesons and baryons should flow the same if scaled by the number of quarks they contain⁶, a property that experiments at RHIC⁷ have observed and that is shown in Figure 2.9.

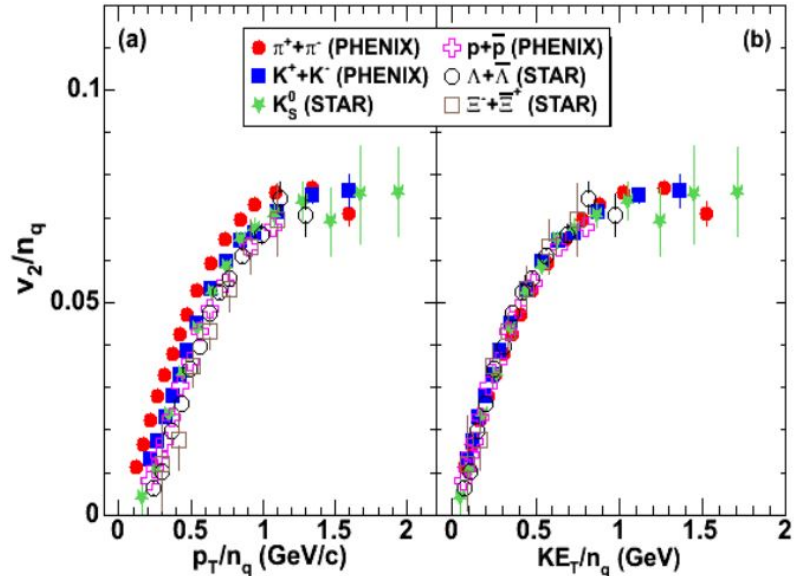


Figure 2.9: Quark Scaled Elliptic Flow Results from PHENIX and STAR[26] in $Au+Au$ $\sqrt{s_{NN}} = 200\text{GeV}$ collisions. Left plot shows flow vs (quark scaled) transverse momentum, right plot tests for partonic degrees of freedom by plotting vs transverse kinetic energy.

⁶Two quarks for mesons, three quarks for baryons.

⁷PHENIX and STAR

Recombination and Fragmentation

Following the idea that a phase change in nuclear matter happens when a critical energy density causes deconfinement of quarks and gluons from their bound states as neutrons and protons, and that the post-collision evolutionary behavior of this QGP is one that expands rapidly, Rudolph Hwa and C.B. Yang postulated that the enhancement of particle production could be explained with a freeze-out mechanism, namely by the ways in which the outgoing partons interacted[27]. They defined two momentum classifications for outgoing partons: *soft* partons with low transverse momentum (in the hundreds of MeV/c) created by the collective thermal expansion of the QGP, and *hard* partons with high transverse momentum created by hard nuclear scattering processes. Since these hard partons result in jet formation, and jets are comprised of a shower of particles, they use the terminology *shower parton* to describe these hard scatter produced partons. The production of particles could then be described by the way these various partons combined to produce hadrons, i.e., the way soft partons combined with other soft partons, the way they combined with hard partons, and the way hard partons combined with other hard partons. This mechanism was termed *recombination* since it relied on the recombining of quarks in partons created from the nuclear collision.

Fries, Müller, et al. simplified this picture, postulating that the reason why protons were produced in abundance was simply that following a collision, the building blocks of protons, up and down quarks, are plentiful and that they simply recombine back into

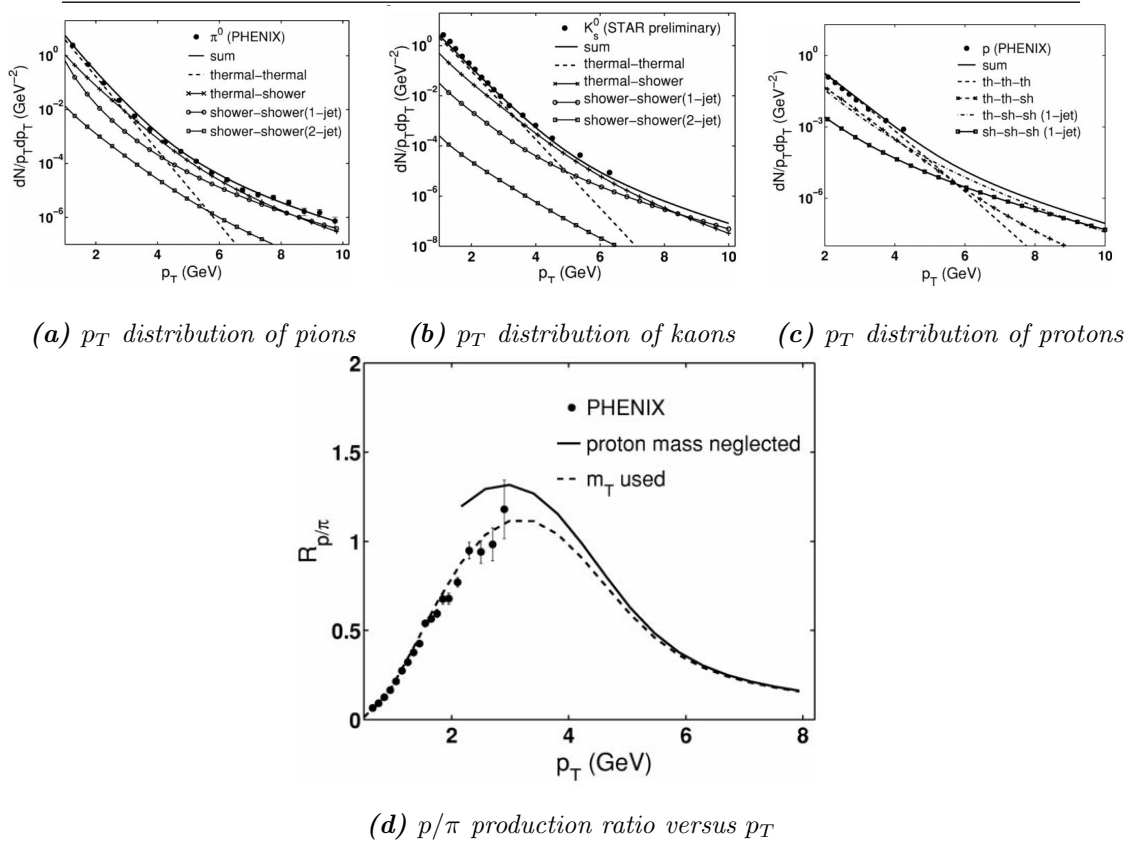


Figure 2.10: $Au+Au$ identified particle measurements compared with recombination model predictions. For the p_T distributions we see three distinct regions of recombination, the low p_T range where soft thermal parton recombination dominates, the high p_T range where hard parton recombination dominates, and the middle range where thermal-hard recombination best describes the data.

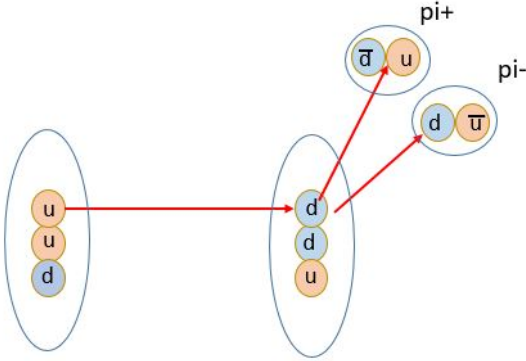


Figure 2.11: Illustration of an example hard scatter resulting in fragmentation to two pions. Here an up quark scatters with enough energy to scatter and release the down quark from being bound in another nucleon. This occurs with enough energy to create antiparticle partners from the vacuum resulting in the formation of charged pions.

their confined states. This mechanism dominates for low p_T (soft partons) since outgoing partons are traveling slowly enough that the constituent quarks remain connected due to color confinement. In contrast, hard partons are more likely to have enough energy to briefly break color confinement, thereby isolating quarks into *fragments* which then create jets of quark/anti-quark pairs, i.e., mesons. This two-regime model naturally creates a baryon preference for low p_T partons by recombination that is met with proportional meson production when the parton p_T is adequately high enough for fragmentation (see Figure 2.10).

2.4 Collective Flow at the LHC

Until now, it had appeared as if the lines in the proverbial sand were clear with respect to the nuclear matter phases and that we had two distinct ways with which to describe the properties of these two states. On the one side, there was cold, hadronic⁸ matter which had its own experimental signatures that could be observed in the collisions of light ions with heavy ones (such as d+Au). On the other hand, there was hot, deconfined, quark matter which behaved another way and was measured using collisions of two heavy nuclei (as in Au+Au). This notion that the two experimental methods allowed the temperature dependent phenomena to be studied separately was brought into question in 2015 when the *Large Hadron Collider* (LHC) at CERN turned on and entered its second era of measurements. At the Compact Muon Solenoid (CMS) they collected data from p+p and p+Pb collisions at 5.02 TeV and compared it to Pb+Pb collisions at 2.76 TeV [28]. While hydrodynamic phenomena like collective flow was expected in the Pb+Pb data, they did not expect to find flow in systems consisting of a small number of interacting nucleons such as p+Pb (see Figure 2.12).

The appearance of flow in systems previously thought of as “cold” was a sign that perhaps the QGP forms much more easily than was previously expected and that perhaps some phenomena found in cold systems, such as baryon enhancement, could be attributed to mechanisms used to explain similar phenomena in hot heavy ion systems.

⁸Quarks confined in hadron states.

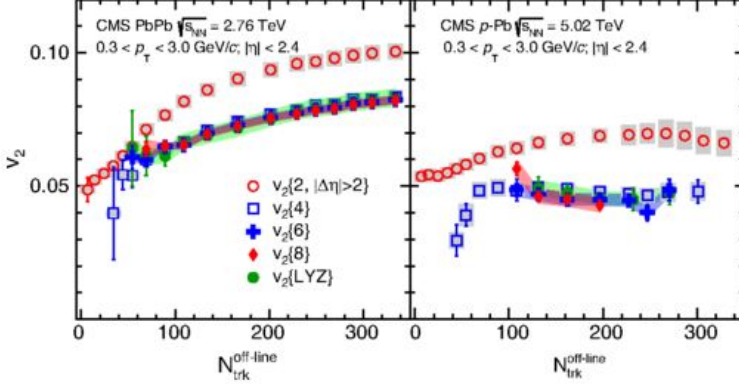


Figure 2.12: CMS result from 5.02 TeV $p+Pb$ collisions showing a nonzero elliptic flow signal versus track multiplicity. [28]

2.5 Recombination and Fragmentation for All?

Furthermore, experimental evidence that the two systems behave quite similarly has been found. In Figure 2.13 particle production ratios (p/π) are compared and it is seen that the baryon enhancement, which was indicative of the QGP formation in peripheral Au+Au collisions, is followed extremely closely by data from central d+Au.

It may seem that the behaviors of the two results in Figure 2.13 are contradicting since the effect happens in central events for the d+Au system but in peripheral events in the Au+Au system, but it is seen upon inspection that the two cases are similar. In the Cronin result, the quantity of effective nucleons described the number of nucleons that interacted in a system. If we make the hypothesis that the QGP would most likely form with a higher number of interacting nucleons, then it follows that, if a QGP were to be formed in d+Au, it would be most likely to form in central collisions. And so, since physicists love

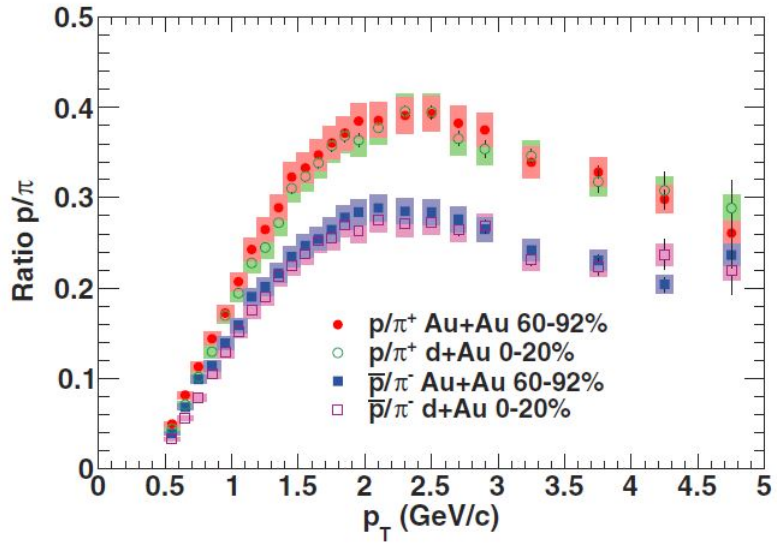


Figure 2.13: p/π ratios compared for central $d+Au$ and peripheral $Au+Au$ [29]

reductionism and unification, and that the evidence makes one wonder if a QGP is formed in these simpler systems, it would be advantageous to be able to describe the two systems with a single mechanism.

Are there even the building blocks to support such a notion that QGP is created in such a simple system as $d+Au$? Recombination is easy to justify in $Au+Au$ since the large number of interacting nucleons makes the formation of the QGP easily achieved and leaves a great abundance of free quarks that are able to recombine. Could there be analogous members at work in the $d+Au$ system? Hwa and Yang set out to adapt their recombination model to fit the phenomena in $d+Au$ [30]. They asserted that since hard scattering creates jets, jets traversing the nuclear medium generate many soft outgoing partons. They argue that these soft partons could behave like an expanding QGP, that is to say, they behave

like the thermal partons in Au+Au collisions. Since thermal parton recombination seems to explain baryon enhancement well, and if soft partons behave like thermal partons, could there be recombination in d+Au as well? Additionally, if there is, could it be a sign that we should see other signs of QGP formation, such as collective flow?

2.6 The Big(ger) Picture

What other phenomena could hint at the formation of a QGP? Many of the mechanisms discussed thus far pertain to the collective behavior post-thermalization, that is, the nature of the thermal-equilibrated quark fluid and its subsequent hadronization or *freeze-out*. However, as noted when discussing the hydrodynamic model, the initial conditions of the relativistic ions and the intermediary evolution of the thermalization process had proven to affect the behavior of the created QGP. These are the leading models of the initial conditions that precede the equilibrated QGP state.

2.6.1 The Glauber Model

The Glauber Model of nuclear interaction, developed by Roy Glauber, pioneered the use of quantum mechanical scattering for systems comprised of many particles. It treats the nucleus as a distribution of nucleons over the volume of a sphere that can be reduced to a continuous nucleon density distribution as a function of the nucleus' radius[31]. Glauber pictured the collisions of two nuclei as a sequence of collisions involving the constituent

nucleons within them. Specifically, that the number of these collisions could be counted by assuming inbound particles travel in straight lines through a nucleus. When combined with the cross sectional nucleon density distribution, it followed that the resulting number of interactions depended on the radius from the center of the nucleus with which the colliding nucleon's trajectory passed through, as shown in Figure 2.15.

The Glauber model is easy to grasp from first principles and is useful for describing such quantities as the multiplicity of produced particles as a function of centrality. It relies very little, however, on the forces at work within the nucleus and physics of matter at relativistic speeds. We know that objects with relativistic velocities experience various effects such as length contraction and time dilation. Additionally, there has been much theoretical work on how the constituents of a nucleus change in the context of asymptotic freedom along with growing collision energy [33].

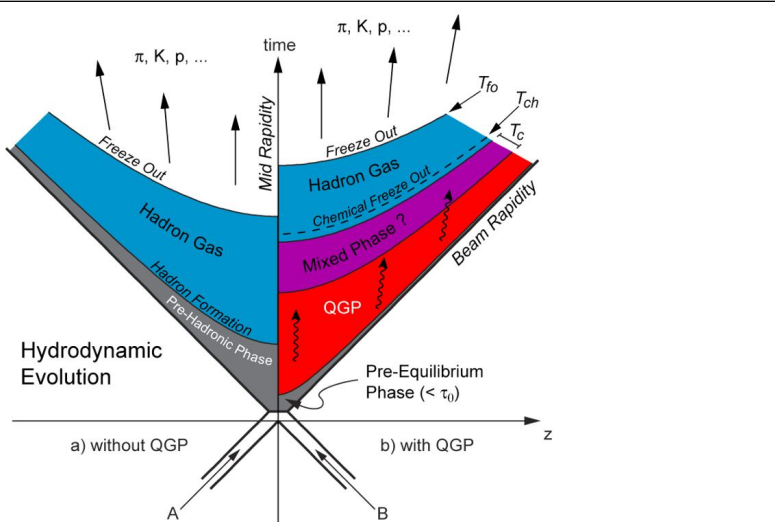


Figure 2.14: A diagram of QGP hydrodynamic evolution.

2.6.2 Color-Glass Condensate

A leading model that describes the behavior of nuclei at ultra-relativistic speeds is the *Color-Glass Condensate* (CGC). The H1 and ZEUS experiments at the Hadron Electron Ring Accelerator (HERA) in Germany studied the structure of protons by colliding them with electrons at a center-of-mass energy of 318 GeV [34]. Their experiments better mapped the *Parton Distribution Function* (PDF), which describes the probability density of particles versus fractional longitudinal momentum. This momentum, the Bjorken x , is how much of a relativistic hadron's momentum is carried by a particular parton within it. We know that the proton is made up of three quarks, the so-called *valence quarks*, but it also has gluons that pop into and out of existence as the mediators of the strong force that holds the quarks together. These gluons cannot carry much momentum since the bulk is carried

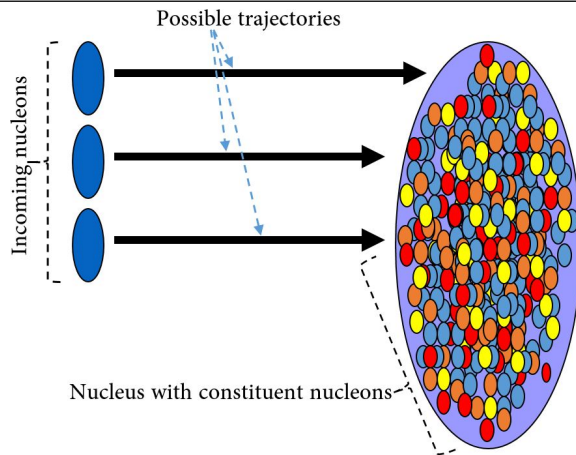
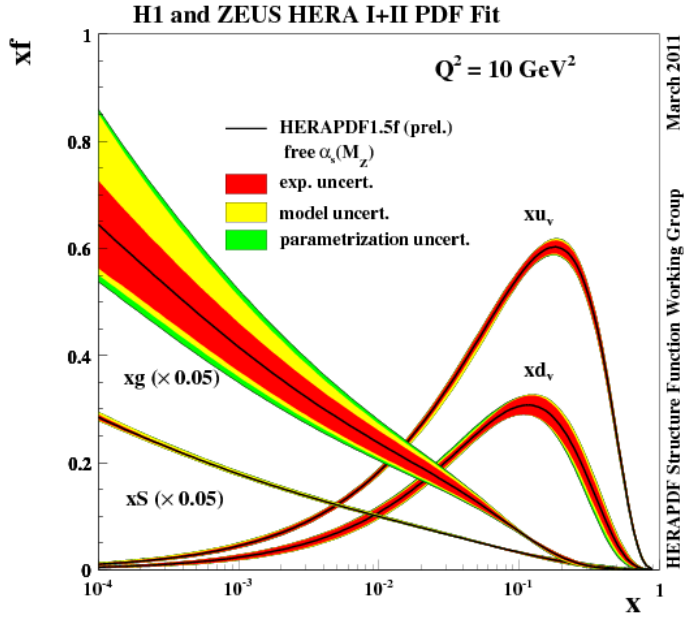


Figure 2.15: A Cartoon of the Glauber Model. The density of constituent nucleons varies by radius. Nucleons from incident nucleus interact with a variable number of nucleons in the other nucleus depending on the radius of the possible trajectory from the center of that nucleus. [32]

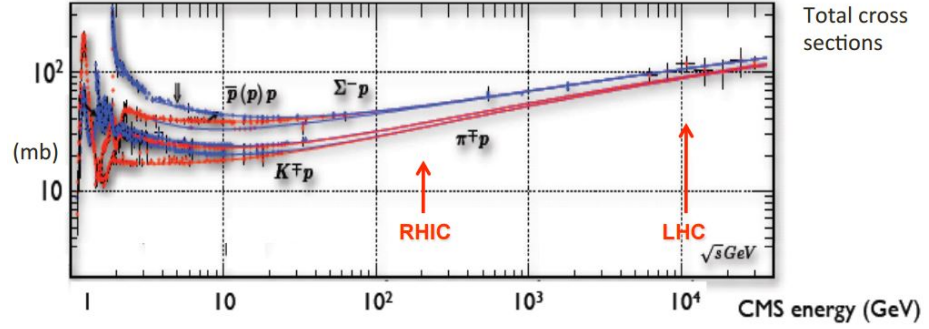
by the valence quarks. Therefore, these gluons have lower and lower fractional momentum, x , as the energy of the proton increases. Furthermore, the PDF from HERA showed that as x decreased, the gluon probability density increased exponentially. At low enough x , the gluon probability dominates the PDF by a factor of 20 (see figure 2.16a), implying that the more energy given to a proton, the more gluons there are packed inside of it.

Additional support for the model comes from the experimental cross section versus energy. The hadron cross section quantifies the likelihood of a scattering event for an incident beam on a hadron. The classical limit of this cross section is the cross sectional area of a target, but for high energy physics it quantifies the number of interactions that could take place inside of a target (in this case a proton). Figure 2.16b shows that the proton cross section increases above its geometrical cross section ($\pi R_{prot}^2 = 30 \text{ mb}^{-1}$) to over 100 mb^{-1} [35][36]. That is, as the energy of a proton increases, it fills with “something” that can interact with incident particles, resulting in an increase of the interaction cross section above the geometrical cross section. Given the PDF at low x , it is extremely likely that this “something” is an abundance of gluons.

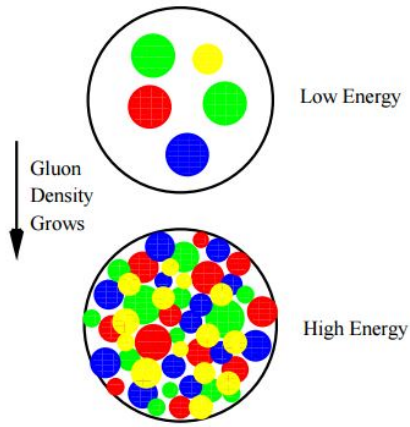
The increase in the number of gluons in high energy protons has interesting implications in the context of Lorentz contracted nucleons. Longitudinally (i.e., along the direction the proton travels), the valence quarks are flattened together due to this contraction; but transversely, the radius of the proton does not change. This leads to a diminishing amount of space inside the proton for the ever-increasing number of these low x gluons to



(a) Combined Parton Distribution Function (PDF) results from HERA experiments[34] shows probability of finding specific species of particles with fractional momentum, x (Bjorken), inside a proton of squared energy $Q^2 = 10 \text{ GeV}^2$. Carrying the bulk of the momentum are the valence up (xu_v) and down (xd_v) quarks as expected, however at low x , “sea quarks” (quarks created by quantum fluctuations, xS) and gluons (xg) dominate. The gluon PDF, specifically, dwarfs the rest by over a factor of 20 at low x . (xg and xS , the gluon and sea quark PDFs as plotted here are divided by 20 so they would easily fit on the graph.)



(b) Proton Cross Section versus Center of Mass Energy with a variety of probes [35]/[36]. Effective cross section increases with energy implying that there is more inside the proton for incident particles to interact with as the energy of the proton increases.



(c) An illustration of gluon saturation for high energy nucleons[37]. As energy increases, the occupation of space by low- x gluons increases.

Figure 2.16

occupy. However, from the PDF, we know that the numbers of gluons have to *increase* as we increase the energy of the proton, and thereby go to lower and lower x for constituent gluons. This implies that the lower the fractional momentum, the more *saturated* the proton becomes with gluons, even more so in larger nuclei systems⁹. This phenomena of large numbers of bosons occupying the same state is where we get the term *condensate* in CGC.

Furthermore, we know that these gluons are force carriers responsible for holding the constituent valence quarks together; however, due to the PDF, we know that they move orders of magnitude slower than the quarks they are binding together. This inhomogeneity of momentum leads to an inhomogeneity of time scales, due to relativistic time dilation. That is, the constituent quarks' relativistic speeds cause the attached slow moving gluons to move incredibly slowly, appearing to be stationary at time scales the high- x valence quarks

⁹Larger by a factor of 10.

experience. This relativistically hindered movement, or *frustration*, has drawn analogs to the condensed matter physics term *glass* which is a classification of materials that have the property of behaving like solids on short time scales and flowing like liquids on long ones.

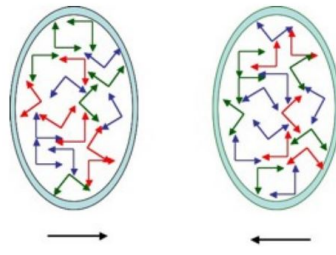
But to what end can we continue to add gluons? Current experimental evidence¹⁰ appears to say that the gluon density can continue to increase boundlessly, but we know that in order to preserve unitarity¹¹, it must reach some limit at some point. This process is called gluon *saturation* and it implies that nature has a *maximum gluon density* that, when reached, points to the existence of a CGC [38]. Due to the prevalence of valence quarks in heavy ions, gluon saturation can be achieved at lower accelerator energies than with protons, making heavy ion collisions ideal for studying these phenomena.

2.6.3 Glasma

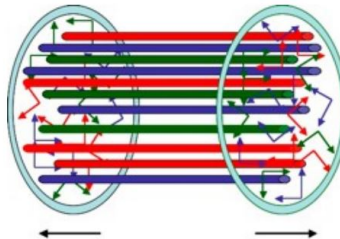
The CGC has found favor in its ability to describe the initial conditions of the ions before the collision, and relativistic hydrodynamics describes well the thermalized QGP, but the transition from collision to equilibrated phase may be described by another mechanism. This equilibration process, called *thermalization*, can be described by the post-collision behavior of the color fields in the ions [40] and depends on the model used to describe the initial conditions. In the moments just before a collision, the ions are Lorentz contracted into a disk-shaped sheet of color glass. The gluon fields on this sheet exist only in the transverse directions as shown in Figure 2.17a. At the moment of impact, the fields interact, and

¹⁰HERA PDF results

¹¹The integrated PDF must equal the total momentum of the proton [38]



(a) A cartoon of two color glass sheets just before collision. Color fields on the sheets exist only in transverse directions.[39]



(b) A cartoon of Glasma formation. The collision of color glass sheets causes the transverse fields from the two sheets to interact and form cylindrical-shaped, longitudinal fields called color flux tubes in the moments just after the collision.[39]

Figure 2.17: The Formation of Glasma from the collision of Color Glass Sheets.

it can be shown [5] that the resulting color fields of this interaction are all longitudinal and must have a net colorless charge for any transverse cross sectional circle whose radius is $> 1/Q_s$. These fields may possess color charge within this cross sectional circle which projects a cylindrical tube of color charge in space (as shown in Figure 2.17b), sometimes called *Color Flux Tubes*. The overall behavior of this thermalization process through the formation and evolution of color flux tubes is a time dependent, intermediary stage between the CGC and QGP called the *Glasma*, a portmanteau of **Glass** **plasma**, so named since it shares properties of both the initial and thermalized states, however it is clearly a new state of matter altogether.

2.6.4 Strangeness Enhancement

The enhancement of strange particle production has historically been promoted as a sign of QGP formation. As mentioned in Section 1.2, NA49 and WA97 collaborations observed the enhancement of kaons compared to pions in their measurements. Kaons provide an interesting probe into the mechanisms inside the QGP since they do not exist prior to the collision, rather, they are created freshly from interactions within the newly produced medium. Rafelski and Hagedorn calculated the rates for the production of strange quarks[41] and found that strange quark production was greater than light flavor quark¹² production in the QGP, implying that an increase in strange hadron production could also be a sign of the nuclear phase transition. Furthermore, strange hadrons are easily measured

¹²up and down (anti)quarks.

in heavy ion collisions. Berndt Müller noted that, since “quark flavor is conserved under strong interaction [...], strange quarks, once produced¹³, are not easy to destroy during the [...] freeze-out stage of a heavy ion reaction.” [42] In the context of the CGC model, strange quarks could be plentiful given the abundance of gluons and that $gg \rightarrow s\bar{s}$ is the dominant channel for producing strange quarks [43].

2.7 Moving Forward

I will show that there is sufficient evidence to say that the nuclear matter created by d+Au behaves collectively and that there should be a non-zero elliptic flow measurement. Furthermore, this elliptic flow is dependent on particle species in that it exhibits baryon enhancement in the mid p_T range, indicative of the formation of a QGP. Unknown phenomenon of interest is the enhancement of strangeness. Proton and pion flow is an indicator of first generation quark recombination due to the presence of these quarks in atomic nuclei, however strange quarks do not exist in the nucleus and are rather created “fresh” from the QGP. Evidence of strangeness enhancement via kaon flow independent of quark scaling may be further evidence of QGP formation in the previously thought-to-be-cold d+Au system. Due to system geometry, flow effects should be maximal with the most central collisions since they create the most interaction of nuclear material (see Section 2.5). Furthermore, as the collisions become more peripheral, the behavior of the system should become more p+p like.

¹³by pair processes, $\rightarrow q\bar{q}$

Chapter 3

Experimental Apparatus

3.1 The Relativistic Heavy Ion Collider

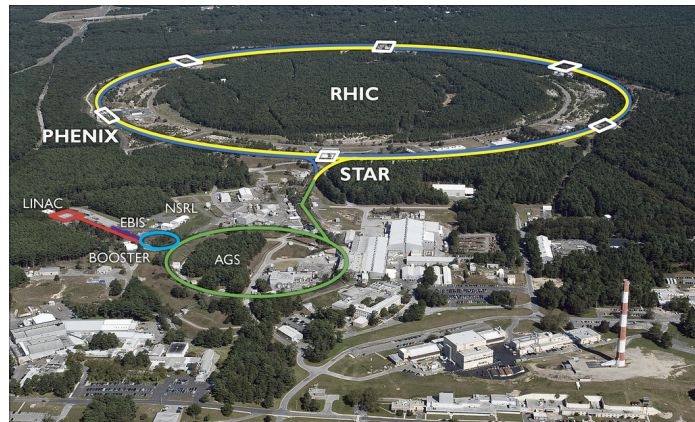


Figure 3.1: An Aerial view of BNL with RHIC and the AGS outlined and the locations of PHENIX and STAR mapped

Based at Brookhaven National Lab (BNL) (Figure 3.1) on the east end of Long Island, New York, the Relativistic Heavy Ion Collider (RHIC) is a particle accelerator and

storage ring that is used to study the properties of nuclear matter. Specifically, it is used to observe the properties and formation of the new state of matter, the QGP, formed by nuclear material at extreme temperature and pressure. RHIC accelerates nuclei which are stripped of their electrons (heavy ions) to energies of up to 200 GeV per nucleon, after which the nuclei are steered to collide together with enough energy to raise the system to extremes of pressure and temperature.

3.2 The Particle Acceleration Process

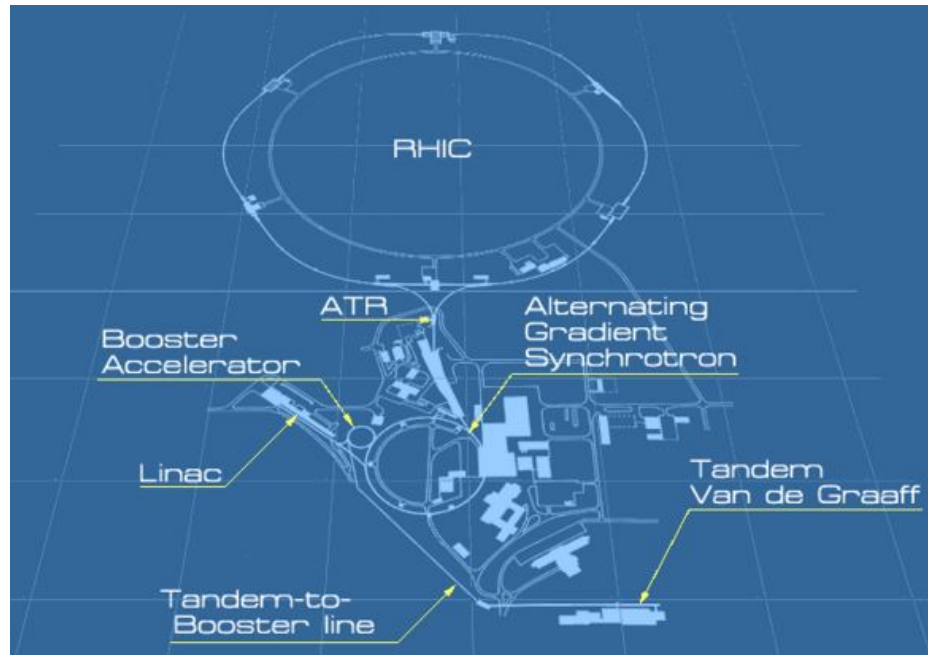


Figure 3.2: Illustration of all the smaller accelerators which are used together in order to boost ions to relativistic speeds at RHIC

The speeds achieved at RHIC are the result of many smaller accelerators working

in concert in order to boost the ions' speed increasingly faster [44]. Ions begin their journey at a compact source and heavy ion accelerator called the Electron Beam Ion Source (EBIS) (located by the Linear Accelerator (LINAC) in Figure 3.2). From there they are transferred to a circular accelerator called the *Booster Synchrotron* which utilizes long-wavelength radio frequency electromagnetic waves, allowing the ions to “surf” on their downward slope. The ions are then fed into the Alternating Gradient Synchrotron (AGS). The AGS was once the proverbial end-of-the-line where the experiments were conducted and studies took place. It is responsible for three Nobel Prizes itself: the discovery of the muon neutrino in 1962, the discovery of charge-parity violation in 1963 (awarded in 1980), and the joint discovery of the J/ Ψ in 1976. The AGS uses the alternating fields of 240 magnets in order to focus and boost the ions to 99.7% the speed of light, after which it is transferred to the *AGS-to-RHIC* transfer line (AtR). The AtR is like a train switchyard wherein bunches of ions are fed into the RHIC rings. These ion bunches are sent through either clockwise in one ring or counterclockwise in the other using a switching magnet.

RHIC is comprised of two concentric rings which are 3.8 kilometers in circumference. These rings use 1,740 helium cooled superconducting magnets to hold beams of these heavy ions which circulate in opposite directions within the two rings. Along the circumference of RHIC there are six points where the counter-circulating beams can be steered to collide (Interaction Regions or IR). Of these six IR, four house different detectors: the smaller PHOBOS and BRAHMS experiments, and the larger PHENIX and STAR experiments.

RHIC is a flexible machine capable of colliding various species of nuclei from protons to uranium [45] over a wide range of energies. Heavy ions such as Au can be accelerated as low as 3.85 GeV/nucleon and as high as 100 GeV/nucleon [46], with a combined center of mass energy of 200 GeV/nucleon. When accelerating protons, RHIC is able to reach up to 250 GeV since the mass/charge ratio is smaller, and is able to do so with spin-polarized beams. It is also able to do this asymmetrically, that is to say, with two different species of nuclei, one in each ring. The system studied in this thesis is one such asymmetric system wherein a deuteron is collided with a gold ion with a center of mass energy of 200 GeV/nucleon (this system is referred to as “d+Au” in shorthand).

3.3 The PHENIX Detector

The analysis described in this thesis was made using the PHENIX detector which stands for *Pioneering High Energy Nuclear Interaction eXperiment*. PHENIX is the largest of the experiments at RHIC and was designed specifically to study the QGP using a wide variety of particle probes at a very high rate with high accuracy. It consists of a collection of various detectors assembled into four spectrometers called *arms* (see Figure 3.3). The muon arms are used for studying physics phenomena at forward rapidity¹ ($\eta = |1.1 - 2.4|$). [47] The system of detectors used for the reconstruction of event tracks of import for this analysis are contained in the *Central Arm*. Accompanying the Central and Muon Arms is a magnet system called the *Central Magnet* and *North and South Muon Magnets* according

¹See Appendix A for discussion on rapidity.

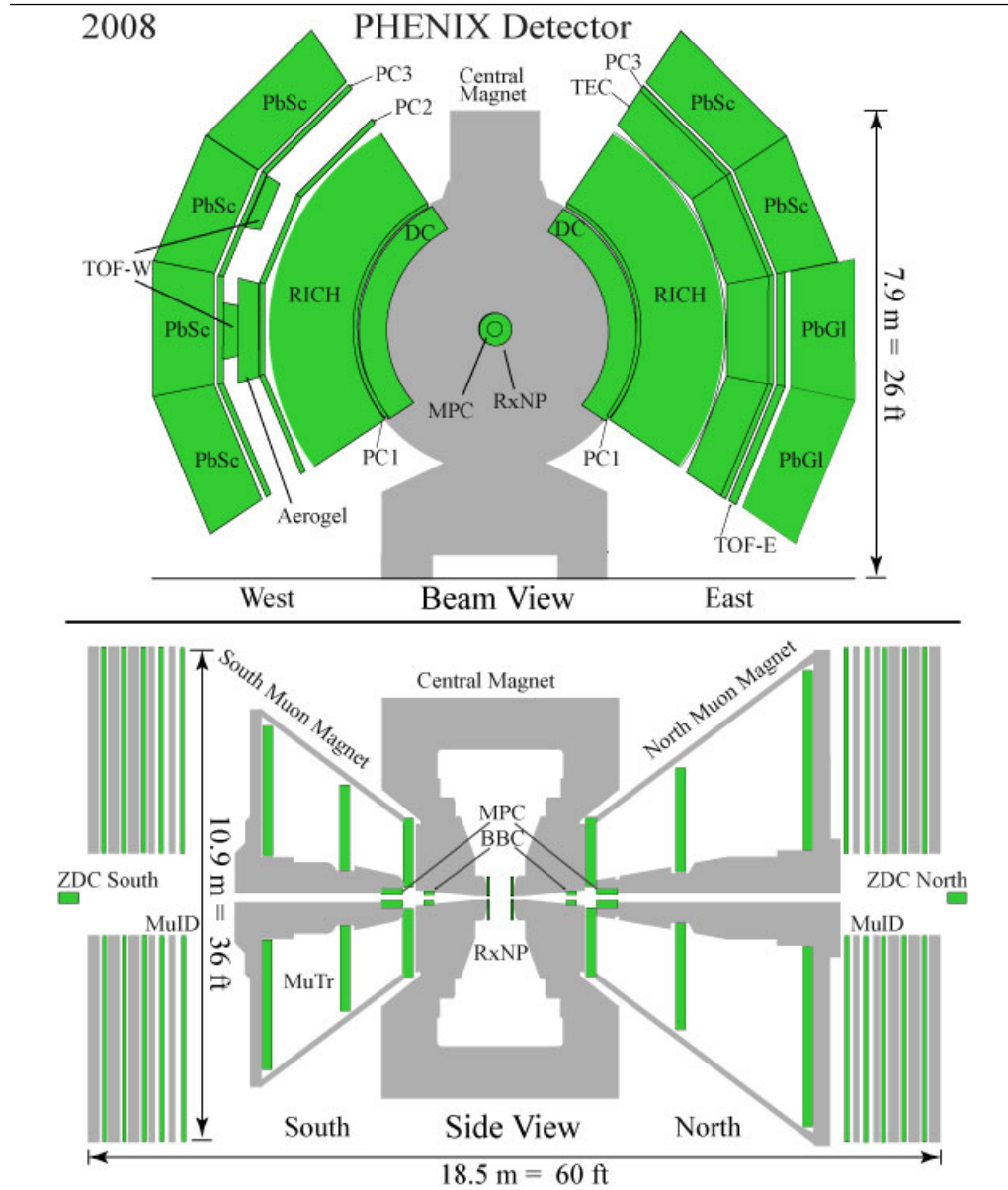


Figure 3.3: The configuration of the PHENIX detector for Run 8 (2008). The diagram labeled Beam View shows the East and West Central Arm spectrometers. In this picture the ion beams would travel into or out of the page through a hole in the center of the region MPC detector. The Side View shows the North and South Muon Arms and the location of event characterization detectors such as the ZDC, BBC and RXNP.

to their location in PHENIX. The Central Magnet is an axially symmetric field around the beam axis generated by two pairs of Helmholtz coils. The coils are operated independently and are able to be run in various configurations of positive and negative orientation in order to determine systematics [48]. A plot of the field strength vs radius for different configurations of the central magnet is shown in Figure 3.4.

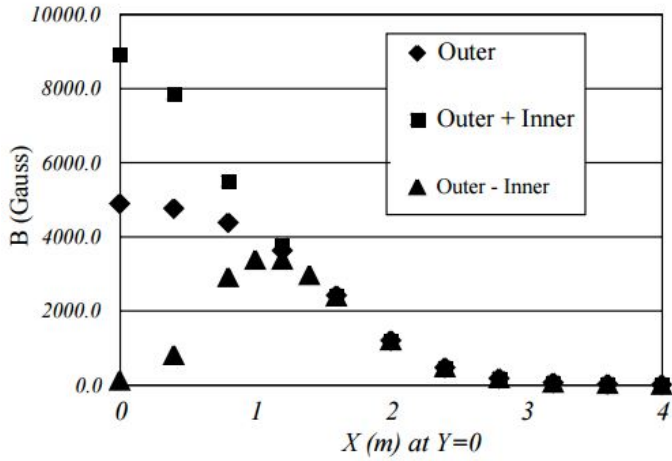


Figure 3.4: PHENIX Central Magnet Field Strengths for different polarities of inner coils vs radial distance from center of IR

3.3.1 Central Arm

Covering a rapidity range of $\eta \leq |0.375|$, the Central Arm consists of an East and a West Arm that each cover 90° azimuthally [49] and is a complex, multi-layered, multi-system spectrometer capable of measuring a variety of particle probes. The Central Arm is shown in Figure 3.3 as its individual subsystem detectors highlighted in green². No single

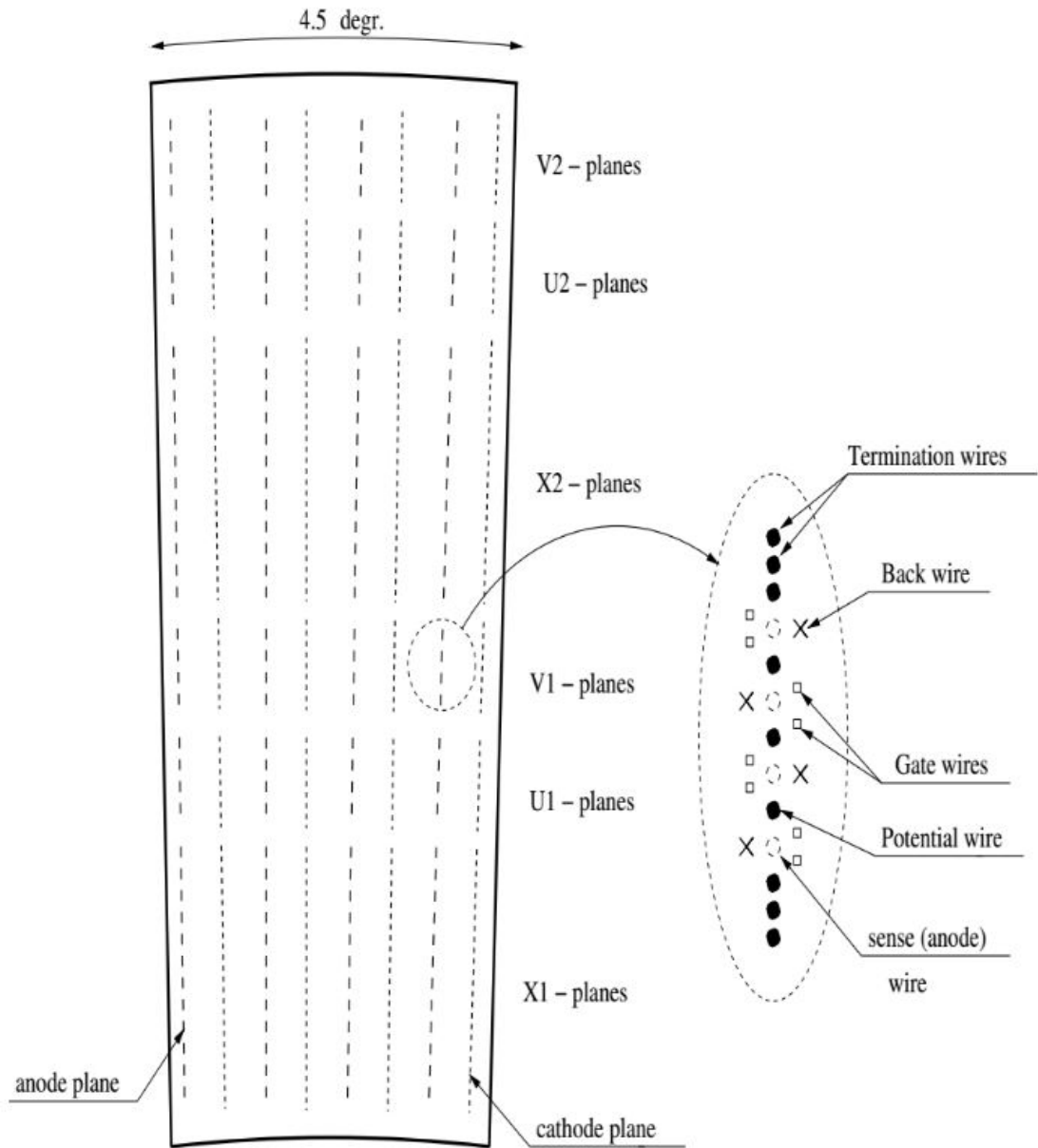
²With the exception of the MPC and RxNP which are not part of the Central Arms, but are in the Muon Arms.

device is ideal for measuring every aspect of a collision event, and, as such, different device technologies that are ideal for measuring specific quantities can be used in concert to gather clean and precise data. In this section the various individual detectors in the Central Arm used in this analysis are discussed.

Drift and Pad Chambers

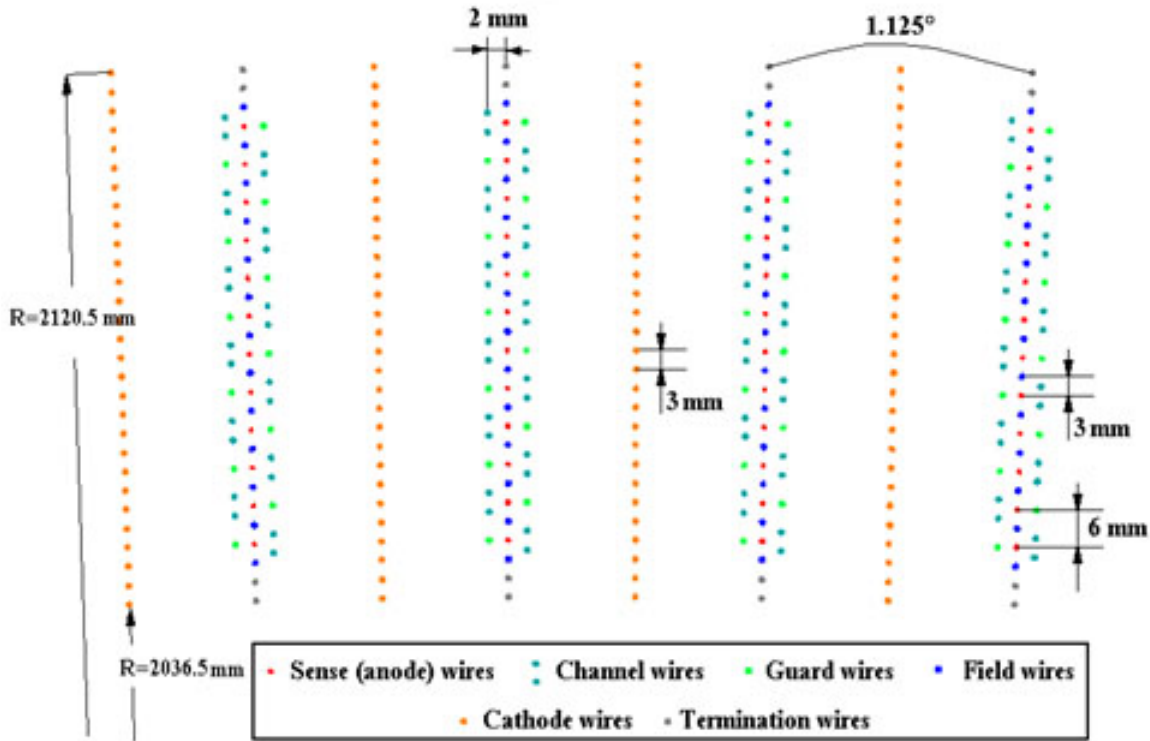
Particle trajectories are tracked using the Drift Chamber (DC) and the Pad Chambers (PC 1,2, and 3) [50] (labeled DC, PC1, PC2, and PC3 in Figure 3.3). The DC is a multiwire jet-type drift chamber located between 2.02 and 2.48 m radially from the interaction point, constructed from 6 modules comprised of networks of wires or *nets* in each arm. In principle the DC is similar to a wire chamber; when a charged particle travels through the gas in the DC, the gas atoms are ionized and these electrons and ions are accelerated to anode and cathode wires, respectively, which collect this ionization and send a signal proportional to the ionization effect of the traveling particle. The DC is filled with a gas that is selected to have a uniform drift velocity close to the anode wires, i.e., a gas where the ions and electrons created by outgoing charged particles have a linear relation in position and time such that $x(t) = v_{drift} * t$ within the active region. The gas chosen is a mixture of equal parts argon and ethane, also chosen for the mixture's high gas gain amplification and low diffusion coefficient. The wire nets in the DC are arranged in different predetermined ways with respect to the beam axis. The six modules containing the wire nets are designated names: X1, U1, V1, X2, U2, and V2 (see fig. 3.5). There are twelve

anode wires in each X net and the wires are configured to be parallel to the beam axis so that they can be used to measure the azimuthal angle, ϕ . The U and V nets are stereo pairs with four anode wires in each net and are tilted by an angle of 4.5° with respect to the beam axis. This angular bias allows for measurement of the track's z-component with high resolution. Furthermore, all wire nets are oriented in layers radially such that outgoing tracks deposit linear, correlatable signals in the DC. Additionally, since the DC is the first detector subsystem that outgoing particles created in a collision pass through, it is also used in conjunction with other detectors in order to accurately determine track trajectory through all of the detectors in the central arm. The method of track reconstruction will be discussed in Section 4.3.



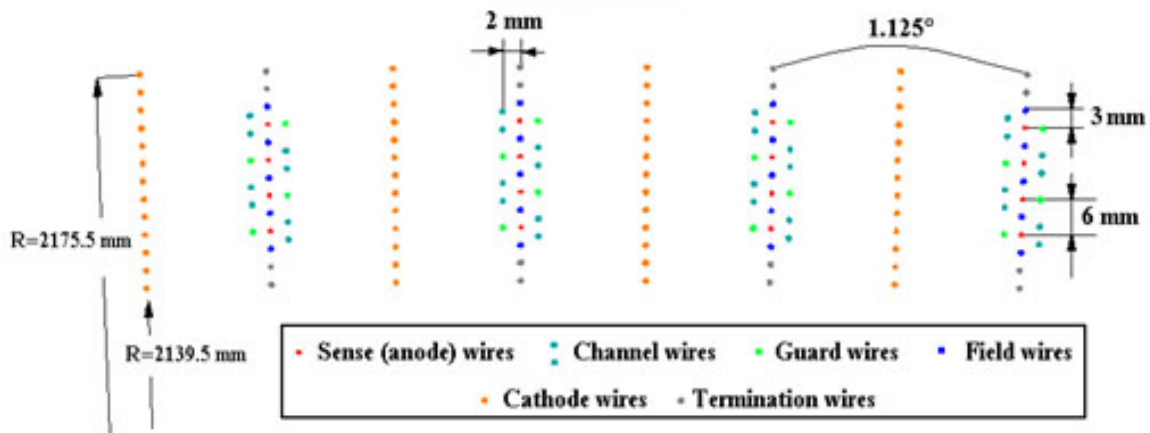
(a) A diagram showing the radial configuration of the various wire nets in the DC. The X1 plane is the innermost radius DC wire network, followed by the stereo pair U1 and V1, X1, and another stereo UV pair.

X1 plane



(b) The radial configuration the X-type wire nets in the X1 plane. Each X-type wire net consists of twelve anode wires.

U1 plane



(c) The radial configuration the U-type (and V-type) wire nets in the U1 plane. Each U-type wire net consists of four anode wires and are paired with a radially following identical V-type wire net.

Figure 3.5: Diagrams of DC wire configurations.

The Pad Chambers [51] (PC) are three individual layers of pixel detectors. The PCs have the same azimuthal coverage as the DC and the rest of the Central Arm and are located at increasing concentric distances from the collision vertex, the DC being the inner most detector, followed immediately by PC1³ (see fig. 3.6). PC2⁴ only exists in the west arm however PC3⁵ exists in both arms. The pixels in these detectors are arranged into nine pixel clusters called “pads” which are read out by a single channel. The pads in the innermost radius PC (PC1) are 8.4 mm x 8.45 mm and the pads in PC2 and PC3 are sized to maintain the same angular resolution at further radial distances. The small size of the individual pads allows for a large pixel density which is important for maintaining the separation of individual track signals in a high luminosity, high multiplicity event such as that of central heavy ion collisions. Since these detectors can be used to accurately determine particle track trajectories, and since charged particle trajectories curve under the influence of a magnetic field, the track curvature can be used to determine the particle’s momentum. This track location data is also used to match with other detector data such as calorimetry, time of flight, and Cherenkov counters.

TOF: Time Of Flight Detectors

In addition to the tracking detectors, this analysis utilizes high accuracy Time of Flight (TOF) detectors that are used to measure the time it takes for charged particles traveling through the Central Arm to go from the event vertex to the detector. [52] There

³Located 2.5 m radially from nominal IR.

⁴Located 4.2 m radially from nominal IR.

⁵Located 4.9 m radially from nominal IR.



Figure 3.6: Pad Chamber 1 on top of the Drift Chamber.

are two TOF detectors in PHENIX, one on the East Arm and one on the West Arm. Located five meters away from the collision vertex and in the lower two sectors of the east arm (see Figure 3.3) the TOF East (TOFE) is a scintillation detector with a timing resolution of $\Delta t_{res} \leq 100ps$. It covers $\Delta\phi = \pi/4$ and $\eta < |0.35|$.

Scintillators are a special type of material that fluoresces when hit by a charged particle or high-energy photon. The TOFE is comprised of 1000 15.1 mm "slats" of plastic scintillation material with two photomultiplier tubes (PMT) on either end of the slats (see Figure 3.7). These PMTs are devices that utilize the photoelectric effect to translate photons generated in the scintillator into an electric signal. The strength of this signal is often proportional to the number of electrons generated by the photons incident on the PMT, hence they are called photoelectrons. Since we know the length of the slat and the

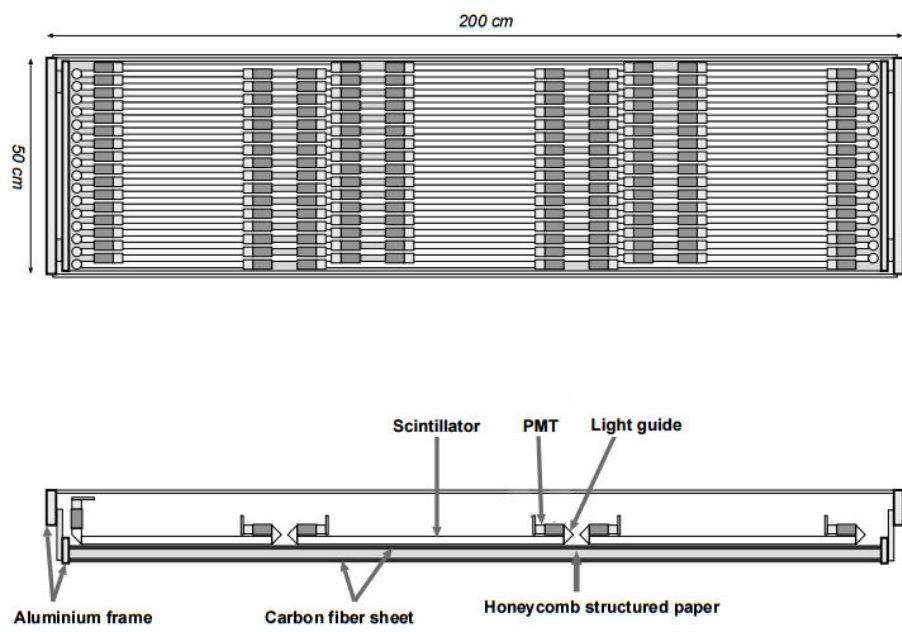


Figure 3.7: A schematic of the slat layout in the TOFE. The top figure depicts the slat layout facing the IR, the bottom figure is a side view of the slats showing the configuration of the subparts of each slat.

speed of light in the scintillation material we can easily calculate both the time when the particle first hit the slat (T_0) and the position where the particle hit the slat (y),

$$T_0 = \frac{(T_1 + T_2) - L/v}{2}, \quad y = \frac{T_1 - T_2}{2}v \quad (3.1)$$

where T_1 and T_2 are the times measured by PMTs 1 and 2 relative to the event start time measured by the BBC (see Section 4.2.2), L is the length of the slat, and v is the speed of light in the scintillator.

Figure 3.8: An illustration of a single slat in the TOFE

In the West Arm, the TOF West (TOFW) is a 1024 channel Multi-gap Resistive Plate Chamber (MRPC) detector with a timing resolution of $\Delta t_{res} < 100ps$, located 4.85 m from the collision vertex and also covering $\Delta\phi = \pi/4$ and $\eta < |0.35|$. The MRPC works on the same general principle as a basic Resistive Plate Chamber (RPC) which is comprised of two high resistivity plates separated by a volume of gas. On one resistive plate is a sheet of conducting material that is used to maintain a constant electric field across the gas gap. The other resistive plate has an array of conducting readout strips. When a charged particle travels through the gas it causes an electron-ion avalanche similar to what happens in a drift chamber. The electron avalanche is accelerated under the influence of an externally applied electric field toward one of the readout strips resulting in a “hit” signal which is then amplified by electronics.

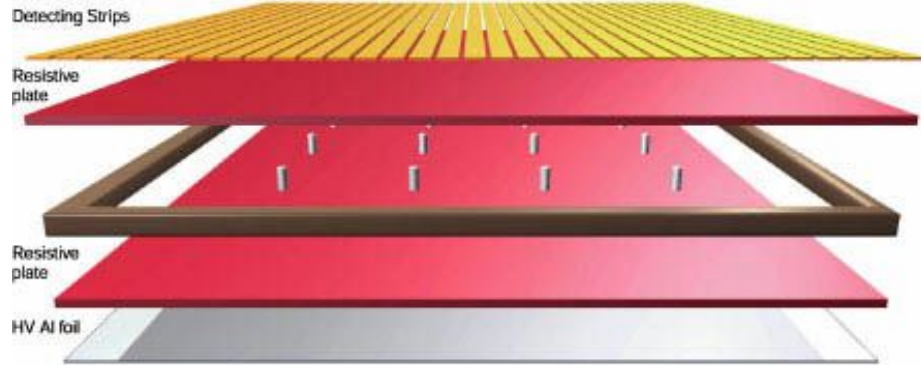


Figure 3.9: Diagram of a basic RPC [53]

A MRPC is a version of an RPC with alternating layers of the resistive material and gas gaps sandwiched together with the high voltage surface and readout strips on the outermost sides of the device [54] (see Figure 3.9). The resistive plates inside the sandwich are electrically isolated and are transparent to the fast signals of incoming particles. An externally applied electric field induces charges on the surfaces of the resistive plates, causing each of the small gas gaps to be held at the same potential. Like the basic RPC design, incoming particles ionize the gas causing an avalanche of electrons and ions in each of the gas gaps and an electric signal is deposited on the readout strips. The total signal the strips see is the *sum* of all of the electrical activity in each of small gaps. By using this configuration of small parallel uniform gaps, a greater precision is allowed than conventional RPC designs, which lends itself well to high precision timing detectors.

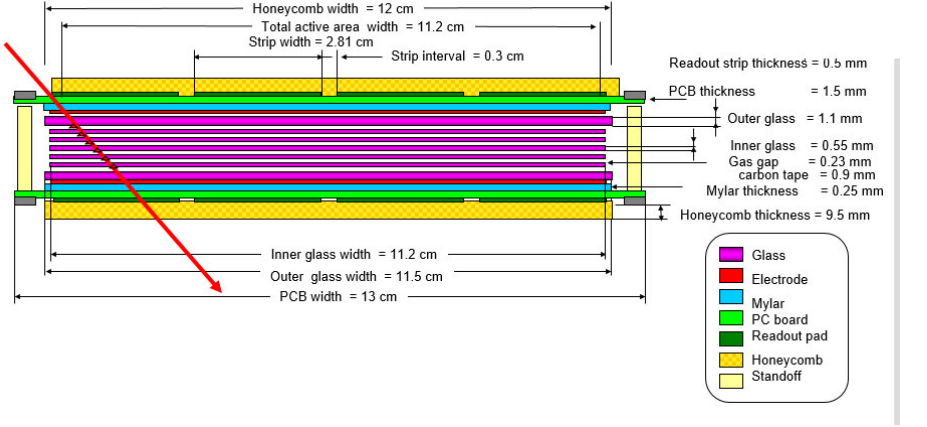


Figure 3.10: Cross sectional diagram of the MRPCs used in the TOFW

ACC: Aerogel Cherenkov Counter

As measured track momentum increases, the timing resolution of the TOF detectors causes larger uncertainty in the timing measurements which, in turn, leads to a larger uncertainty in the particle mass. This uncertainty broadens the Gaussian-shaped particle mass distribution, gradually causing individual mass distributions to overlap, and eventually become inseparable, as p_T increases. The high resolution capabilities of the TOF detectors only allow them to separate π^\pm , K^\pm , and p / \bar{p} signals up to certain transverse momentum p_T thresholds (π/K separation becomes difficult above $p_T = 2.1$ GeV/c impossible above 2.8 GeV/c, K/p separation is possible only up to 4 GeV/c). The distinct masses of the particles of interest do provide an additional method of separating particle signals, since two particles of different mass with the same momentum have distinct velocities. This is the principle with which a Cherenkov detector works. Cherenkov radiation is light that is emitted in a material when a charged particle travels through it with a velocity faster

than the speed of light in that medium. This medium, called a Cherenkov radiator, can be carefully selected such that its intrinsic speed of light is such that lighter particles with higher velocities cause Cherenkov radiation but heavier particles which travel slower given the same momentum will not. This threshold is given by

$$E_{threshold} = \frac{nm}{\sqrt{n^2 - 1}} \quad (3.2)$$

where n is the index of refraction in the Cherenkov radiator and m is the mass of the particle.

Using this, a Cherenkov detector acts as a logic detector categorizing tracks as those that either “fire” or “veto”, that is to say tracks that radiate versus tracks that don’t. In the case of separating π^\pm mesons from K^\pm mesons for p_T tracks where their mass signals overlap so strongly that they cannot be uncorrelated, the radiator was chosen such that the pions will radiate in the detector, but the kaons will not. Pions and kaons are indistinguishable for $p_T > 2.8$ GeV/c, so the radiator chosen to separate the signals is a silica aerogel ($n \approx 1.011$).

The Aerogel Cherenkov Counter (ACC) is comprised of 160 tiles of silica aerogel. Each tile is affixed to a cube which forces radiated Cherenkov photons to reflect internally until they hit a PMT (see Figure 3.11a). These cubes are filled with air and are covered on all exposed sides by a Gore-Tex reflector except for the “front” facing aerogel tile side and the two cutouts where the PMTs attach. Due to the fact that the cube uses internal reflection to maximize the number of photons collected by the PMTs it is called an integration cube.

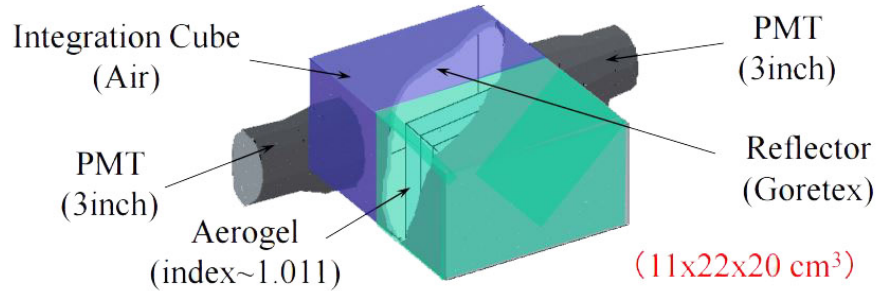
There are two PMTs located opposite from each other for each cube. To account for the space taken by PMTs on the ends of the tiles, the ACC is two sided and the tiles are oriented such that the opposite side tile occupies the gap where PMTs would be situated (this configuration can be seen on the “Top View” labeled diagram on Figure 3.11b). There are ten rows of eight tiles on each side for a total of 160 tiles.

The ACC is located in the west arm covering the half of the azimuthal coverage that the TOFW covers and with the same rapidity coverage (see Figure 3.3). When used in conjunction with the TOFW, it can provide pion/kaon separation for $p_T < 4$ GeV/c and can discriminate protons for $p_T < 7$ GeV/c. The total particle identification capabilities of the combination of the TOFW + ACC is shown in Figure 3.11c.

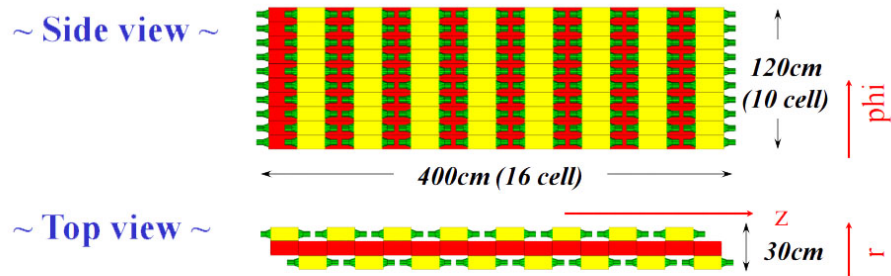
EMCal and RICH: Electromagnetic Calorimeter and Ring Imaging Cherenkov Counter

Two other detectors that provide important track data are the *Electromagnetic Calorimeter* (EMCal) and the *Ring Imaging Cherenkov Counter* (RICH). Each arm has full coverage with both the RICH and the EMCal and they are often used together in order to study electrons via the EMCal/RICH Trigger (ERT). For the scope of this analysis, only the RICH is used in order to reject electron tracks which can contaminate the pion signal; the EMCal will be discussed for completeness.

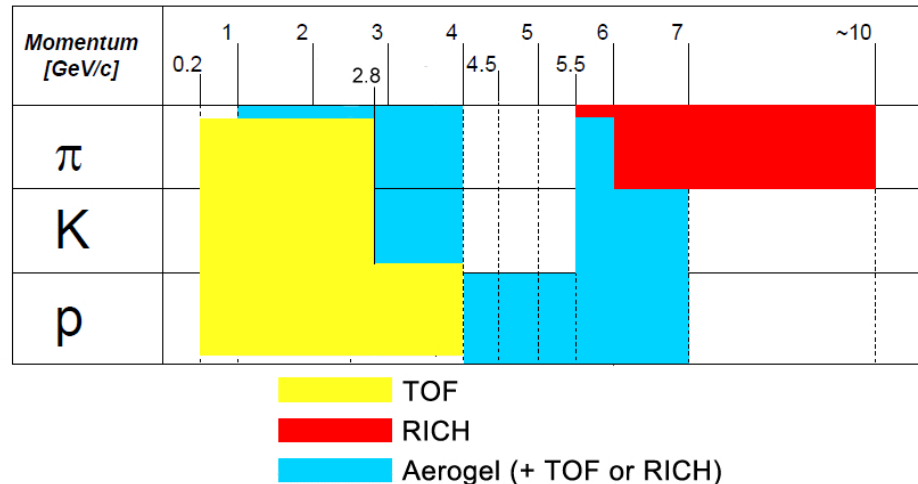
As evident from its name, the RICH (Figure 3.12) is a Cherenkov counter that is used in a similar fashion as the ACC, namely, to discriminate between particle species



(a) A schematic of one tile in the ACC



(b) A schematic of the layout of the Aerogel Cherenkov Counter. Yellow boxes represent Aerogel tiles and integration cubes. Green cylinders on either end of the yellow boxes are the PMTs.



(c) Chart of Particle Identification capabilities over a range of transverse momentum with combinations of detectors.

using Cherenkov radiation as a logic trigger. In the case of RICH, we are interested in separating pion and electron signals. It is filled with CO₂, which was chosen because it would allow electrons to radiate at very low p_T (> 0.018 GeV/c) while pions would not until the relatively high p_T of 4.87 GeV/c. Cherenkov radiated photons are emitted parallel to each other along the track path as electrons move through the detector. The outer surface of the RICH is a series of mirrors arranged to form a spherical mirror which focuses that Cherenkov light onto the 2560 PMTs/arm which line the inner surface of the RICH. This results in a ring shaped Cherenkov signature as measured by the PMTs, hence the name: Ring Imaging Cherenkov Counter.

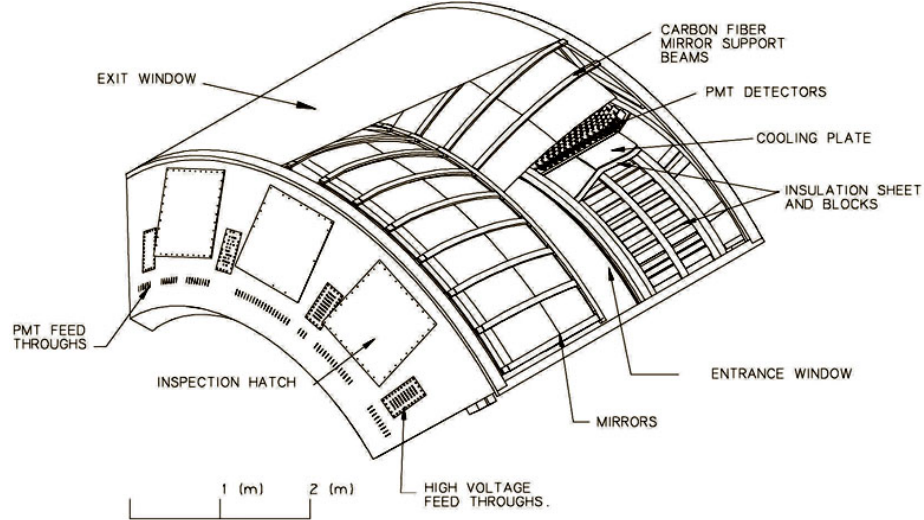
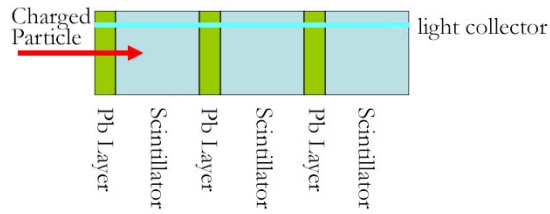
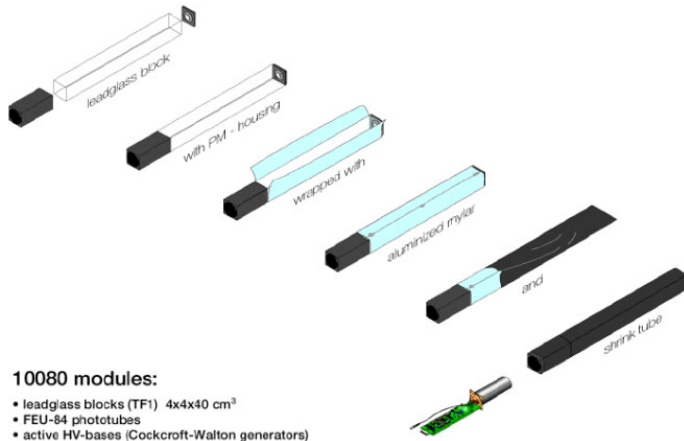


Figure 3.12: A diagram of the RICH

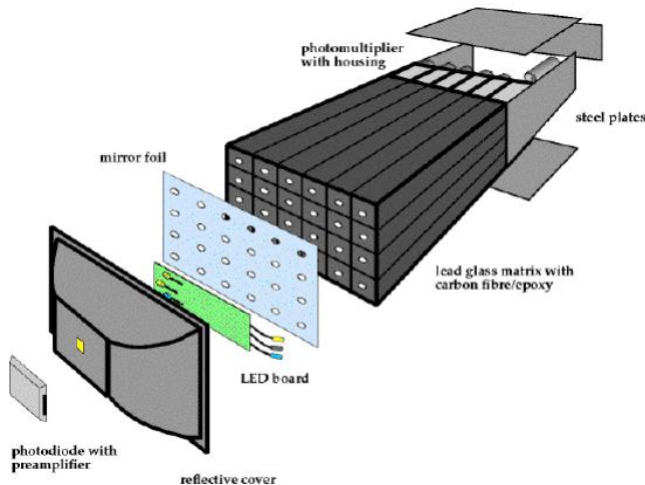
The EMCAL measures the energy of charged particles and is broken up into eight sectors, with four sectors in each arm [49]. Six of the sectors (all four of the west arm and



(a) Schematic of a PbSc module. Pb layers cause EM showers which create light in the scintillators and are detected by the light collectors.



(b) Construction of PbGl modules.



(c) One PbGl super module

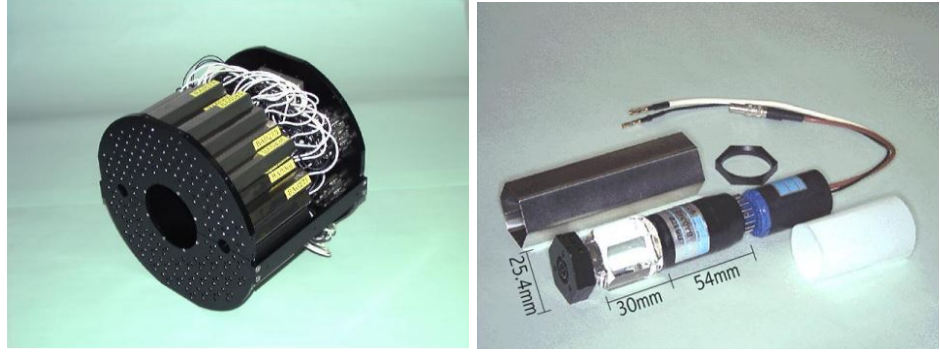
Figure 3.13: Schematics of EMCAL components

the top two in the east arm) are made of channels comprised of alternating layers of lead and scintillator (PbSc) material (fig 3.13a). The lead layers cause incoming particles to shower into the scintillator layers that generate light which is detected by PMTs. The lower two sectors in the East Arm are comprised of 10,080 uniform lead glass Cherenkov radiator towers (PbGl) (Figures 3.13b and 3.13c). These towers have PMTs attached on one end and are wrapped individually in reflective Mylar and shrink wrapped to form *modules*. They are then placed in grid-like networks and each 16 module x 12 module structure is read out by one photodiode/preamplifier combination.

Two types of detector are used in the EMCal because they each have their own strengths. PbSc is more linear in response and is better at timing than PbGl thanks to its alternating layers, whereas PbGl is a tried-and-true design used in previous experiments such as WA98 at the SPS at CERN for its exceptional granularity and accurate energy measurement. Because they are two separate systems, they have different systematics, and, therefore, we have a higher confidence level for the physics results from the EMCal.

3.3.2 Forward and Global Detectors

Though the bulk of this analysis is dependent on the central arm detectors, many aspects of reconstruction, namely event characterizations (start of the event timer, the event vertex, centrality, and event reaction plane), are dependent on a handful of forward-rapidity detectors which will be briefly discussed here.



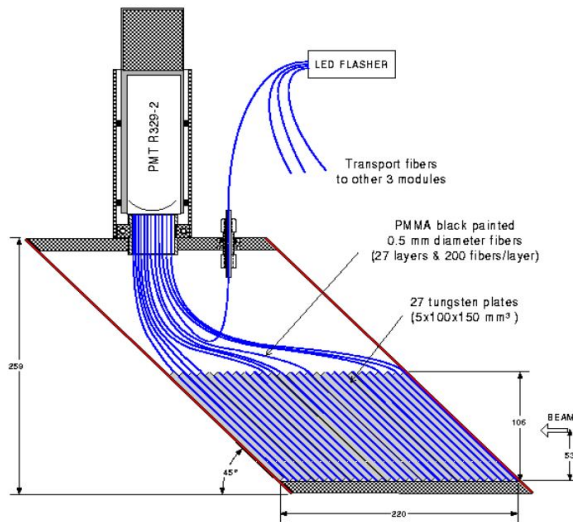
(a) An illustration of a BBC

(b) A single element of the BBC

Figure 3.14: The Beam Beam Counter

BBC: Beam-Beam Counter

Of the forward detectors, the *Beam-Beam Counter* (BBC) [55] is probably the most important because of its ability to measure the various global event parameters. There are two BBCs, one on the north side and one on the south side of PHENIX both equidistant (144 cm) from the center of the interaction region (IR). The constituent detector (Figure 3.14) elements are made of quartz Cherenkov radiators attached to meshed dynode PMTs housed in hexagonal encasements. These elements are arranged in a toroidal shape (inner and outer radii of 5 cm and 30 cm respectively) in order to allow the ion beams to pass through the center while still getting full 2π azimuthal coverage. The BBCs cover $3.1 \leq \Delta\eta \leq 4$ in pseudorapidity.



(a) Schematic showing the layout of fiber optic ribbons in the ZDC.



(b) A picture of an SMD. 21 scintillators resting on top of a ZDC module. Another ZDC module will go in front of this. The beam would hit from the lower left going right if this were installed in the beam pipe like this.

Figure 3.15: The ZDC and SMD.

ZDC/SMD: Zero Degree Calorimeter and Shower Max Detectors

Crucial to the determination of event centrality is the ability to count the number of spectator particles. Since neutrons have no charge, we can place a calorimeter at high rapidity behind an IR dipole magnet (18 m away from the nominal event vertex) which we can use to “sweep” away charged particles like proton spectators and other charged track noise (see “Side View” on Figure 3.3). The *Zero Degree Calorimeter* (ZDC) [56] is comprised of ribbons of acrylic fiber optic strands sandwiched between two tungsten plates (Figure 3.15a). The tungsten plates act as a dense absorber for the neutrons to hit and shower into resulting in detectable photon yield in the fiber optic ribbon. There are three ZDC modules on each side of PHENIX. Sandwiched between modules of the ZDC is a hodoscope called the *Shower Max Detector* (SMD) (Figure 3.15b). The SMD is comprised of 21 0.5 cm x 0.5 cm scintillators and is used to measure the centroid of the shower in Cartesian coordinates since the ZDC only measures energy [57]. This shower location determination of the SMD makes it useful as another detector with which to determine the *event plane* (see Section 6.1. The ZDC is used in conjunction with the BBC in order to determine centrality. Since more peripheral collisions mean more spectators and therefore more neutrons to hit the ZDC, the higher the energy measured by the ZDC the more peripheral the event (see Figure 4.1c [58]).

MPC: Muon Piston Calorimeter

The *Muon Piston Calorimeter* (MPC) was a needed upgrade to PHENIX that provided calorimetry at very high rapidity [59]. It was installed in two parts as follows, first in the south in 2005, then in the north in 2006, and was commissioned to reconstruct π^0 and η mesons for various forward physics analyses. Due to its forward location ($3.1 \leq |\eta| \leq 3.7$ (3.9 in the north)) and full azimuthal coverage, it is another detector that is ideal for determining the reaction plane. Nestled in a gap in the piston of the Muon Magnet Arms, the MPC is comprised of lead tungstate $PbWO_4$ ⁶ crystal scintillator towers attached to avalanche photodiodes with preamplifiers to measure the electromagnetic shower photons as in Figure 3.16, with its location in PHENIX labeled on Figure 3.3.

RXNP: Reaction Plane Detector

The *Reaction Plane Detector* (RXNP) is a forward detector subsystem [60] with full azimuthal coverage in 12 segments. It has two segments in rapidity as follows: an inner segment that covers $1.5 \leq \eta \leq 2.8$ and an outer segment that covers $1.0 \leq \eta \leq 1.5$. There are two RXNP detectors, one on each muon arm. All segments are made of 2 cm thick plastic scintillators with a 2 cm layer of lead placed directly in front that acts as a converter, causing all tracks to shower before hitting the scintillators [61].

⁶196 in the south, 220 in the north.

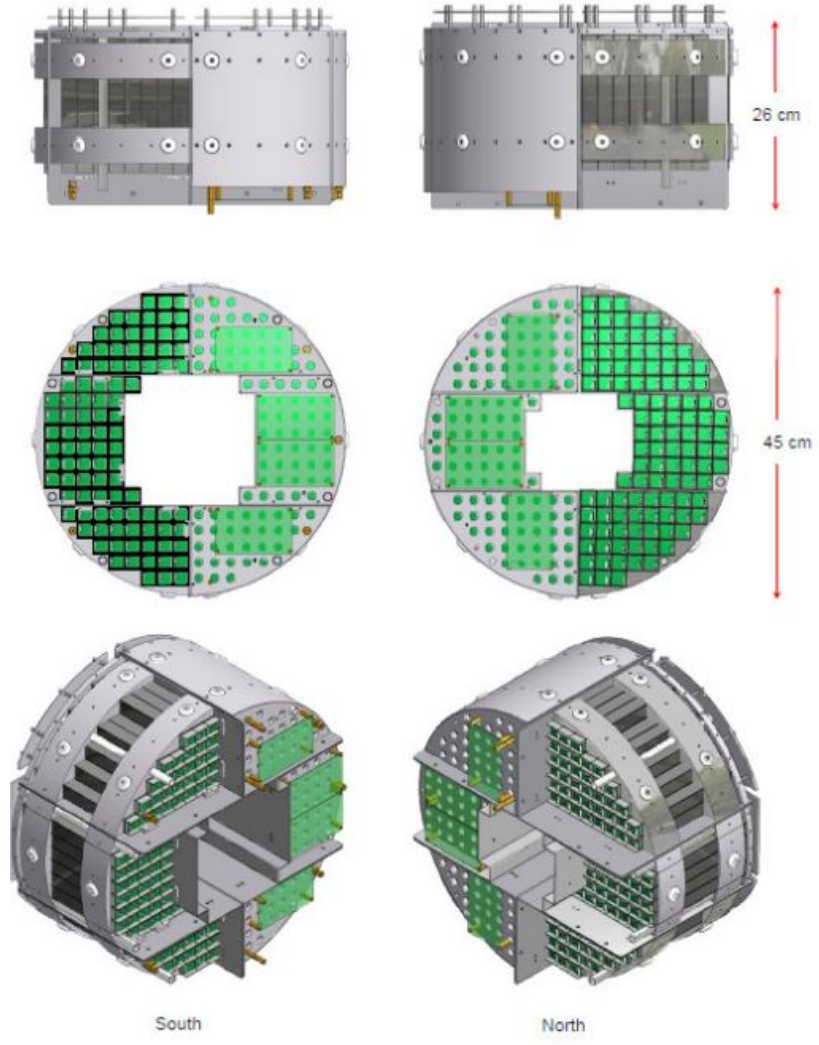
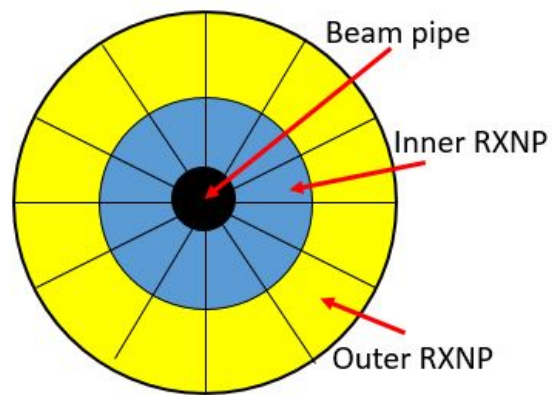


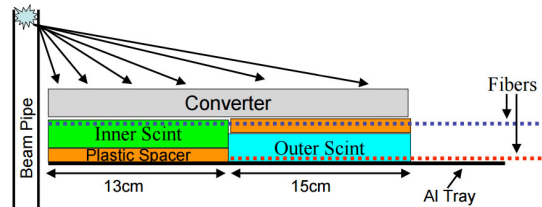
Figure 3.16: Schematic of the MPC. The toroidal shape of the tower configuration allows it to nestle inside the piston of the muon arms while allowing ion beams to travel through the center.

3.4 The DAQ

Each of these detector subsystems capture large amounts of data per event, and the high luminosity of RHIC collisions resulting from millions of events per second doesn't



(a) The beam axis view of the RXNP. The blue ring is the inner RXNP, the yellow, the outer RXNP.



(b) Cross sectional diagram of RXNP layers. Produced particles hit a lead layer that causes them to shower into the scintillators.

Figure 3.17: Diagram and picture of the RXNP detector

allow the computation systems, reconstruction, or network storage capabilities time to catch up. The process of optimizing collecting data created from a high-event-rate, high track multiplicity experiment, in the form of dozens of event and track variables collected by thousands of individual readout channels in a handful of individual subsystems, all funneled through a single data acquisition system that organizes everything and prepares the data for analysis is an intricate and chaotic symphony [62]. In order to do this, the *Data Acquisition* system (DAQ) breaks up the data flow into smaller groups called *partitions* which are assembled from the small collection of data channels called *granules*, typically consisting of sectors of detector subsystems. RHIC is authorized to take data for only a few months out of the year. In practice, this results in three 8 hour manned shifts a day, 7 days a week, for the duration of the run, with data taking only stopping when re-injecting RHIC with ions.

Each granule consists of a *Granule Timing Module* (GTM), a *Front End Module* (FEM), and a *Data Collection Module* (DCM). The GTM synchronizes with the overall DAQ clock, which is also synchronized with the RHIC clocks. These clocks optimize the amount of time the DAQ is actively processing data (called its *livetime*) so that the DAQ is live when bunches of ions are colliding at a maximum rate. The FEMs take the raw output from the preamplifiers in the individual readout channels of a detector subsystem and organizes them into coherent data packets that are transferred over fiber optics to the DCMs. The DCMs act as a sort of stop light regulating the flow of data into buffers with the GTM clock so that data packets from various subsystems are in sync with each other from the same event as they go into the buffer boxes before being transferred to storage. Even

with this timing and granule optimization, RHIC’s event rate is so high that it is impossible to collect every track that passes through its subsystems. The process of utilizing real time detector data to discern which events should be kept and what should be rejected is called *triggering*. There are many triggers at different levels of the DAQ, for example the aforementioned ERT is a trigger that allows us to only collect electron events (or vice versa, reject electron events), events that are of interest for dilepton analyses such as Drell-Yan and J/Psi measurements (or to remove electron noise from charged pion analyses such as this one). The master trigger that sets the timing for the whole DAQ is called the *Global Level 1* trigger or the GL1. It synchronizes large track multiplicity signal coincidence collected by the ZDC to the start of the event and checks to see if the buffers in each granule are clear. Other triggers such as *Local Level 1* (LL1) utilize data from the BBCs to ensure the event vertex happens within a region that will result in acceptable track acceptance and scale down the overall event collection rate so that the buffers have time to clear between event data processing cycles.

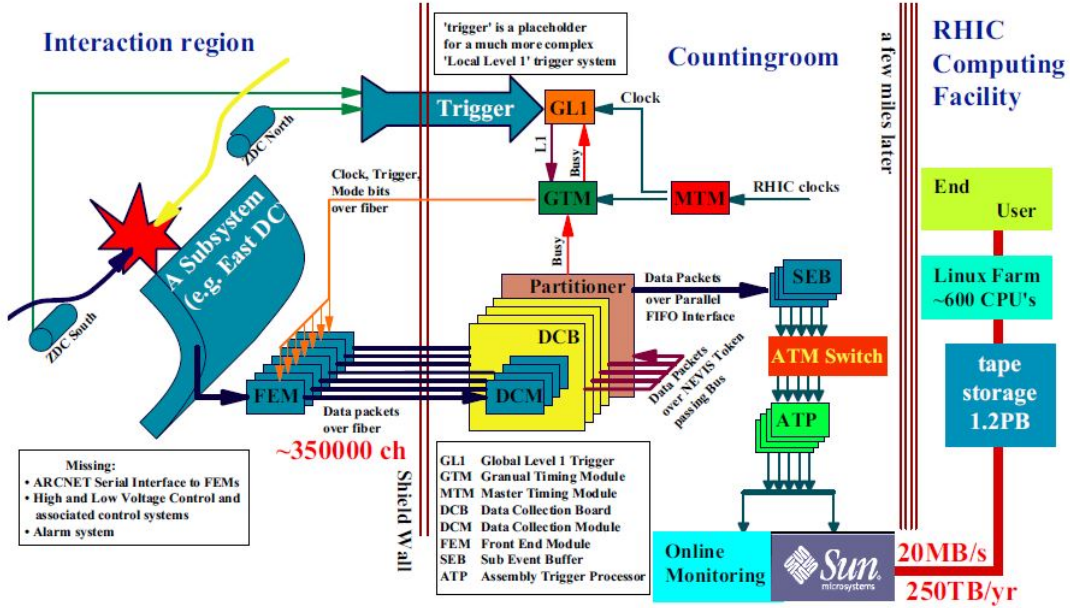


Figure 3.18: A flow chart of the data collection, triggering, and processing through PHENIX's DAQ. Collisions happen in the left side of the chart. The ZDCs calculate the start time of the event and tells the Global Level 1 (GL1) trigger that an event has started. Concurrently, particles created in the collision fly out of the IR and deposit track data into detector subsystems. These subsystems send raw analog data to the Front End Modules (FEM) which convert the signals to digital packets of data. This data is sent to Data Collection Modules (DCM) and is associated with a specific collision event via the Granule Timing Modules (GTM) which interface with the GL1. When the GL1 confirms the start of the event, data coming through the DCMs is sent to the Sub Event Buffers (SEB) which throttles the flow of data and stores data short term from all the subsystem granules so that it can all be transferred to the RHIC Computing Facility (RCF) for storage. This last stage of data flow is controlled by the Assembly Trigger Processors (ATP) which not only manages the data flow from the SEBs to RCF but also sends real time diagnostic information about the status of various detector subsystems, buffer size, data rate, etc. to the Control Room (Online Monitoring).

Chapter 4

Heavy Ion Collisions in PHENIX: A Primer

4.1 Measurable Quantities

Due to the complexity inherent in colliding large nuclei containing a large number of nucleons (for instance 197 nucleons in Au), there are a multitude of metrics we can use to quantify the collision and the evolution of what happens after. For clarification, when talking about high energy physics analyses, we refer to all data gathered from a single collision of two nucleons as an *event*. The location where the collision takes place is called the *event vertex*, or often in collaboration literature since the z-axis is along the beam axis, the *z vertex*. The high luminosity of heavy ion collisions (437 nb^{-1} in 9 weeks for the data used in this analysis: Run 8 d+Au) produces a plethora of events (10.6 billion events for Run

8). As these particles travel from the event vertex through the various layers of detectors under the influence of the PHENIX magnetic field, they leave their own signature on each detector they pass through. These signatures for each given particle can be matched to form a trajectory from the event vertex through PHENIX. The set of data corresponding to location, kinematic, and detector specific variables (i.e., charge deposited, clusters fired, Cherenkov photons, etc.) is called a *track*. The determination of these variables is the topic of this chapter. Many of the illustrations are made assuming the Au+Au system, however, the ideas still apply to d+Au.

4.2 Event Characterization

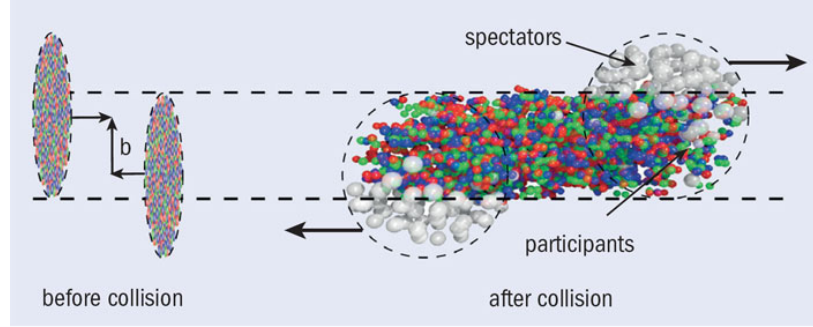
When describing a heavy ion collision, it is useful to introduce quantities that describe the initial conditions of the interacting nucleons. The set of variables that correspond to these conditions are called the *event* or *global* variables. They are used to accurately locate where the event took place inside the detector and the geometric configuration of the nuclei at the time of collision. Since the ions are infinitesimally small and are traveling at ultra-relativistic speeds it cannot be said with certainty where the ions are at the point of collision. This means, before the collision, we have very little idea (or control of) what the event parameters such as centrality, event vertex, and the orientation of the event plane will be. The remnants of the collisions are used to determine these event parameters. Because the particles that do not interact in the collision continue down the beam pipe, these event variables are best reconstructed by the ZDC because of its extremely forward location.

4.2.1 Centrality

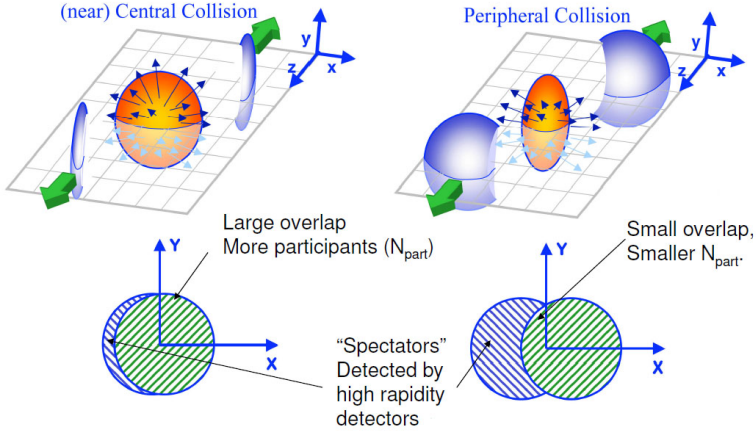
One such variable is *centrality* and is used to describe how “head-on” two ions collide, that is, do they collide with complete cross sectional overlap or do they just barely glance each other (see Figure 4.1b). It is useful to quantify this overlap with a quantity called the *impact parameter*, **b**. This impact parameter is defined by measuring the distance between ion centers, as depicted on the left-hand side of Figure 6.1a. Note that the ions in this illustration appear contracted in the x-axis due to Lorentz contraction. Small impact parameters correspond to large ion-ion overlap in the collision and large impact parameters refer to glancing collisions. In heavy ion physics, collisions with small impact parameters are called *central collisions*, and those with large impact parameters are called *peripheral collisions*. Experimentally, it is impossible to measure the distance between the two ion centers. In practice, centrality can also be quantified by the number of *participants*, or the number of nucleons that collide/interact with each other, versus the number of *spectators*, or the number of nucleons that do not collide. Colliding nucleons will produce particles in all directions; however, spectator nucleons will continue to travel down the beam pipe. Therefore, spectators can be detected by using detectors at very high rapidity. As mentioned in Section 3.3.2, the ZDCs are used to detect neutrons at very high rapidity just past a dipole magnet which sweeps away charged particles. The BBCs, on the other hand, measure charged particles. Because of the rapidity coverage of the BBC, these particles are forward-going particles created in the collision. Since the more central the collision, the more charged particles the BBC detects, there are fewer spectators for the ZDC to measure, and therefore

less energy deposited in the ZDC. There is, therefore, an inverse correlation between the energy deposited in the ZDC and the total charge in the BBC for each event, due to spectators being both neutral and charged; the more charge measured by the BBC, the higher number of colliding nuclear participants in the collision, and the lower the expected energy in the ZDC. Conversely, the lower the charge measured in the BBC, the higher the expected energy measurement in the ZDC corresponding to a higher amount of nucleon spectators. This correlation can be seen in Figure 4.1c.

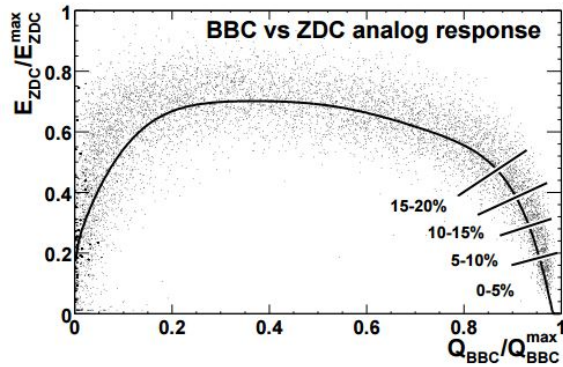
Extending the terminology from impact parameters, a *central* collision is defined as one with a large number of participants, and a *peripheral* collision is one with a large number of spectators. These are quantified in percents, 0% being most central collisions, i.e., highest number of participants, $b = 0$, two colliding ions overlap completely, and 100%, when ions completely miss each other, i.e., there are no participants, $b > R_{nucleus}$. Since ions are spherical in shape, centrality can be used as a way of describing the geometry of the collision region; central collisions have a more circular shape whereas peripheral collisions have a more almond-like shape. In practice, the asymmetric system of d+Au only has spectators on the “gold-going” side. For this, BBC and ZDC correlations are done on the gold side and compared with the BBC (participant count) measurement on the deuteron side. The almond-like shape is inherent in all d+Au collisions, however, the amount of nucleon-nucleon interaction increases with increasing centrality, as shown in Figure 4.1d.



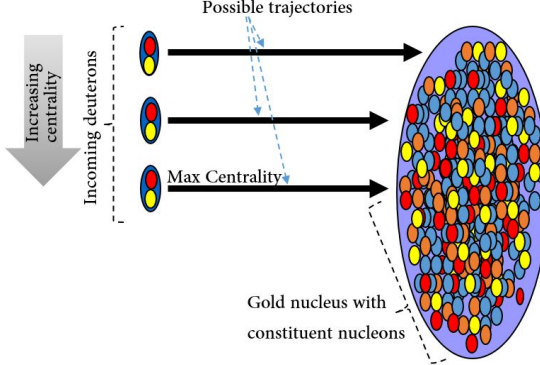
(a) Diagram showing impact parameter versus $N_{\text{spectators}}$ and $N_{\text{participants}}$ [63]



(b) Central vs Peripheral collisions, geometry of initial conditions.
The beam axis goes into and out of the page for the lower diagrams.



(c) Centrality bins as determined by ZDC energy versus BBC charge sum[58]. ZDC counts spectators, BBC counts particles produced by spectators, correlation of the two gives centrality parameter.



(d) Cartoon of $d+Au$ possible centralities.

Figure 4.1: Central versus peripheral ion collisions, BBC vs ZDC determination of. Diagrams of collision geometry.

4.2.2 Event Vertex and Timing

The event vertex is the location along the beam axis where the collision happened relative to the equidistant point between the two beam beam counters. That is, an event vertex value of 0 would be exactly in the center of the PHENIX detector, at equal distance from both BBCs. When a collision happens, participant nucleons scatter and their remnants are detected at two different times on the other side of the IR by the two BBCs (see Fig 4.2). These two time measurements, T_1 and T_2 , can be used to calculate both the event vertex (z_{vtx}) and the initial time the collision takes place (T_0) as follows [64]:

$$z_{vtx} = \frac{T_1 - T_2}{2c} \quad \text{and} \quad T_0 = \frac{T_1 + T_2}{2} \quad (4.1)$$

This initial time is used to start the stopwatch of the event and is used in conjunction with other detectors in order to find the time a produced particle takes to travel

from the vertex to a detector. The event vertex is the z-coordinate location where the collision takes place and is used to optimize outgoing track acceptance in the spectrometer. Too large of a vertex value and the collision is no longer happens in the ideal location for the central arms to detect outgoing tracks. The event vertex for the data set used in this analysis can be seen in Figure 4.3 with an applied cut of $z_{vtx} \leq 30$ cm for optimal central arm track acceptance.

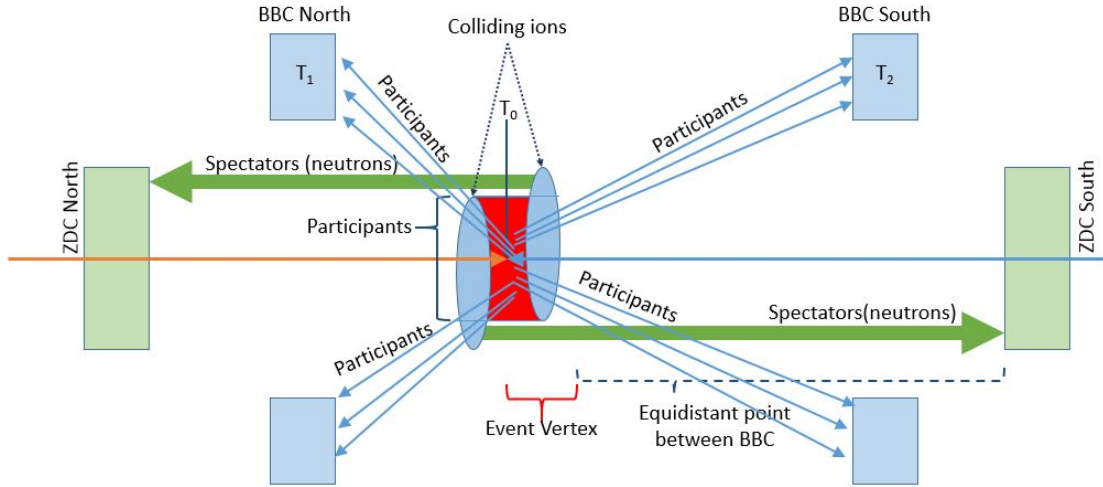


Figure 4.2: A cartoon of BBC and ZDC event characterization. North and South BBCs compare time measurements to determine the time of the start of the event and the vertex of the collision. ZDC measures energy of spectator neutrons and compares with the total charge measured from the participant remnants in the BBC in order to determine event centrality. This diagram is not to scale.

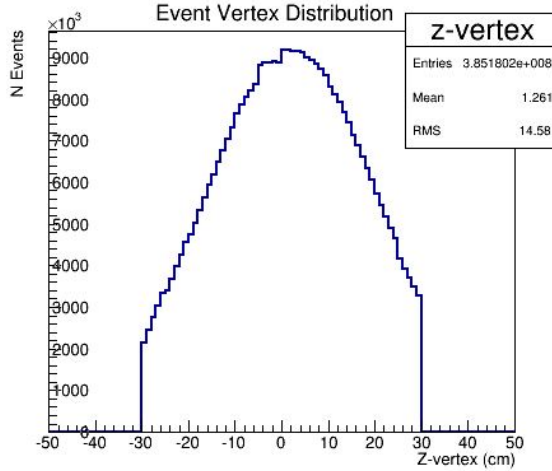


Figure 4.3: Event vertex distribution for Run 8 d+Au, the data set used in this analysis. There is an applied cut for all events to be $|z_{vtx}| \leq 30$ cm.

4.3 Track Reconstruction

4.3.1 Variables for Track Selection

After the collision, created particles fly outward from the vertex and traverse the various layers of the PHENIX spectrometer, depositing information about their kinematics and species along the way. Due to the high multiplicity of tracks resulting from a heavy ion collision, there are a large number of hits in the various detectors that all must be matched to form coherent particle tracks. This high multiplicity makes it combinatorially difficult to come up with possible particle trajectories. The process of rejecting combinations of hits that are unlikely or are background and accepting hits is called *track matching*. Track reconstruction is not perfect, not all hits can be correlated to a clean particle trajectory, and not all trajectories will deposit hits perfectly lined up in every detector subsystem.

Therefore, it is important to come up with a metric with which to measure the quality of the tracks in order to discern which tracks have enough subsystem data to be reconstructed cleanly versus those which do not.

Track Matching: DC and PC1

Track reconstruction utilizes various layers of the Drift Chamber and Pad Chambers in concert to determine track momentum due to the varying curvature of tracks of different momenta traveling through a magnetic field. Tracks are reconstructed in the DC and PC1 using an algorithm called a *Combinatorial Hough Transform* (CHT) [64]. A CHT is a reconstruction algorithm used on a set of points that we know were created by single particles in order to fit them with likely linear track candidates [65]. The set of points are connected combinatorially and probabilities are assigned to each connection based on other kinematic variables and the likeliness that the connection describes a real particle track. For instance, we know all tracks must start at or reasonably close to the event vertex, therefore if any connected points point back to a point that we know is not the event vertex, it is unlikely that that connection reconstructs a real track created in the collision. Furthermore, further out from the vertex additional hits should happen at radially more distant detectors, and there should be corresponding points at those detectors as well. We use a parameter called track *quality* in order to quantify our confidence that a CHT reconstructed track is a likely fit. Track quality is a function of how many points in the different tracking detector layers were used to reconstruct a track. Since this is a combinatorial reconstruction, it is

possible that other tracks such as cosmic events and background events are reconstructed. Because of this we also make the assumption that the origin of all probable tracks is the event vertex as determined by the BBC. This analysis uses tracks whose accepted reconstructions were made with at least three hits in the inner tracking detectors; at least one hit each in X1 and X2 wire nets in the DC (Section 3.3.1) and one hit in PC1.

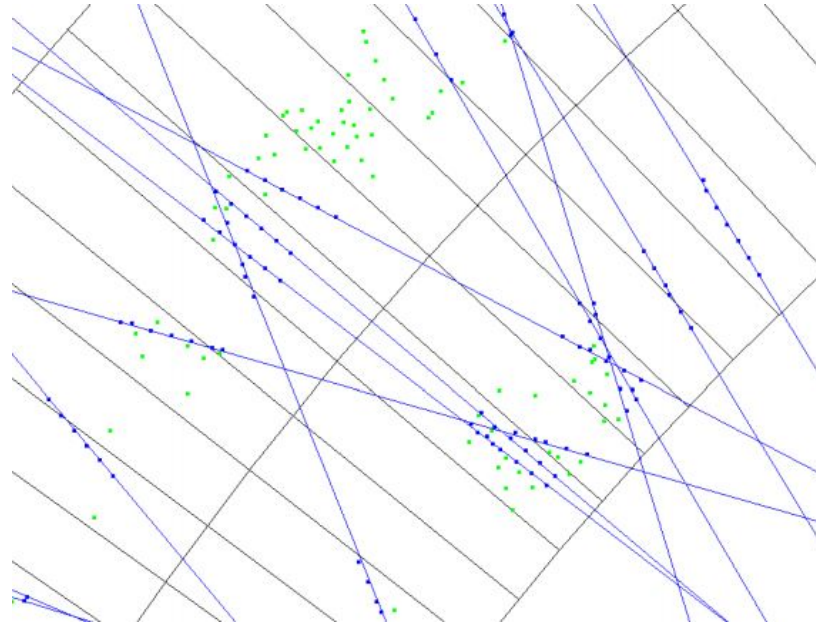


Figure 4.4: Hits in the DC matched to tracks using a Hough transform. A CHT aims to provide these matched track lines by weighting combinatoric solutions with the probability of it being a physical track.

Track Matching: TOF and PC3

The magnetic field in PHENIX is strongest in the IR where $R < 2m$ and negligible within the central arms [48]. Therefore, once tracks are matched in the DC and through

the PC1, we can project the track linearly through the rest of the central arms. We can then match these projections with hits in the PC3 and TOF as illustrated in Figure 4.5 and assign variables (called *residuals*) to the difference between where a hit landed in the TOF/PC3 versus where it was projected to be, one in azimuthal angle ($d\phi$) and one along beam axis (dz). Therefore, track purity can be increased by setting limits to how large a track's residuals can be. These residuals are set per strip in the TOFW and slat in the TOFE. DC/PC reconstructed track residuals for a given strip/slat are plotted and fit with a Gaussian. The corresponding width (σ) of this Gaussian is used to set the acceptance threshold for matched tracks projected out to the TOF/PC3. For this analysis, the maximum residual allowed for both TOF and PC3 in both z and ϕ is three standard deviations (3σ) from the mean residual to allow for more statistics needed due to the lower multiplicity d+Au system (compared to larger systems) while still maintaining good track reconstruction purity. Combined with the DC/PC track quality cut, the TOF and PC3 matching cuts require that all reconstructed tracks used in this analysis be made with at least five points in four detector subsystems that are spread out over 5 m radially from the event vertex.

4.3.2 Particle Identification

Using the TOF detectors' high resolution timing measurements, charged particles that are created in heavy ion collisions can be identified. For this analysis, the particles of interest are the charged pions (π^\pm), charged kaons (K^\pm), and protons/antiprotons (p/\bar{p}).

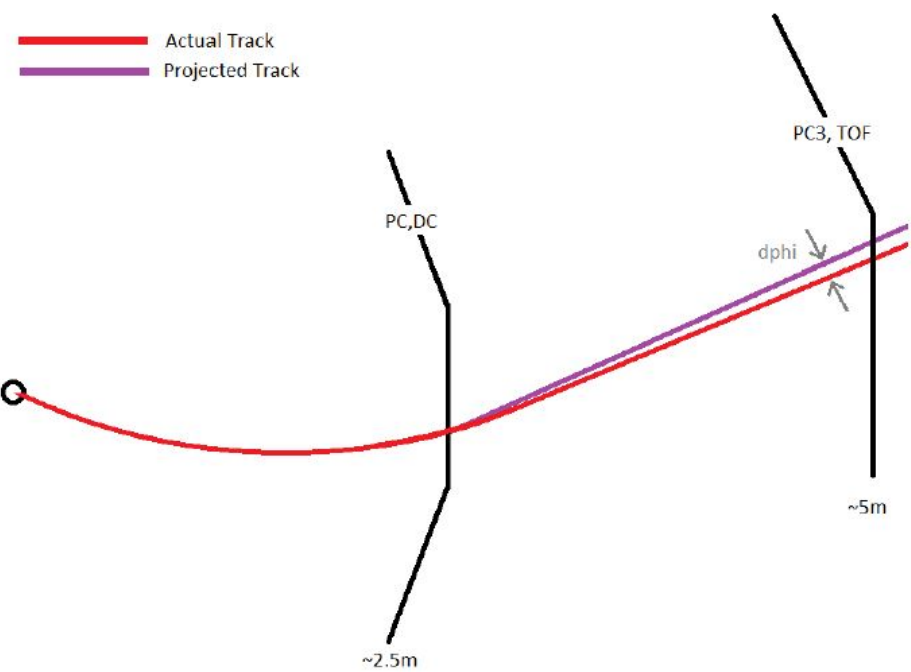


Figure 4.5: Diagram of track reconstruction by the DC/PC1 projected linearly onto the TOF/PC3. [66]

Since the masses of these particles are distinct, plotting particle charge/momentum versus time of flight can show clear separation between pion, kaon, and proton signals (see Figure 4.6).

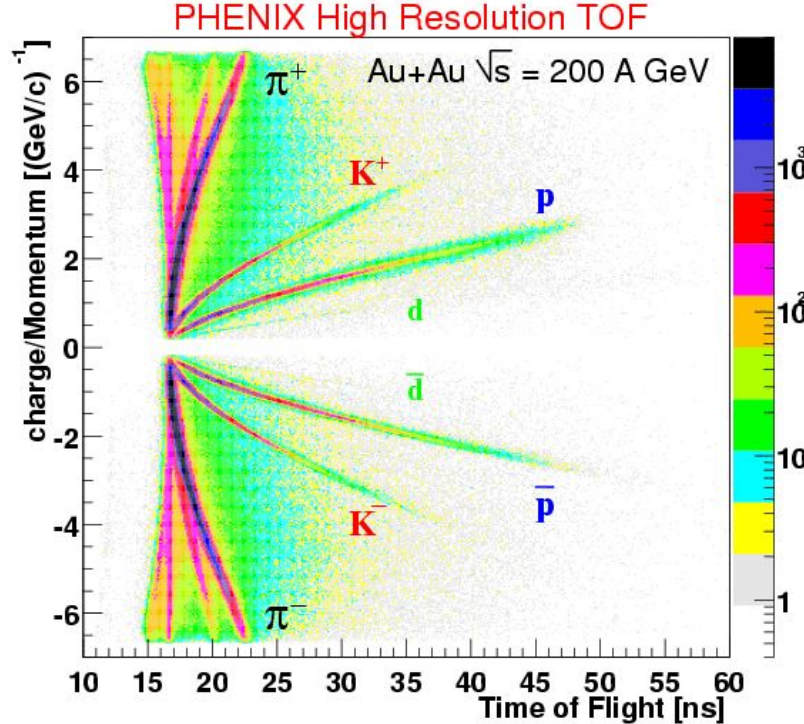


Figure 4.6: Charge/momentum vs Time of Flight [67] is plotted to show particle separation in the TOF vis-à-vis Equation 4.3. Pions, kaons, protons, and deuteron signals are labeled. Other signals corresponding to shorter flight times in the plot are other particles; the closest to the pion signal are electrons, followed by photons which notably have a constant time of flight at all momenta (as they should).

While visually the individual particle signatures are easily identifiable in Figure ??, computationally it is advantageous to convert units so that the signatures only depend

on a single variable. It is known from basic kinematics that it is possible to calculate the velocity, v , of an object traveling at a constant speed,

$$v = \frac{L}{t} \implies t = \frac{L}{v}, \quad (4.2)$$

where t is the time it takes to travel some path length, L . It is useful to define the relative speed of the particle compared to the speed of light, c , as $\beta = v/c$ and substitute it in for v . We also know from the relativistic identities that $\beta = p/E$ and $E^2 = p^2 + m^2$. The equation is then,

$$t = \frac{L}{v} = t = \frac{L}{c\beta} = \frac{L}{c} \frac{E}{p} = \frac{L}{c} \frac{\sqrt{p^2 + m^2}}{p}. \quad (4.3)$$

which can be solved for m^2 to give the mass versus time relation:

$$m^2 = p^2 \left\{ \frac{t^2}{L^2} - 1 \right\}, \quad (4.4)$$

and is shown in Figure 4.7.

Since the distance from the event vertex to the detector is constant and the velocity (and therefore momentum) of the particle is constant, m^2 depends on two constant terms if we take measurements in bins of p . Since we are talking about radially outward traveling tracks, this p is, in practice, p_T (transverse momentum). From this we can see that the time of flight for particles created in ion collisions can be used to identify their species.

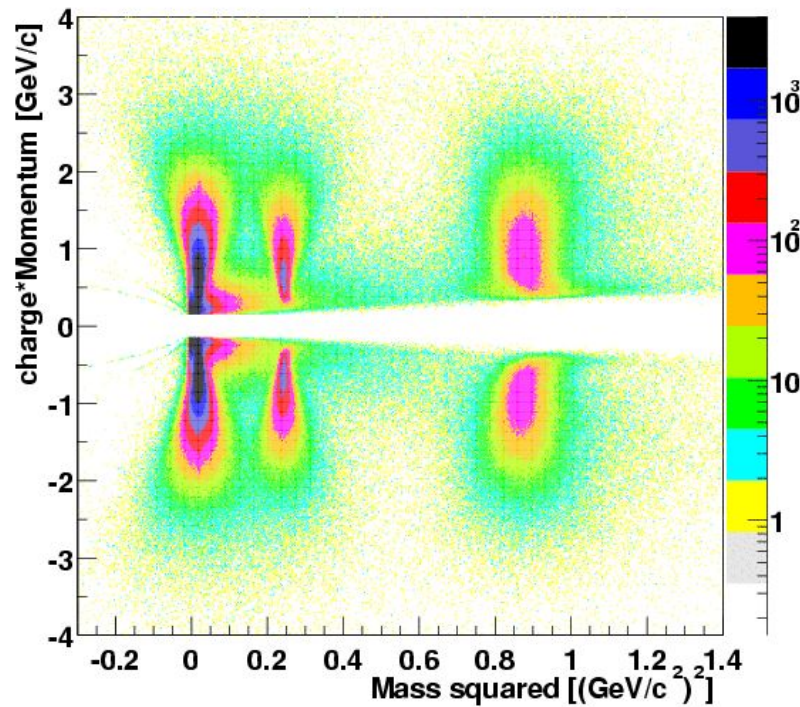


Figure 4.7: m^2 vs p_T showing clear constant separation of particle signatures [67]. Under this transformation, electron peaks overlap strongly with pions and need to be cut out by using the RICH. Photons are massless leading to the wisp-like distribution for $m^2 < 0$.

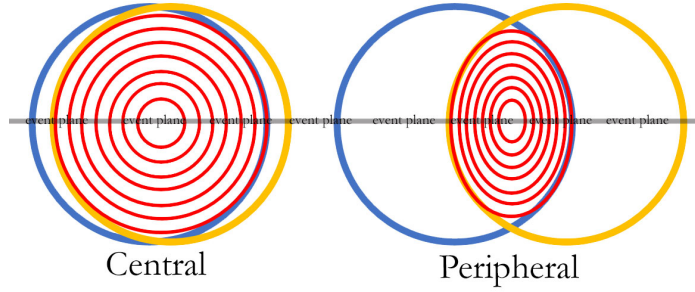
Chapter 5

Anisotropic Flow

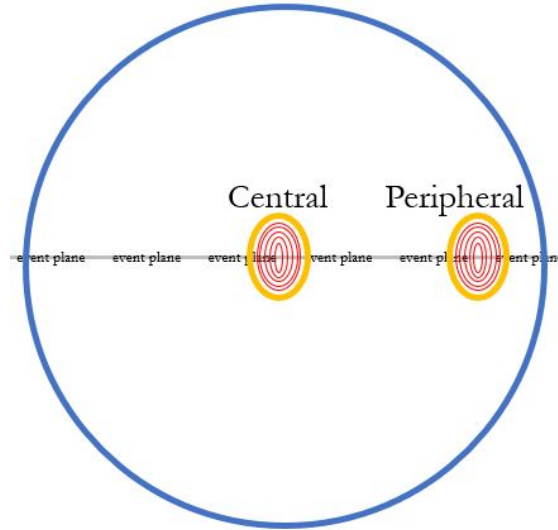
5.1 Flow from Geometry of Initial Conditions

In the moments immediately after a collision event, the outward expansion of the newly formed QGP can be studied to better understand the QCD processes that take place both during formation as well what happens as the temperature of the system drops to below the freeze-out threshold. Though fluctuations in collision geometry can happen, if they are ignored for the moment, it can be said that the shape of the colliding ions' cross-sectional overlap provides a good approximation of the initial conditions of the medium after collision. Therefore, the geometry of the initial configuration of participants is dependent on the collision's centrality¹. Because of this, peripheral events in symmetric systems such as Au+Au have an inherently elliptical shape (as shown in Figure 5.1a). The azimuthal

¹See Section 4.2.1



(a) Symmetric systems (i.e. $Au+Au$, $Pb+Pb$, etc.).



(b) Asymmetric systems. In this case ($d+Au$) the smaller ion is inherently elliptically shaped since it only contains two nucleons.

Figure 5.1: Cartoons showing pressure gradients in central versus peripheral collisions in symmetric and asymmetric systems. Here the yellow and blue circles represent the colliding ions, one going into the page and one coming out of the page. The red circles denote surfaces of equal compression in the region of nucleon interaction. Peripheral collisions have the steepest gradient of compression along the event plane. Thus, an ellipsoidal ion collision anisotropy corresponds to a pressure anisotropy in the created medium leading to an elliptically shaped momentum anisotropy of flow which hadronizes and is measured as an azimuthal anisotropy of particles produced in the azimuth.

asymmetry of this interaction creates different amounts of pressure, or *pressure gradients*, about the azimuth. These pressures are strongest along the waist of the collision and weakest at the poles. Because of this, though it expands in all directions, it is the stronger expansion about the azimuth that best describes the behavior of this fluid. Asymmetric systems, such as the one studied in this analysis ($d+Au$), have a different dependence on centrality. As shown in Figure 5.1b, since deuterons contain only two nucleons, they are inherently elliptical in shape, and the pressure gradients then only depend on how many of the gold ion's nucleons the deuteron interacts with. By the Glauber model, the nucleon distribution in an ion can be approximated as a density function that decreases with increasing radius. Therefore, it follows that for $d+Au$, pressure gradients are maximal with central collisions since nuclear interaction is maximal at maximum centrality. Consequently, flow should be strongest in central collisions due to this maximal pressure.

Often physicists describe the behavior of phenomena using a series expansion of orthogonal functions. Since the azimuthal angle runs from 0 to 2π , this azimuthal expansion can be treated as a harmonic function, which lends itself well to parameterization using a Fourier series. Recall that a Fourier series can be used to approximate the shape of a periodic function, $f(x)$, over a fixed period, L , as follows:

$$f(x) = \sum_{n=-\infty}^{\infty} A_n e^{i(2\pi n x/L)}, \quad (5.1)$$

where

$$A_n = \frac{1}{L} \int_0^L f(\phi) e^{-i(2\pi n x/L)} dx \quad (5.2)$$

are said to be the Fourier *coefficients* or often, since they approximate harmonic functions, Fourier *harmonics*. For azimuthal periodicity, $L = 2\pi$ and this equation becomes

$$f(\phi) = \sum_{n=-\infty}^{\infty} A_n e^{i(n\phi)}, \quad (5.3)$$

where

$$A_n = \frac{1}{2\pi} \int_{-\pi}^{\pi} f(\phi) e^{-i(n\phi)} d\phi. \quad (5.4)$$

These coefficients describe the amount a particular harmonic's functional shape contributes to the overall shape of the periodic function. The exponential term can be written as the sum of a real cosine term and an imaginary sine term, as follows:

$$f(\phi) = \sum_{n=0}^{\infty} A_n \cos(n\phi) + i \sum_{n=0}^{\infty} B_n \sin(n\phi), \quad (5.5)$$

where

$$A_n = \frac{1}{2\pi} \int_{-\pi}^{\pi} f(\phi) \cos(n\phi) d\phi \quad (5.6)$$

and

$$B_n = \frac{1}{2\pi} \int_{-\pi}^{\pi} f(\phi) \sin(n\phi) d\phi. \quad (5.7)$$

Since we define $\phi = 0$ to be along the waist of the ellipsoidal shaped QGP and not

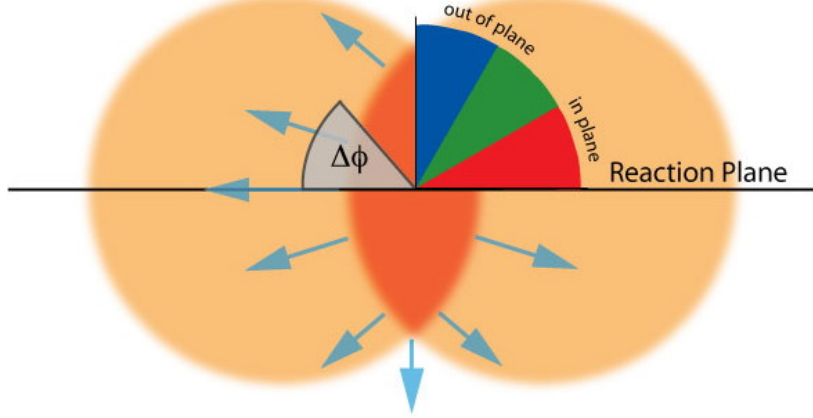


Figure 5.2: Reaction plane coordinates. $\phi = 0$ is oriented along the reaction plane therefore track vectors with $\Delta\phi$ values at $\pi/2$ and $3\pi/2$ correspond to particles produced out of the event plane and $\Delta\phi$ values of 0 and π correspond to vectors in the event plane.

at the poles (see Figure 5.2), odd function contributions (sine terms, B_n) to the Fourier series can all be ignored. Therefore, the shape of the outgoing QGP flow can be approximated by defining the rate of change of outgoing particle tracks versus transverse momentum and approximating it with a Fourier series. Flow anisotropy of the QGP can then be written as

$$E \frac{d^3N}{dp^3} = \frac{1}{2\pi} \frac{d^2N}{p_T dp_T dy} \left(1 + \sum_{n=1}^{\infty} 2v_n \cos(n\Delta\phi) \right), \quad (5.8)$$

where

$$v_n = \left\langle \cos(n\Delta\phi) \right\rangle \quad (5.9)$$

are the n-th order Fourier coefficients that describe the azimuthal shape of the QGP's outward expansion, and $\Delta\phi = \phi_{lab} - \Psi_{RP}$ is the azimuthal angle with respect to the reaction

plane angle relative measured in the lab coordinate system, changing the lab coordinate phi to the angle phi with respect to the event plane. Each n-th order coefficient scales the amount of expansion that behaves like $\cos nx$.

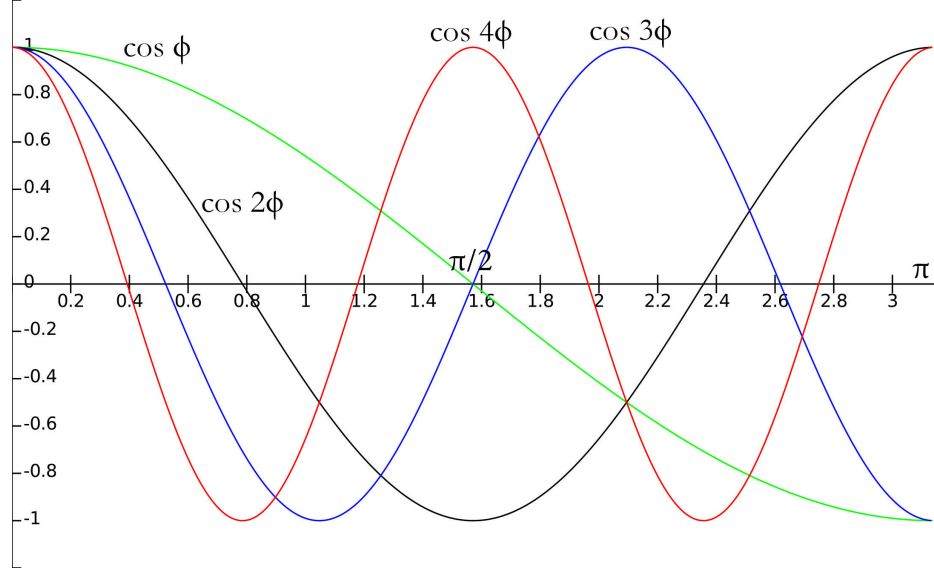


Figure 5.3: Plots of the first four harmonics of a cosine series. $\phi = 0$ is along the event plane and increasing ϕ goes clockwise as shown in Figure 5.2.

From studying the behavior of these various harmonics we can see that $n = 0$ corresponds to a constant term since $\cos 0 = 1$ for $n = 1$. Furthermore, $\cos x$ is a maximum at $\phi = 0$ and a minimum at $\phi = \pi$, which would correspond to a collective flow in the $\phi = 0$ direction. Therefore, the $n = 1$ flow coefficient is often called *directed flow*. For the case of $n = 2$ we see that again there is a maximum at $\phi = 0$ and another at $\phi = \pi$, which corresponds to maximal flow along the event plane of the ellipsoidal QGP. This anisotropic expansion that is strongest along the reaction plane in an elliptical collective flow, a term

which is shortened to *elliptic flow*. There are higher order harmonics which can describe various other phenomena of QGP flow which are beyond the scope of this analysis.

5.2 Flow from Fluctuations

Geometric sources of initial conditions are a good approximation; however, it has been seen that higher harmonics can be measured in elliptic systems such as peripheral Au+Au previously thought to be only elliptic [68]. This effect has been attributed to secondary scattering processes of the participant nucleons. These nucleons that interact with spectators in secondary reactions are called *wounded nucleons* and the overall effect of these additional collisions increases both the number of binary collisions and alters the initial shape of the created medium. An example of this shown in Figure 5.4 where a symmetric Au+Au system collided peripherally and a strong v_2 is expected, however fluctuations and wounded nucleons create a triangular shaped initial condition, which would correspond to a v_3 signal.

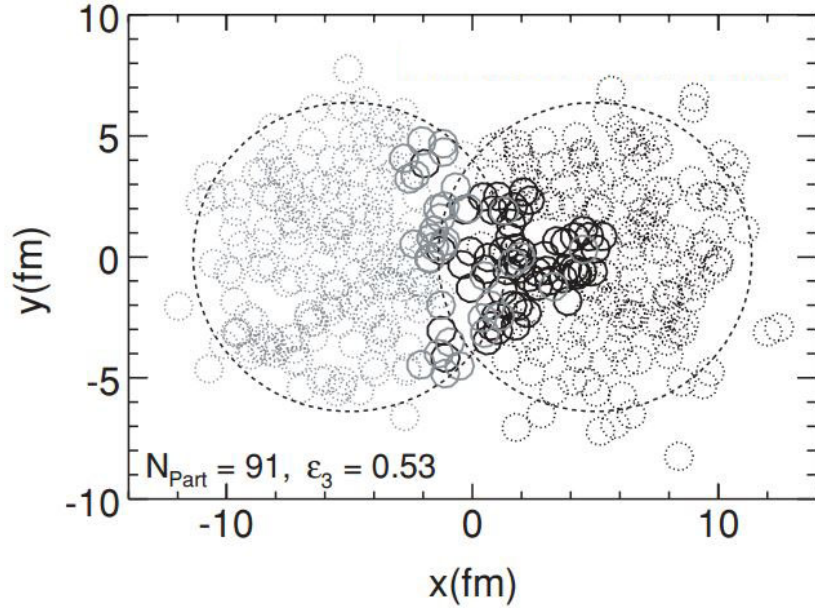


Figure 5.4: An example of how fluctuations can cause flow with the shape of higher Fourier harmonics. Here Au+Au collisions are modeled with Glauber Monte Carlo. The distribution of nucleons at the point of collision in the x - y plane is plotted. Wounded nucleons cause secondary collisions which alter the initial elliptic shape from the overlap into a triangular shape [68]. In this plot small dotted circles are spectators and solid circles are participants, the large dotted circle that contains the various circles are outlines of the two colliding ions.

Chapter 6

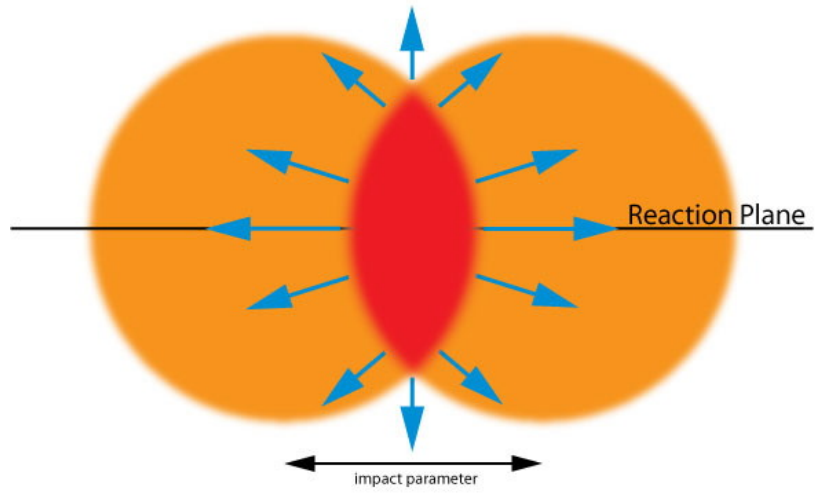
Event Plane

6.1 Determination of Event Plane

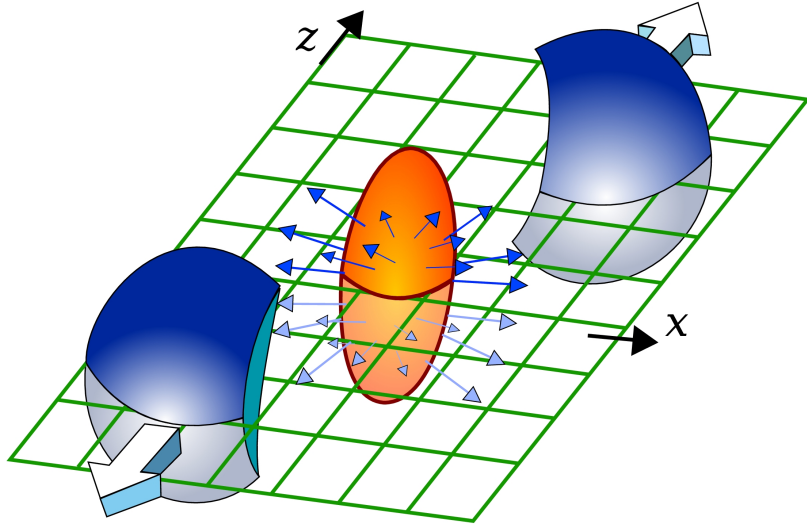
Pivotal to this analysis is the ability to determine an event characterization variable called the *event plane*. Given the geometry of a heavy ion collision, the event plane is defined as the two-dimensional plane that bisects both ions equally through their centers as shown in Figure 6.3. Recall that the impact parameter is the distance between the two colliding ions' centers. A vector can be formed from this distance, and the plane containing both the impact parameter vector and a vector that represents the direction one of the ions is traveling down the beam axis, is the event plane¹.

In practice, this plane is determined by detecting the spectator nucleons at high rapidity, or participant-created tracks at forward rapidity using detectors with full azimuthal

¹It is irrelevant which direction the impact parameter vector points and which direction we pick to point the beam axis vector, this is merely for creating a plane



(a) A two-dimensional representation of the event plane. Recall the impact parameter is the distance between the two colliding ions' centers. In this illustration the orange spheres represent the ions, one is going into the page and one is coming out of and the red overlap is the matter created by the participant nucleons.



(b) A three-dimensional render of the initial conditions just after a collision. The two blue spheres are the remnant spectator nucleons from the colliding ions, the orange/yellow ellipsoid is the nuclear matter created by the collision of participant nucleons. The green grid here represents the plane that bisects all three of these bodies which we call the event plane

Figure 6.1: Illustrations of the event plane in heavy ion collisions

coverage. Ideal candidates for this are the MPC, BBC, SMD, and RXNP. Particle signals would appear in the Northern detector as a cluster of hits on one side in azimuth and in the Southern detector as a cluster of hits 180° azimuthal degrees across (as shown in Figure 6.2). The event plane can therefore be constructed using the locations of these signal clusters and creating a plane that bisects them.

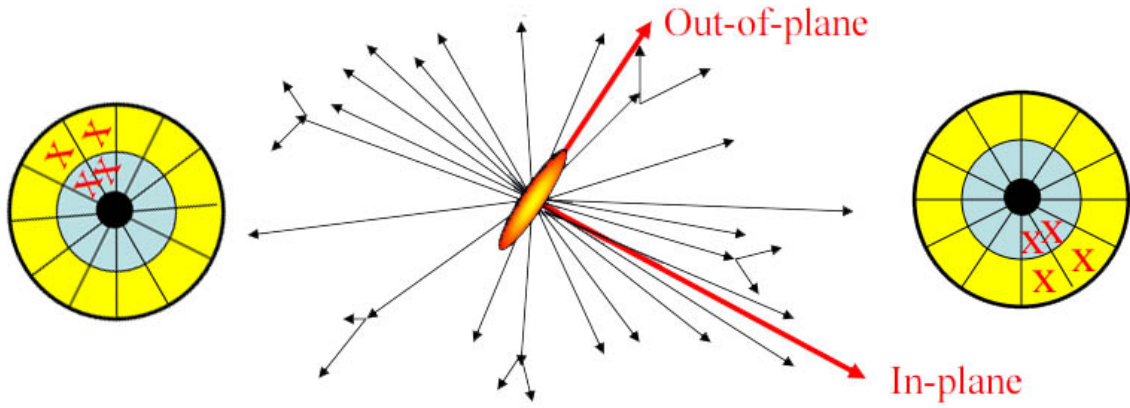


Figure 6.2: Cartoon of Event Plane determination with forward detectors. The two target shapes represent forward detectors, in this case RXNP. The largest cluster of hits in one detector will happen along the event plane and will be correlated to a large cluster of hits in the complementing detector on the other muon arm. The orientation of these hits can then be used to reconstruct the event plane. [60]

6.2 Q-vector Re-centering

Since there is little control over the precise impact parameter and event plane orientation for each collision, the precise orientation of the ions at moment of impact cannot

be controlled. As such, the event plane orientation for each event happens randomly. In order to make a meaningful flow measurement a way of aligning each of the event planes is needed. To do this, collective flow is utilized to find the plane of largest particle production along the beam axis. The weighted detector response in the x and y axes define an event plane characterizing vector called the *Q-vector*. The Q-vector points in the direction of largest particle production as expected from the n-th flow harmonic. Therefore, specific event planes are determined for each flow coefficient studied, i.e. if a second order particle distribution is used to determine the Q-vector, the Q-vector characterizes the second order event plane. The BBC and SMD detect the remnants of a collision and are able to analyze their distribution in the x and y axis. This distribution is Gaussian and models the direction the Q-vector points. Shifting the x and y mean of this distribution to 0 in both axes aligns the planes for all events.

6.3 Event Plane “Flattening”

Furthermore, because event plane orientations populate a distribution randomly, the distributions are expected to be uniform. However, the imperfections and acceptance limitations of the event plane characterizing detectors cause this distribution to be non-uniform. The process of making this distribution uniform in azimuth is called *flattening*.

The d+Au system is asymmetric by construction, therefore track multiplicities on the north and south detectors are not the same. Since gold ions have a considerably larger

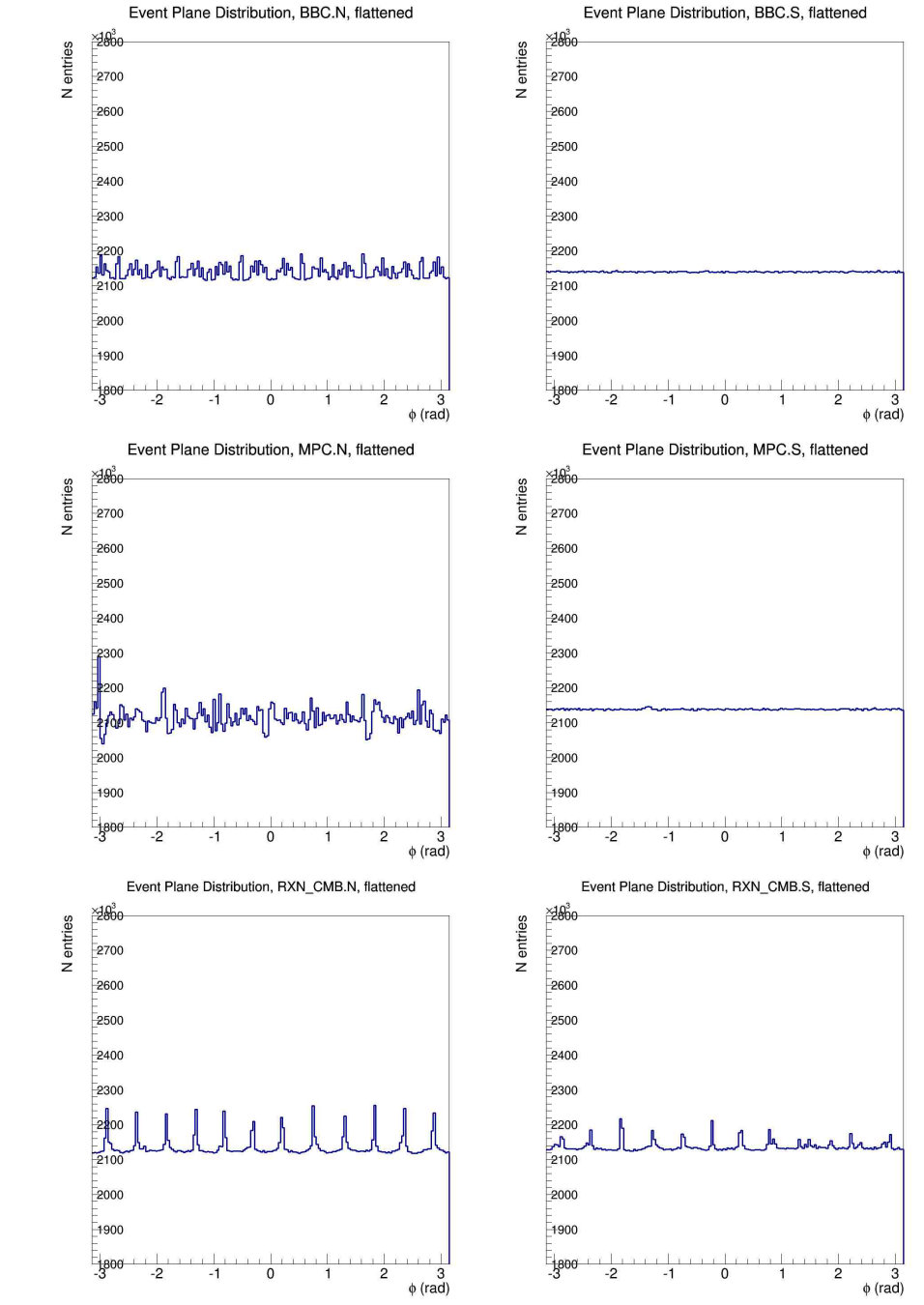


Figure 6.3: Flattened event plane distributions in the BBC, MPC, and RXNP. Note that this flattening is significantly better in the “gold-going” south arm.

number of nucleons than deuterons, they therefore have higher forward track multiplicity, and their event plane signature in the forward detectors is much stronger. In practice, the north side is the deuteron-going side, and the south side is the gold-going side. This can be seen clearly in Figure 6.3 where the event plane is much easier to flatten in the south than in the north, regardless of which detector subsystem is chosen.

6.4 Event Plane Resolution Correction

Since there is a finite track multiplicity, the track distribution is not smooth and continuous across the detectors; rather there is an associated resolution limitation for each measurement made with a specific detector. This resolution limitation affects how well flow anisotropies can be measured, and, because of the nature and shape of various Fourier harmonics, higher harmonics are more strongly affected by resolution limitations since their shape is quickly varying over the azimuthal distribution compared to lower harmonics. Due to this, resolution corrections must be calculated for each harmonic separately. The apparatus makes different measurements of the event plane assuming the shape of specific Fourier harmonics; therefore, the resolution corrections made for each detector are specific to the n of the harmonic. That is to say, the harmonic dependence and detector resolution dependence of the resolution correction are not separable. Additionally, by collision geometry, the ability to determine each correction is dependent on event centrality, implying that these corrections must be made for each centrality bin as well. The measured flow anisotropy decreases as the ability to resolve changes in flow decreases, so this resolution

error is corrected by defining some multiplicative scaling such that

$$v_n = \frac{v_n^A}{Res(\Psi_n^A)} \quad (6.1)$$

where v_n^A is the n^{th} order anisotropic flow coefficient measured with some detector, arbitrarily designated A , and $Res(\Psi_n^A)$ is a single valued correction factor for the v_n measurement using a specific detector and a single bin in centrality. Since device resolution is independent of particle species, the calculation of a different correction for each particle flow is not needed.

The method of determining resolution corrections used for this analysis is called the *Three Subevent Method*. It can be calculated by comparing the event plane measured by one detector with measurements made by two other detectors. For instance, the resolution correction for detector A using the three subevent method with detectors B and C can be defined as [69]

$$Res\{n\Psi_n^A\} = \sqrt{\frac{\langle \cos(n[\Psi_n^A - \Psi_n^B]) \rangle \langle \cos(n[\Psi_n^A - \Psi_n^C]) \rangle}{\langle \cos(n[\Psi_n^B - \Psi_n^C]) \rangle}} \quad (6.2)$$

where Ψ_n^X is the event plane as measured with detector X using the n^{th} Fourier harmonic.

Chapter 7

Results

7.1 Charged Track v_2

Here I present measurements of elliptic flow in $\sqrt{s_{NN}} = 200$ GeV d+Au collisions.

Recall that the Fourier coefficients parameterize the shape of the azimuthal hydrodynamic flow by describing it as a superposition of cosine harmonics:

$$\frac{d^2N}{dp^2} \propto v_0 + v_1 \cos(\phi - \Psi_1^{RP}) + v_2 \cos(2(\phi - \Psi_2^{RP})) + v_3 \cos(3(\phi - \Psi_3^{RP})) \dots \quad (7.1)$$

where v_0 , v_1 , v_2 , and v_3 are the values that scale the amount of spherical, directed, elliptic, and triangular flow respectively, and are indicative of collective behavior of the nuclear matter. The angle, ϕ , is the azimuthal angle in the lab frame and Ψ_n^{RP} is the angle of the reaction plane in the lab frame¹. This can be simplified by defining the coordinate:

¹for the n -th Fourier harmonic.

$\Delta\phi_n = \phi - \Psi_n^{RP}$ which gives:

$$\frac{d^2N}{dp^2} \propto v_0 + v_1 \cos(\Delta\phi_1) + v_2 \cos(2\Delta\phi_2) + v_3 \cos(3\Delta\phi_3) \dots \quad (7.2)$$

effectively redefining eqn. 7.1 relative to the event plane. To measure the elliptic flow (v_2) we count number of tracks in bins of $\Delta\phi_2$ and fit this with a function of the form:

$$f(\Delta\phi_2) = v_0[1 + v_2 \cos 2\Delta\phi_2] \quad (7.3)$$

where v_0 is a term that accounts for an overall shift in the number of tracks due to statistics and v_2 is the 2nd order Fourier harmonic of the azimuthal momentum anisotropy. By the orthogonality of Fourier harmonics and because the event plane is determined for each harmonic independently², all other v_n contributions must be calculated independently.

7.2 Separating Particle Signals

Following the re-centering of the Q-vectors, the flattening of the event plane, and checking for calibration of the TOF detector, 2-d histograms of p_T vs m^2 are plotted following the method described in section 4.3.2 to identify the species of charged track hits in the TOF.

In order to do a statistical analysis, these 2-d histograms will need to be “sliced”

²and therefore $\Delta\phi$ is specific to a particular harmonic.

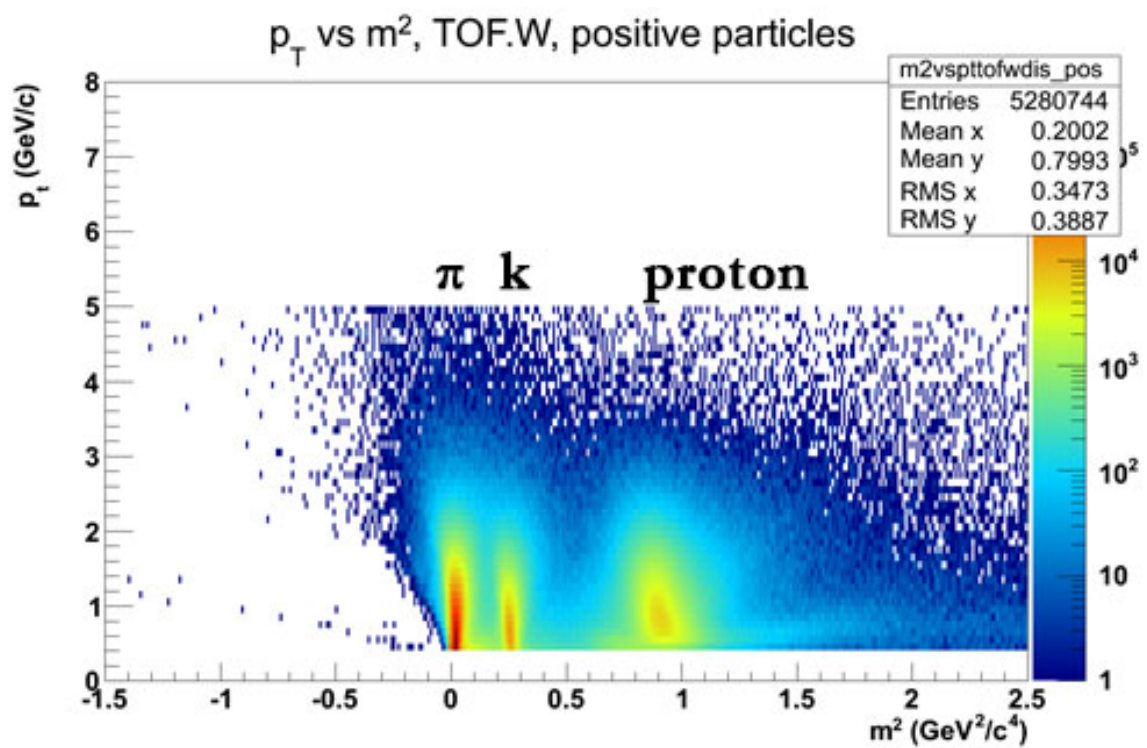


Figure 7.1: Track p_T vs m^2 determined by the TOF.W showing separation of π , K , and proton particle signals.

into a series of 1-d histograms in small bins of p_T which will give a 3-peak histogram showing the signatures of the pion, kaon, and proton which are Gaussian in shape. There are 15 bins of p_T starting at $0.5 \leq p_T \leq 0.7$ GeV/c and increasing by steps of 0.2 GeV/c per bin up to $p_T = 2.9$. At this point, to increase statistics, bins are increased to 0.5 GeV/c per increment for the last 3 bins, starting at $p_T = 3.0$ GeV/c, up to $p_T = 4.5$ GeV/c. Over the range of p_T in this analysis, the widths and heights of the particle peaks will change and overlap in various ways, because of this I will divide the p_T range into three ranges, each of which will be analyzed with different methods with corresponding systematics. After fitting the particle distributions, the Gaussian fit functions are then integrated to calculate the particle yield for each species. Integration bounds can be set to increase track ID purity at the expense of statistics and vice versa. The yields from the integrated Gaussians of each particle species are then fit with the Fourier function to determine the 2nd harmonic coefficient as per equation 7.3.

7.2.1 Single Gaussians

For $p_T < 1.3$, there is enough separation between the pion, kaon, and proton signals to fit each particle peak with a single Gaussian (fig. 7.2). This will take the form:

$$f(m^2) = \frac{N_0}{\sqrt{2\pi}\sigma^2} e^{-\frac{(m^2 - \mu)^2}{2\sigma^2}}, \quad (7.4)$$

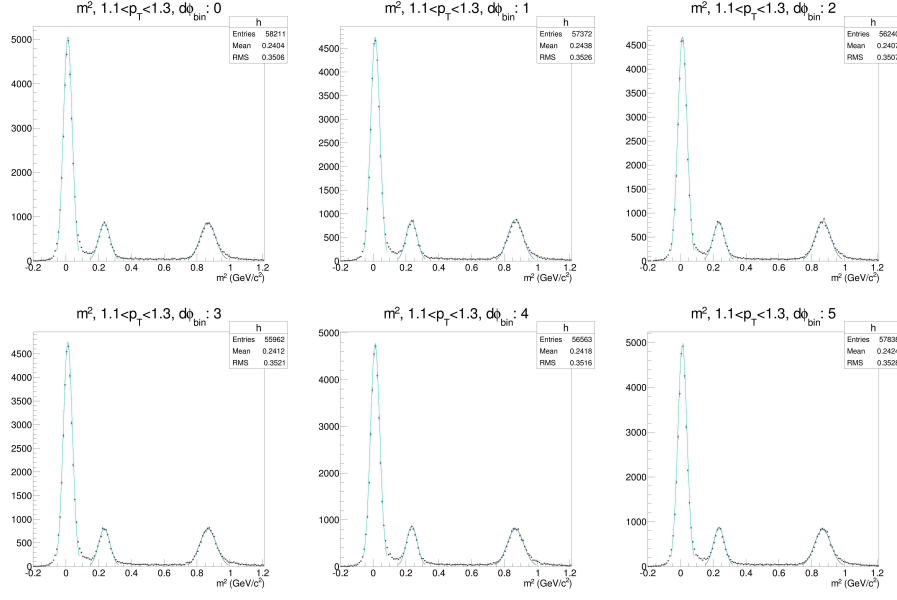


Figure 7.2: Example single Gaussian fits of m^2 for $p_T \leq 1.3$ GeV/c in 6 bins of $\Delta\phi$.

where σ is the width of the identified particle peak, μ is the location of the peak's mean along the x-axis, and N_0 is the height of the peak. To determine the identified particle yield, the Gaussians are then integrated from $\mu - 2\sigma$ to $\mu + 2\sigma$ for each particle distribution, i.e. the number of particles of each type are counted out to two standard deviations around their mean mass. Since the means of the mass and the widths of the mass distributions are not expected to change in bins of $\Delta\phi$, as a check, the values of the means and the widths are plotted for the specific bin of p_T in order to verify that they do not change. The yields for each particle species are also plotted in the bins of $\Delta\phi$ (fig. 7.3). (full set of fits and data can be seen in Appendix C.1.1)

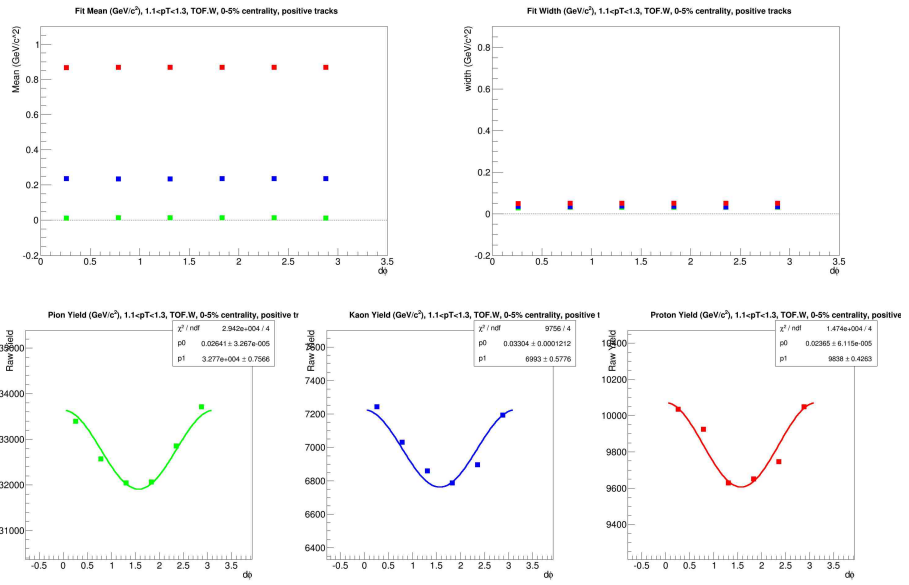


Figure 7.3: Particle distribution fit mean and width QA. π , K , p yield vs $\Delta\phi$ and corresponding Fourier fits for $p_T \leq 1.3$ GeV/c. Yield plots are zero suppressed and statistical error bars are plotted.

7.2.2 Multiple Gaussians

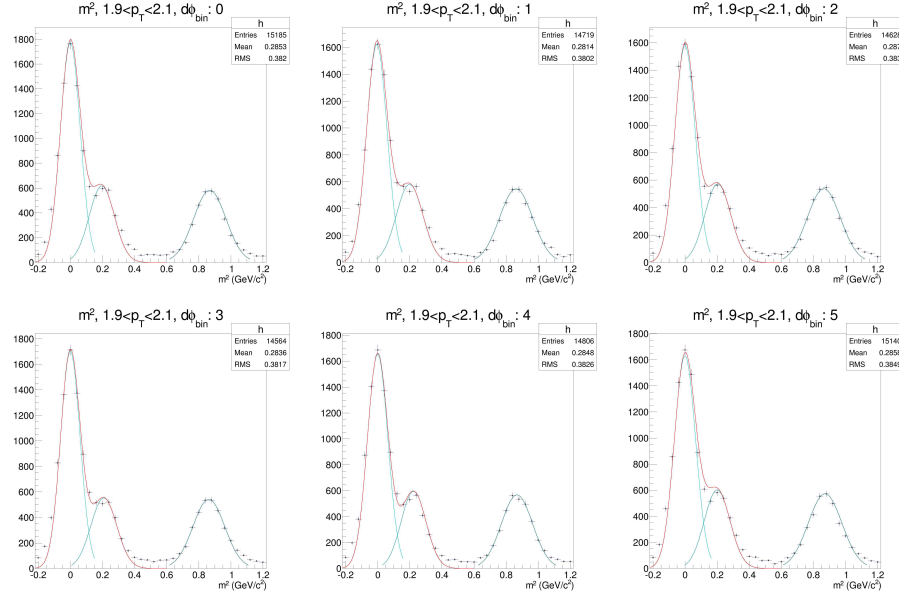


Figure 7.4: Example mixed Gaussian fits of m^2 for $1.3 \leq p_T \leq 2.1$ GeV/c in 6 bins of $\Delta\phi$.

For $1.3 < p_T < 2.1$, kaon and pion mass distributions become overlapped. To decouple the two, I fit the distribution with a combination of two Gaussians in order to fit the overlapping tails of the distributions without over counting (see fig. 7.4). This function takes the form:

$$f(m^2) = \frac{1}{\sqrt{2\pi}} \left(\frac{N_\pi}{\sigma_\pi} e^{-\frac{(m^2 - \mu_\pi)^2}{2\sigma_\pi^2}} + \frac{N_k}{\sigma_\pi - \sigma_k} e^{-\frac{(m^2 - \mu_k)^2}{2(\sigma_\pi - \sigma_k)^2}} \right), \quad (7.5)$$

where N_x , μ_x , and σ_x are the parameters that describe the shape of particle x 's (π/K) distribution. These parameters can then be used to reconstruct single Gaussian distributions

which are then integrated out to 2σ as mentioned in the previous section. (full fits and data in Appendix C.1.3).

Triple Gaussian fits were attempted, however pion and kaon peaks were so strongly merged that many possible ratios of pion and kaon heights reproduced the same peak in the data. This occurs in a region where the ACC can be utilized so a triple Gaussian fit attempt was abandoned.

7.2.3 ACC as a Particle Discriminator

Above $p_T = 2.3$ pion/kaon mixing becomes inseparable. In this region I utilize the ACC to trigger and veto pion and kaon events respectively by setting Cherenkov radiation threshold which is done by counting the number of photoelectrons collected by the two PMTs on each channel of the ACC (see fig. 7.5). This utilization of the ACC therefore sorts tracks into two separate histograms, one with an *ACC fire* condition that contains mostly pions with minimal kaon contamination, and another with an *ACC veto* condition that contains the remaining kaons and protons with minimal pion contamination. These two histograms can then be analyzed with single Gaussians since the distributions are now separate. This ACC threshold is the sum of the number of photoelectrons ($N_{p.e.}$) in both PMTs. The total number of $N_{p.e.}$ is plotted versus m^2 in a 2-d histogram and a threshold is set in order for there to be a maximum separation between pion and kaon signals. This 2-d histogram is then projected from the threshold up to the highest $N_{p.e.}$ bin for the pions and projected from the threshold down to the lowest $N_{p.e.}$ bin for kaons and protons. These 1-d

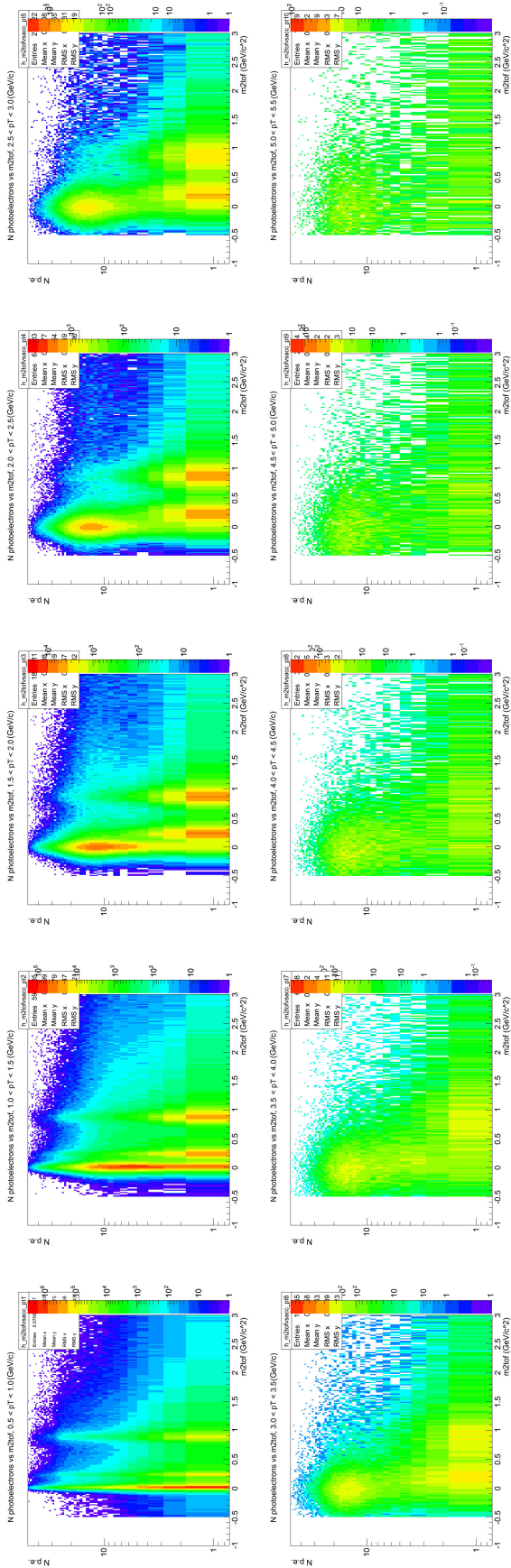


Figure 7.5: Number of ACC photoelectrons vs m^2 in bins of p_T . As p_T increases, the number of ACC photoelectrons can be used to discriminate pions from kaons and protons.

projections can then be modeled with either single Gaussians (pions) or mixed Gaussians (kaons and protons). (full fits and data in Appendix C.1.4)

7.2.4 High p_T : Fixed Width and Mean

Above $p_T=3.5$, the strength of particle signatures decreases, approaching level of the background, making individual peaks hard to fit. Though statistics may be very low in the six bins of $d\phi$, there are still enough statistics if all the bins are combined. Means and widths of particle signals should only depend on p_T and not on $d\phi$, therefore I can merge all $d\phi$ bins to calculate the statistical mean and width for each particle species at a given p_T and fix these means and widths as constant for each bin in $d\phi$ and allow the heights of the Gaussians to dictate the yield.

7.3 Identified Particle v_2

The end result of each of these particle identification methods is a Yield vs $d\phi$ plot for the three particle species: pions, kaons, and protons. These plots can be treated like the $dN/d\phi$ vs $d\phi$ plots that provided the charged track v_2 measurement which was acquired by fitting with the functional form of equation 7.3. The parameters of this Fourier fit are the uncorrected v_2 coefficients. Dividing by the event plane resolution gives the corrected v_2 (fig 7.6) (see section 8.1). Statistical error bars on this plot come from the associated parameter errors in the Gaussian fits, propagated through and combined with the errors of

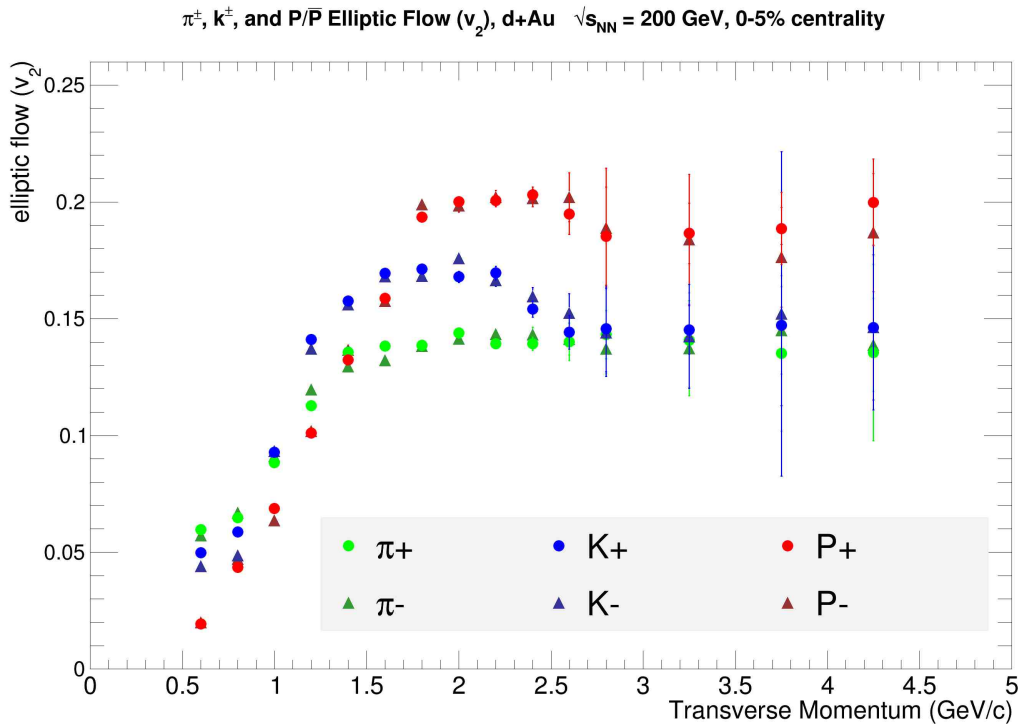


Figure 7.6: π^\pm, K^\pm , and p/\bar{p} elliptic flow, resolution corrected. Error bars are statistical errors.

the cosine fits. Systematic errors are treated in the next chapter.

Chapter 8

Error Analysis

There are various sources of systematic error that could contribute to uncertainty in this measurement. These include certainty in how the event plane was determined (sect. 8.1), how well the event centrality can be determined (sect. 8.2), various uncertainties pertaining to the identification of the particles (sect. 8.3), and the effects of detector acceptance (sect. 8.4). In this chapter I will quantify the uncertainty for each of these contributions and then use these values to find the possible variance in the flow measurement due to these uncertainties. It will be shown that event plane resolution and PID systematics due to Gaussian fitting dominate and other errors are negligible.

Any uncertainty that would affect the value of this flow measurement would do so in one of two ways: either by shifting individual v_2 data points (changing inherent shape of the data set) or by changing the overall scaling of the whole measurement in a net direction (simple scaling of entire data set). Errors that would simply shift all values of v_2

are the event plane resolution and centrality determination errors. Errors that would shift individual points consist of the various PID uncertainties and detector acceptance effects. The way the uncertainties in this category would shift individual data points is by changing the shape of the particle yield distribution in $d\phi$. Recall that there are two terms that parametrize the shape of the yield in $d\phi$:

$$yield(d\phi) = v_0[1 + v_2 \cos 2d\phi] \quad (8.1)$$

In this equation, v_0 corresponds to an overall shift in the function, that is to say it describes the up-and-down displacement of the whole curve and doesn't affect the general shape of it. The remaining parameter, v_2 , describes the shape of the yield distribution in $d\phi$. Changes to the shape of this distribution happen when yield values are perturbed up or down in individual bins of $d\phi$ which results in a change in the associated v_2 . In order to study the strength of v_2 -affecting uncertainties I will apply the variances discussed in this chapter to individual points in the yield vs $d\phi$ distribution and re-fit with a cosine in order to see the effect varying individual points has on the flow coefficient.

8.1 Event Plane Resolution Correction

As mentioned in section 6.4, the limitations of the detectors to precisely resolve the event plane result in a weaker anisotropic flow measurement. We therefore define a

Table 8.1: Event Plane Resolution Corrections for MPC, 0-5% centrality, calculated using the Three Sub Event method (see sect. 6.4)

Detectors Used	$\Psi_{RES.3SE}$
<i>MPC, SMD, RXNIN</i>	0.200718 ± 0.0001312
<i>MPC, SMD, RXNOUT</i>	0.261658 ± 0.0001312
<i>MPC, SMD, RXNCMB</i>	0.241446 ± 0.0001311
$\langle \Psi_{RES.MPC} \rangle$	0.234607
$\sigma_{RES.MPC}$	0.03104

resolution correction to the overall v_2 measurement such that:

$$v_n = \frac{v_n^A}{Res(\Psi_n^A)} \quad (8.2)$$

where $Res(\Psi_n^A)$ is the resolution correction for the n-th order event plane determined using detector A. Because of this definition, detectors that are able to resolve the event plane more precisely require less of a correction, so larger values of resolution correction would come from detectors that are better suited to measure the event plane. These resolution limitations are exacerbated by the asymmetric nature of the d+Au system. From the way ions are fed into RHIC and the orientation of PHENIX in the RHIC ring, the north arm is the “deuteron-going” side and the south side is the “gold-going” side, i.e. deuteron remnants and forward produced particles hit the north arm and spectators and particles produced from the gold beam hit the south arm. The significant increase in the number of nucleons in a gold nucleus result in higher track multiplicity in the south arm which, in turn, makes the determination the event plane using south arm detectors significantly easier for the d+Au system. This can be seen by comparing the event flattening plots for the north and south

detectors in fig 6.3. This combination of higher track multiplicity in the south arm and a smooth flattened event plane distribution in the MPC makes it a good choice for event plane determination. Furthermore, because each of the sub event terms in the three sub event method for determining the resolution correction is calculated using the average values for the differences of event plane measurements for two detectors, these average values can be calculated for all combinations of detectors which can, in turn, be used to combinatorially determine the resolution correction for every detector. In doing so, it was seen that the MPC has the best resolution of all the detectors possible. Additional independent measurements of the event plane are used to correct further resolution limitations in the MPC (using the Three Subevent Method, eqn. 6.2). The resolution correction measurements displayed in table 8.1 were determined using 5 detectors: the SMD, MPC, inner RXNP, outer RXNP, and the combined RXNP. Since any 3 detectors can be used to determine an event plane resolution correction, this correction can be calculated for the MPC using various detectors as subevent comparisons. This was done using combinations of detectors as listed in the table and the mean was calculated of all combinations. The corresponding variance of this set of measurements can be attributed to systematics inherent in each detector subsystem. Doing so gives a 13% systematic variance on the MPC resolution correction.

8.2 Centrality Resolution

Flow is at its strongest in most central collisions and uncertainty in the determination of centrality could affect the flow measurement. Collaborators have addressed the

centrality categorization in Run 8 d+Au[70] by correlating the charge sum in the BBC to the number of binary collisions ($\langle N_{coll} \rangle$). They found a systematic uncertainty of 7% on the determination of $\langle N_{coll} \rangle$ for this data set for centralities from 0-20% when compared to Glauber model Monte Carlo simulations. Furthermore, centrality systematics do little to change the shape of the yield vs $d\phi$ distribution and only increase the statistics. As a check, I performed the flow measurement on a centrality range from 0-4% and 0-6% to see if the value was changed appreciably or not. In figure 8.1 I have plotted the fractional deviation:

$$\sigma_{sys}^{centrality} = \left| \frac{v_2^{0-5\%} - v_2^{0-4\%(6\%)}}{v_2^{0-5\%}} \right|, \quad (8.3)$$

as a measure of the effect of varying size of the centrality bin on the flow measurement. This deviation was maximally 5% and appeared to have no correlation to the p_T of the tracks.

8.3 Particle Identification Methods

There are three sources of error that can come from the identification of these particle species. Since the separation of signals is dependent on the time of flight and the momentum, uncertainty in either of these propagates to the error in identification. Furthermore, imperfections in the Gaussian fits can systematically miscount particles contributing to further uncertainty in flow coefficients.

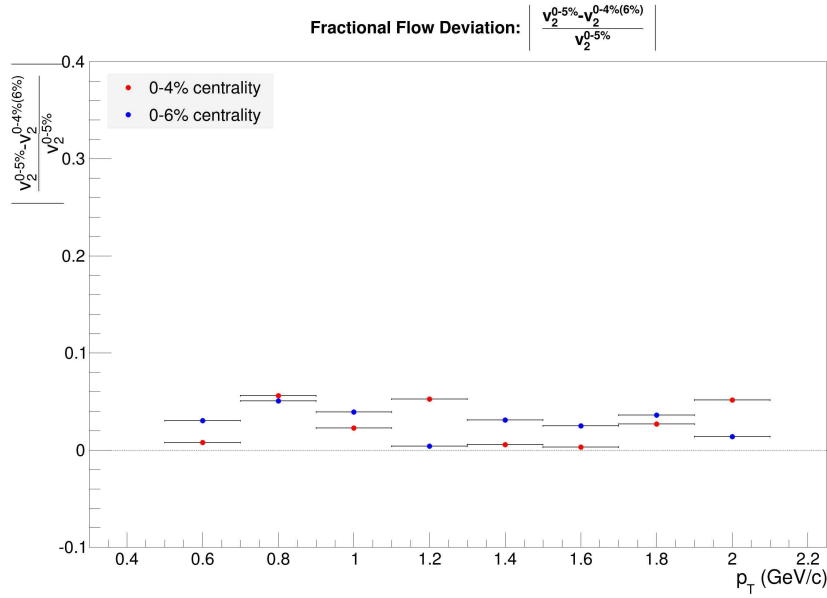


Figure 8.1: Centrality uncertainty contribution to Systematic Error

8.3.1 Momentum Uncertainty

Track momentum is determined by track curvature in the DC/PC1 as described in section 4.3. Track curvature and certainty of this calculation is correlated to the ability to match hits in the DC and PC which is quantified by the *track quality* designation. As mentioned, only tracks which have at least 3 hits in the DC and PC1 are accepted for analysis. Additionally, TOF and PC3 tracking adds additional confidence to the tracing of individual hits to reconstructed tracks. Track projections that pass the quality cut in the PC1 are projected onto the TOF and PC3 and only hits that fall within 3σ of the projected hit are accepted for analysis. Furthermore, momentum reconstruction resolution has been studied with single particle simulations[64]. This resolution was shown to be linear in p_T with the highest p_T bin used in this analysis (5 GeV/c) having a resolution of 2%.

8.3.2 TOF Timing

Since the TOF boasts a very high timing resolution and since the preamplifier gains, cable lengths, and various other systematics can affect the timing measurement from strip to strip, it is important to calibrate the response across all the strips in the TOF. Conventionally, the tracks are shifted to some expected value. Since pions are by far the most plentiful particles created in heavy ion collisions, we pick them to be our normalization. Specifically, the track time distribution is plotted for each strip individually. We know the start of the event time as given by the BBC and we know the expected time of flight for a pion (t_π) of mass m_π with a measured momentum, p :

$$t_\pi = \sqrt{\frac{m_\pi}{p^2} + \frac{1}{c^2}}. \quad (8.4)$$

Each strip is then fit with a normal distribution and the distance from the mean to $t = 0$ is the timing offset (Δt) for the strip. This offset is then applied to each track's measured time:

$$\Delta t = t_{TOF\,measured} - t_{collision/BBC} - t_\pi \quad (8.5)$$

Given the TOFW's known resolution of $\sim 80\text{ps}$, if we propagate this error through eqn. 4.4 with the known distance from the vertex of the TOF.W and a maximal p_T value for this analysis of 5 GeV/c, the maximum variance in m due to resolution is $\pm 2 \text{ eV}/c^2$)

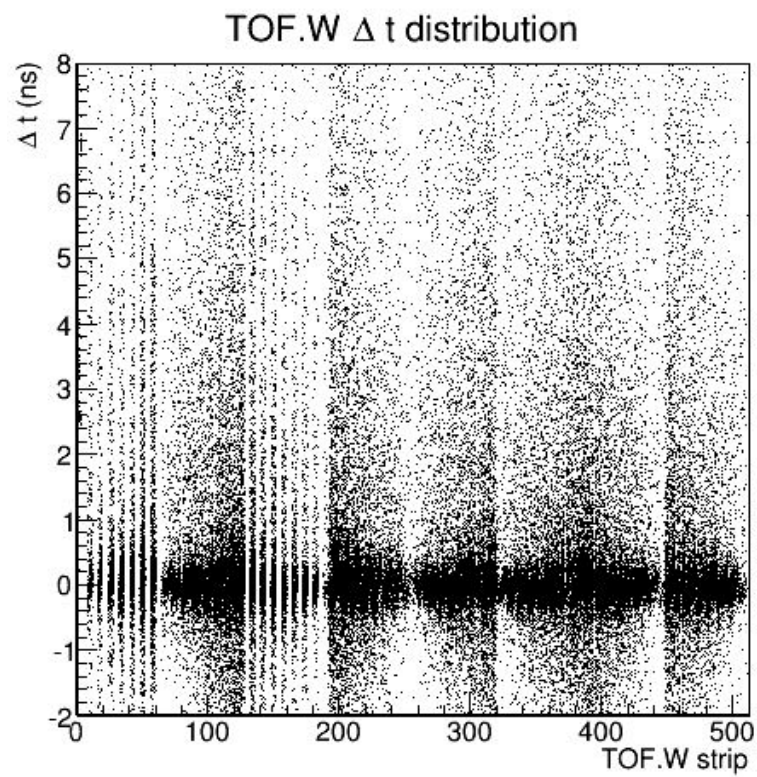


Figure 8.2: Timing QA in the TOF.W, Δt vs TOF.W strip id

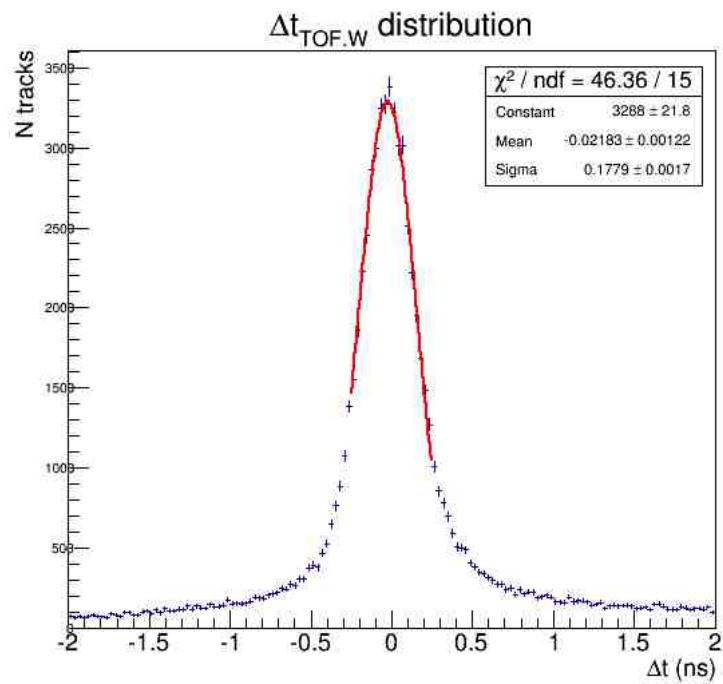


Figure 8.3: Systematic Timing Offset in the TOF.W

which, when compared to the smallest mass measured ($m_\pi \approx 139$ MeV/c²), is negligible. Furthermore, the systematic offset of the detector after calibration is 21 ps, well below the TOFW's resolution limitation (fig. 8.3).

8.3.3 Uncertainties from Gaussian Models

Single and Mixed Gaussians, no ACC, $p_T \leq 2.1$ GeV/c

Species purity is integrated out to 2σ which accounts for 95.45% of particles about the mean of their distribution. Therefore, systematics due to mixing in the tails of the particle distributions is at most 4.55%. Gaussian distributions do not perfectly match the particle distributions, often there is a tradeoff between fitting the shape of the peak or the shape of the tails. Given the $2-\sigma$ integration of the Gaussians, fitting the shape of the peaks took priority as the tails would contribute very minimally. This systematic uncertainty in the tails always *under* counts the number of particles in a distribution, however it can be seen from inspection (see App. C) that and over and under counting done by the models is uniform across each bin in $d\phi$ for within the same bin of p_T . Any systematic over/under counting such as this only serves to shift the y-position of the flow curve a net value up or down without changing the value of the harmonic. This appears to remain true for $p_T \leq 2.1$ GeV/c. There are a few instances where fitting algorithms appear to have not matched the shape of the peaks perfectly but the functions fit nicely through the waist of the distribution. Each of these bins were inspected and allowed to vary by hand to fit various misshapen regions of the distributions. The maximal variance in the yield from the

fit functions was 2% for the pions and kaons and <1% for the protons in this range of p_T .

ACC Meson Separation and Gaussian Tail Cross Contamination, $2.1 \leq p_T \leq 2.9$

For $p_T \geq 2.1 GeV/c$, the ACC is used to separate pions from kaons and protons. Over/under counting in the tails is still the most likely place for systematic errors to accrue and this effect is strongest in the kaons since the ACC threshold still allows some pion contamination. Because of this, fitting the peaks and the right side waist and tail of the kaon distributions for ACC vetoed tracks took priority. In the lower bound of this p_T range, kaons maintain good separation from protons, however as the p_T increases there is some species contamination in the tails. This is accounted for in two ways. Firstly, as with the low $p_T \pi/k$, mixing happens in the extremes of the tails and particle counting stops at $2 - \sigma$. Secondly. A two peak, Mixed Gaussian model is used to fit the kaon and proton peaks which allows for the additive overlap in the tails to be visualized and accounted for. This accounts for a 5% maximum systematic error for the kaons and 2% max for the protons. Since the ACC operates on Cherenkov radiation, the “ACC fire” condition is far more selective since it requires particles to be traveling fast enough to radiate. This leads to a very pure pion signal with negligible contamination, attributing < 1% systematic uncertainty.

Fixed Width/Mean Gaussians and Background Effects

For $p_T \geq 3$ GeV/c, low statistics cause the means and widths of particle distributions to vary across bins in $d\phi$. Because of this, all $d\phi$ bins are summed for a given p_T bin and are fit as a whole in order to fix a constant mean and width for each particle

species. In doing so, only the heights of the Gaussians are allowed to vary. In practice, this method tends to undercount particles. When the means of particle distributions deviate from the model-fixed values of the Gaussian models it causes only the regions that fall under the Gaussians to be counted, largely missing regions of the distribution that are not encompassed by the curve. This accounts for a 7% under-counting in these bins.

Additionally, background tracks for the very last p_T bin are strong enough to contribute to error. The TOFW along with the PC3 allows for very strong background rejection thanks to the two detectors' high precision tracking and distance from the event vertex. Only tracks with five matching points are accepted for analysis, that is: 2 hits in the DC, 1 matched hit in the PC1 within $2 - \sigma$, 1 matched hit in the TOFW within $3 - \sigma$, and 1 matched hit in the PC3 to $3 - \sigma$. This leads to a negligible background for high statistics analyses. For $4 \leq p_T \leq 4.5$, the numbers of detected particles are low enough that the background may contribute 1 out of every 10 tracks counted for each particle species. This leads to a 10% systematic error for this last bin from background.

8.4 Detector Acceptance

Detectors occupy a limited and constant range in space. The ability of a detector to cover a range in space is called its *acceptance*. Additionally, detectors are imperfect, there are dead channels, hot channels, edge effects, and other phenomena that can ruin the efficiency of a detector and add holes to its acceptance. Because of this, acceptance limitations of detectors can affect measurements in various analyses, however, for reasons

I will discuss, a flow analysis is at best negligibly affected by detector acceptance effects. Analyses where acceptance effects are strongest are those where the coordinate system is “static”. By this I mean that the production of analyzed tracks are studied in the lab frame coordinate system and any repeatedly missed tracks in a hole in acceptance are missed indefinitely and completely. Since event characteristics are random, by the necessity of event plane determination there is a statistical “smearing” that happens from the Q-vector normalization and the event plane flattening. Any holes in azimuthal coverage due to detector limitations in the lab coordinate system are smeared over by this normalization and flattening since we are performing the analysis in the event plane coordinate system which is statistically distributed and normalized. Furthermore, collaborators have studied the systematics of acceptance on v_2 measurements[71] by comparing v_2 measurements made with charged hadrons detected in TOF.E and TOF.W (45° per arm) with charged hadrons detected in full central arm acceptance (90° per arm). They found that a two-fold increase in azimuthal acceptance resulted in less than 2% difference in flow measurements.

8.5 Summary

The particle yield is binned in six bins of $d\phi$ which therefore means that there are six points that can be perturbed systematically. In order to study the propagation of the yield uncertainty to the measured flow coefficient I take the known values of yield in $d\phi$ and perturb them up or down by the percentages quantified in this chapter. The changed yield vs $d\phi$ distribution is re-fit and a new flow coefficient is calculated. This new v_2 is compared

to the original one in order to determine systematic errors on the final measurement which are caused by sources within the process of measuring it. Since the identified track flow follows the behavior of the individual particle flows, I will use it for this study and, for completeness, perturbations both up and down will be studied.

In practice, of these six points, four contribute strongly to the overall shape of the yield distribution, these are: the two end points and the two center points. This is shown by the significantly smaller systematic error in bins 1 and 4 in fig 8.4. Additionally, the direction of perturbation makes a negligible difference; up and down perturbations line up very well on the plots. Yield systematics have the strongest effect on the lower p_T bins. This is because their significantly higher statistics correspond to a larger loss or gain of counted particles with which to skew the flow coefficient.

The resulting systematic errors are summarized in table 8.2.

Figure 8.4: Effects of Systematic Shifts in Yield on v_2 . 1%, 2%, 4%, 5%, 7%, and 10% perturbations are applied to each yield for a particular bin of $d\phi$ and the corresponding v_2 is calculated. Closed circles are downward perturbations, open circles, upward perturbations.

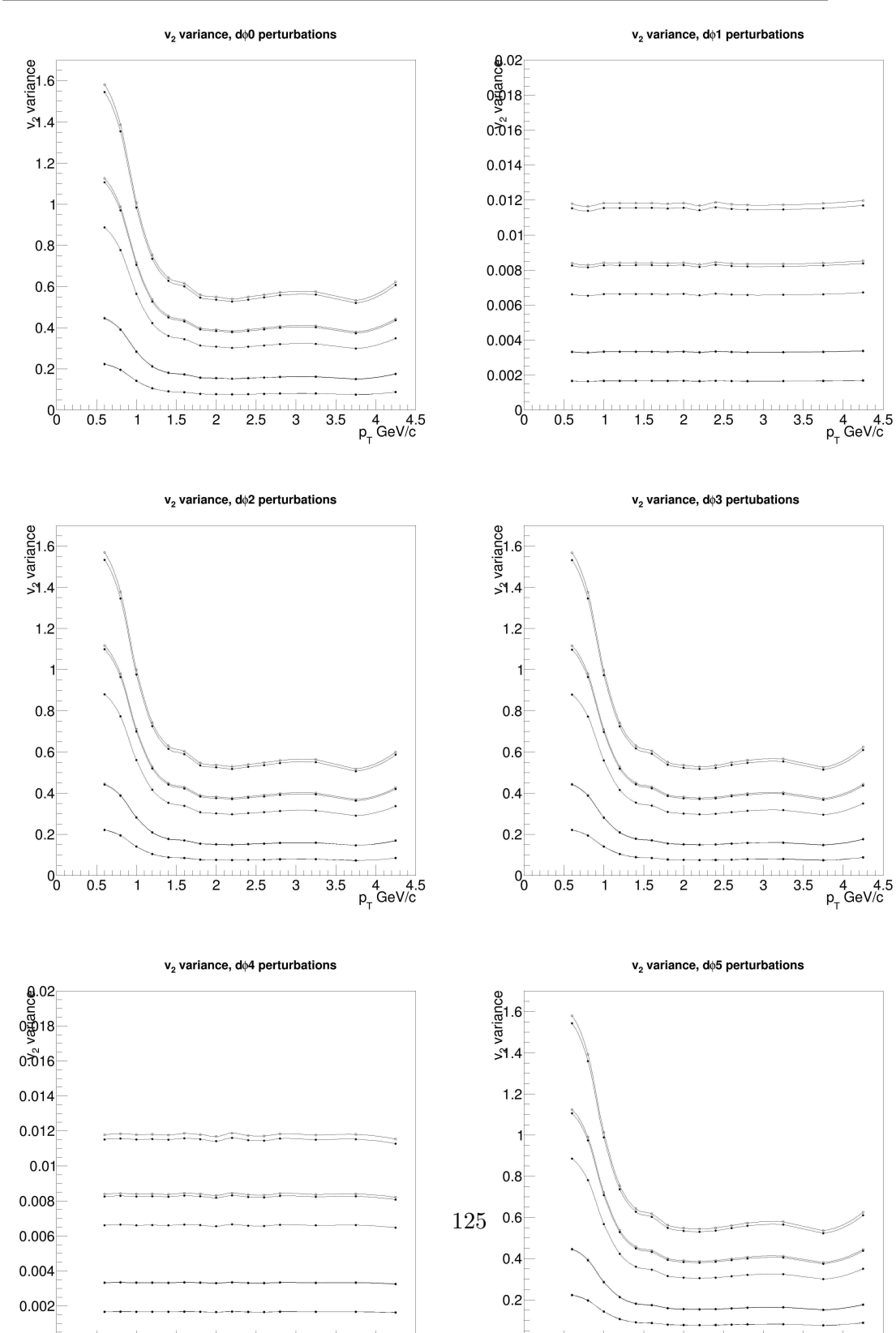


Table 8.2: Table of Systematic Errors in each bin of p_T

Source of Error	Transverse Momentum Bin Range (GeV/c)							
	0.5-0.7	0.7-0.9	0.9-1.1	1.1-1.3	1.3-1.5	1.5-1.7	1.7-1.9	1.9-2.1
Event Plane Resolution	23.40%	23.40%	23.40%	23.40%	23.40%	23.40%	23.40%	23.40%
Detector Acceptance	<2%	<2%	<2%	<2%	<2%	<2%	<2%	<2%
Centrality Determination	5%	5%	5%	5%	5%	5%	5%	5%
PID uncertainty (pion)	22%	20%	14%	11%	9%	17%	16%	15%
PID uncertainty (kaon)	22%	20%	14%	11%	9%	17%	16%	15%
PID uncertainty (proton)	22%	20%	14%	10%	9%	8%	8%	7%

Transverse Momentum Bin Range (GeV/c)

Source of Error	Transverse Momentum Bin Range (GeV/c)						
	2.1-2.3	2.3-2.5	2.5-2.7	2.7-2.9	3.0-3.5	3.5-4.0	4.0-4.5
Event Plane Resolution	23.40%	23.40%	23.40%	23.40%	23.40%	23.40%	23.40%
Detector Acceptance	<2%	<2%	<2%	<2%	<2%	<2%	<2%
Centrality Determination	5%	5%	5%	5%	5%	5%	5%
PID uncertainty (pion)	7%	7%	8%	8%	40%	40%	90%
PID uncertainty (kaon)	35%	35%	35%	35%	55%	53%	90%
PID uncertainty (proton)	15%	15%	16%	16%	55%	53%	90%

Chapter 9

Conclusions

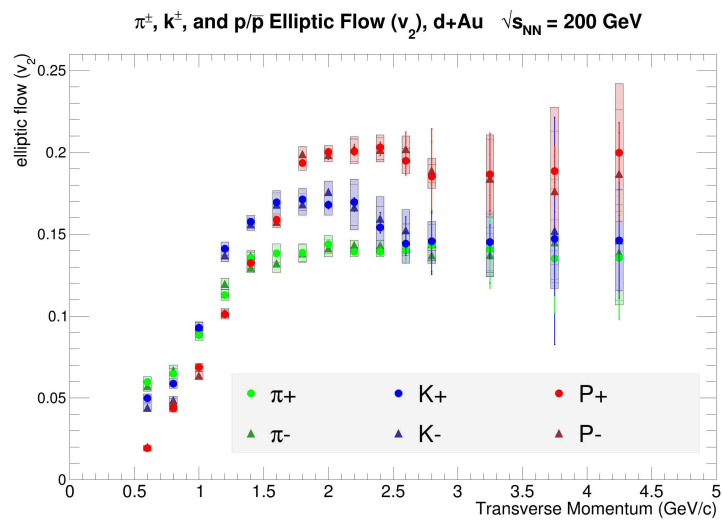


Figure 9.1: Elliptic Flow vs Transverse Momentum, 200 GeV d+Au, 0-5% centrality

Measurements of the second Fourier coefficient corresponding to an elliptically shaped azimuthal anisotropy of pions, kaons, and (anti)protons produced in 200 GeV

deuteron-gold collisions are presented in figure 9.1. Historically, a large number of participant nucleons was thought to be required to be needed in order to produce a QGP. Consequently, it was thought that the low number of participant nucleons in the d+Au system was insufficient for such a phase change. The nonzero flow measurement in this analysis is a sign that collective behavior happens in systems previously thought of as “cold” and is an indication that a QGP could be formed in the simpler system of d+Au. This flow increases steadily for all hadrons up to $p_T \sim 1.5$ GeV/c where the mesons (pions and kaons) seem to reach a saturation and flatten out. The kaons exhibit a flow signal stronger than the pions in this range but eventually decrease to the same nominal value as the pions. The (anti)protons continue to flow increasingly up to $p_T \sim 2$ GeV/c where they too flatten out. The measurement of particles and their corresponding antiparticles was separated throughout the course of the analysis. In doing so, flow coefficients for negative and positive charged particles for a given species can be compared. Here we see that the collision, evolution, and freeze out of the d+Au system does not favor particles or antiparticles, as expected.

9.1 Discussion

9.1.1 Hadronization

The (anti)proton flow enhancement in the mid- p_T range is similar to the baryon enhancement seen in previous experiments and the observation of collective flow is a strong indication of quark deconfinement/QGP formation. Because of this deconfinement, baryon

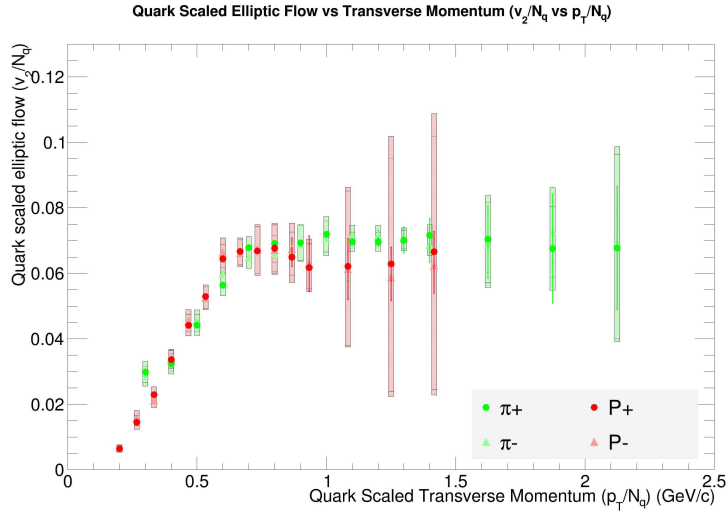


Figure 9.2: Quark Scaled Elliptic Flow (π^\pm and p/\bar{p}) vs Transverse Momentum, 200 GeV $d+Au$

enhancement must happen with some mechanism in the freeze out stage. The leading model describing this phenomenon, recombination, can be seen by scaling the flow coefficient and momentum by the number of quarks that comprise the measured particle¹. Doing so shows that this particle momentum discrepancy may come from the sum of momenta of the constituent quarks. That is to say, the reason why protons appear to have stronger flow is simply because they contain more quarks. For example, if we were to take three deconfined quarks that have the same momentum, they would hadronize to produce a particle with higher momentum than if only two of those quarks had combined. This quark scaled flow is shown in figure 9.2 for pions and protons and shows that both particle signals increase and reach saturation in the same range. That the two quark scaled measurements track each other well through the p_T range is a strong indication of recombination as the

¹2 quarks for pions/kaons, 3 quarks for protons

mechanism for thermal freeze-out and is a result that agrees with similar quark scaled results in ${}^3\text{He}+\text{Au}$ [72], $\text{Au}+\text{Au}$ [23], $\text{Cu}+\text{Cu}$ [73], $\text{Pb}+\text{Pb}$ [74] systems both at RHIC and abroad.

9.1.2 Comparison to Flow Models

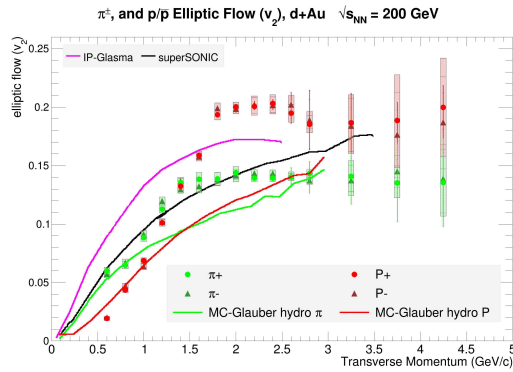


Figure 9.3: π^\pm and p/\bar{p} Elliptic Flow compared to hydrodynamic models: MC-Glauber[75], IP-Glasma[76], and superSONIC[77]

Prior to hadronization, the equilibrated state of deconfined quarks has been described well with viscous hydrodynamic models. The way these models differ is in their assumption of the initial conditions (Glauber versus CGC) and length of equilibration time. A comparison of this measurement with these hydrodynamic models is shown in figure 9.3. Models using Monte Carlo simulations of identified particle flow that utilize Glauber initial conditions (MC-Glauber) describe the data well for low p_T but diverge above $p_T \sim 1 \text{ GeV}/c$, also seen in d+Au in a previous PHENIX analysis[78]². A continuation of MC-Glauber including a longer equilibration time (longer period of *pre-flow* before a thermalized QGP

²though diverging at slightly higher transverse momentum, $p_T < 1.5 \text{ GeV}/c$

flow) and the effect of post freeze-out hadron interaction³ called *superSONIC*[77]⁴ matches data through mid p_T but does not match the flow signal's saturation that begins just below $p_T \sim 2$ GeV/c, an effect also seen in the aforementioned PHENIX d+Au analysis. A model using an impact parameter independent CGC initial condition with a Glasma thermalization phase (IP-Glasma)[76] overestimates the flow strength at low p_T but does appear to model the asymptotic flow behavior at mid-high p_T , albeit overestimating the value of that maximum flow value slightly. These two models can be seen compared to the overall flow in figure 9.4. In order to minimize the effect of baryon enhancement in mid p_T , the elliptic flow of all hadrons is approximated by summing the yields of all identified tracks and performing a flow analysis.

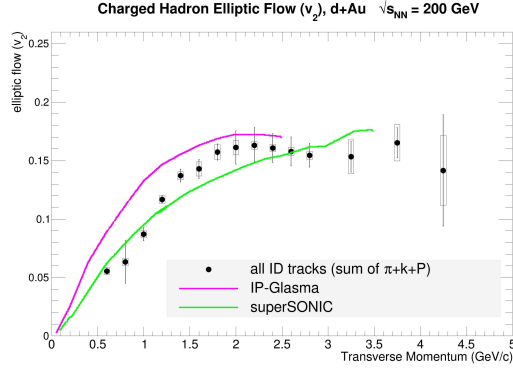


Figure 9.4: Elliptic flow of all charged hadrons measured by summing the yields of all identified tracks. Data is compared to IP-Glasma and superSONIC models.

³referred to in literature as *Hadronic Cascade Afterburner*

⁴an extension of an earlier SONIC model with a longer pre-flow time. SONIC stands for *Super hybrid mOdel simulatioN for relativistic heavy-Ion Collisions*[77]

9.1.3 Strangeness and Initial Conditions

While quark scaling can be used to explain pion and proton flow, implying that these hadrons are made by the combination of light flavor quarks, consistent with recombination, these quark building blocks had already existed before the collision in the form of valence quarks in the ions. What about strange quarks? These are created fresh from the collision, be it because of some process in thermalization⁵, or because of some strange quark producing mechanism in the flowing QGP⁶. Previous enhancement was explained with a hadronization mechanism made evident by quark scaling protons and pions. However, this does not work for kaons as shown in figure 9.5b. Here, the quark scaled kaon flow does not follow the flow of light flavor hadrons in the range $p_T \sim 0.7 - 1.3$ GeV/c, rather, it is stronger.

It is shown in figure 9.2 that quark scaling the hadron flow causes light flavor hadron flow to line up. That is to say, it removes the apparent baryon excess by attributing this excess to recombination of two versus three quarks. However, we see that whatever mechanism creates strange quarks is not well described by Glauber initial conditions since there remains a stronger flow of strange quarks above the flow of light flavor quarks after quark scaling. In this range, the IP-Glasma model best fits the kaon flow (see fig. 9.5a). This implies that the choice of initial conditions and thermalization mechanisms in models may play a part in explaining strangeness enhancement and may be an indication of how

⁵Glasma/pre-equilibrium flow

⁶gluon fusion

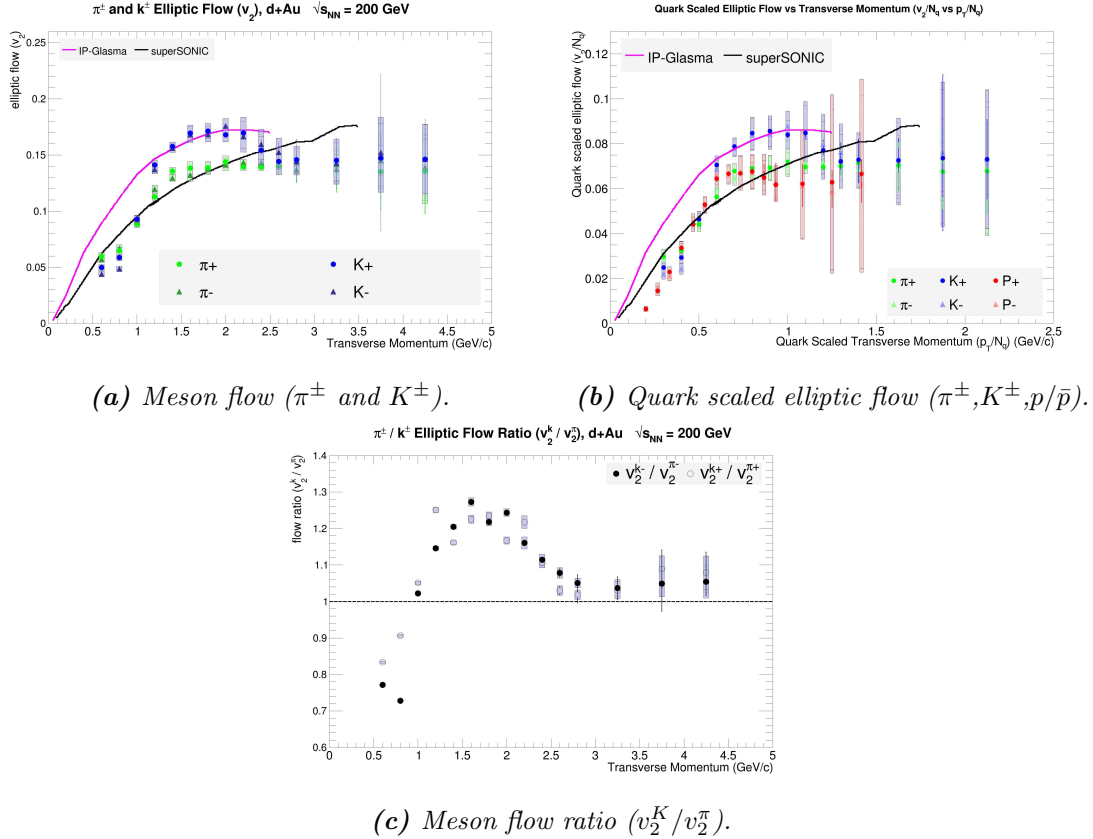


Figure 9.5: Elliptic flow of mesons (π^\pm and K^\pm) are compared to hydrodynamic models. Where hadrons comprised from first generation quarks obey quark scaling, strange quark-containing kaons show an excess. CGC containing model seems to model kaon behavior at mid-pt well.

CGC/Glasma may present itself in simple heavy ion systems. Following this thought, the Glauber model would be appropriate for describing light flavor quark flow since it treats the nucleus as a density function of these light quarks. The flow of light flavor hadrons is then described by the recombination and fragmentation of quarks that had already existed. On the other hand, the CGC initial condition has built within it a plethora of gluons due to low-x saturation. These gluons may generate flow in the pre-equilibrium stage[79]. Strangeness enhancement through gluon-gluon fusion has historically been proposed as a sign of the onset of QGP formation[43], a phenomenon that combines well with the dominant availability of gluons in the CGC model. Similar strange flow enhancement above quark scaling has been seen in⁷ Pb+Pb collisions[80] and at high kinetic energy in ³He+Au[72]. However, previous Au+Au results have shown that although kaon production appears to be enhanced [12], kaon flow seems to follow quark scaling. [73]

Furthermore, it may be advantageous to treat the flow of light flavor and heavy flavor quarks with different models. As mentioned, light quarks already existed and carry the majority of the momentum in the relativistic nucleus before collision. The time scale of these valence quarks makes them appear to move very fast compared to the saturated gluons, which may imply that the model describing the behavior of valence quarks is different from the model describing the behavior of the saturated gluons. We can therefore use the Glauber model as it was originally intended: as a description of quantum mechanical scattering for systems comprised of many particles (the light flavor quarks).

⁷in triangular flow (v_3) measured with K^\pm and $\Lambda/\bar{\Lambda}$ compared to π^\pm and p/\bar{p} .

On the other hand, the “frustrated” low-x gluons move much more slowly and may interact on different time scales than the valence quarks. Additionally, gluons do not exist on their own in nature, we can only detect what they hadronize into. Since heavy quarks are created fresh, they are a good candidate for a probe with which to study the interaction of low-x gluons.

9.2 Comparison to Other Results

Flow has been observed in other analyses of simple systems. Here I will compare my results to published results that analyzed other light-on-heavy ion collisions in order to see my results in the context of other measurements of the same phenomena .

A previously published PHENIX analysis of v_2 in $\sqrt{s_{NN}} = 200$ GeV d+Au collisions is shown in figure 9.6. The flow measurement here was calculated using two particle correlations⁸. The two results track each other well in slope and strength of the flow up to ~ 1.5 GeV/c and both reach saturation at ~ 2.5 GeV/c. Both exhibit a crossover of the proton flow over the pion flow ~ 1.5 GeV/c. I am able to measure in finer bins of p_T since I use the ACC in conjunction with the TOF.W in order to maintain meson separation. Furthermore, this allows me to study kaon flow, a measurement that this previous publication does not include.

Comparison to the published results from ALICE of the elliptic flow of identified hadrons in 5.02 TeV p+Pb collisions is shown in figure 9.7. Although their system has an

⁸In contrast, my measurement uses a direct Fourier analysis of the flow.

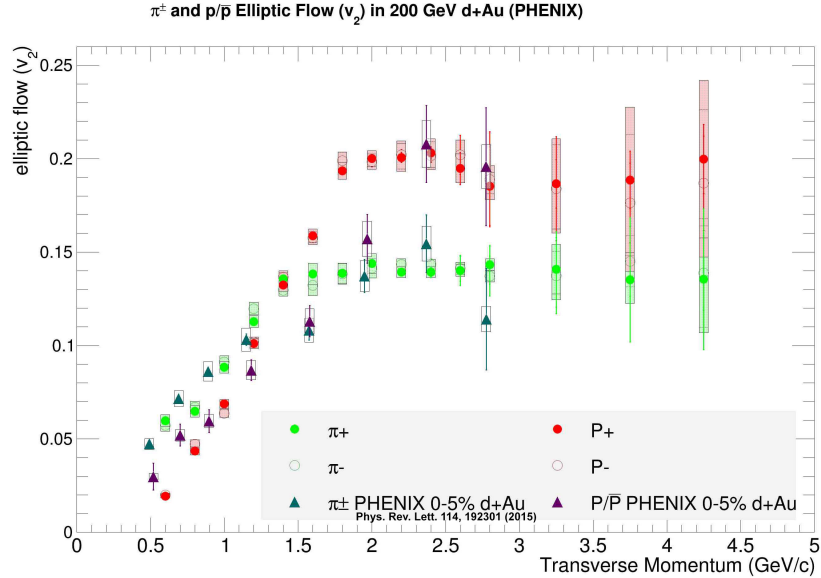


Figure 9.6: Results compared to previous PHENIX $d+Au$ results. [78]

order-of-magnitude higher center of mass energy, light flavor hadrons of the same momentum appear to flow with similar strength up to ~ 1.7 GeV/c. However, their results do not reach a saturation within the p_T range studied and the slope of their increasing flow is slightly broader than my result. It is important to note the difference in geometries of the two systems. While an equilibrated phase created in $d+Au$ collisions is assumed to have an inherent elliptical shape due to deuterons having two quarks, $p+Pb$ collisions cannot have the same initial conditions since protons are circularly symmetric. All flow in the ALICE result is therefore due to fluctuations leading to an initial pressure anisotropy that is elliptically shaped. Furthermore, the ALICE result is also calculated from two particle correlations as opposed to a direct Fourier analysis.

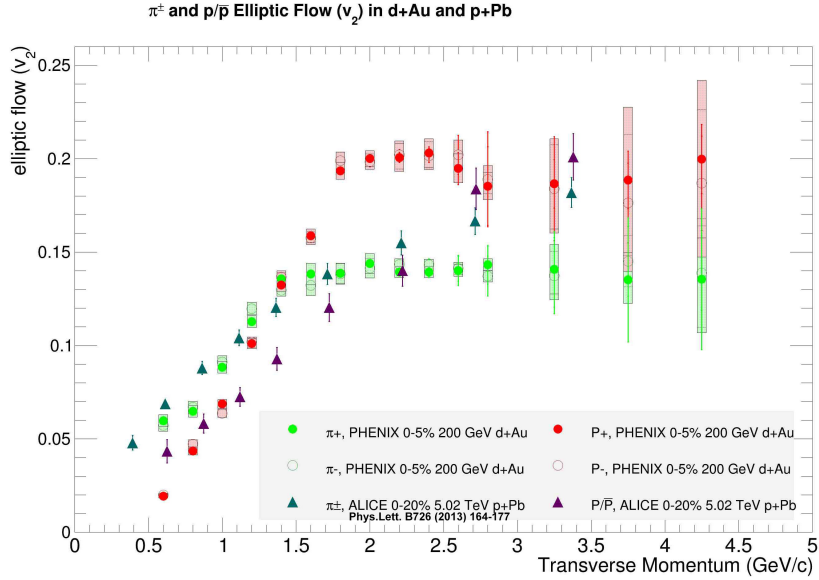


Figure 9.7: Results compared to ALICE $p+Pb$ results. [81].

9.3 Other Signatures of an Equilibrated Phase

Historically, another signature of QGP formation was the suppression of mesons consisting of charm quark/antiquark pairs, also known as J/Ψ mesons. These heavy flavor particles are created from hard scattering processes, and, therefore, their suppression is thought to come from a final state effect. Models have attributed this suppression in large systems⁹ to a color charge screening effect. That is, due to the presence of a dense color field within the QGP, the strength of the color force binding the charm quarks is diminished, allowing them to break apart and form other charmed mesons.

Additional difficulties have arisen when using this signature as a sign of QGP onset. Because the phase transition is not measured directly, and since measurements

⁹Systems presumed to form a QGP.

are made after hadronization, any J/Ψ measurement is sensitive to charm-quark-affecting mechanisms that can take place during the freeze-out. Furthermore, J/Ψ suppression has also been seen as a cold nuclear matter effect [85] in fixed target experiments, though the suppression due to QGP charge screening is expected to be much greater. The question then becomes, “What amount of suppression is indicative of QGP charge screening, and is this threshold sufficiently separated from the amount of suppression in cold systems?”¹⁰

Compared to $p+p$ collisions, J/Ψ production in $d+Au$ collisions is suppressed more strongly in central rapidities compared to forward [82] and the difference in suppression in the two rapidity ranges may be indicative of an equilibrated phase. Consider the reference frame of a collision where the gold ion is at rest. In this frame, the ion behaves as a fixed target¹¹, and, since in the lab frame the ion is actually moving forward, observations of phenomena in forward rapidities (i.e. the gold-going side) are expected to come from cold matter effects. Therefore, measurements in central rapidities that differ from those measured in forward rapidities, may come from a thermalized plasma. That is, if suppression in simple systems is to be completely attributed to cold matter effects then this suppression would not be expected to change in rapidity.

The nuclear modification factors¹², R_{pPb} and R_{PbPb} , versus p_T of J/Ψ compare the suppression between cold and hot systems, and shows that cold J/Ψ suppression follows different behavior than hot. [84] Specifically, forward $Pb+Pb$ J/Ψ mesons are suppressed with increasing p_T , whereas forward $p+Pb$ J/Ψ mesons begin suppressed (presumably due

¹⁰A suppression thought to happen with a different process i.e. nuclear shadowing.

¹¹Though with more gluons due to saturation.

¹²See Appendix B

to cold effects) and gradually increase with increasing p_T .

9.4 Summary

There is ample evidence from this analysis to say that there is collective flow in the previously thought “cold” system of d+Au. Quark scaling proton and pion measurements point to a likely recombination model mechanism for light flavor quark hadronization, and the flow of these hadrons is modeled well with viscous hydrodynamics that use Glauber model initial conditions. There are many questions to be answered regarding strangeness. Since nuclei are made of light flavor quarks, treating their distribution as a density distribution as Glauber does is perfectly adequate, however it does not model the availability of strange quarks with which partons may scatter nor the production processes such as gluon fusion with which strange quarks can be formed. Strange hadrons may also provide a way to better study the initial conditions¹³ and thermalization¹⁴ of the QGP.

In closing, this observation of collective phenomena in simple systems is evidence that there is always something new to be learned from things already studied. As we gaze ever further into the depths of space, ever closer into the intricacies of matter, we are met with increasing profundity. Things we thought we knew we question and things we thought not possible become likely. It is an exciting time as we continue to make discoveries in all subfields of physics and, while we search for the things current theories predict, some of the most exciting discoveries to come will likely present themselves in ways we never conceived

¹³Color-Glass Condensate

¹⁴Glasma/preflow

and in places we never thought to look.

Appendix A

PHENIX Coordinate System

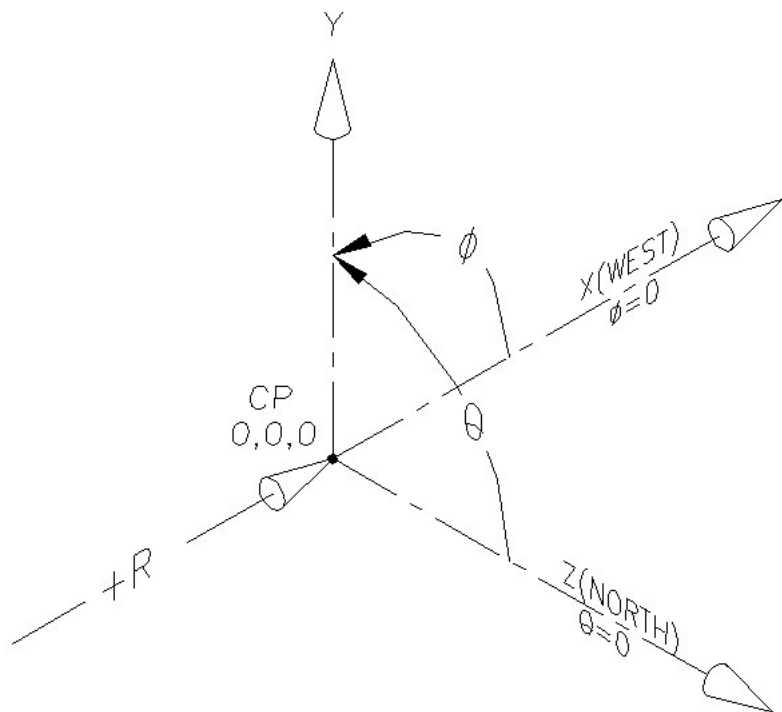


Figure A.1: PHENIX coordinate system

The PHENIX coordinate system in Cartesian coordinates is defines the beam line as the z-axis with the north side of the detector being the positive going direction, due west being the positive going x-axis, and straight up being the positive going y-axis. For spherical coordinates, the azimuthal angle ϕ spans 2π about the z axis with $\phi = 0$ pointing due west, i.e. along the x-axis. The polar angle θ is often converted to pseudorapidity for analysis. Pseudorapidity (η), often referred to colloquially as “rapidity,” (not to be confused with the true rapidity, y) is defined as:

$$\eta = -\ln \left[\tan \left(\frac{\theta}{2} \right) \right]. \quad (\text{A.1})$$

where small values of η refer to processes and measurements in the central arms and larger values of η refer to the forward muon arm regions.

Appendix B

Nuclear Modification Factor

Since heavy ion systems are comprised of many nucleons colliding, we would like to differentiate between phenomena from singular nucleon-nucleon collisions and phenomena created from interactions of nuclear matter. It is therefore convenient to define a quantity that describes how different a system of N colliding nucleons differs from a system of two colliding nucleons scaled up by N , often referred to as *Binary Scaling*. For example, consider the system created with Au+Au collisions. If we wanted to know how pion production was affected by nuclear matter we would be interested in how different pion production was in the collision of 197 nucleons with another 197 nucleons compared to pion production in p+p scaled up by a factor of 197. This quantity is called a *Nuclear Modification Factor* and is usually denoted with the letter R and two subscripts defining what kind of Nuclear Modification Factor it is:

$$R_{AA}(p_T) = \frac{1}{\langle N_{coll} \rangle} \frac{dN_{AA}/dp_T}{d\sigma_{pp}/dp_T}, \quad (\text{B.1})$$

where dN_{AA}/dp_T is the differential yield in the system, $d\sigma_{pp}/dp_T$ is the differential cross section in proton-proton collisions, and $\langle N_{coll} \rangle$ is the number of binary collisions. Given this definition if $R_{AA} = 1$ then we expect no new phenomena in the system, that is, the system comprised of N colliding nucleons behaves exactly as we'd expect N proton-proton collisions to behave. If $R_{AA} > 1$ it is said that interactions with the nuclear material enhances production and vice versa with $R_{AA} < 1$, production is suppressed.

Appendix C

Analysis Data and Plots

C.1 Particle Identification: TOFW

Mass squared plots used for particle identification and corresponding yield vs $d\phi$ are shown here. Fit QA is demonstrated by showing the mean and width for the Gaussian fits across all bins of $d\phi$ for a given p_T range.

C.1.1 Single Gaussian fits, $p_T=0.5\text{-}1.3 \text{ GeV}/c$, TOF.W, negative charged tracks

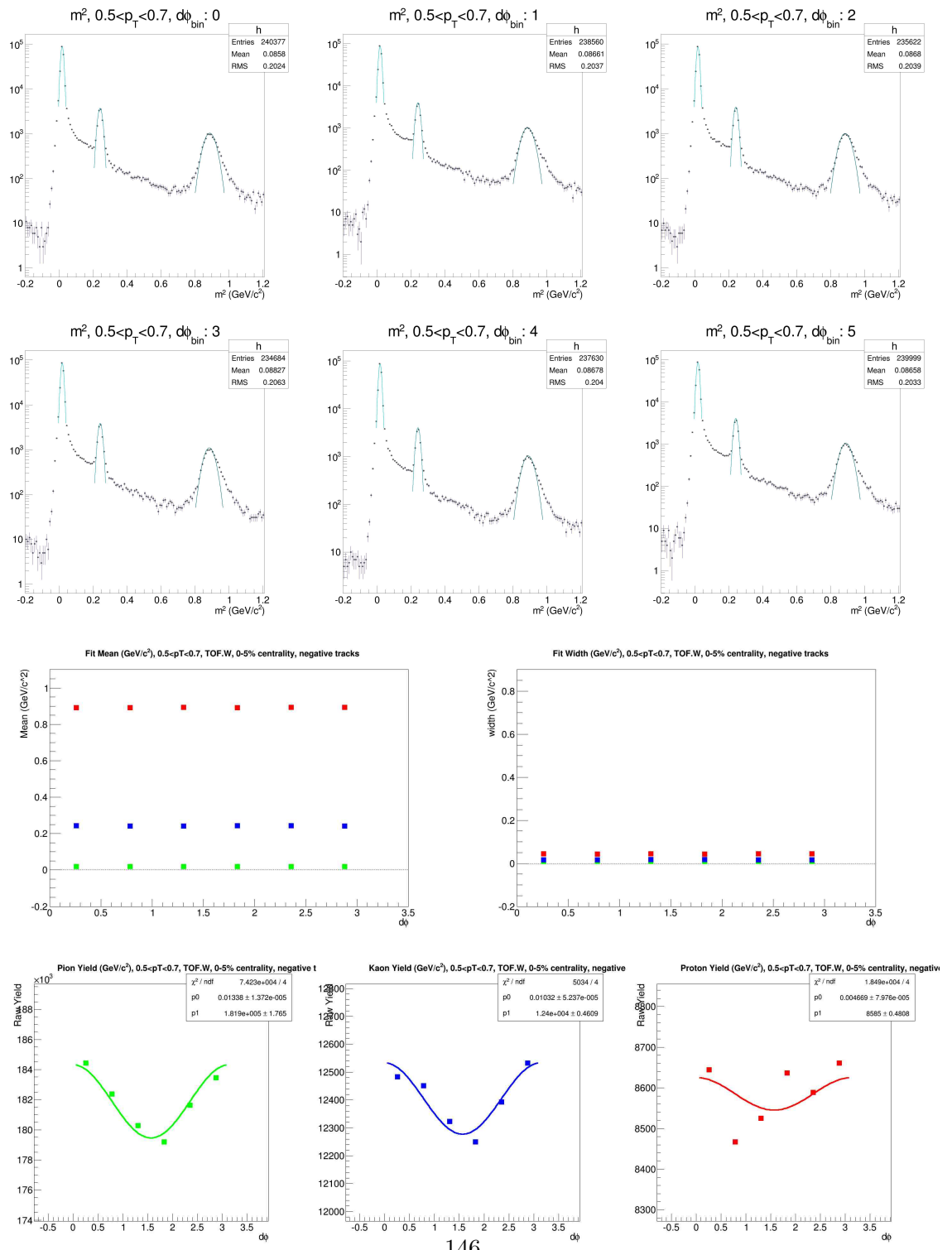


Figure C.1: m^2 Gaussian fits for PID and resulting Yield vs $d\phi$ for $p_T=0.5\text{-}0.7 \text{ GeV}/c$, TOF.W, negative particles

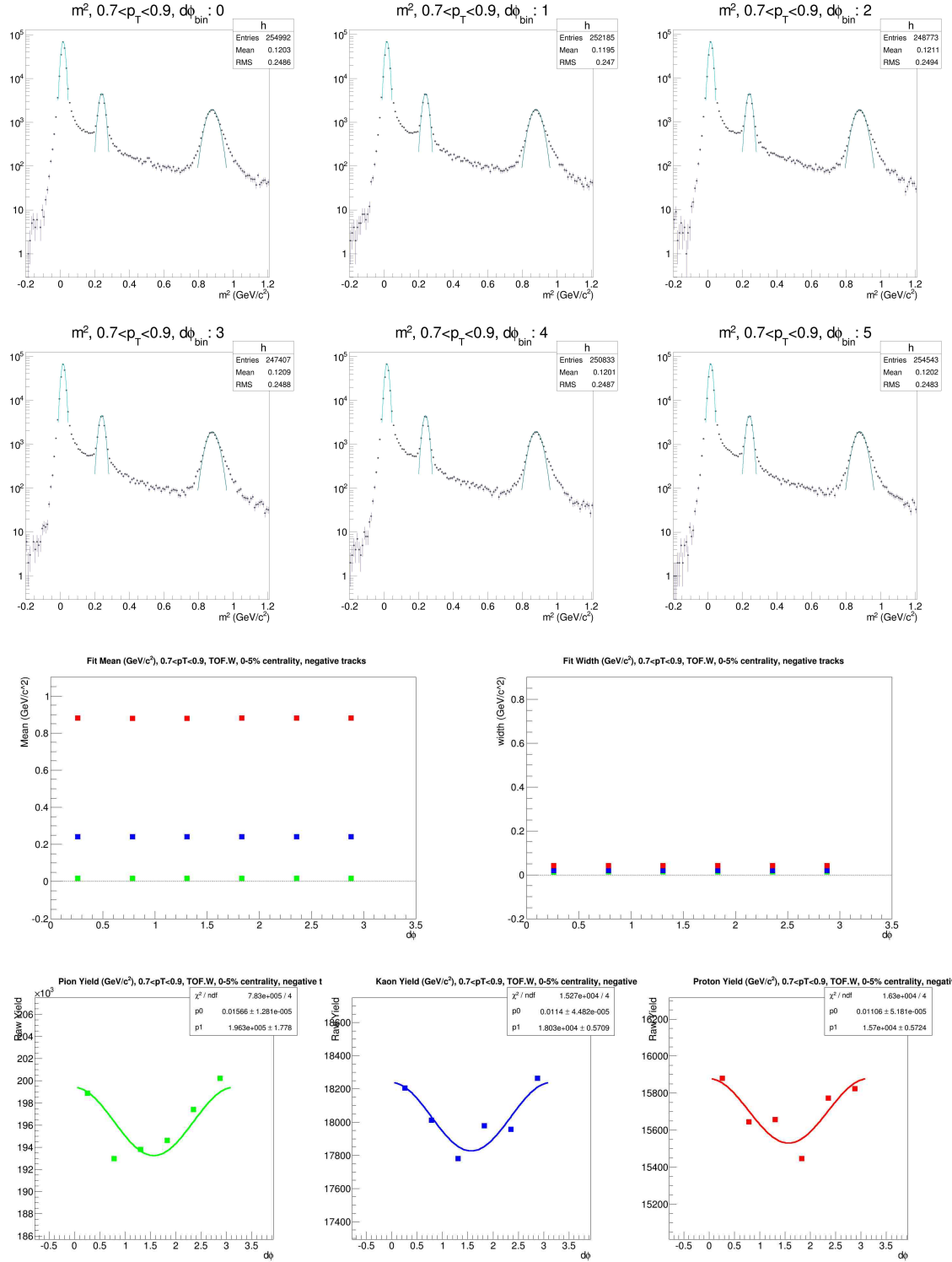


Figure C.2: m^2 Gaussian fits for PID and resulting Yield vs $d\phi$ for $p_T = 0.7$ - $0.9 \text{ GeV}/c$, TOF.W, negative particles

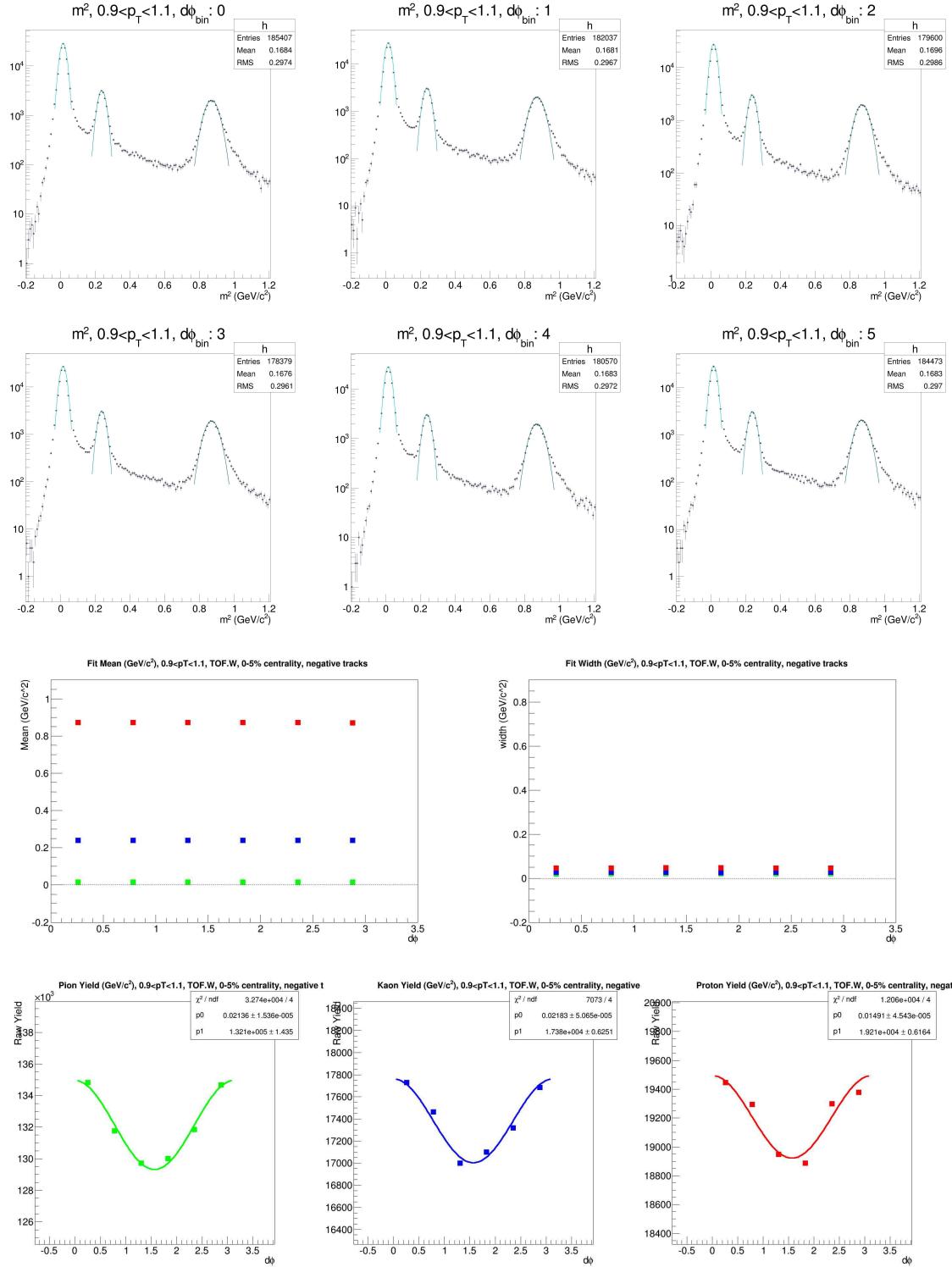


Figure C.3: m^2 Gaussian fits for PID and resulting Yield vs $d\phi$ for $p_T = 0.9$ - 1.1 GeV/c , TOF.W, negative particles

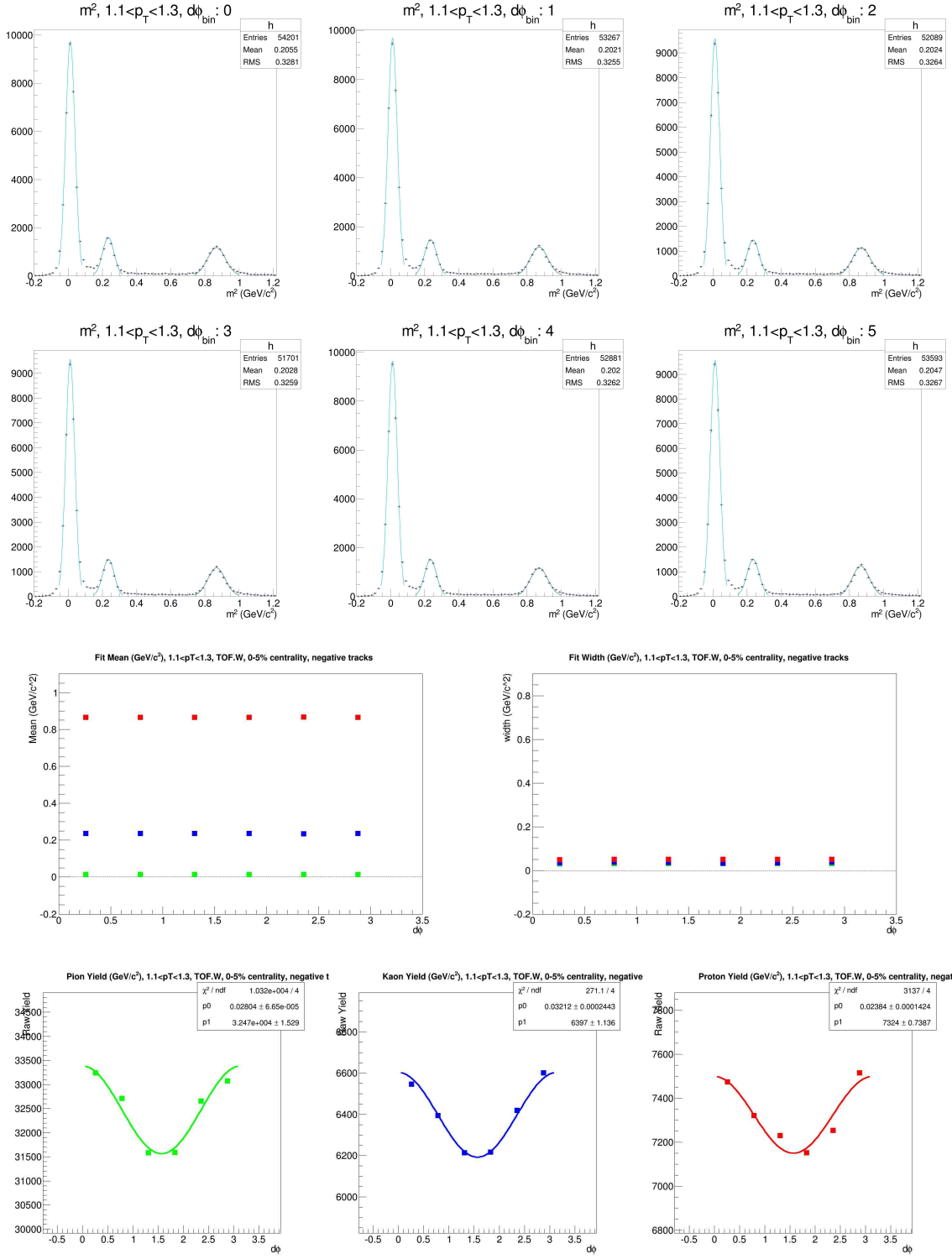


Figure C.4: m^2 Gaussian fits for PID and resulting Yield vs $d\phi$ for $p_T = 1.1 - 1.3 \text{ GeV}/c$, TOF.W, negative particles

C.1.2 Single Gaussian fits, $p_T=0.5\text{-}1.3$ GeV/c, TOF.W, positive charged tracks

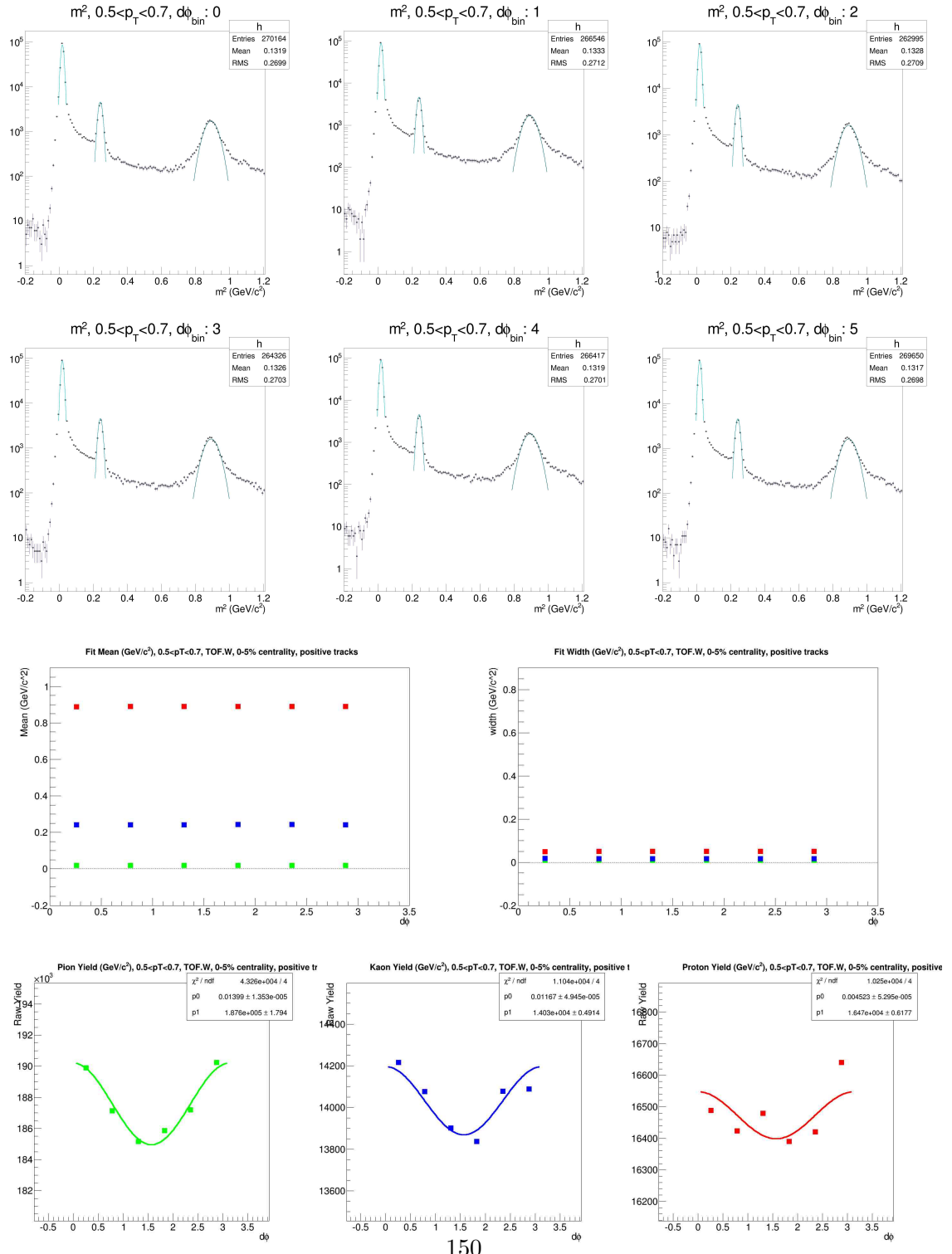


Figure C.5: m^2 Gaussian fits for PID and resulting Yield vs $d\phi$ for $p_T=0.5\text{-}0.7$ GeV/c, TOF.W, positive particles

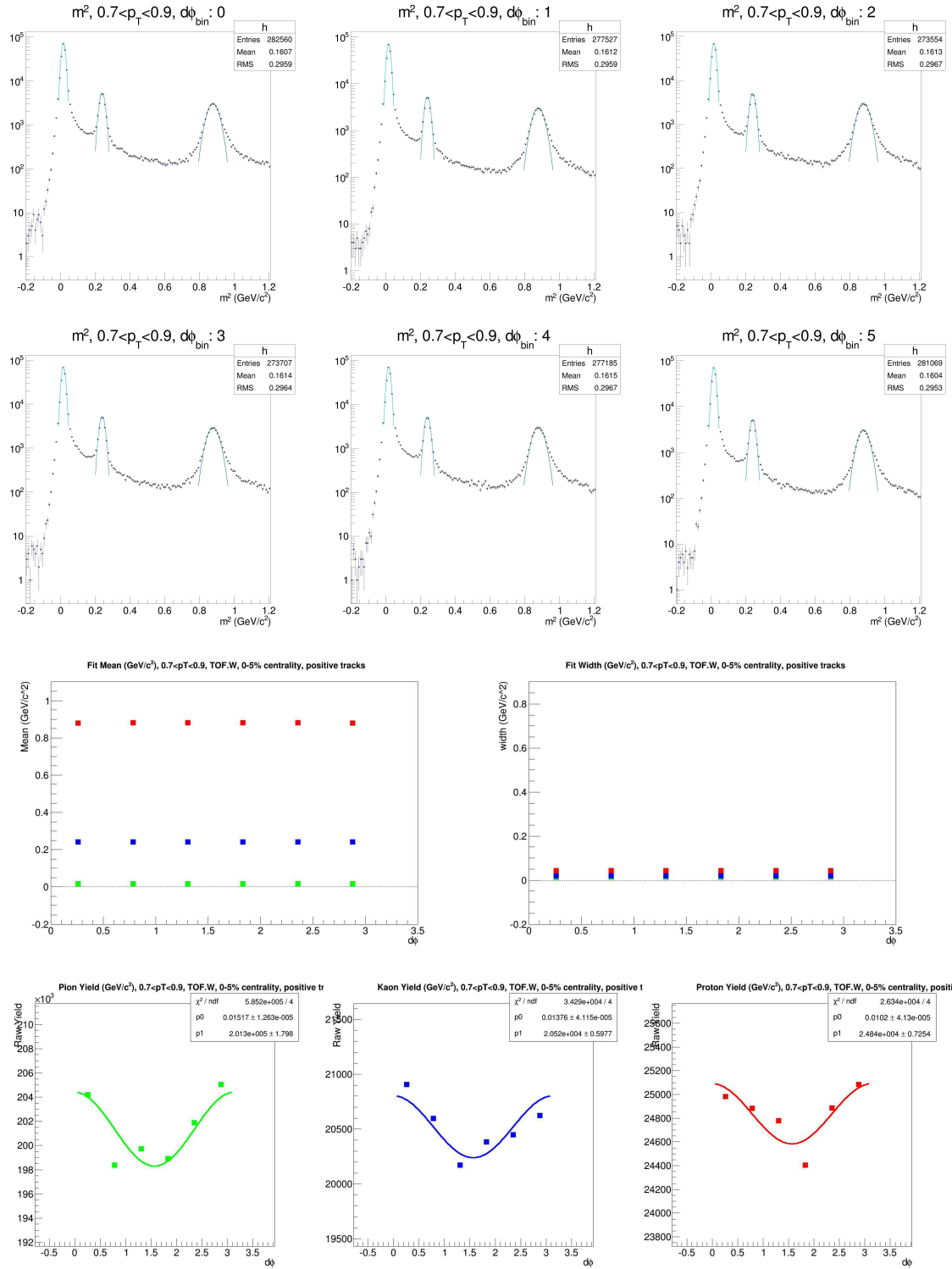


Figure C.6: m^2 Gaussian fits for PID and resulting Yield vs $d\phi$ for $p_T = 0.7$ - 0.9 GeV/c , TOF.W, positive particles

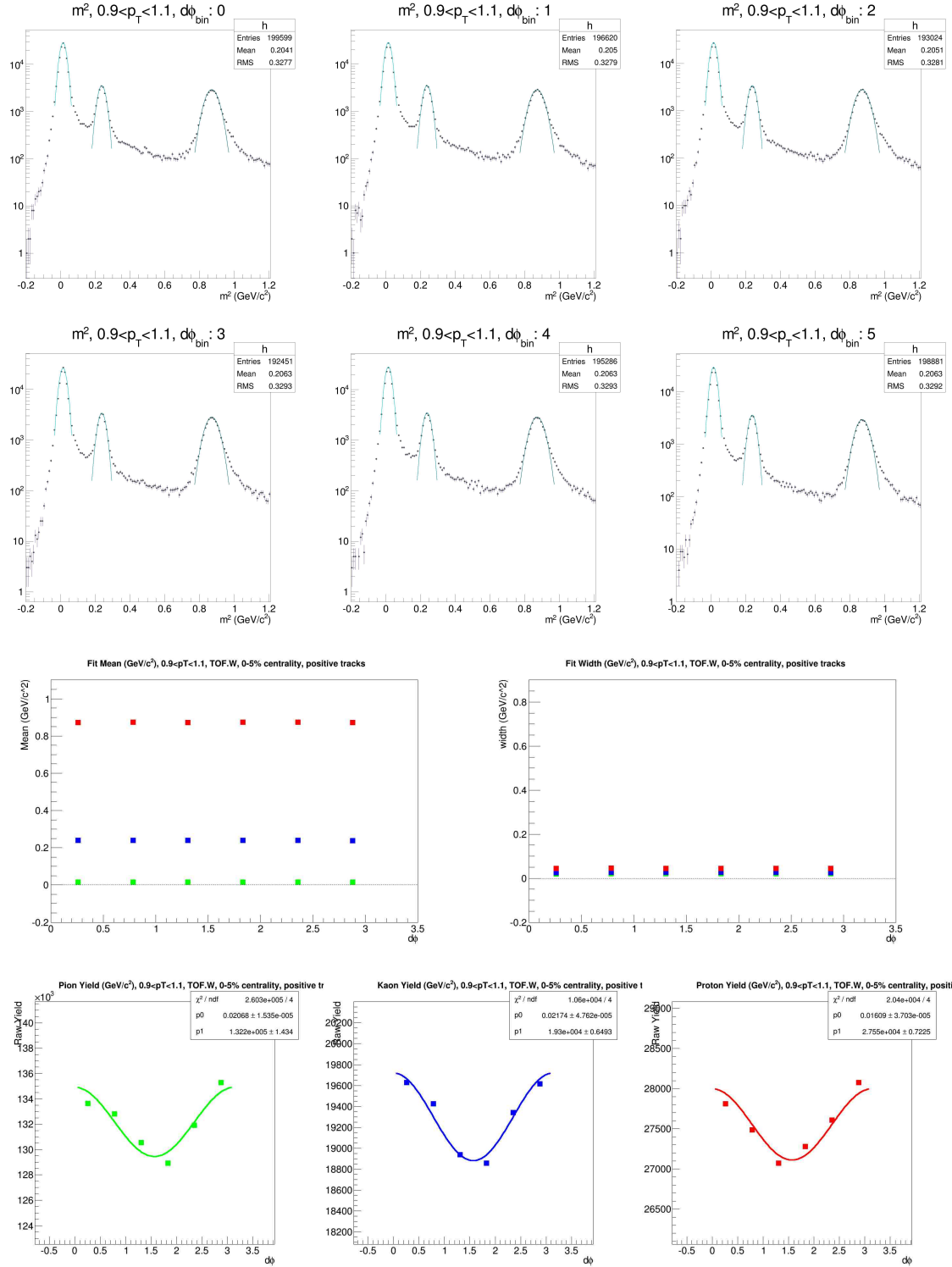


Figure C.7: m^2 Gaussian fits for PID and resulting Yield vs $d\phi$ for $p_T = 0.9-1.1 \text{ GeV}/c$, TOF.W, positive particles

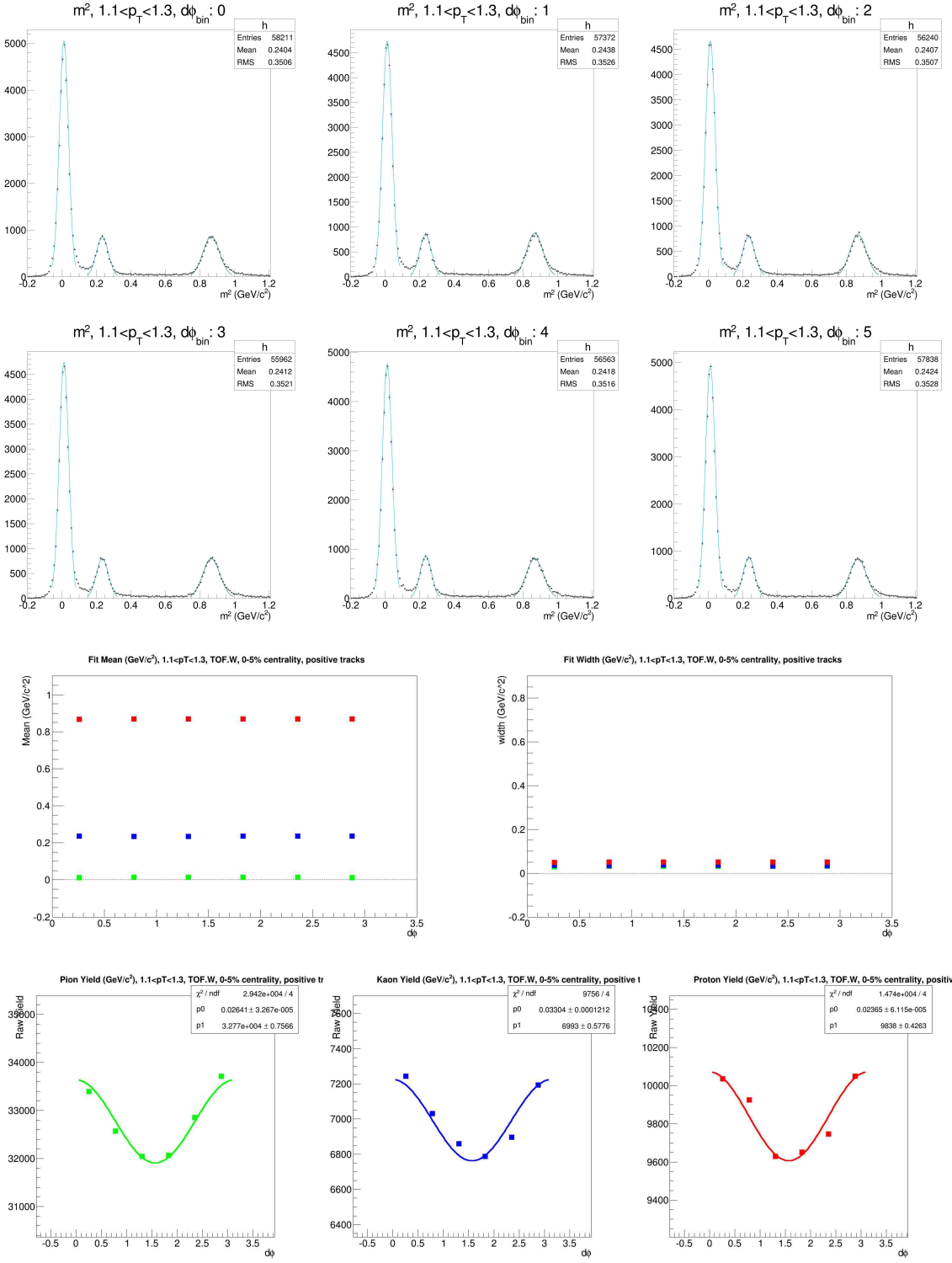


Figure C.8: m^2 Gaussian fits for PID and resulting Yield vs $d\phi$ for $p_T = 1.1 - 1.3 \text{ GeV}/c$, TOF.W, positive particles

C.1.3 Mixed Gaussian fits, $p_T=1.3\text{-}2.1 \text{ GeV}/c$, TOF.W, negative charged tracks

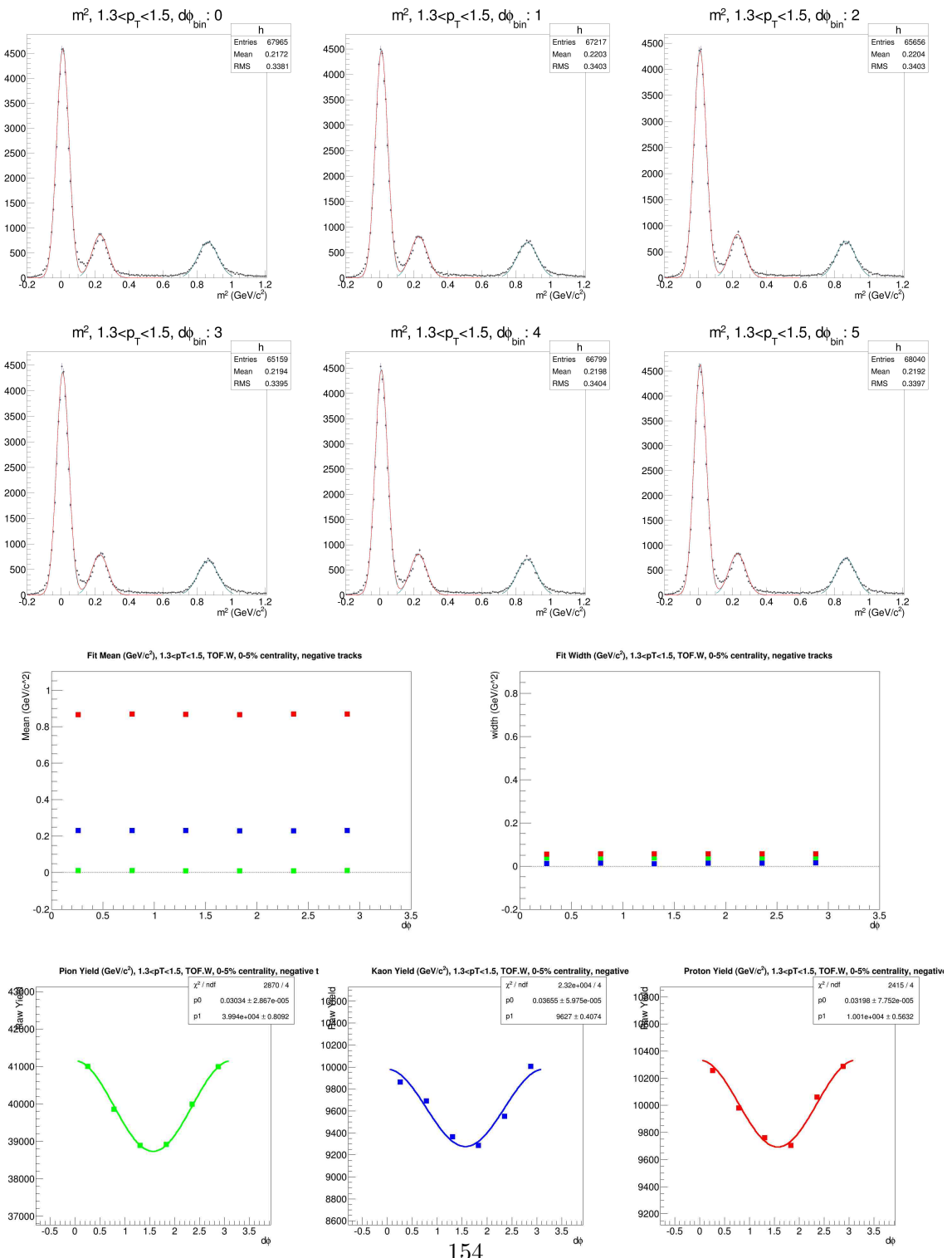


Figure C.9: m^2 Gaussian fits for PID and resulting Yield vs $d\phi$ for $p_T=1.3\text{-}2.1 \text{ GeV}/c$, TOF.W, negative particles

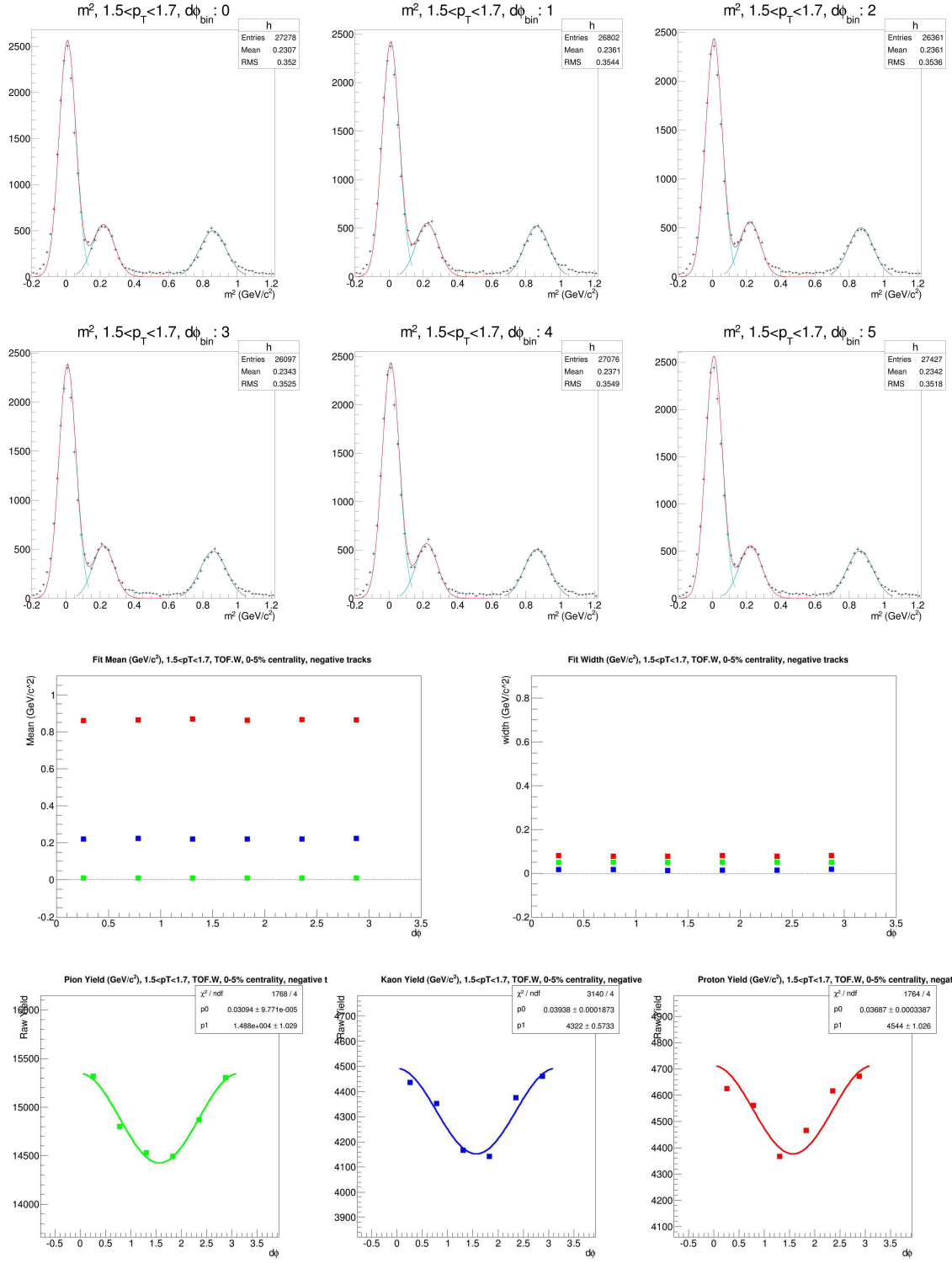


Figure C.10: m^2 Gaussian fits for PID and resulting Yield vs $d\phi$ for $p_T = 1.5-1.7 \text{ GeV}/c$, TOF.W, negative particles

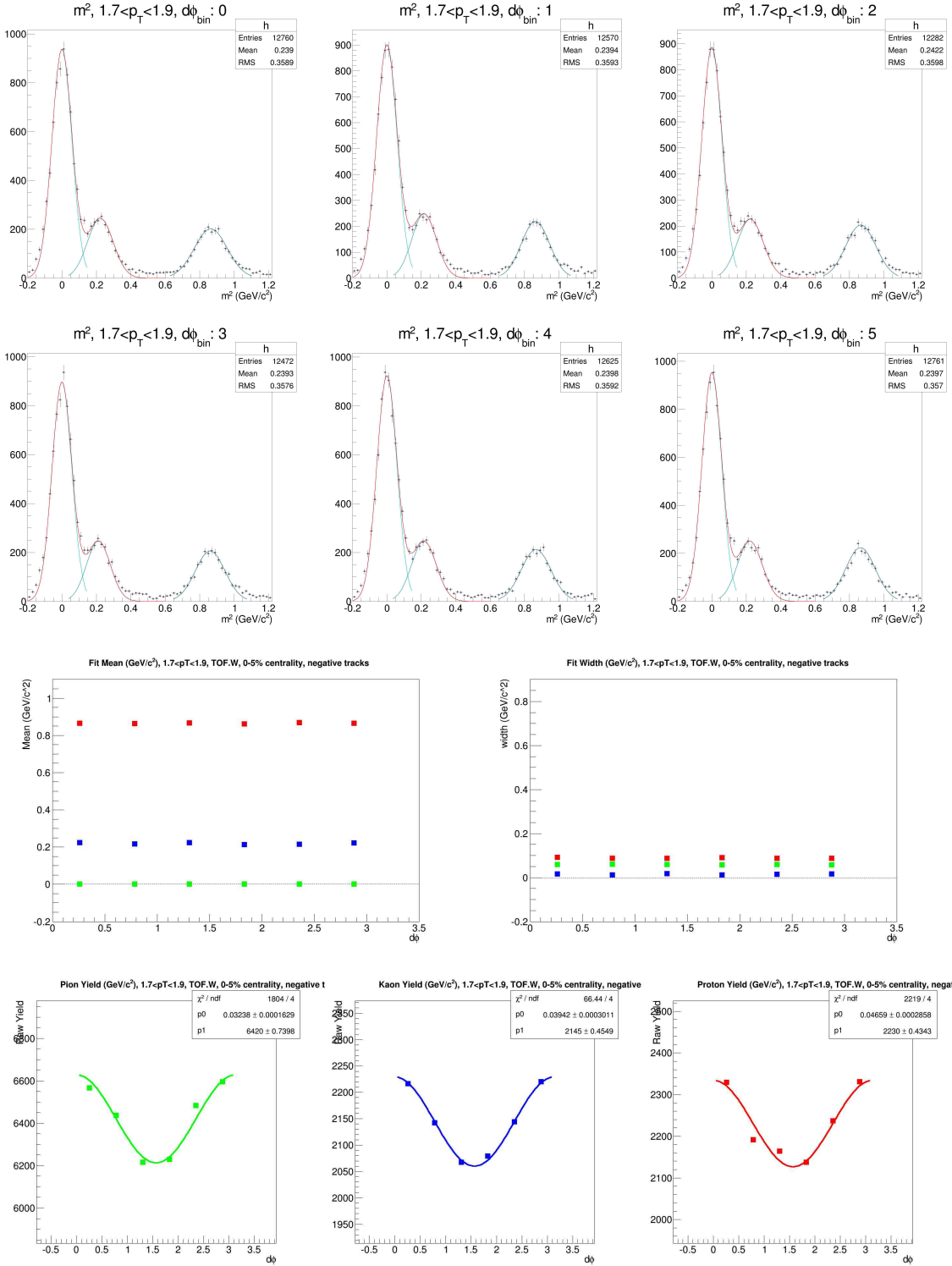


Figure C.11: m^2 Gaussian fits for PID and resulting Yield vs $d\phi$ for $p_T = 1.7$ - 1.9 GeV/c , TOF.W, negative particles

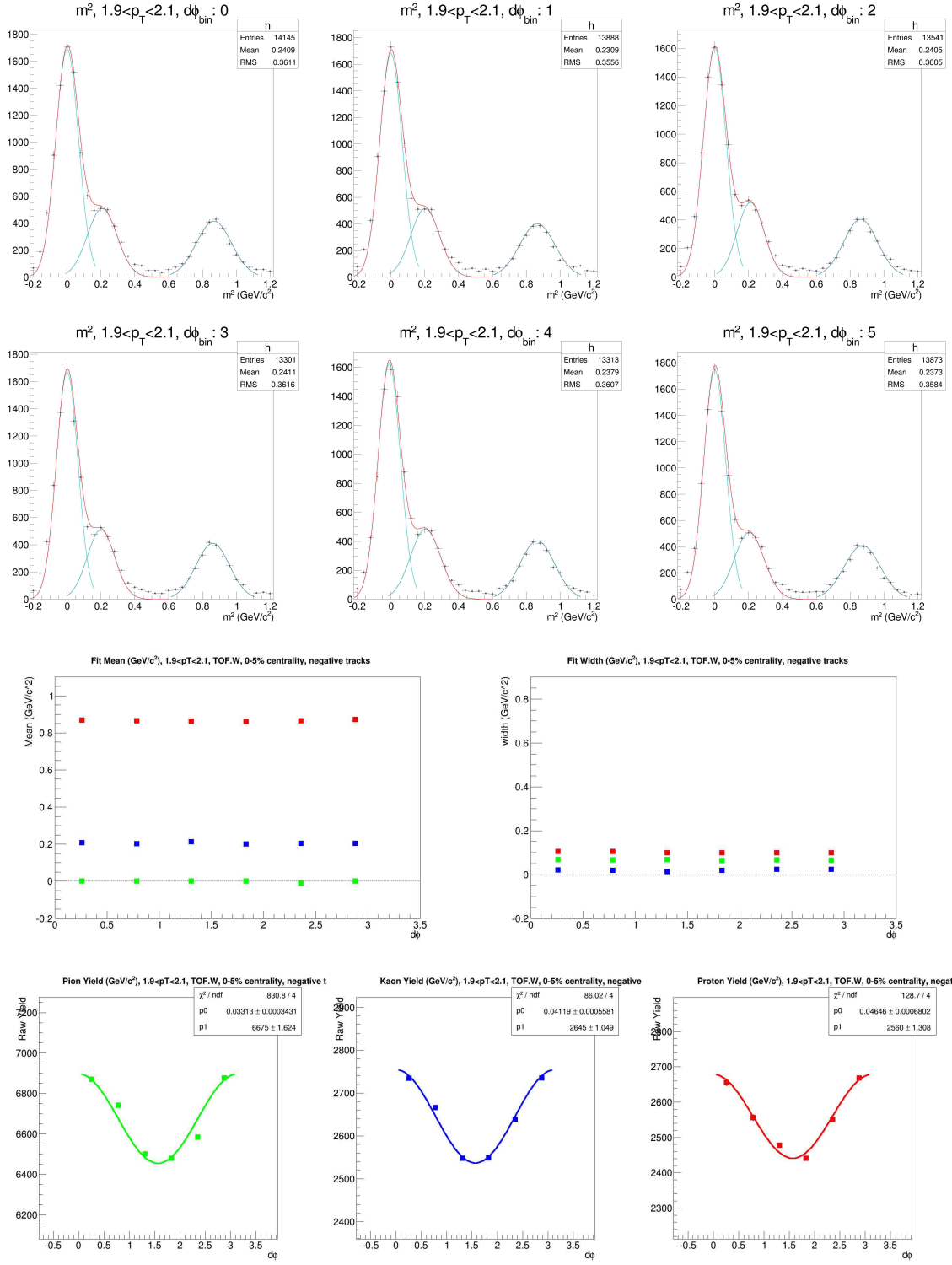


Figure C.12: m^2 Gaussian fits for PID and resulting Yield vs $d\phi$ for $p_T = 1.9-2.1 \text{ GeV}/c$, TOF.W, negative particles

Mixed Gaussian fits, $p_T=1.3\text{-}2.1$ GeV/c, TOF.W, positive charged tracks

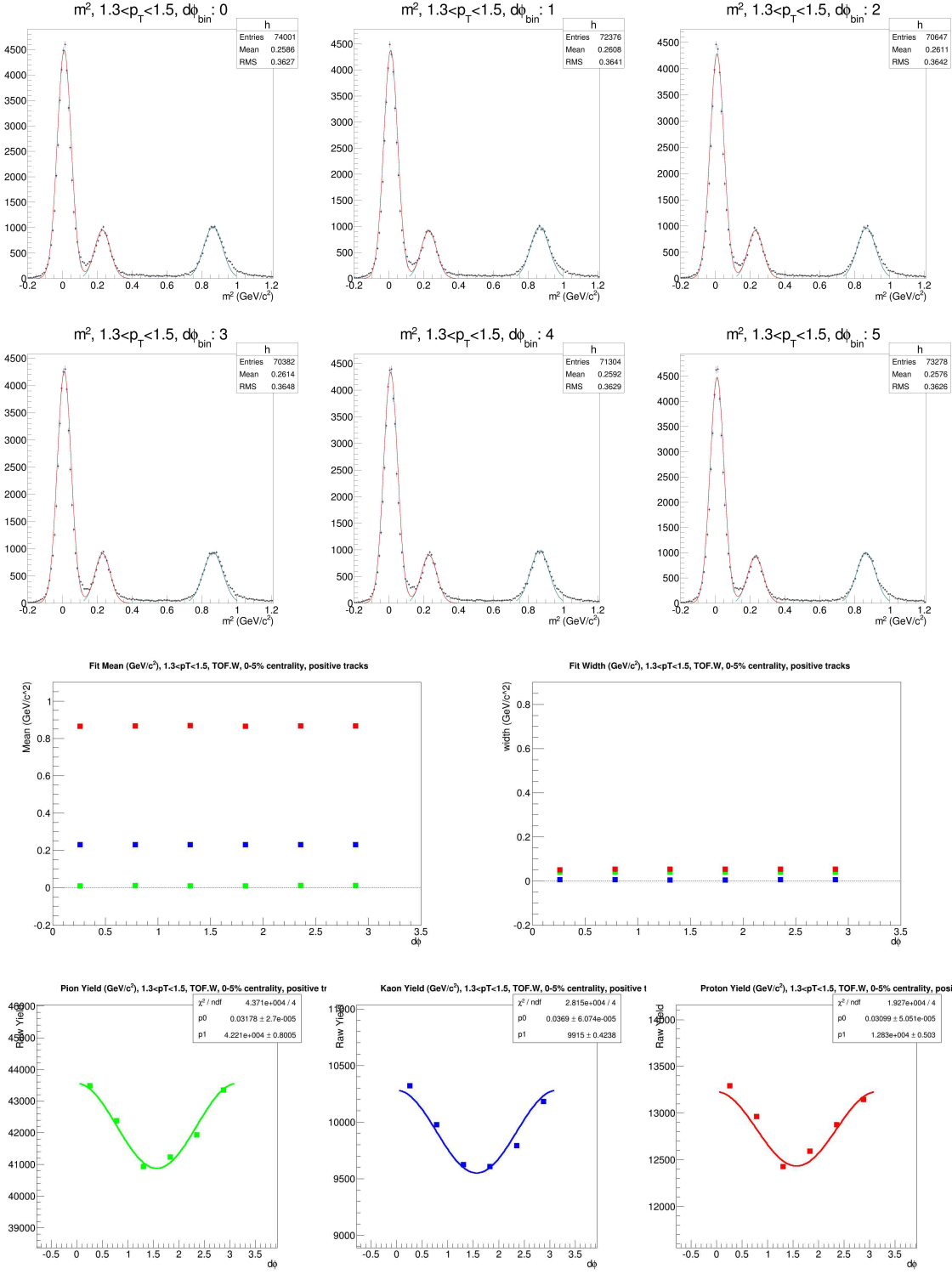


Figure C.13: m^2 Gaussian fits for PID and resulting Yield vs $d\phi$ for $p_T=1.3\text{-}1.5$ GeV/c, TOF.W, positive particles

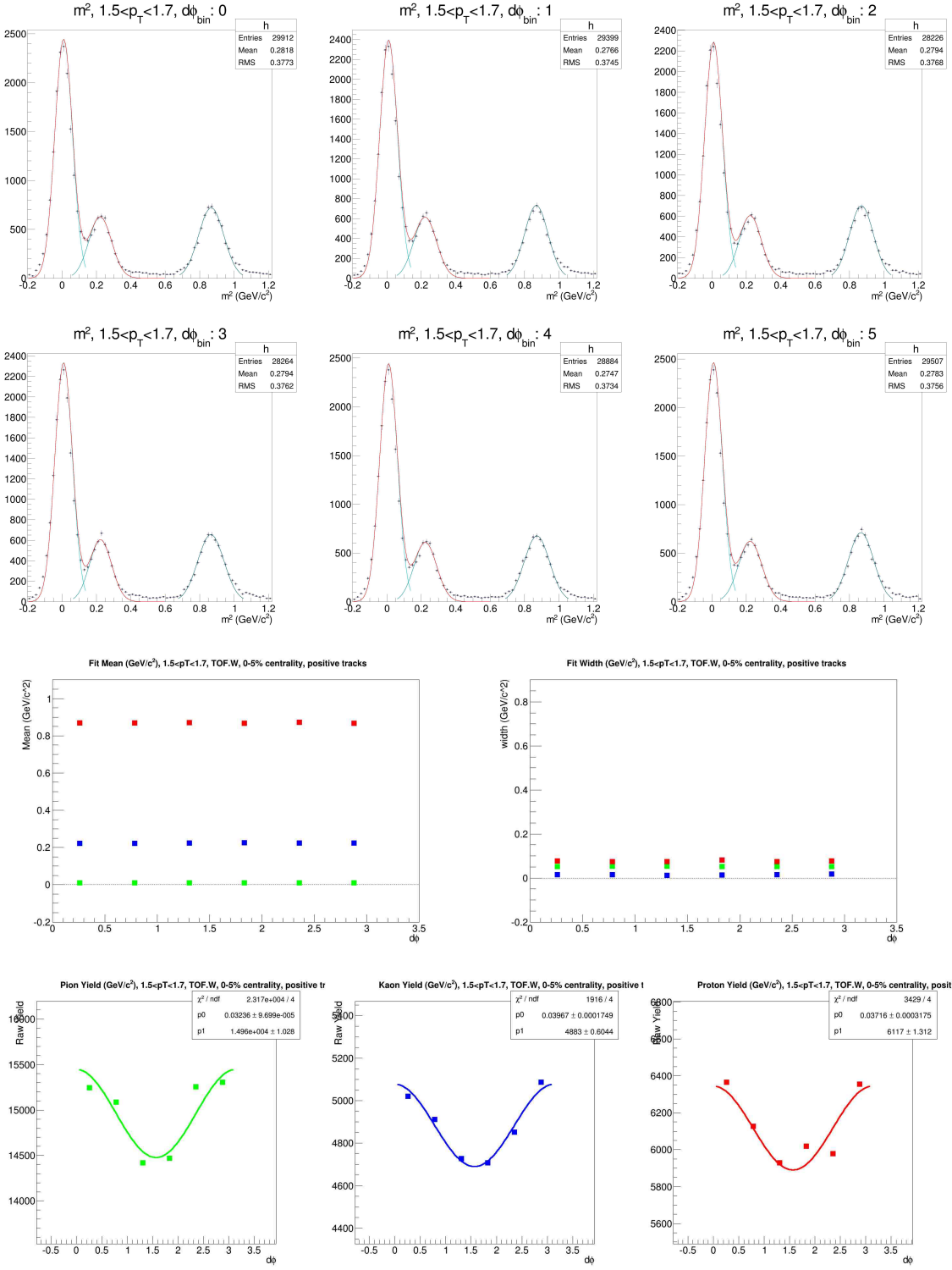


Figure C.14: m^2 Gaussian fits for PID and resulting Yield vs $d\phi$ for $p_T = 1.5-1.7 \text{ GeV}/c$, TOF.W, positive particles

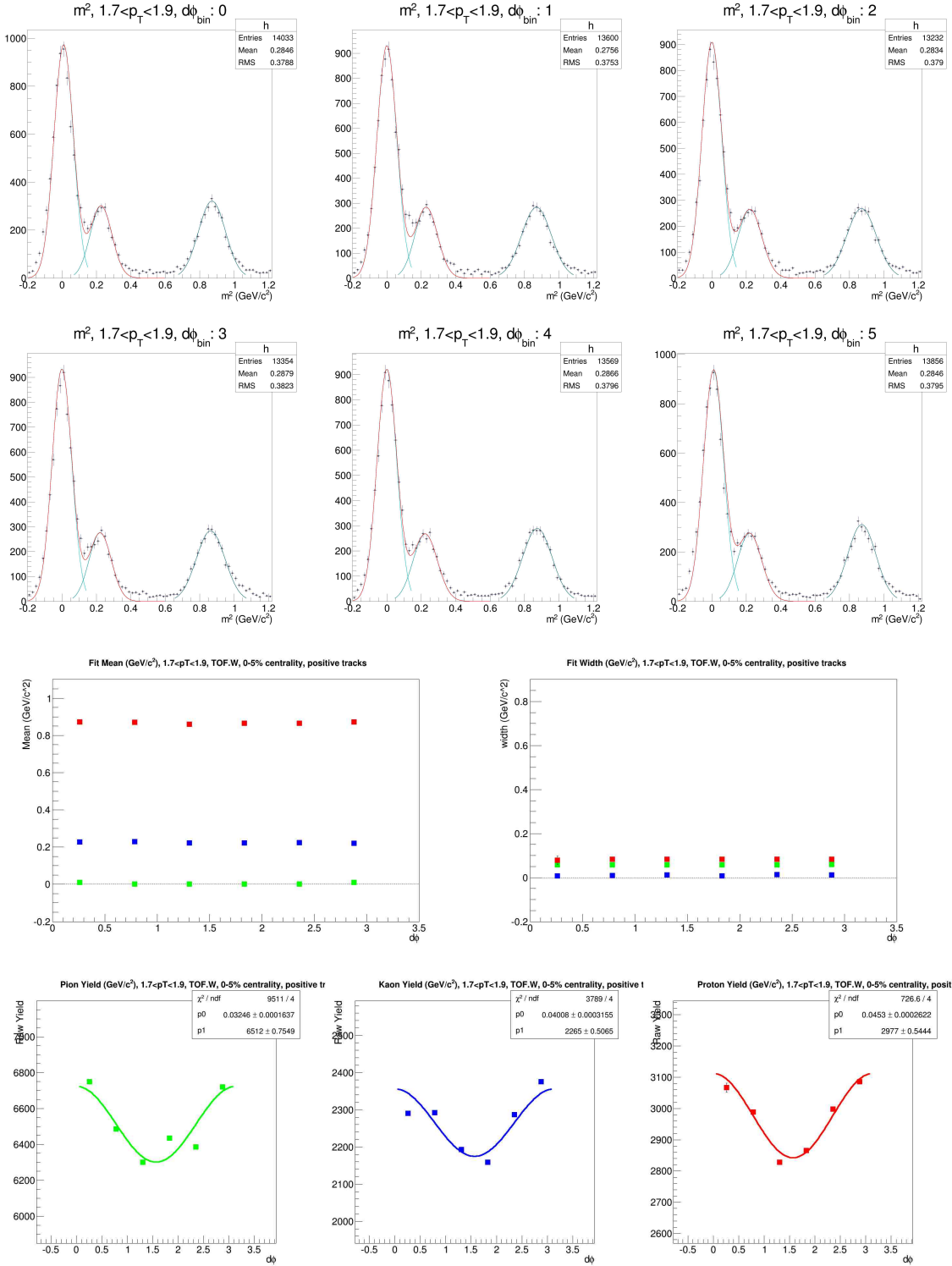


Figure C.15: m^2 Gaussian fits for PID and resulting Yield vs $d\phi$ for $p_T = 1.7$ - 1.9 GeV/c , TOF.W, positive particles

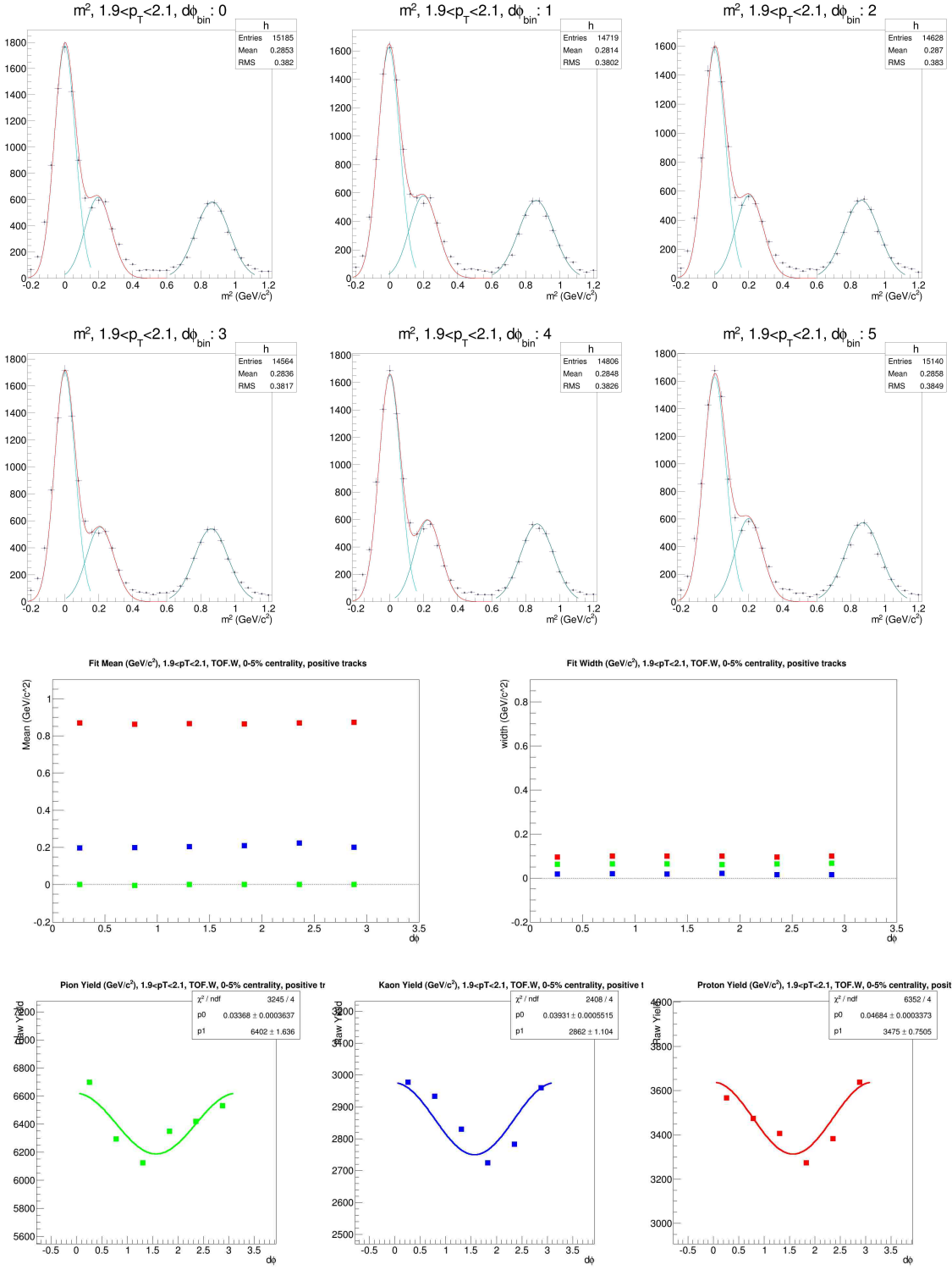
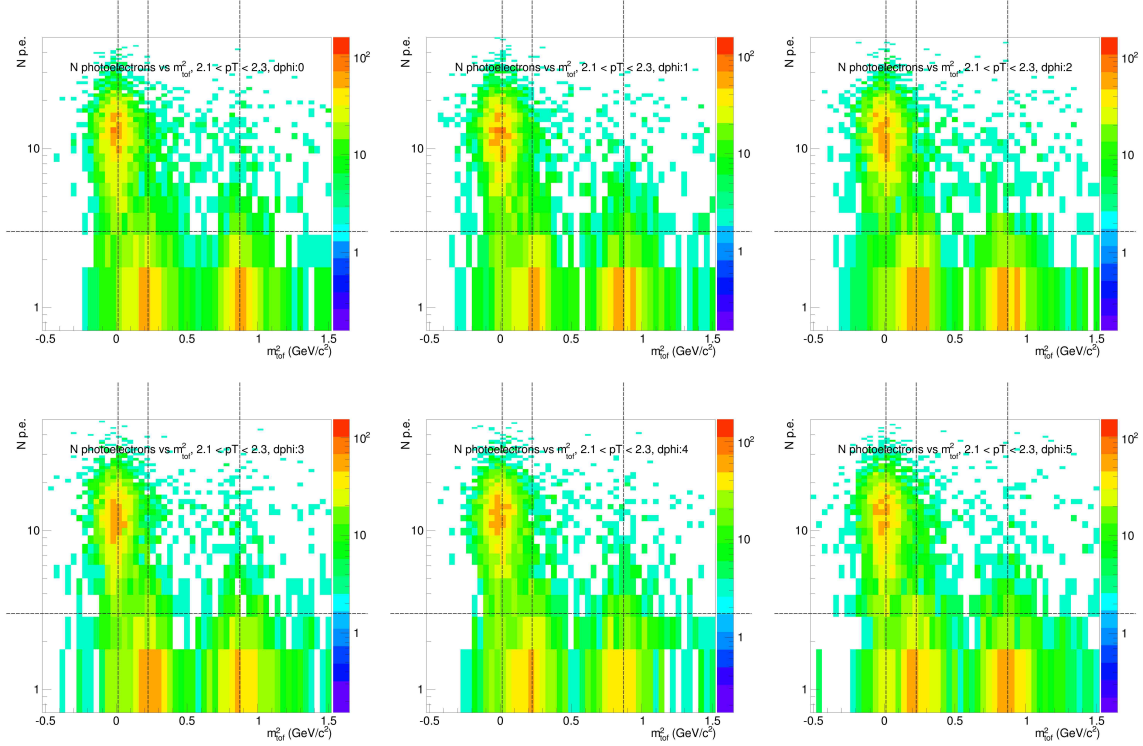
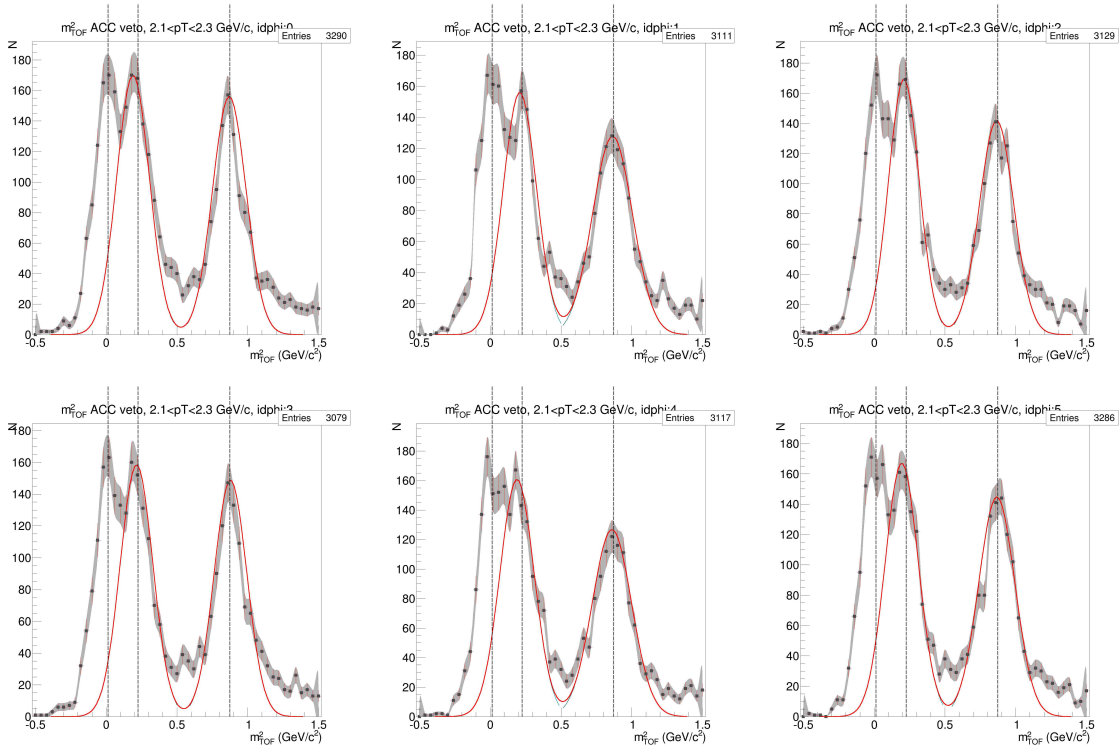


Figure C.16: m^2 Gaussian fits for PID and resulting Yield vs $d\phi$ for $p_T = 1.9-2.1 \text{ GeV}/c$, TOF.W, positive particles

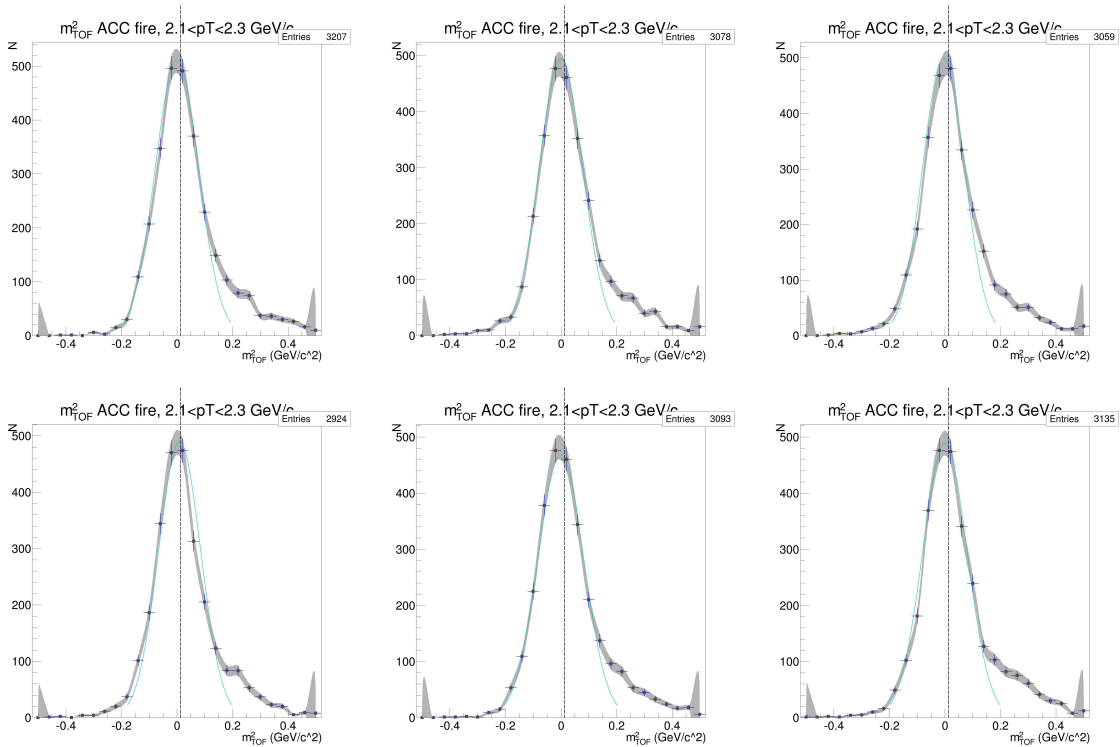
C.1.4 TOF.W and ACC, $p_T=2.1\text{-}3.5$ GeV, negative charged tracks



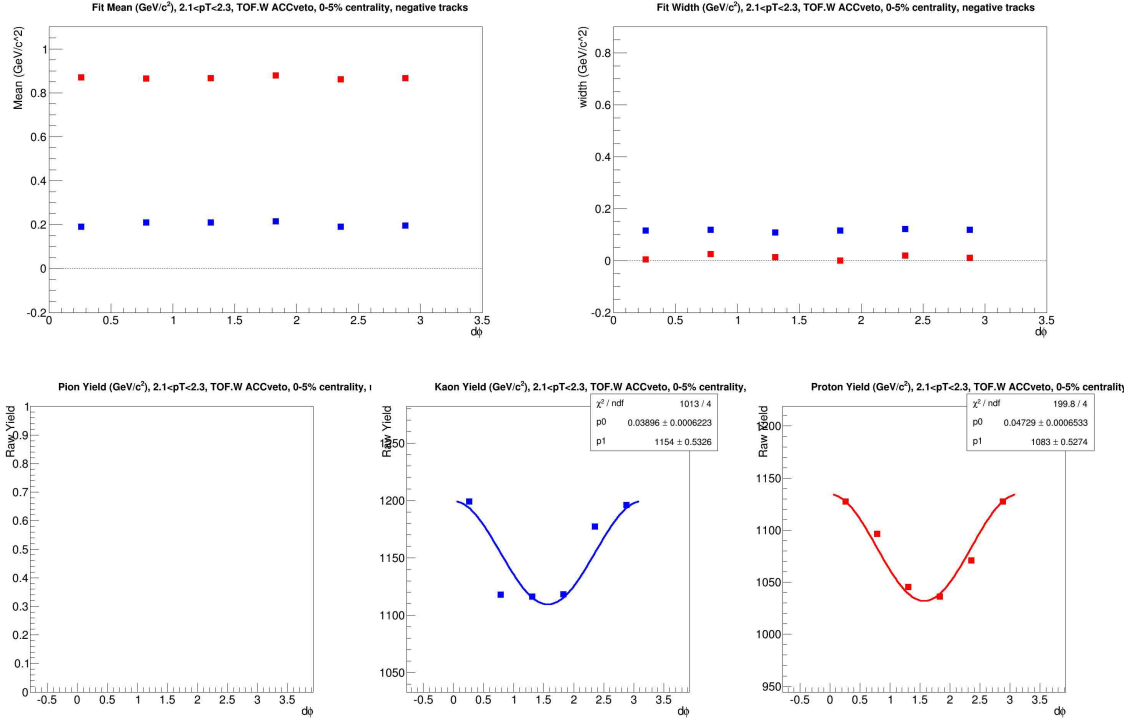
(a) $N_{p.e.}$ vs m^2



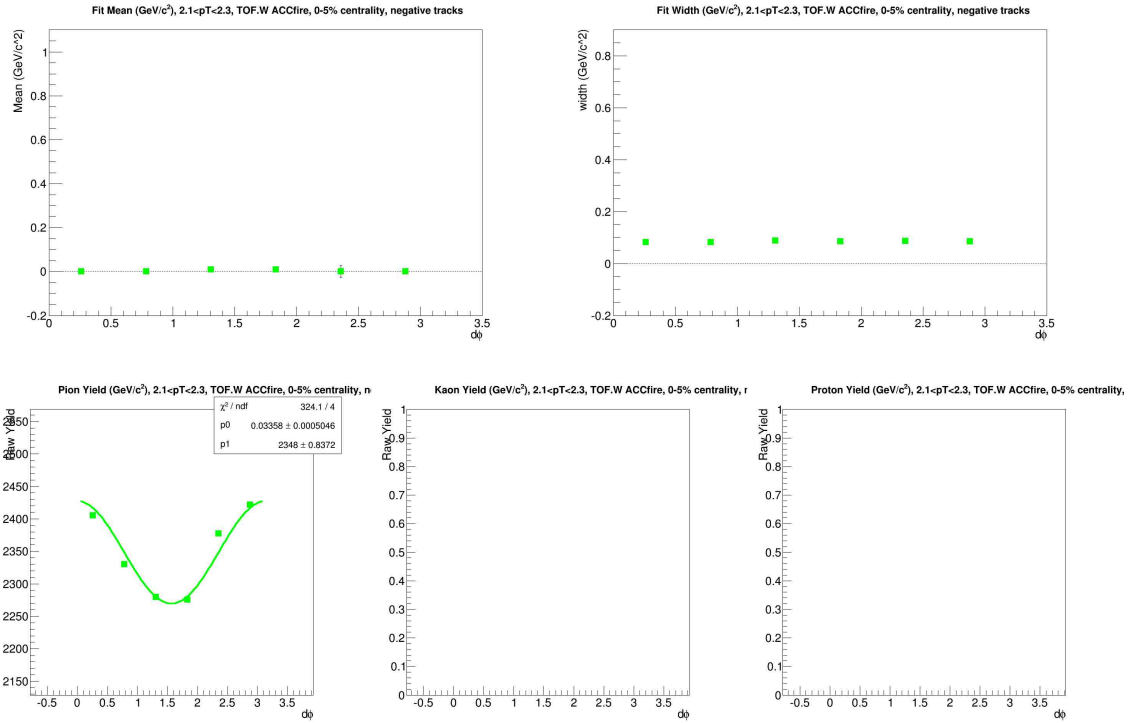
(b) m^2 for ACC vetoed tracks



(c) m^2 for ACC fired tracks

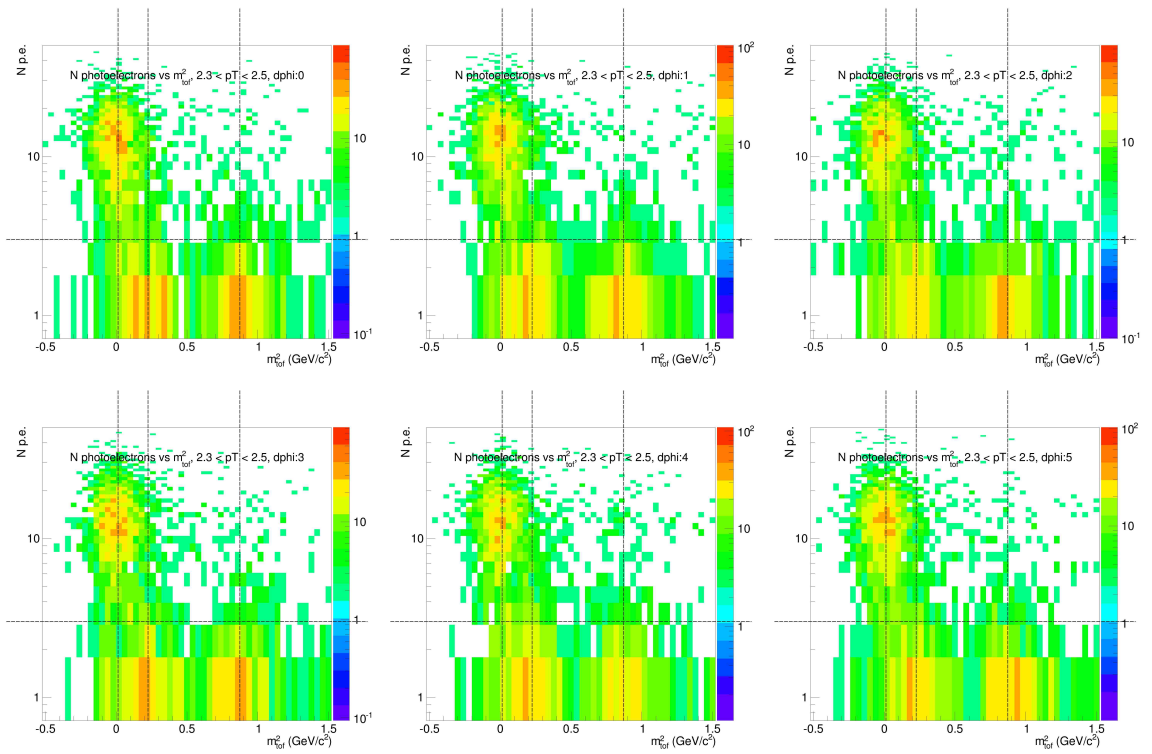


(d) PID parameters and Yields for ACC vetoed tracks

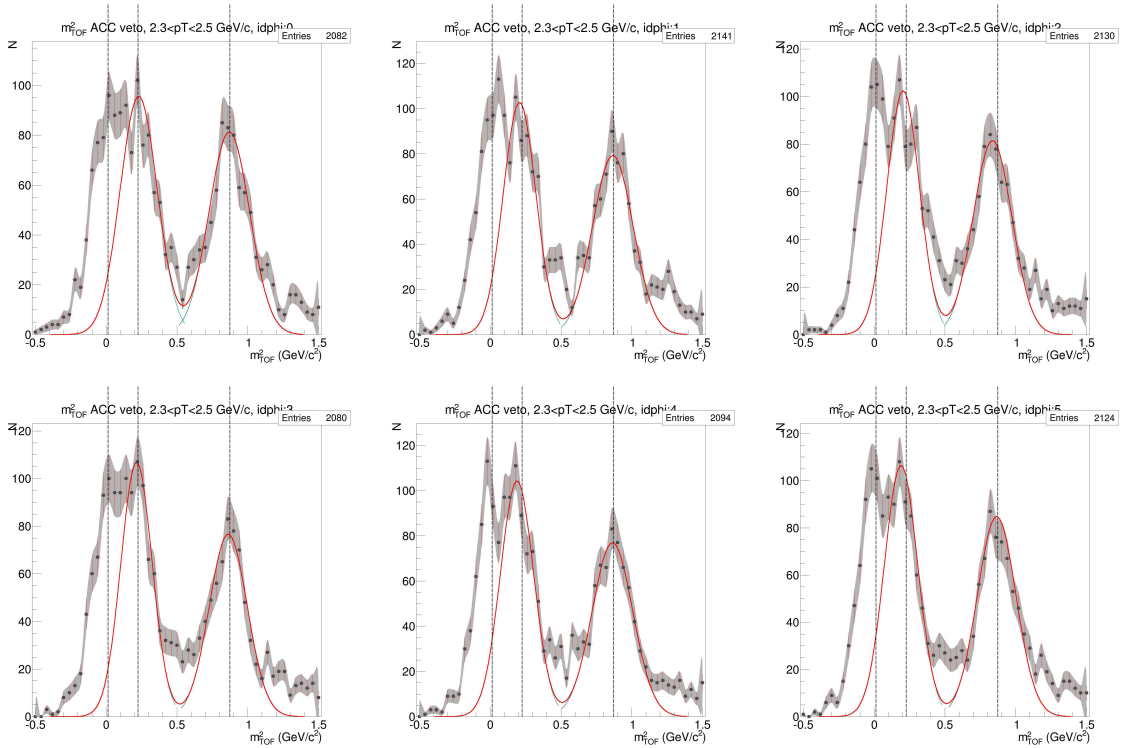


(e) PID parameters and Yields for ACC fired tracks

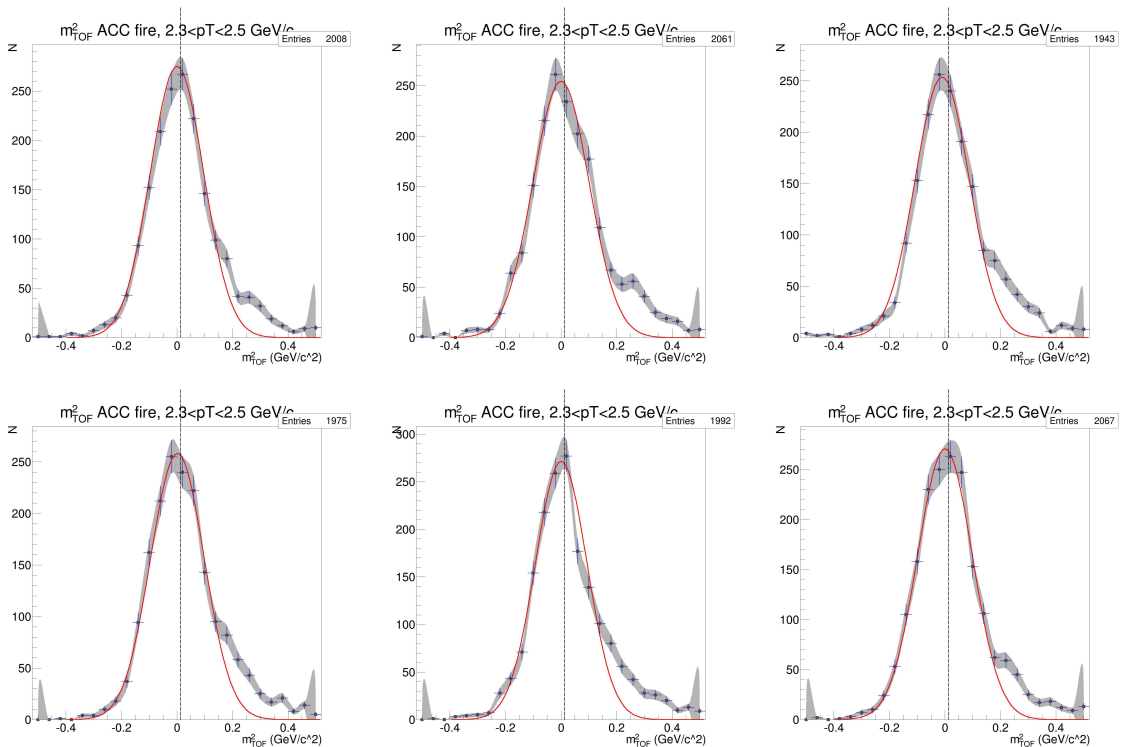
Figure C.17: ACC $N_{p.e.}$ vs m_2 , $P\overline{D}^4$ fits, and Yield vs $d\phi$ for $p_T=2.1-2.3$ GeV/c , TOF.W, negative particles



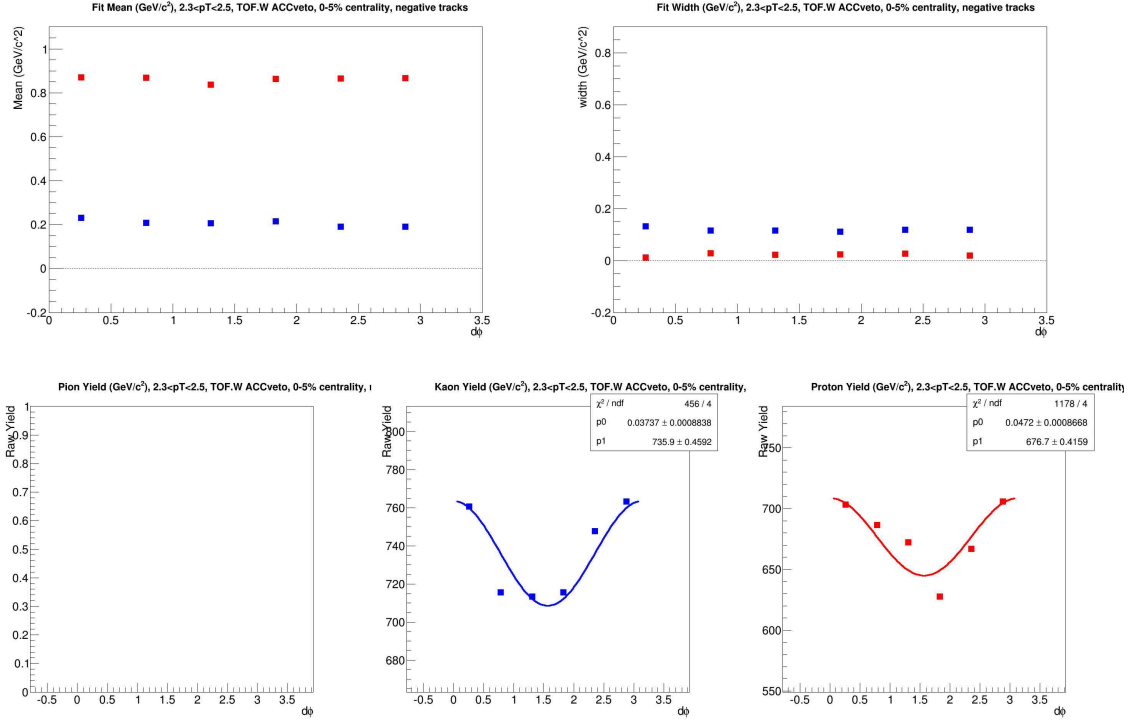
(a) $N_{p.e.}$ vs m^2



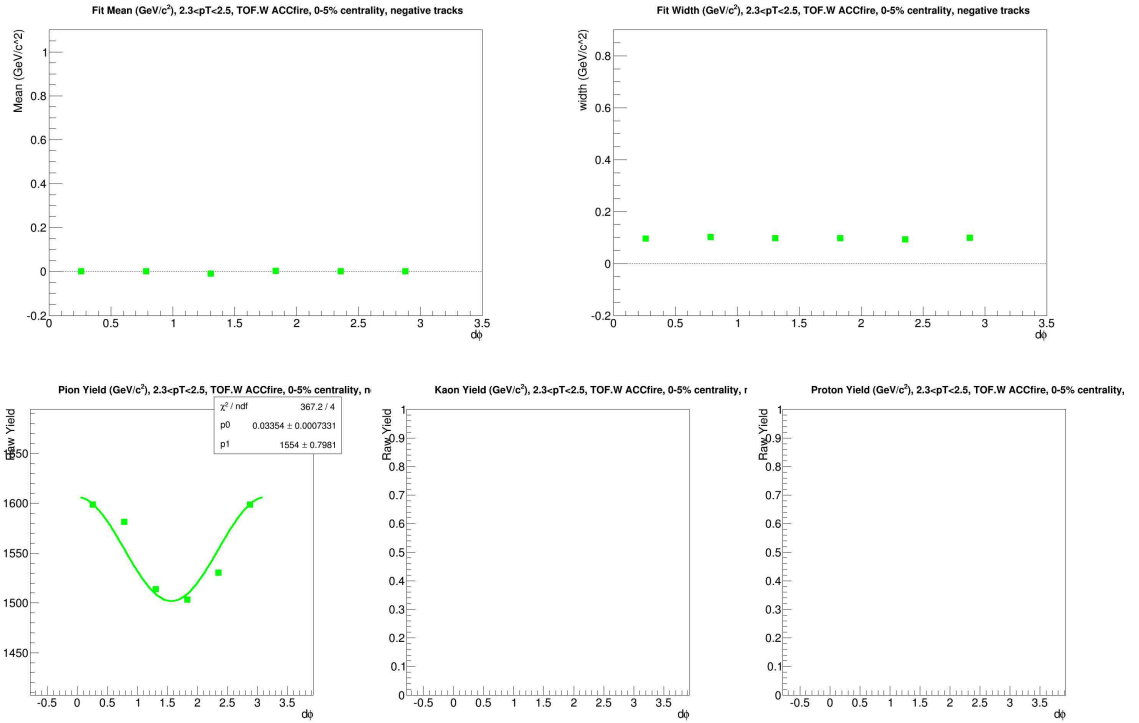
(b) m^2 for ACC vetoed tracks



(c) m^2 for ACC fired tracks

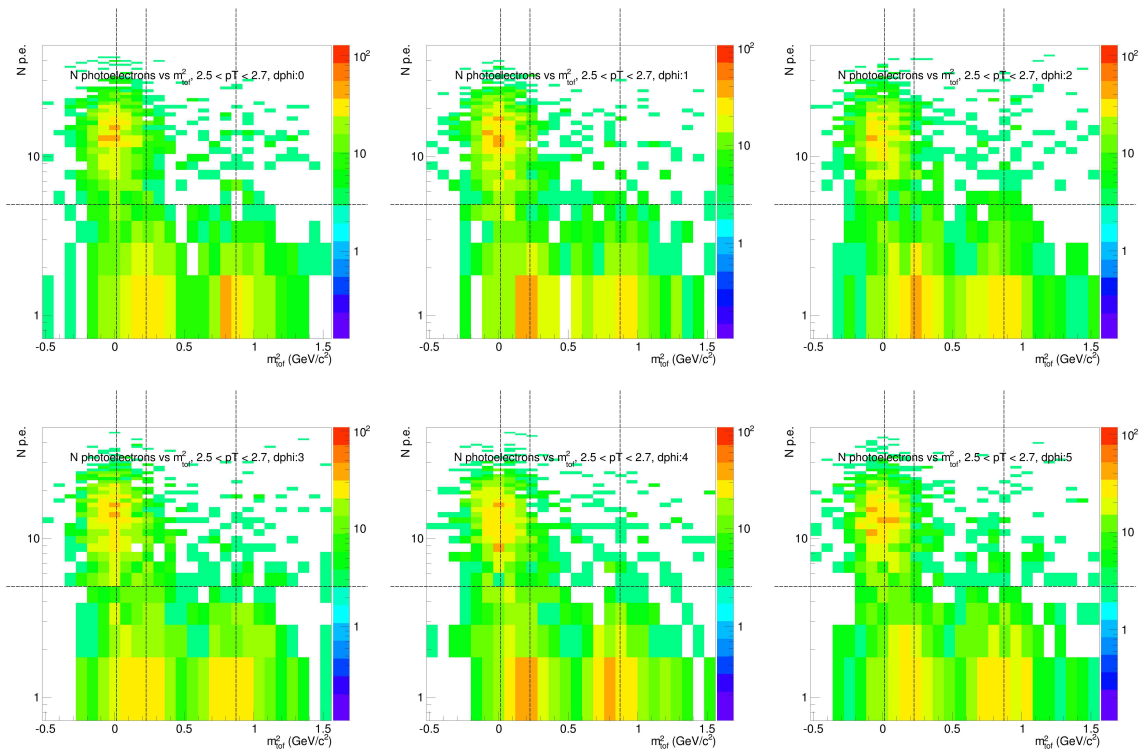


(d) PID parameters and Yields for ACC vetoed tracks

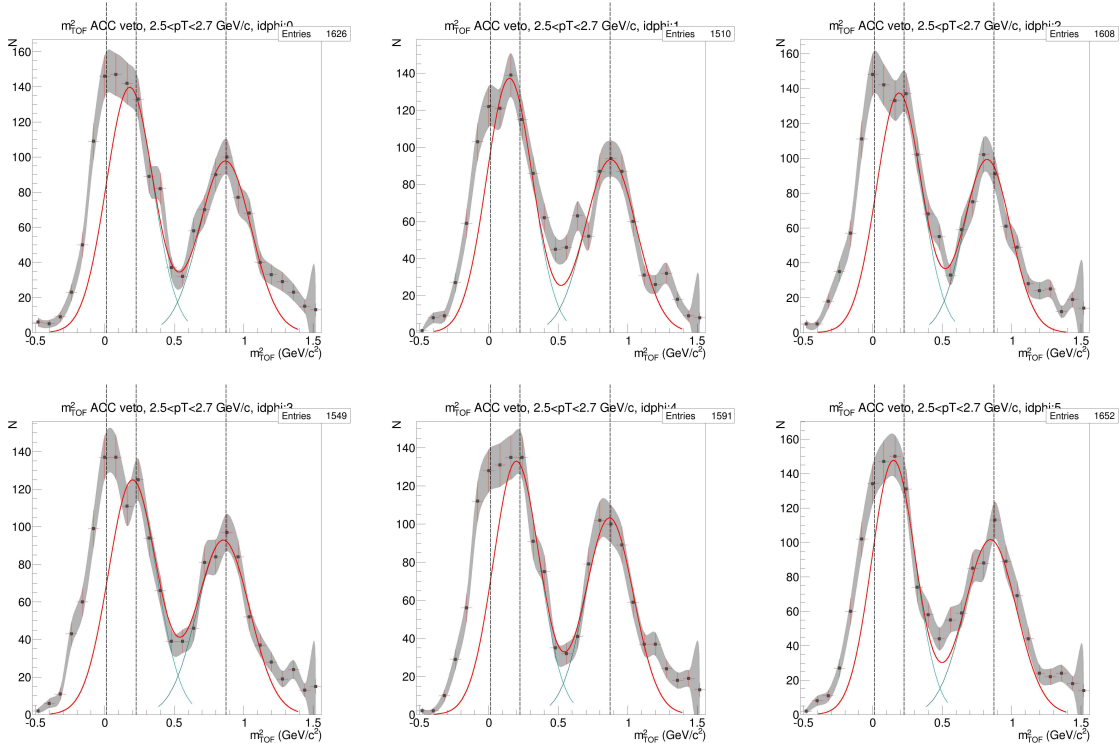


(e) PID parameters and Yields for ACC fired tracks

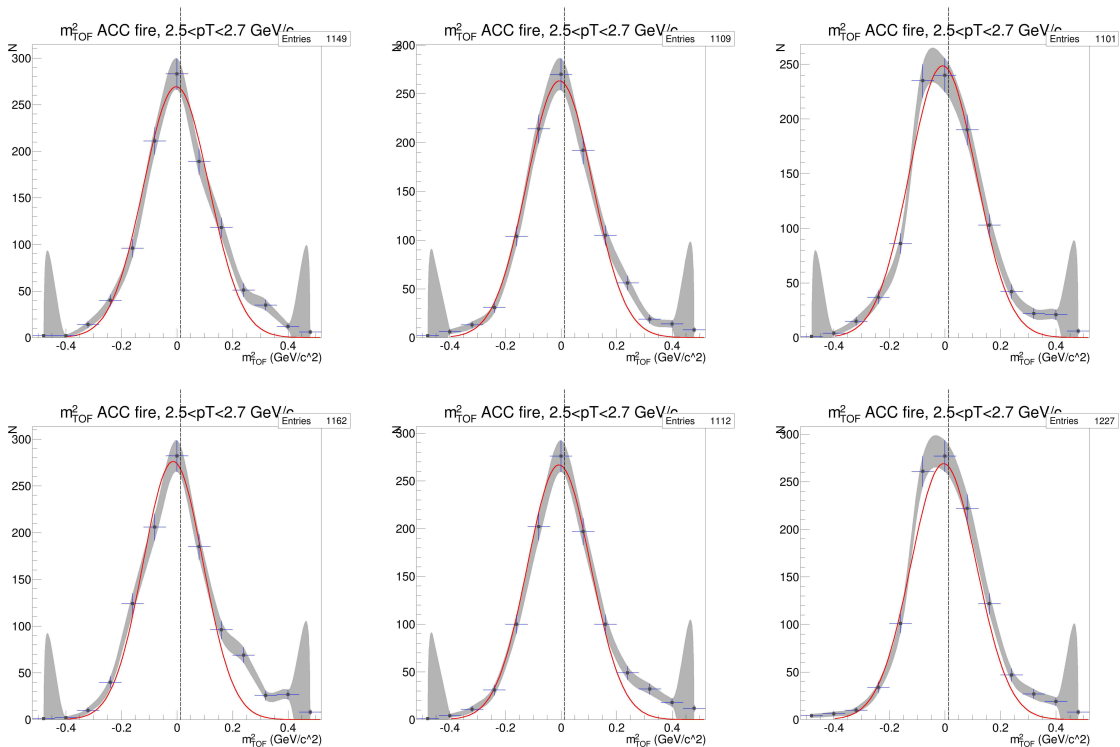
Figure C.18: ACC $N_{p.e.}$ vs m_2 , PID fits, and Yield vs $d\phi$ for $p_T=2.3-2.5 \text{ GeV}/c$, TOF.W, negative particles



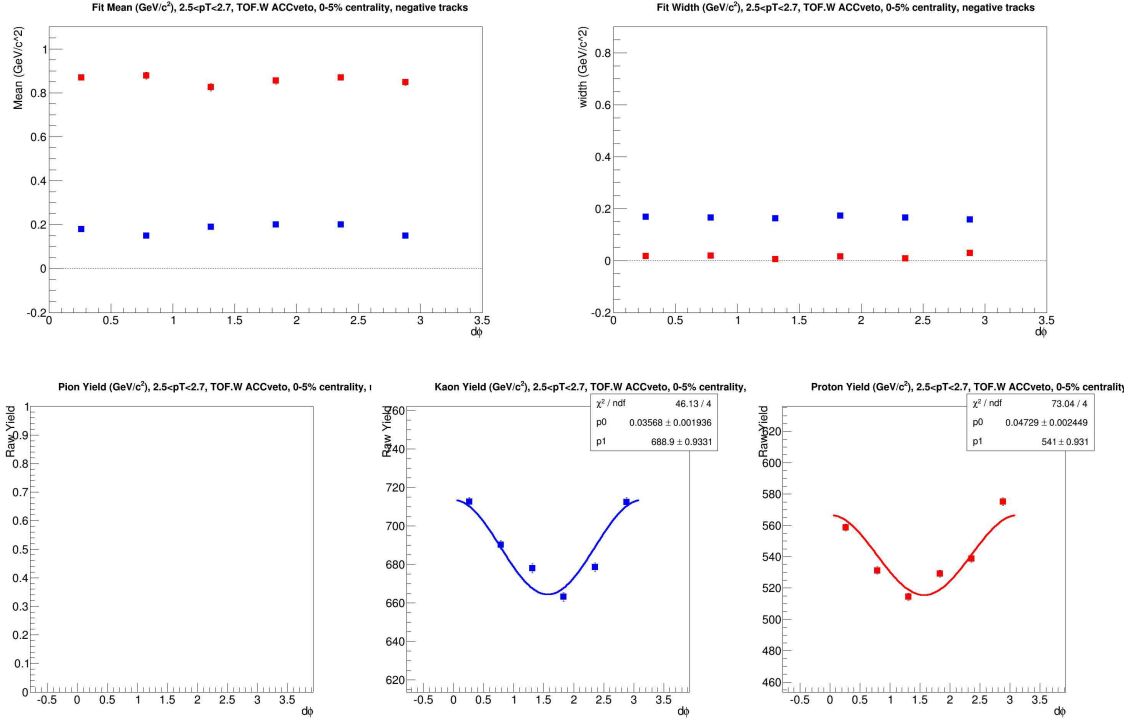
(a) $N_{\text{p.e.}}$ vs m^2



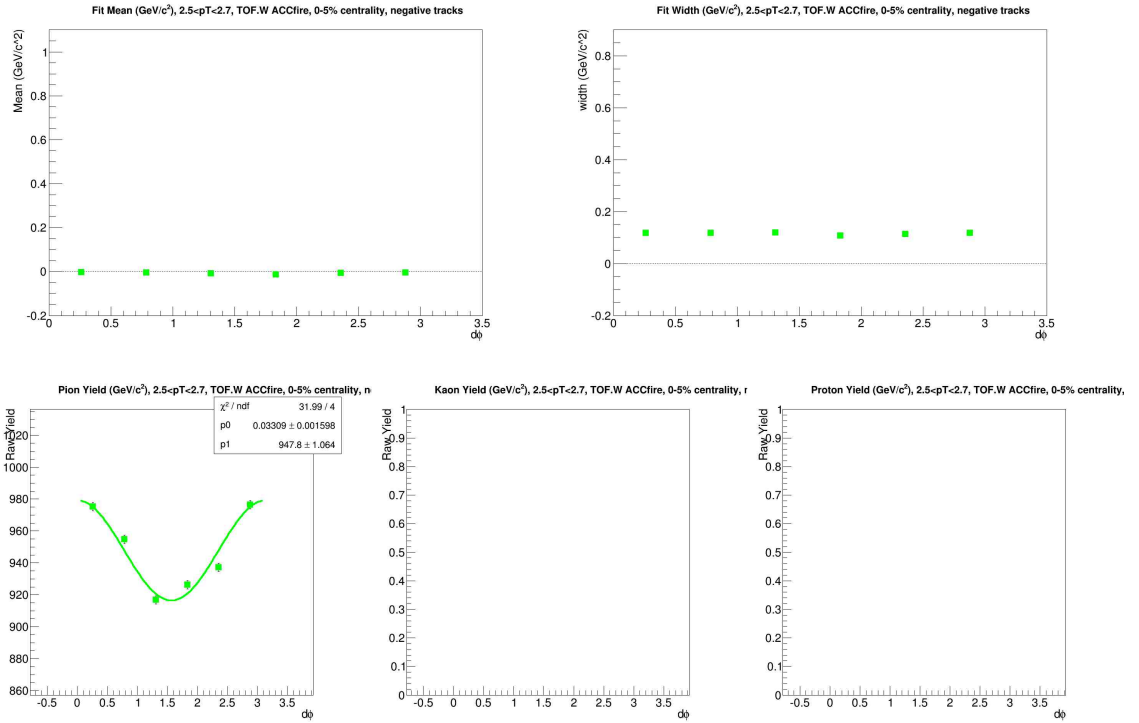
(b) m^2 for ACC vetoed tracks



(c) m^2 for ACC fired tracks

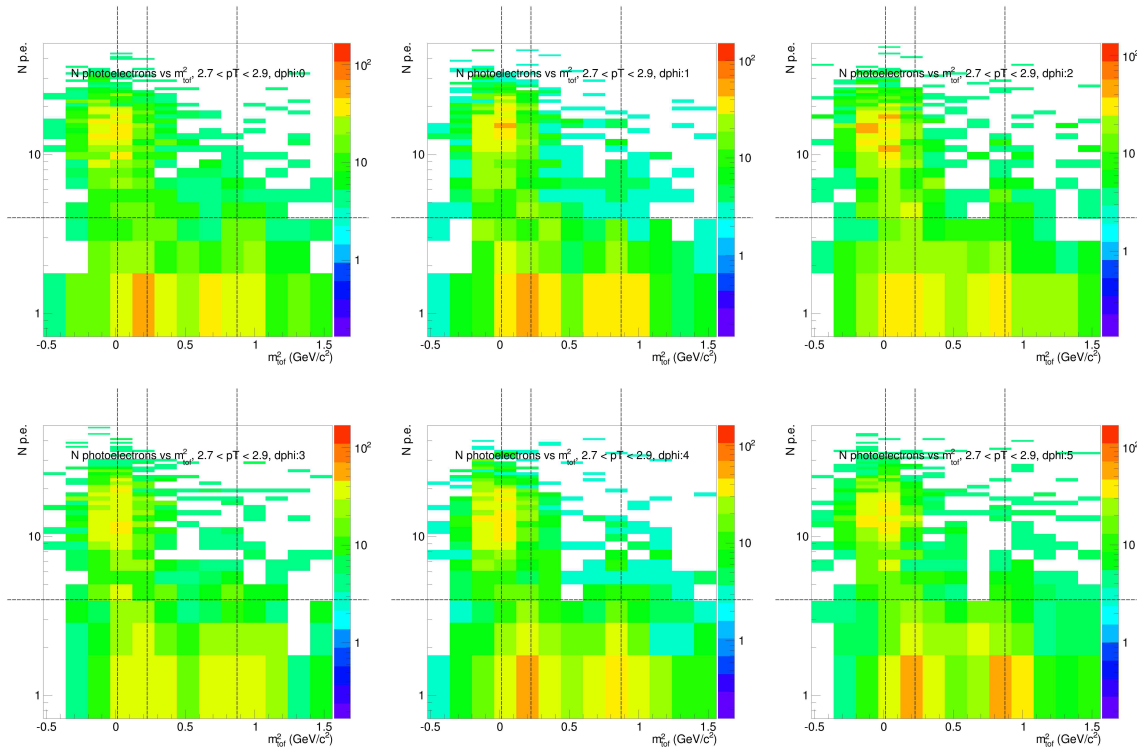


(d) PID parameters and Yields for ACC vetoed tracks

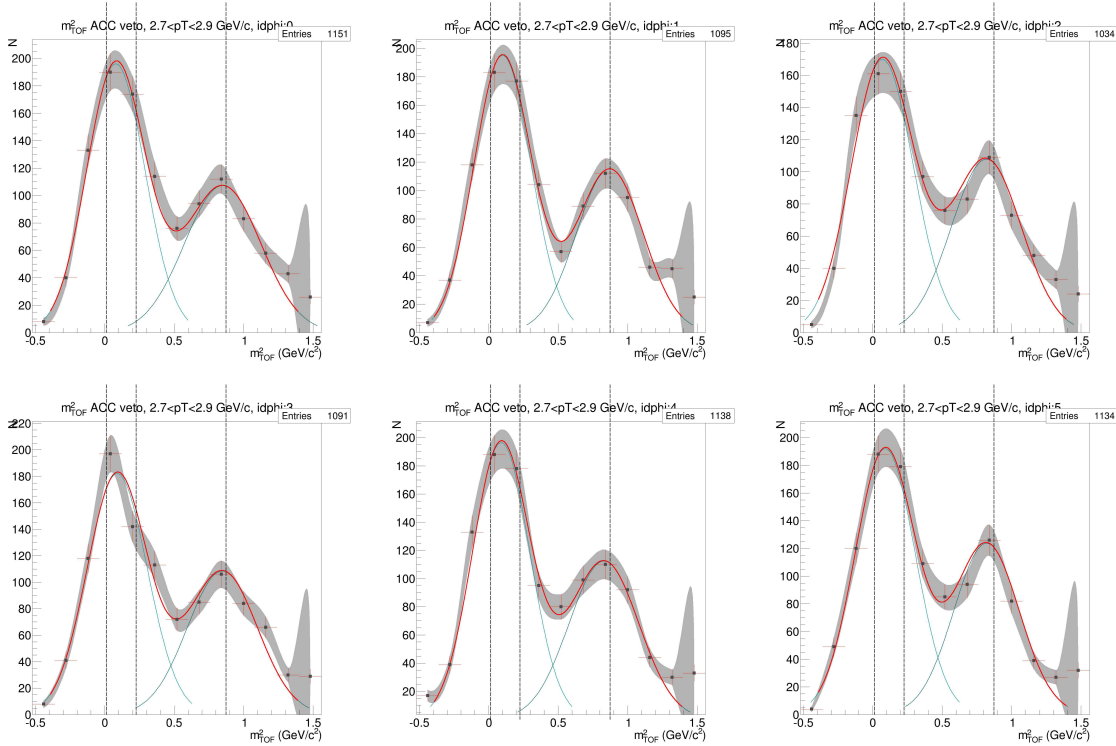


(e) PID parameters and Yields for ACC fired tracks

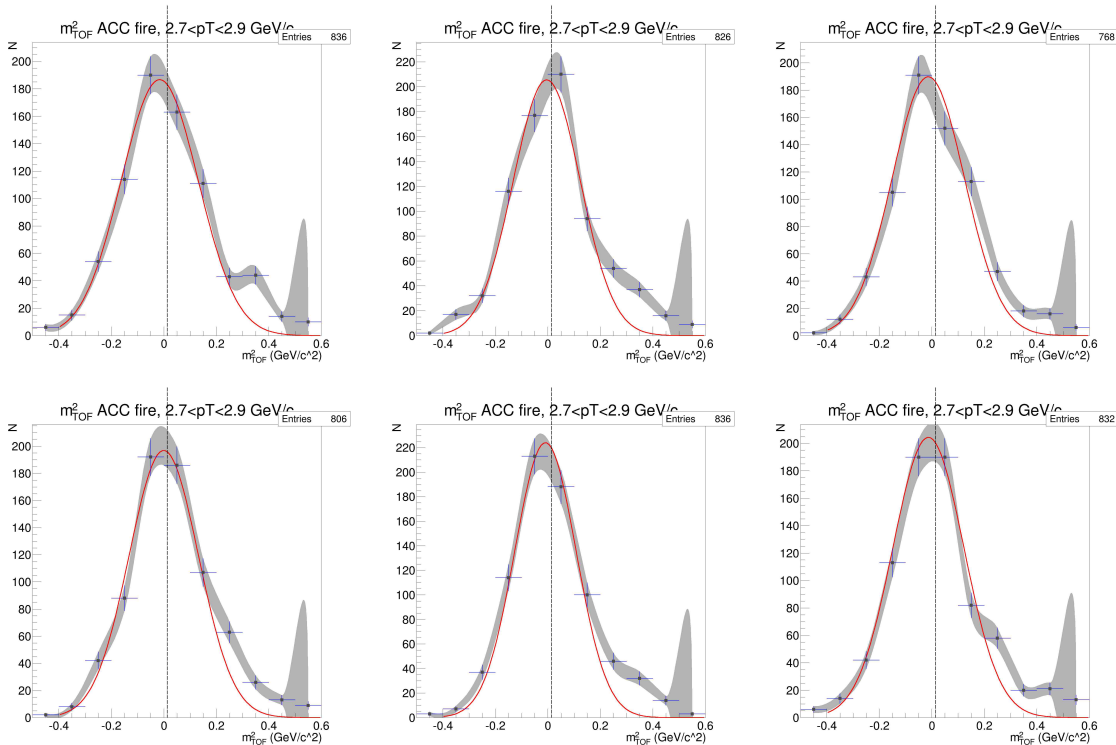
Figure C.19: ACC $N_{p.e.}$ vs m_2 , PID fits, and Yield vs $d\phi$ for $p_T=2.5-2.7$ GeV/c , TOF.W, negative particles



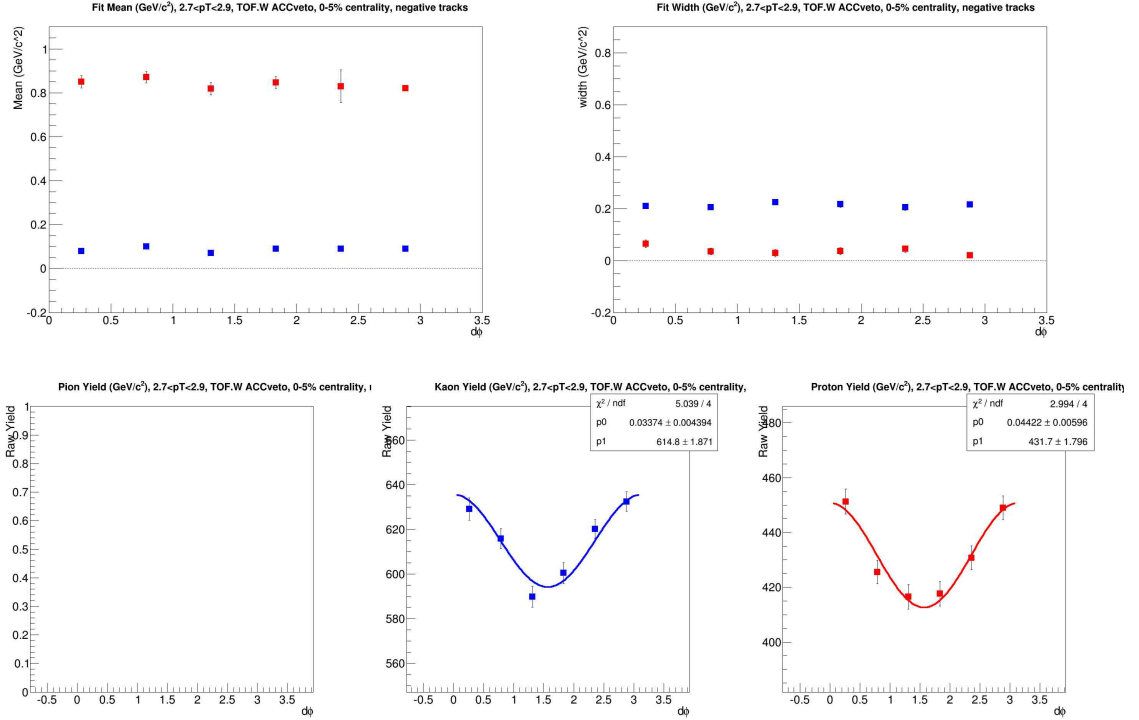
(a) $N_{p.e.}$ vs m^2



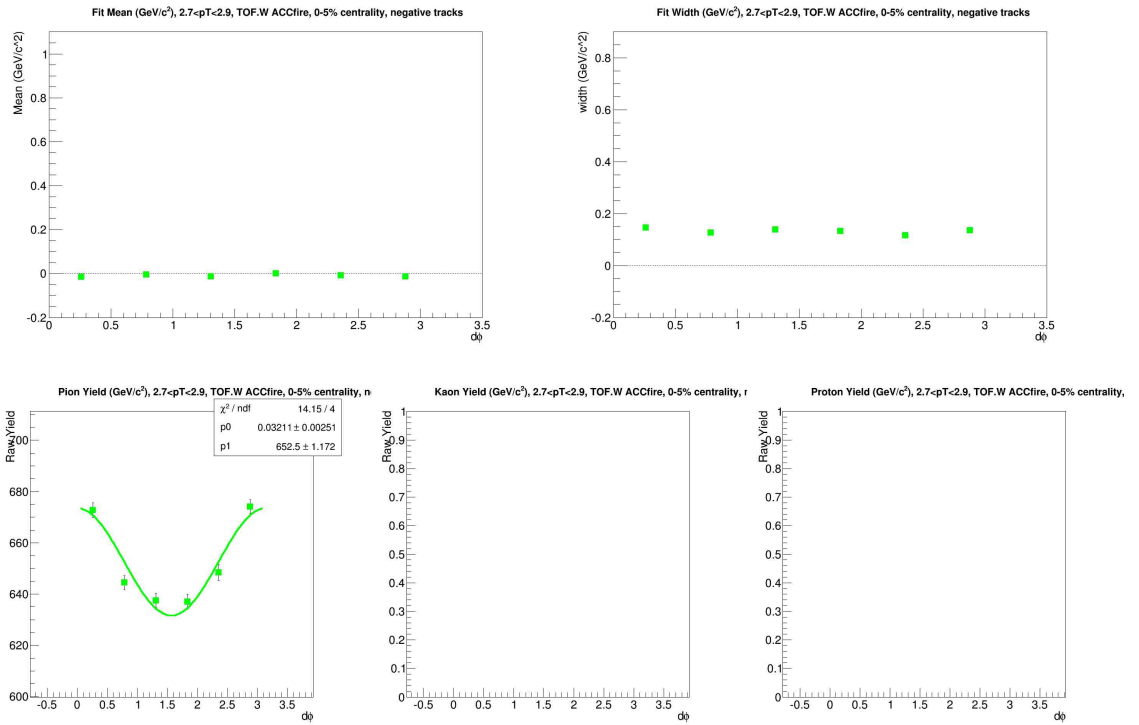
(b) m^2 for ACC vetoed tracks



(c) m^2 for ACC fired tracks

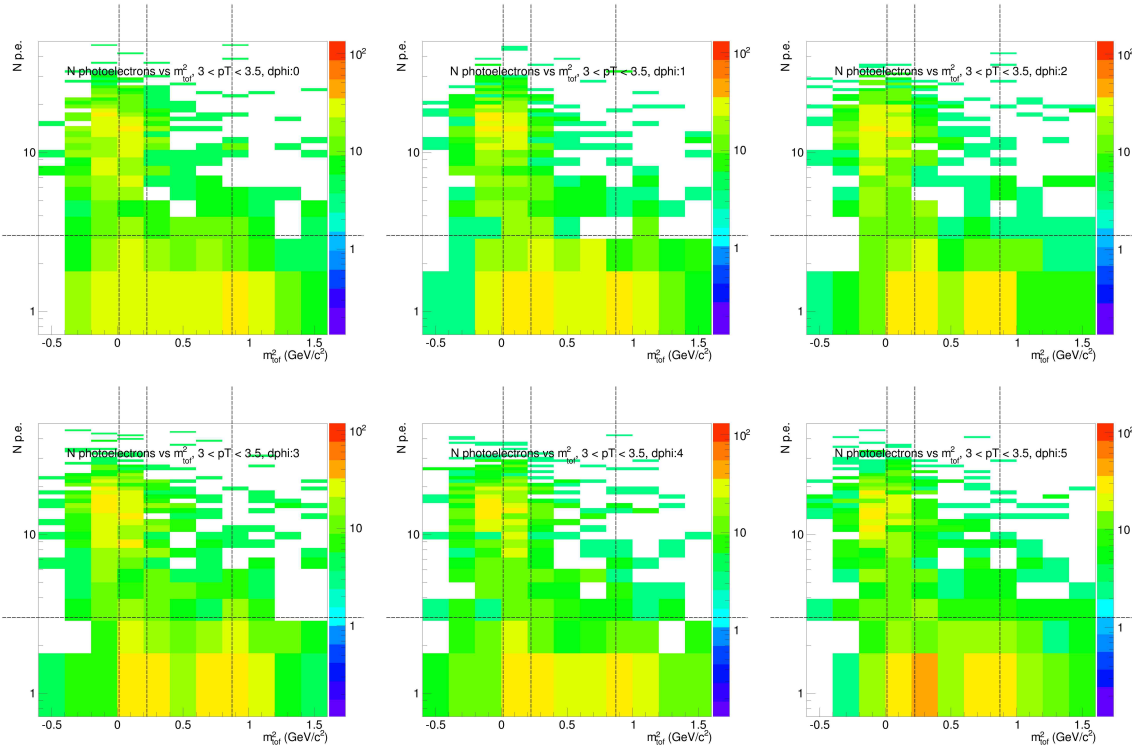


(d) PID parameters and Yields for ACC vetoed tracks

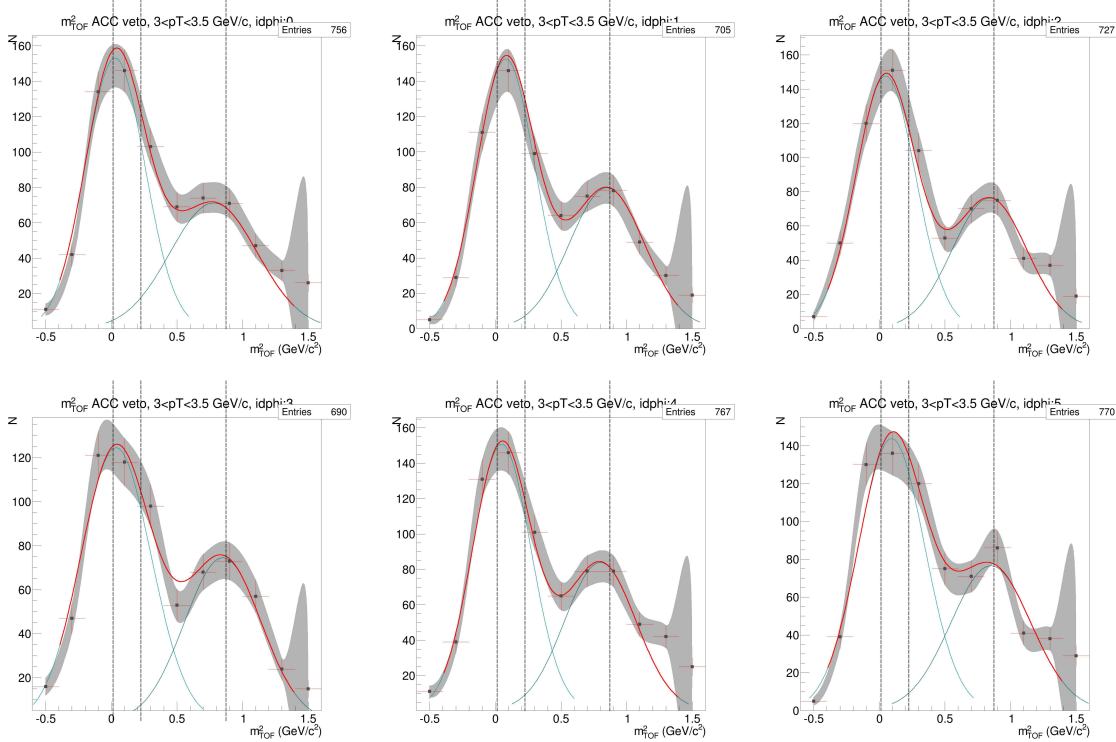


(e) PID parameters and Yields for ACC fired tracks

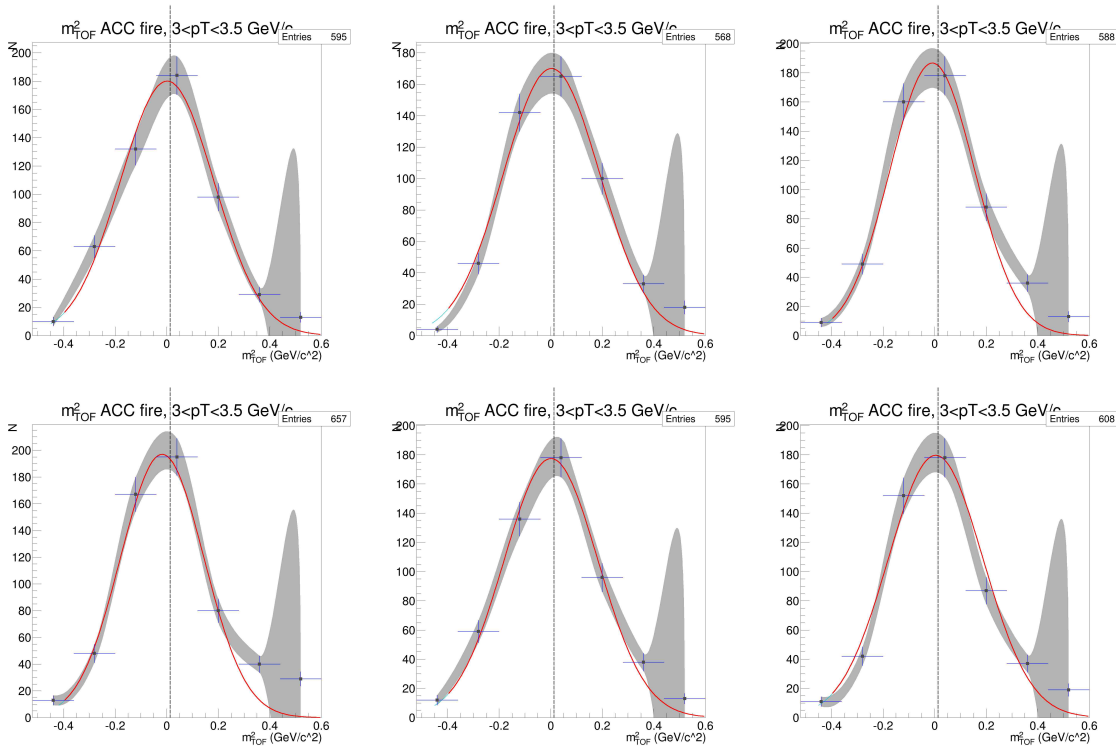
Figure C.20: ACC $N_{\text{p.e.}}$ vs m_2 , PID^3 fits, and Yield vs $d\phi$ for $p\text{T}=2.7-2.9$ GeV/c , TOF.W, negative particles



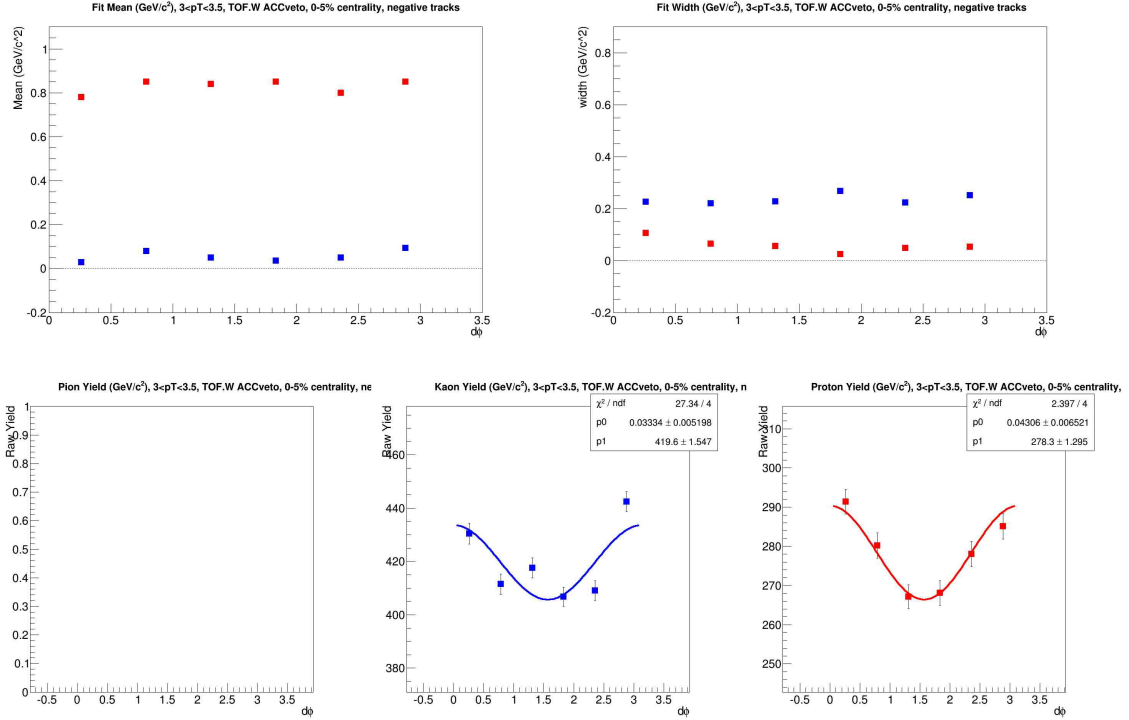
(a) $N_{p.e.}$ vs m^2



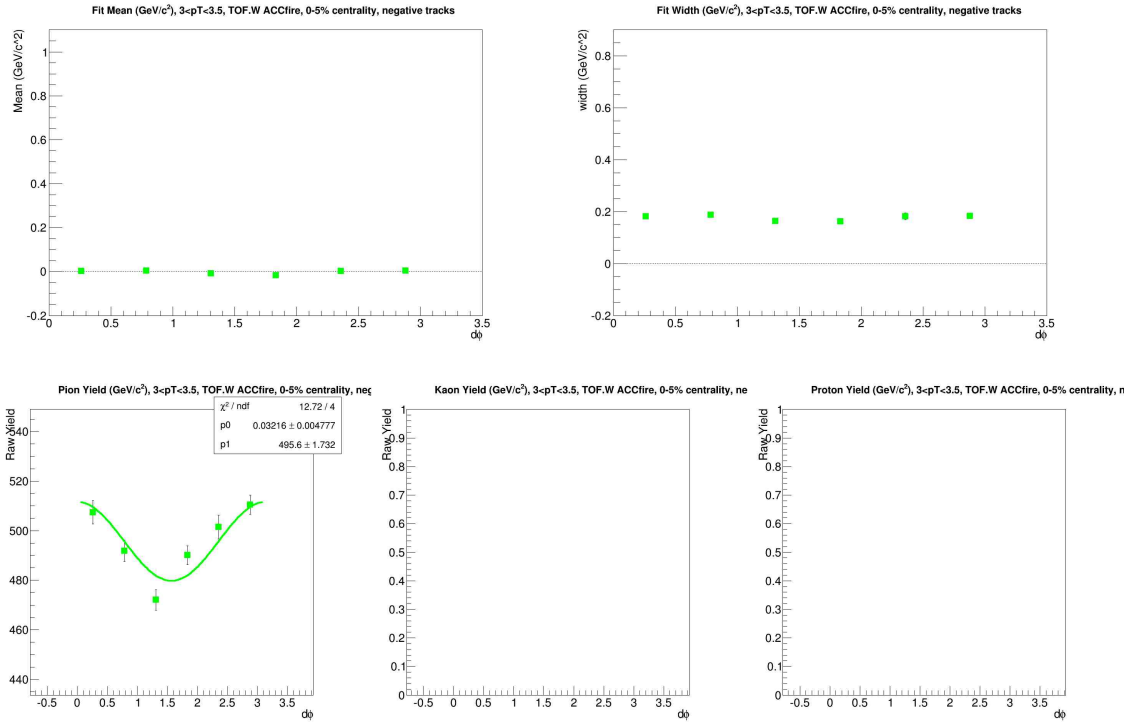
(b) m^2 for ACC vetoed tracks



(c) m^2 for ACC fired tracks

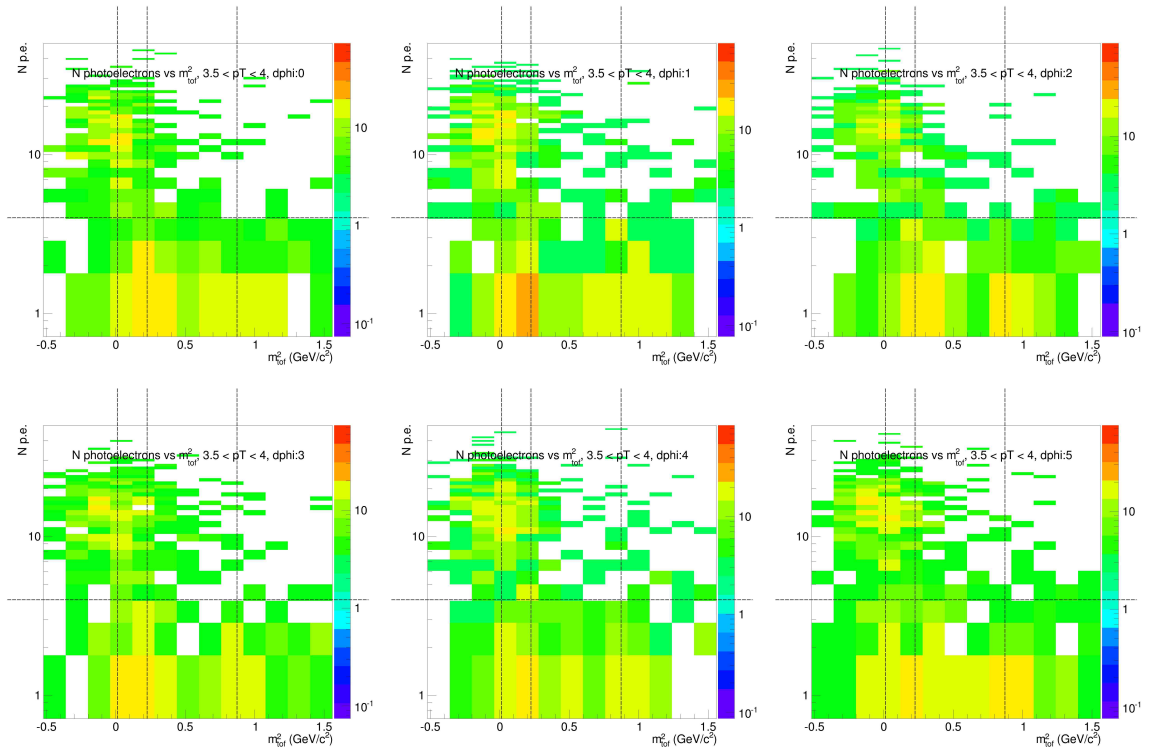


(d) PID parameters and Yields for ACC vetoed tracks

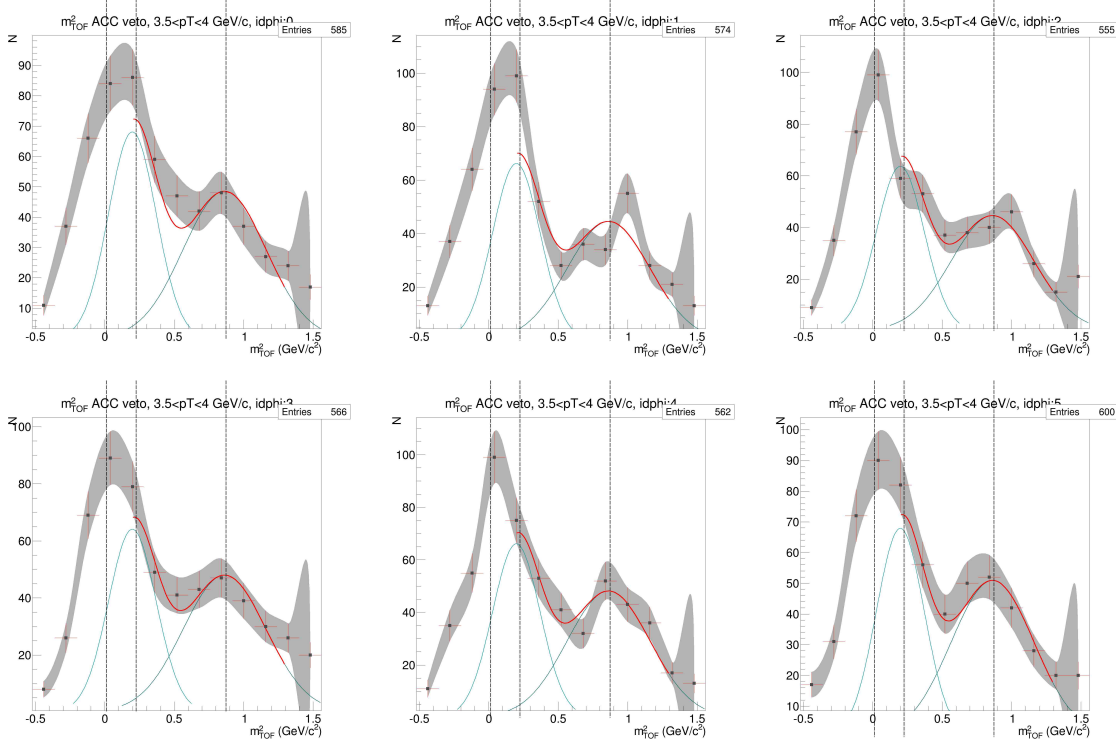


(e) PID parameters and Yields for ACC fired tracks

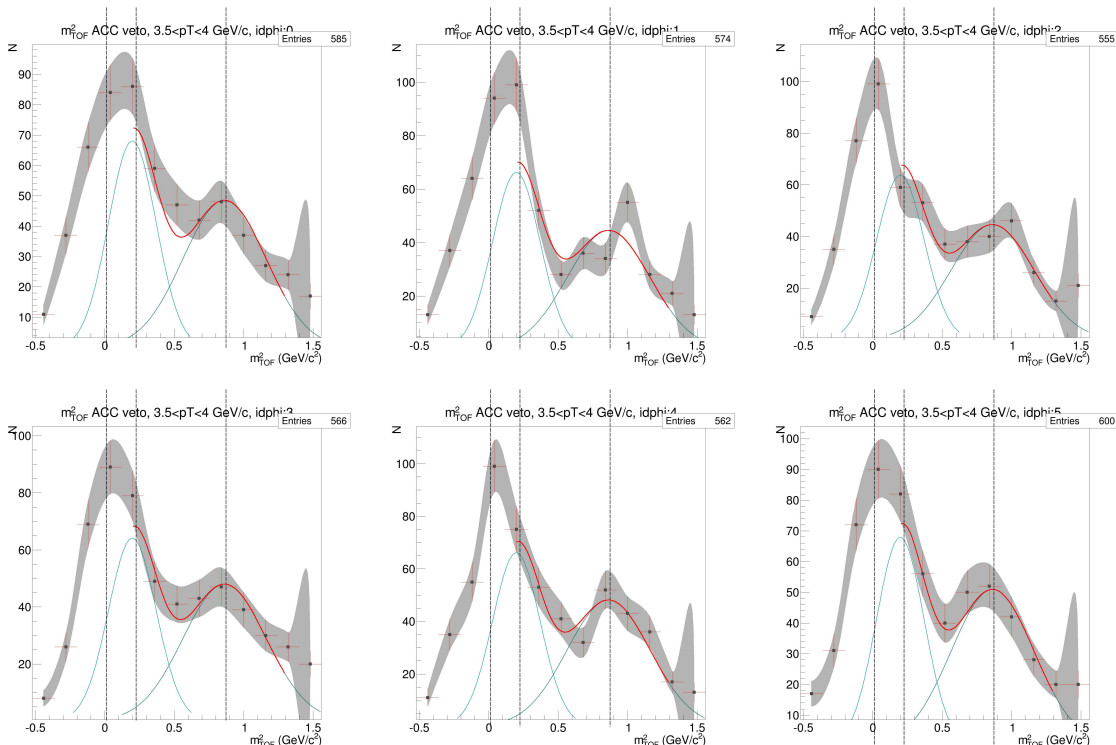
Figure C.21: ACC $N_{p.e.}$ vs m_2 , PID fits, and Yield vs $d\phi$ for $p_T=3.0-3.5$ GeV/c, TOF.W, negative particles



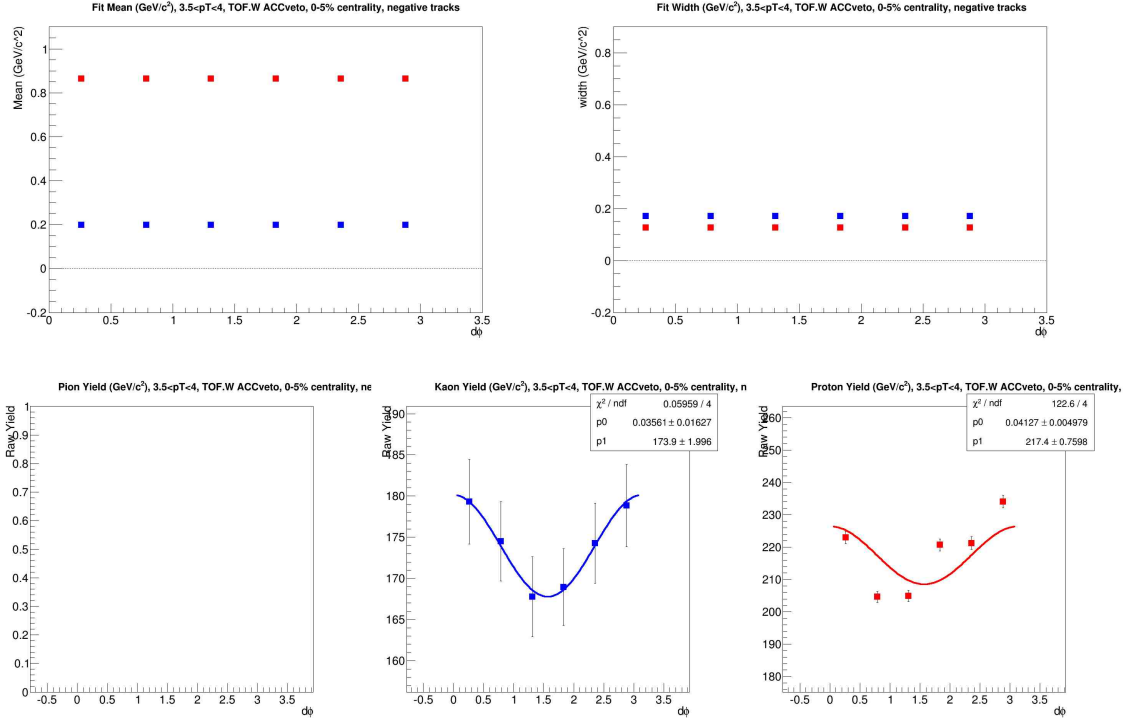
(a) $N_{p.e.}$ vs m^2



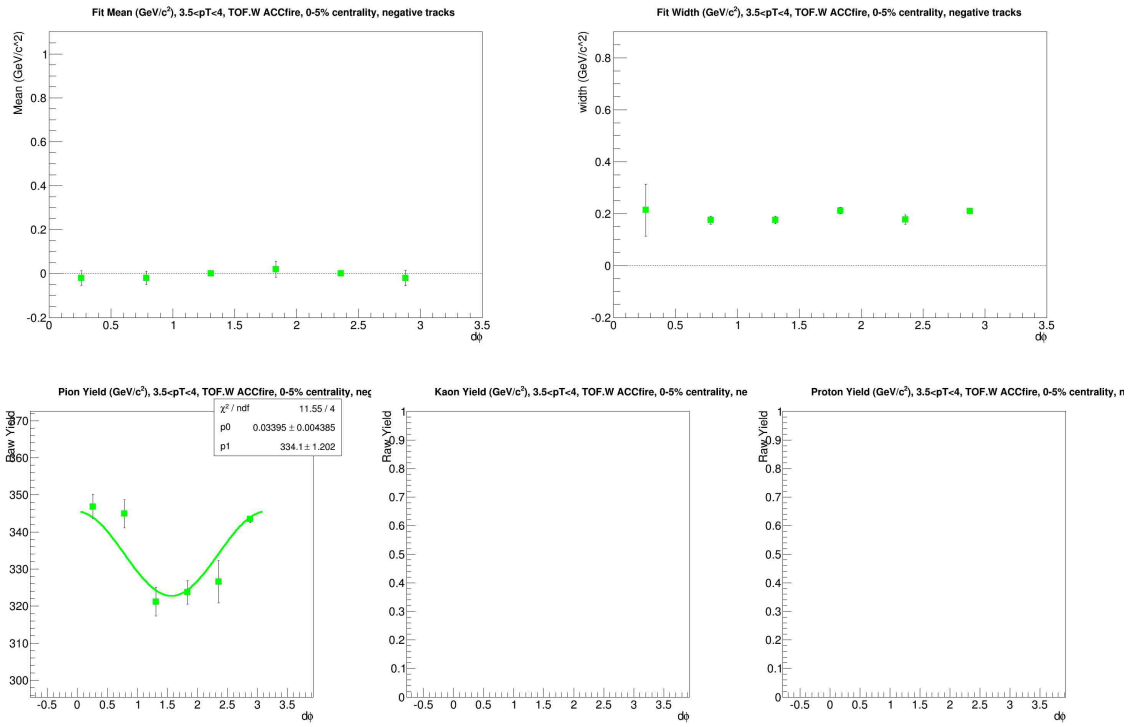
(b) m^2 for ACC vetoed tracks



(c) m^2 for ACC fired tracks

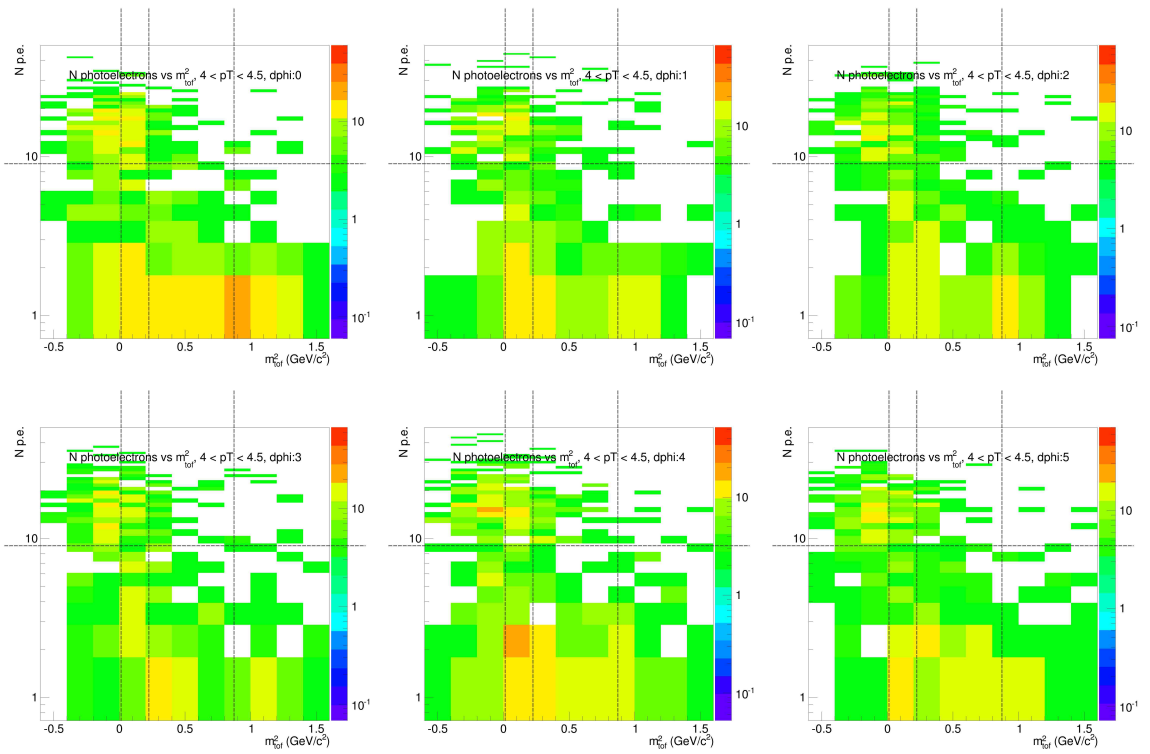


(d) PID parameters and Yields for ACC vetoed tracks

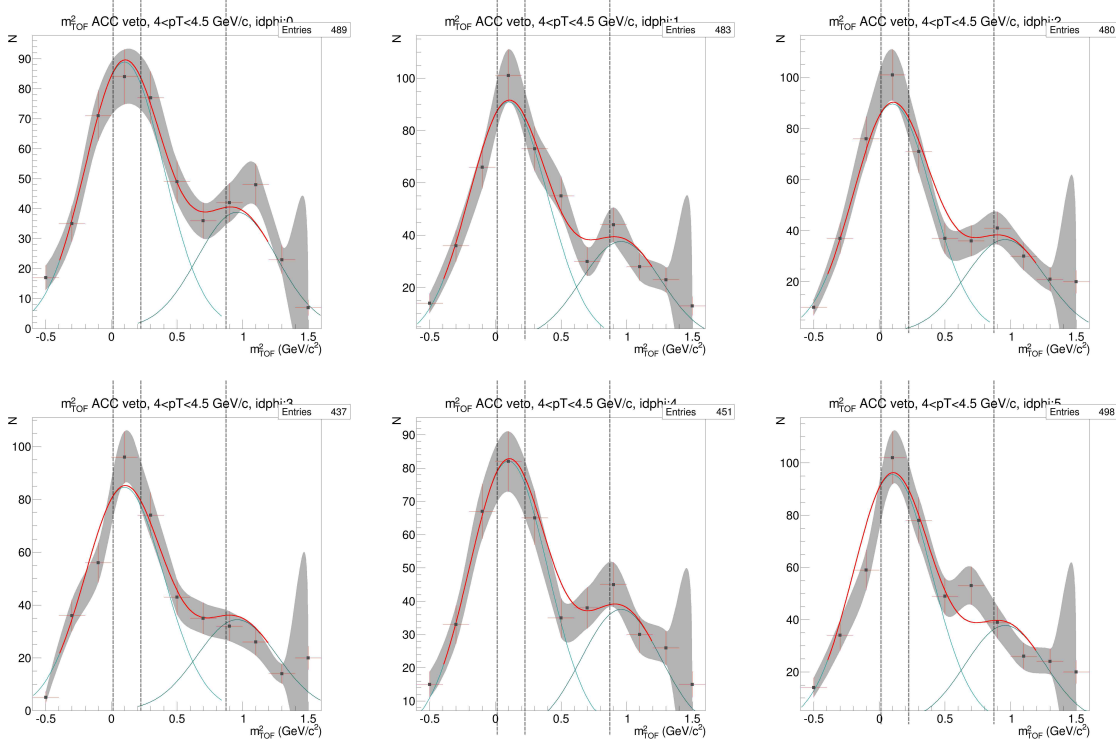


(e) PID parameters and Yields for ACC fired tracks

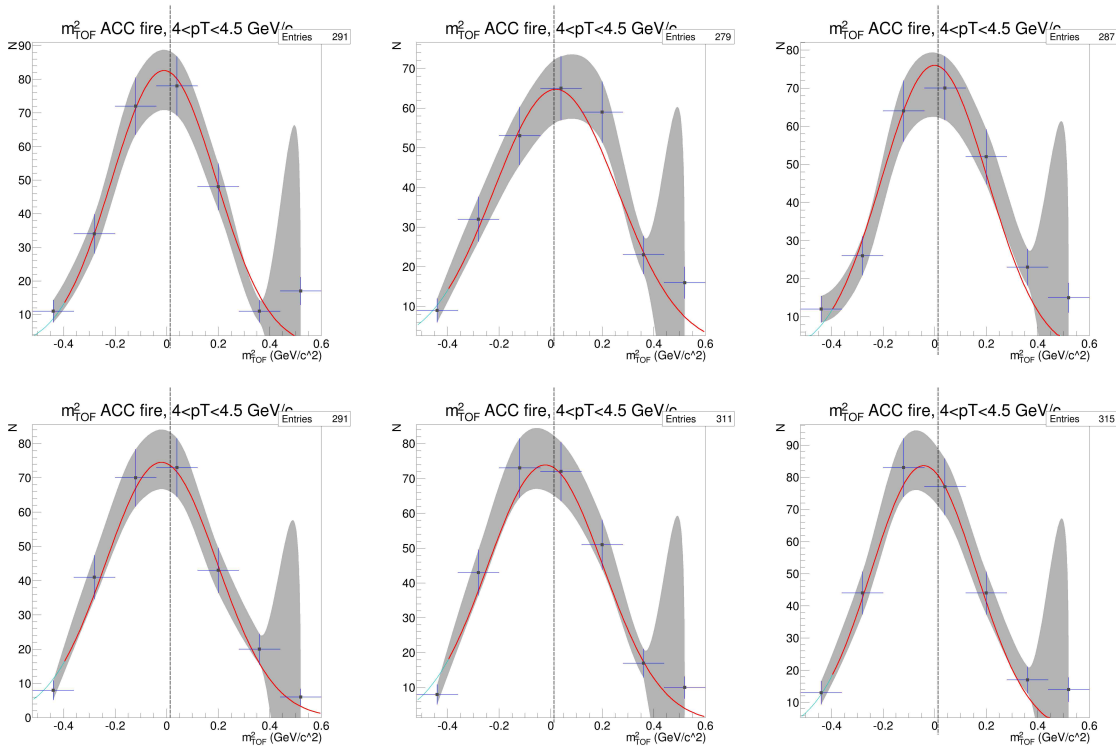
Figure C.22: ACC $N_{p.e.}$ vs m_2 , PID^0 fits, and Yield vs $d\phi$ for $p_T=3.5-4.0$ GeV/c , TOF.W, negative particles



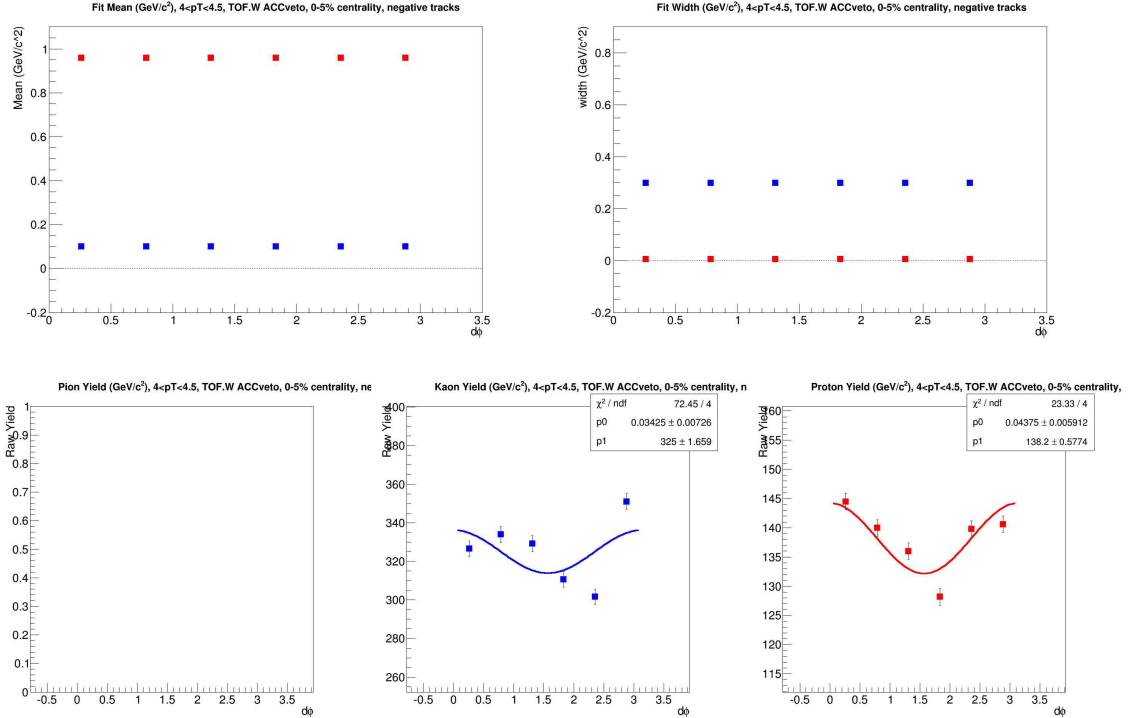
(a) $N_{\text{p.e.}}$ vs m^2



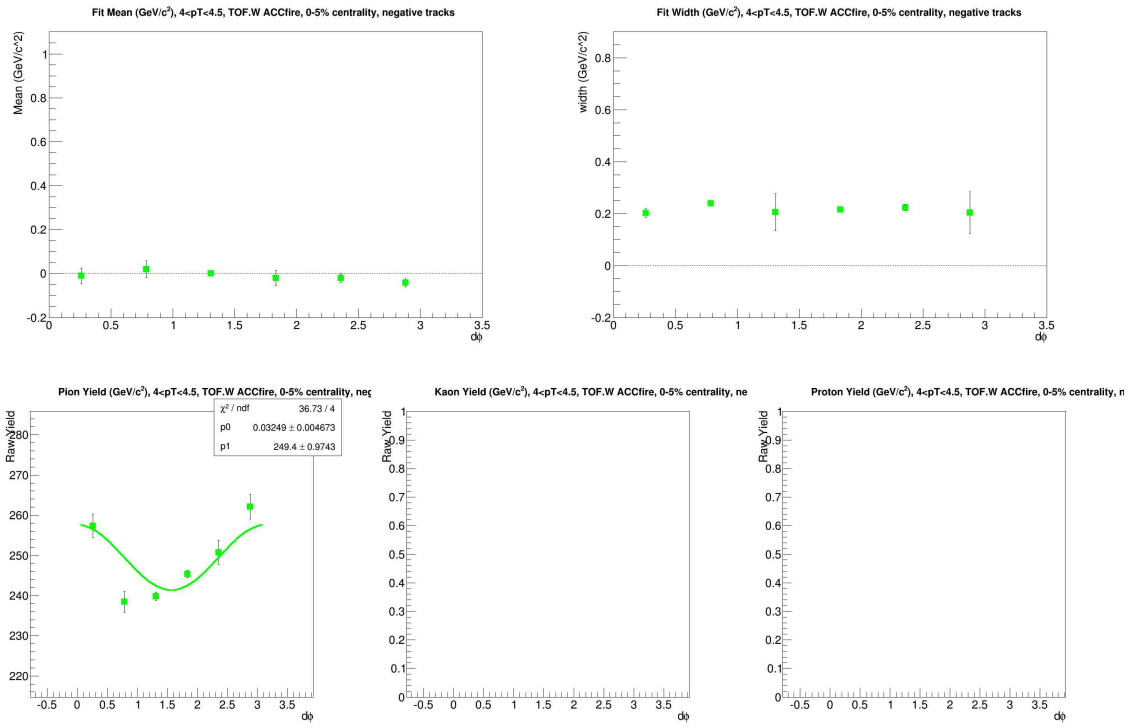
(b) m^2 for ACC vetoed tracks



(c) m^2 for ACC fired tracks



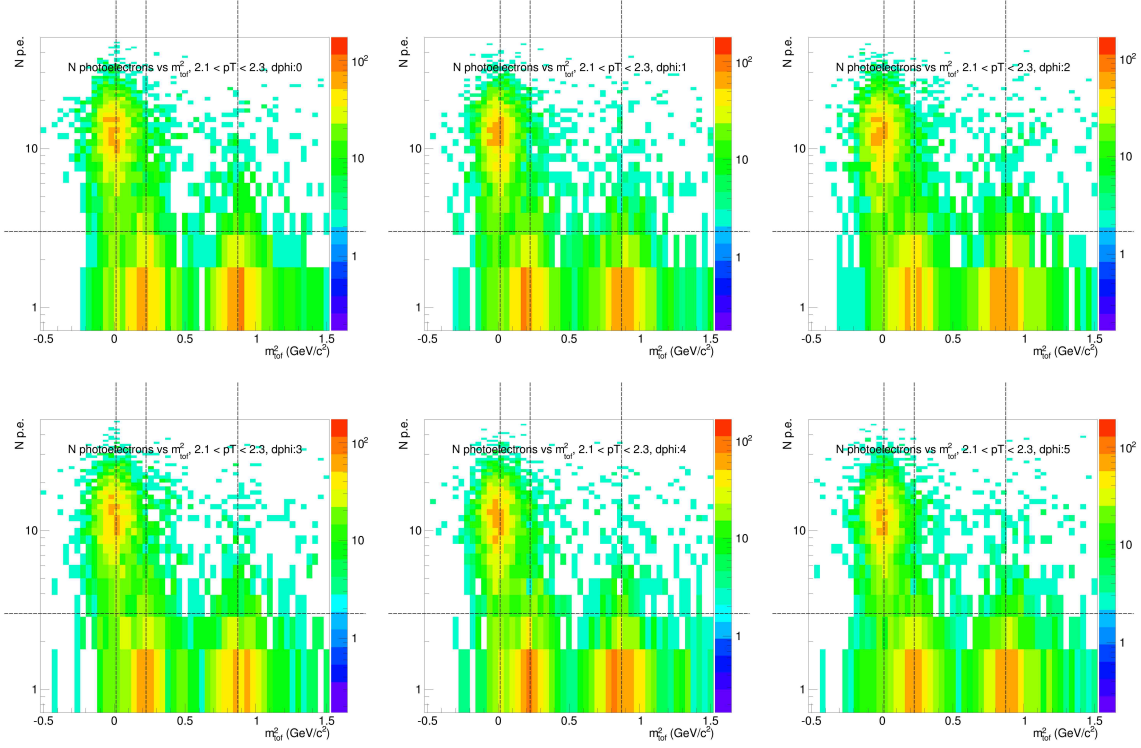
(d) PID parameters and Yields for ACC vetoed tracks



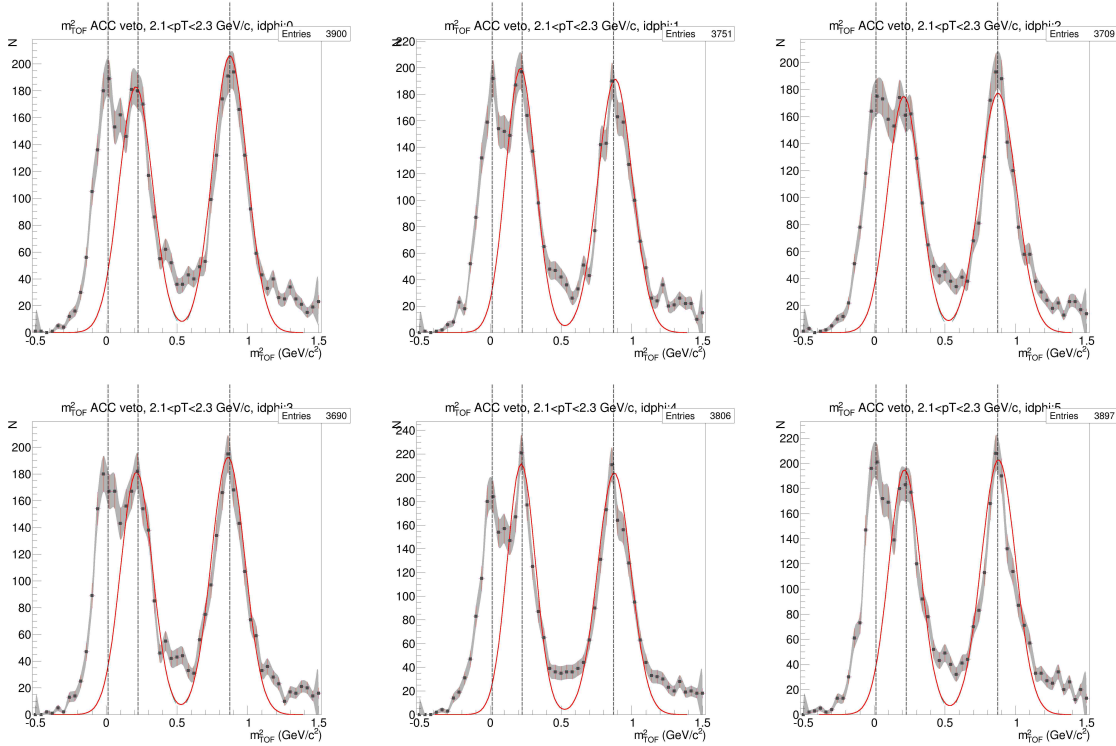
(e) PID parameters and Yields for ACC fired tracks

Figure C.23: ACC $N_{p.e.}$ vs m_2 , PID fits, and Yield vs $d\phi$ for $p_T=4.0-4.5$ GeV/c , TOF.W, negative particles

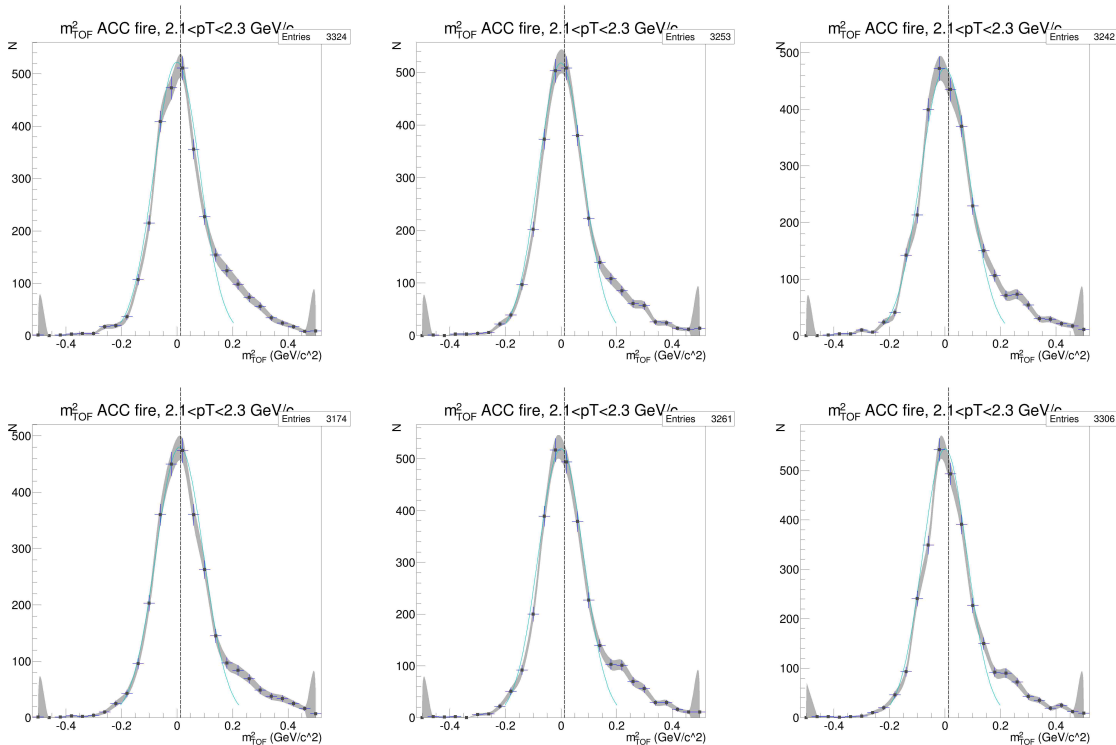
C.1.5 TOF.W and ACC, $p_T=2.1\text{-}3.5$ GeV, positive charged tracks



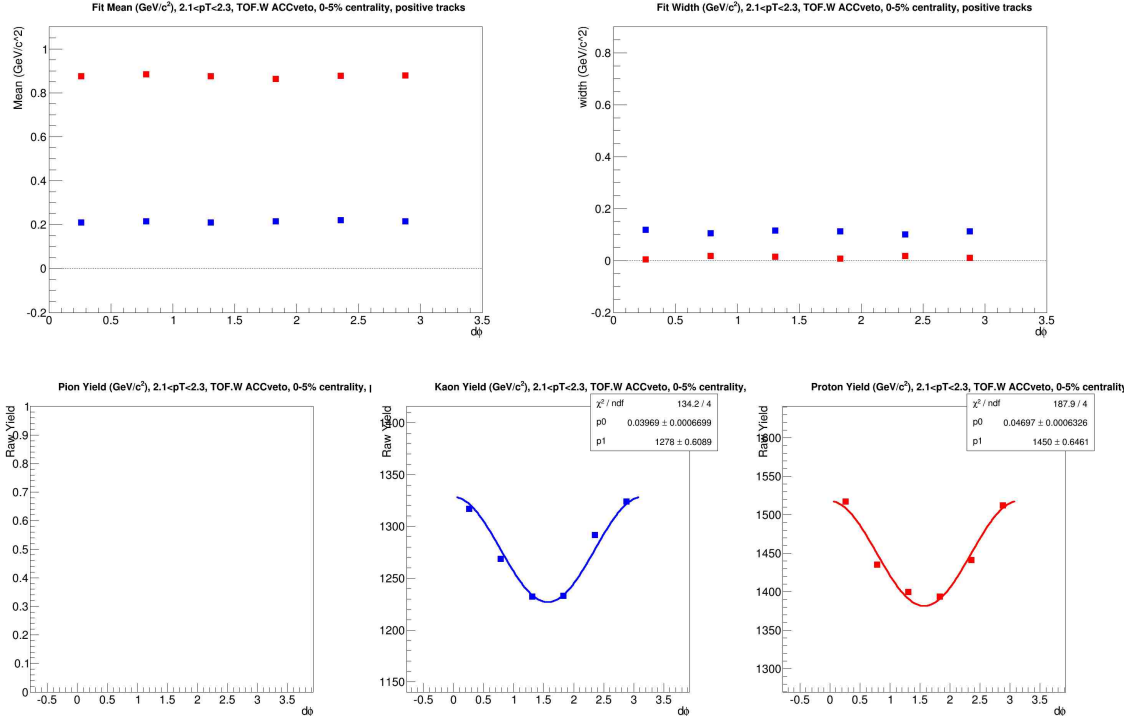
(a) $N_{p.e.}$ vs m^2



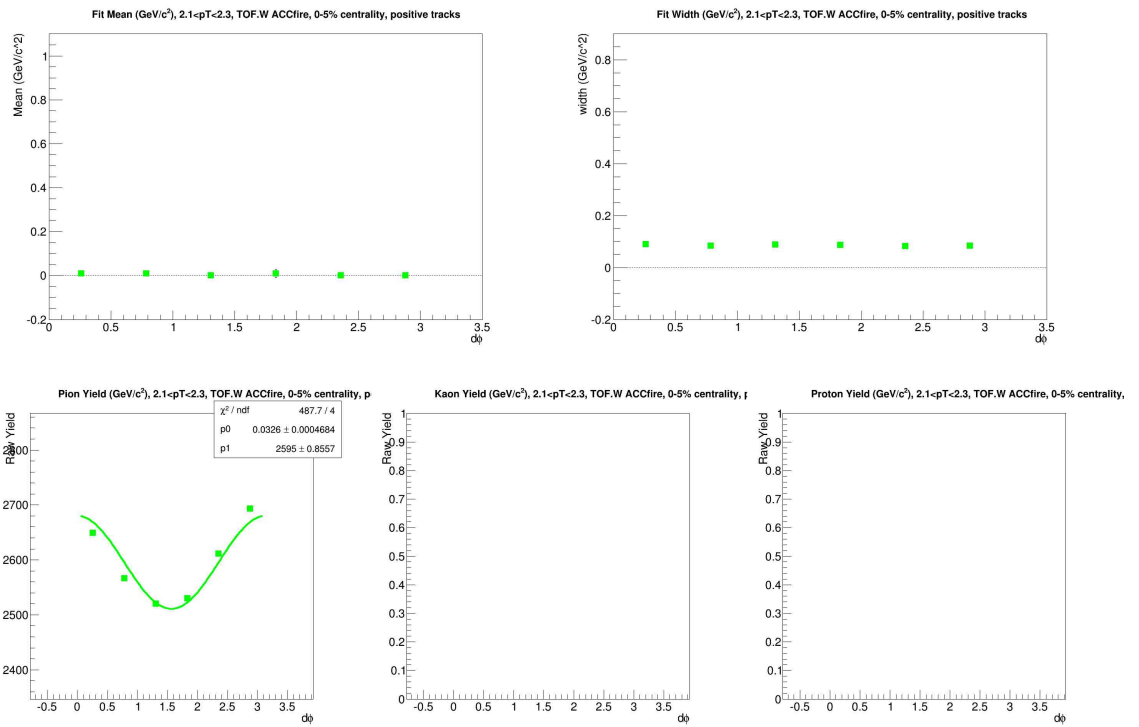
(b) m^2 for ACC vetoed tracks



(c) m^2 for ACC fired tracks

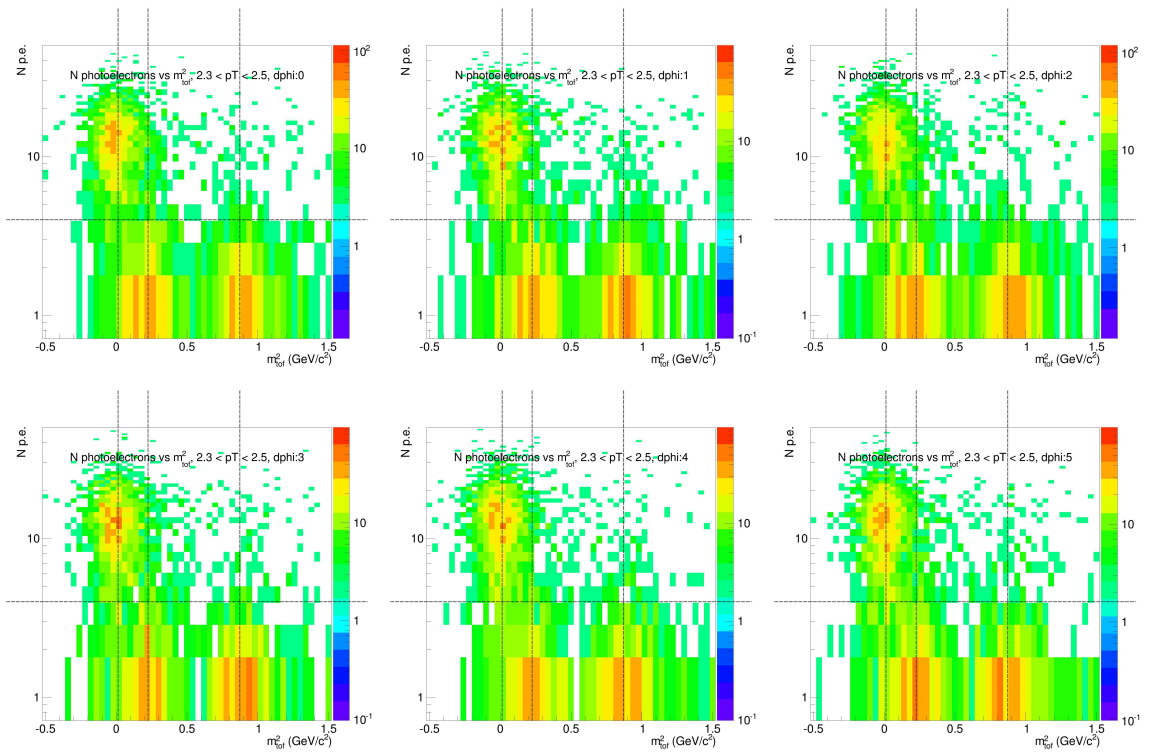


(d) PID parameters and Yields for ACC vetoed tracks

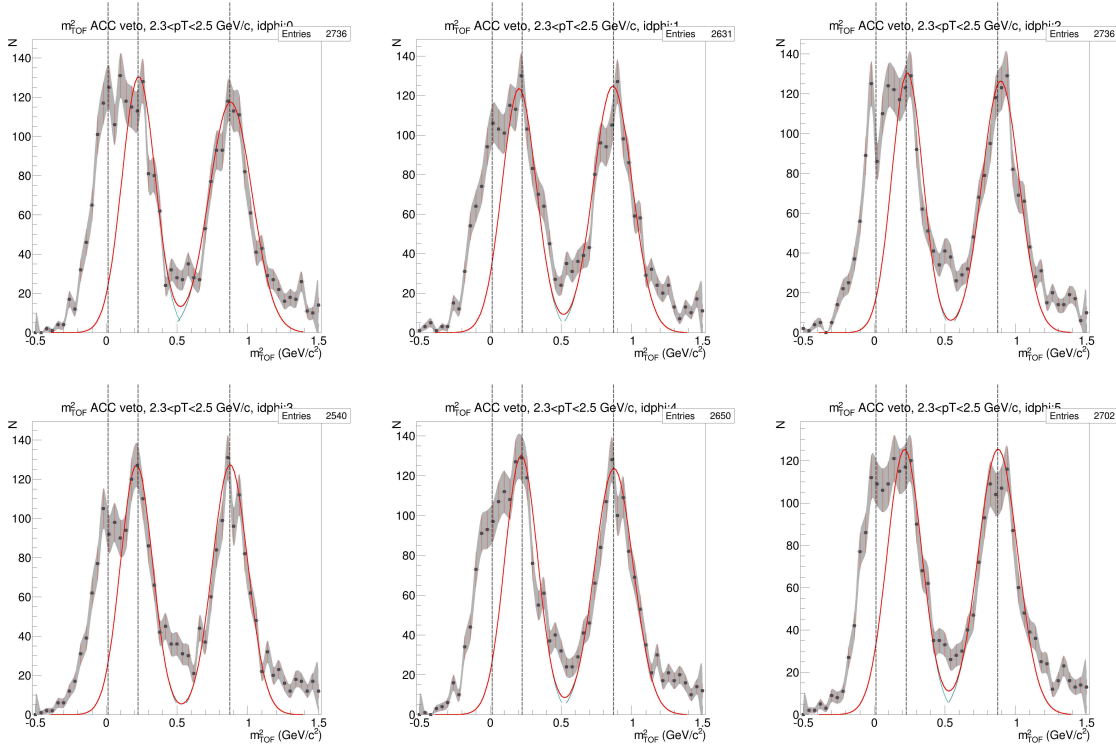


(e) PID parameters and Yields for ACC fired tracks

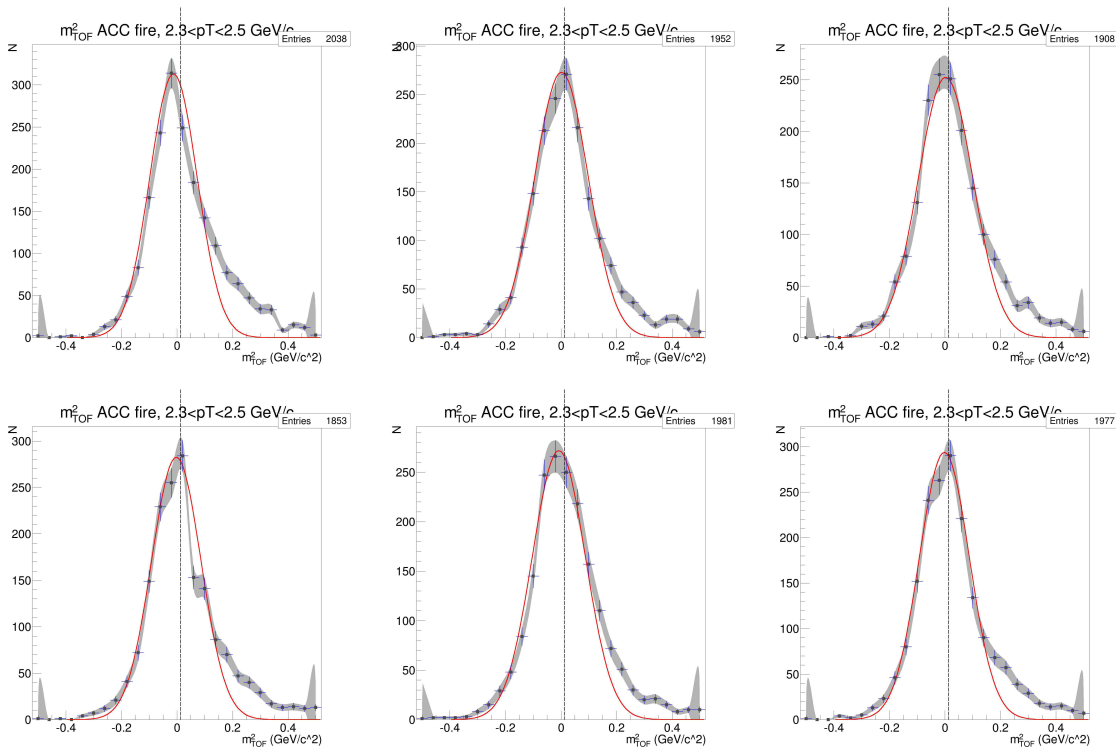
Figure C.24: ACC $N_{p.e.}$ vs m_2 , PID fits, and Yield vs $d\phi$ for $p_T=2.1-2.3$ GeV/c , TOF.W, positive particles



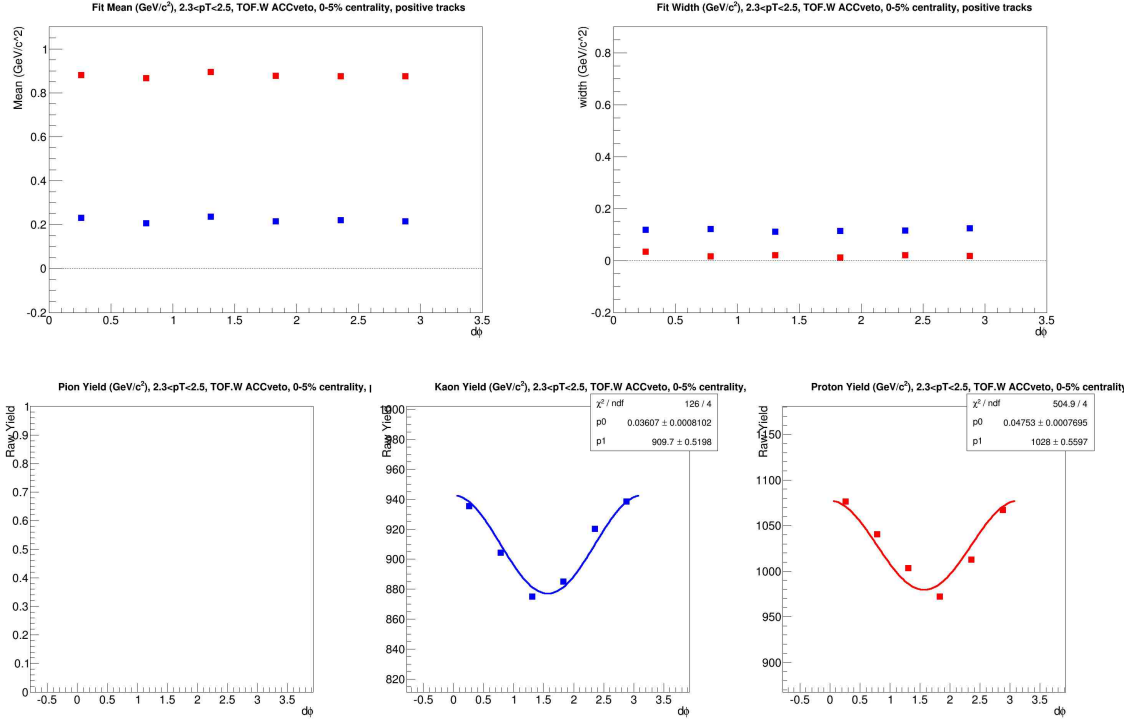
(a) $N_{p.e.}$ vs m^2



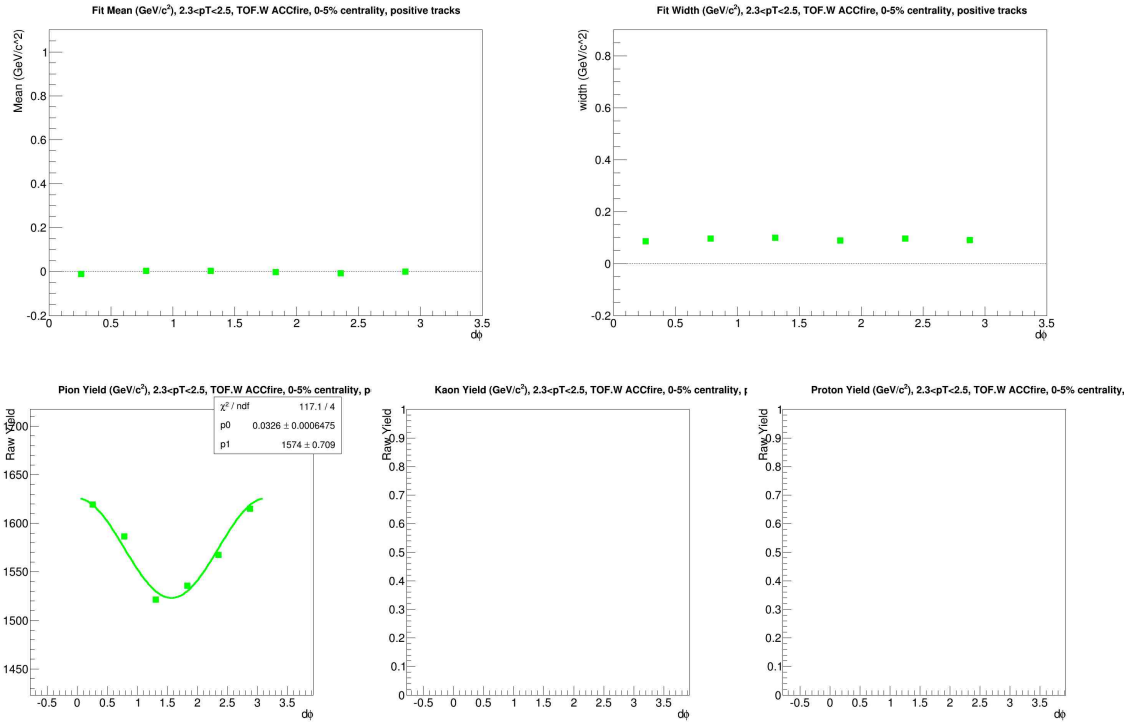
(b) m^2 for ACC vetoed tracks



(c) m^2 for ACC fired tracks

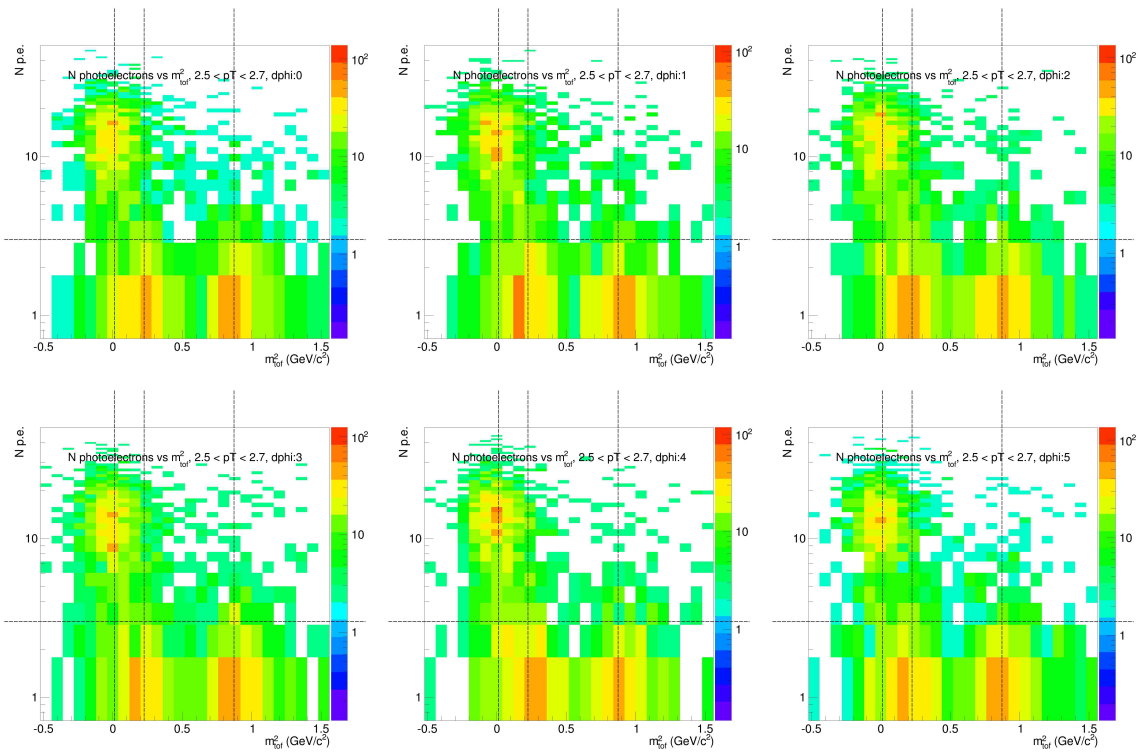


(d) PID parameters and Yields for ACC vetoed tracks

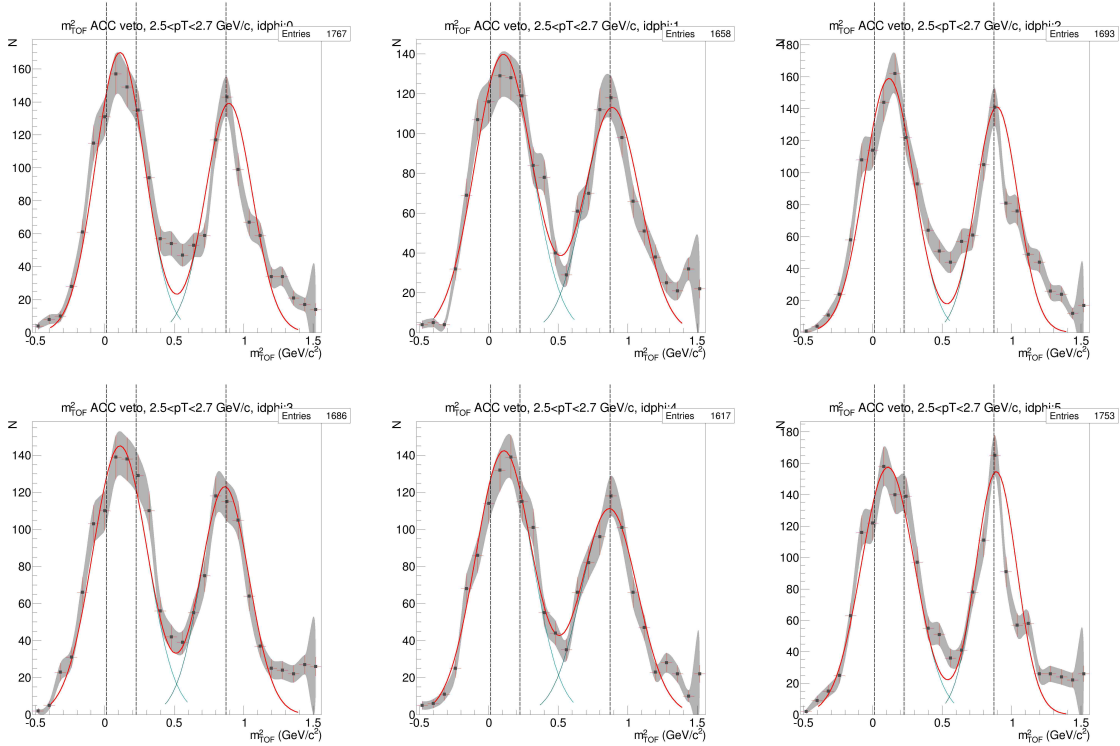


(e) PID parameters and Yields for ACC fired tracks

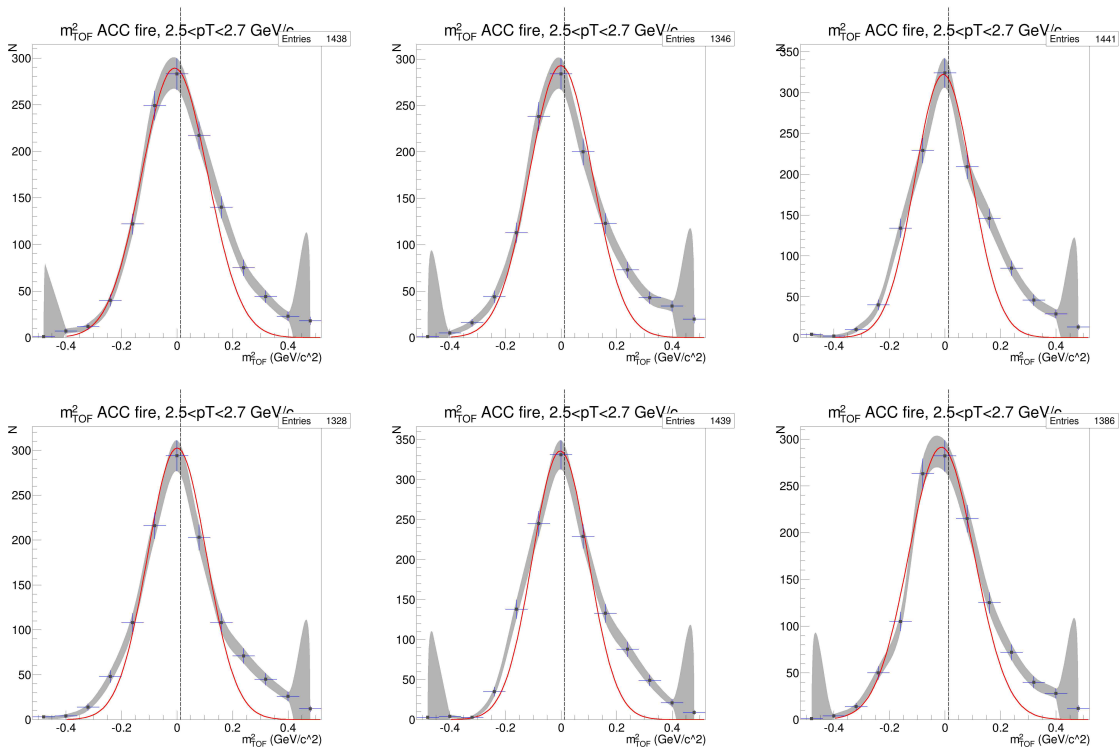
Figure C.25: ACC $N_{p.e.}$ vs m_2 , PID fits, and Yield vs $d\phi$ for $p_T=2.3-2.5$ GeV/c , TOF.W, positive particles



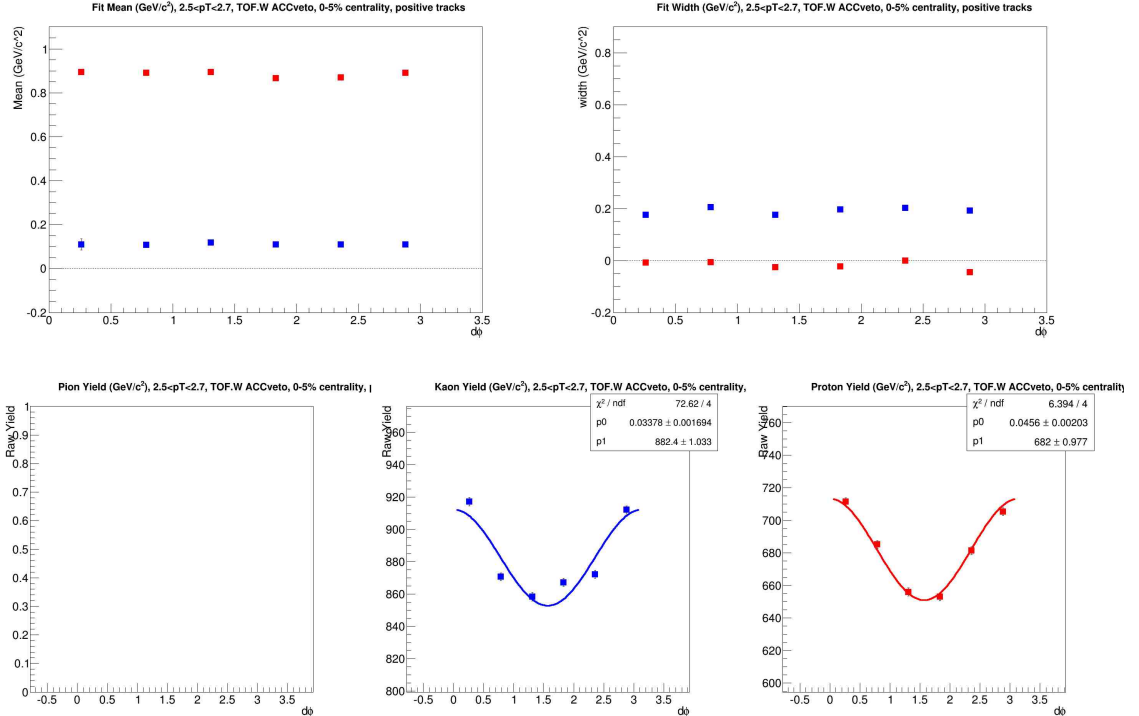
(a) $N_{p.e.}$ vs m^2



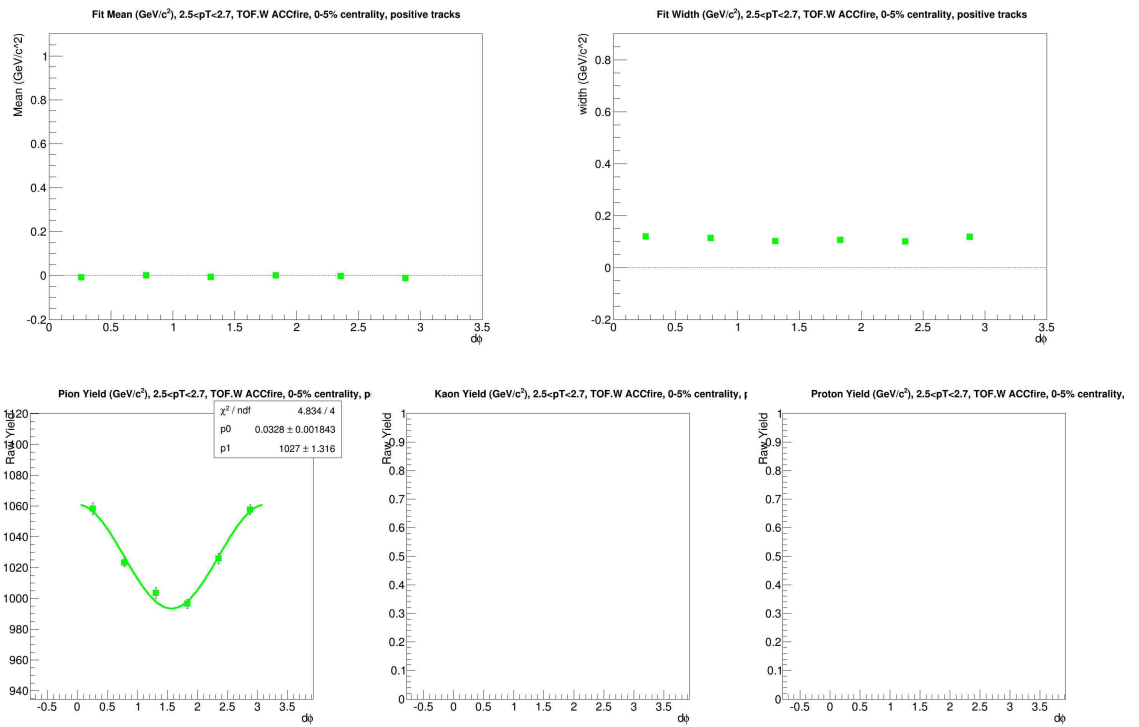
(b) m^2 for ACC vetoed tracks



(c) m^2 for ACC fired tracks

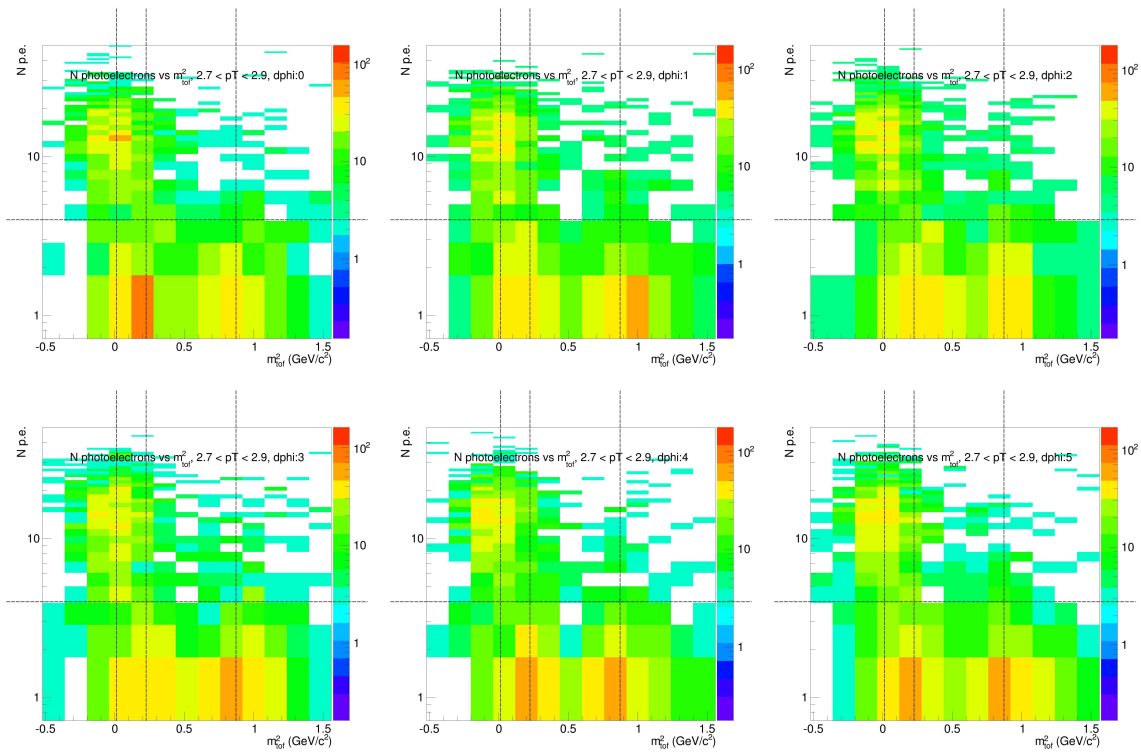


(d) PID parameters and Yields for ACC vetoed tracks

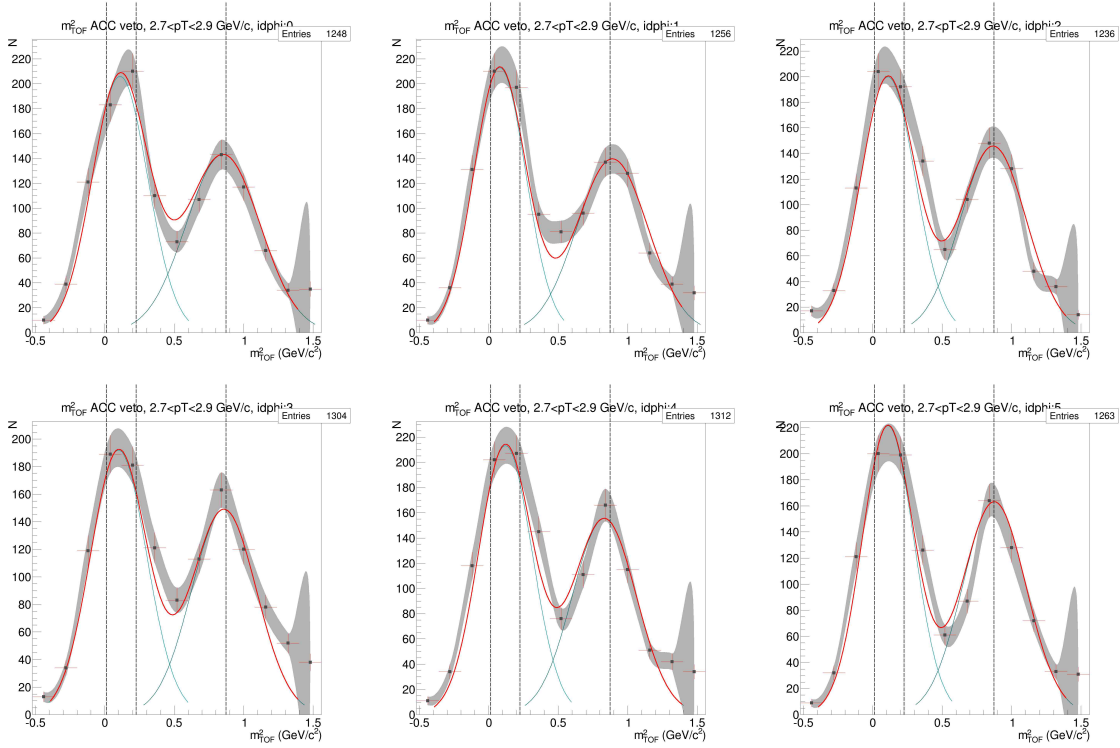


(e) PID parameters and Yields for ACC fired tracks

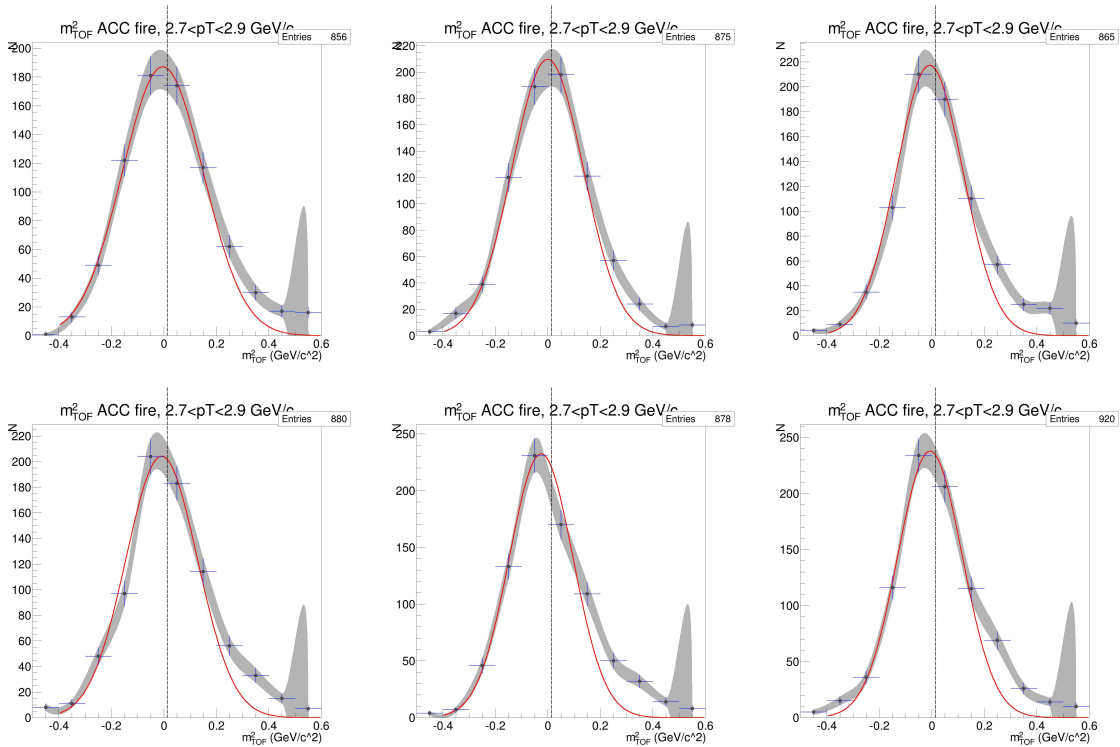
Figure C.26: ACC $N_{\text{p.e.}}$ vs m_2 , PID fits, and Yield vs $d\phi$ for $p\text{T}=2.5-2.7$ GeV/c , TOF.W, positive particles



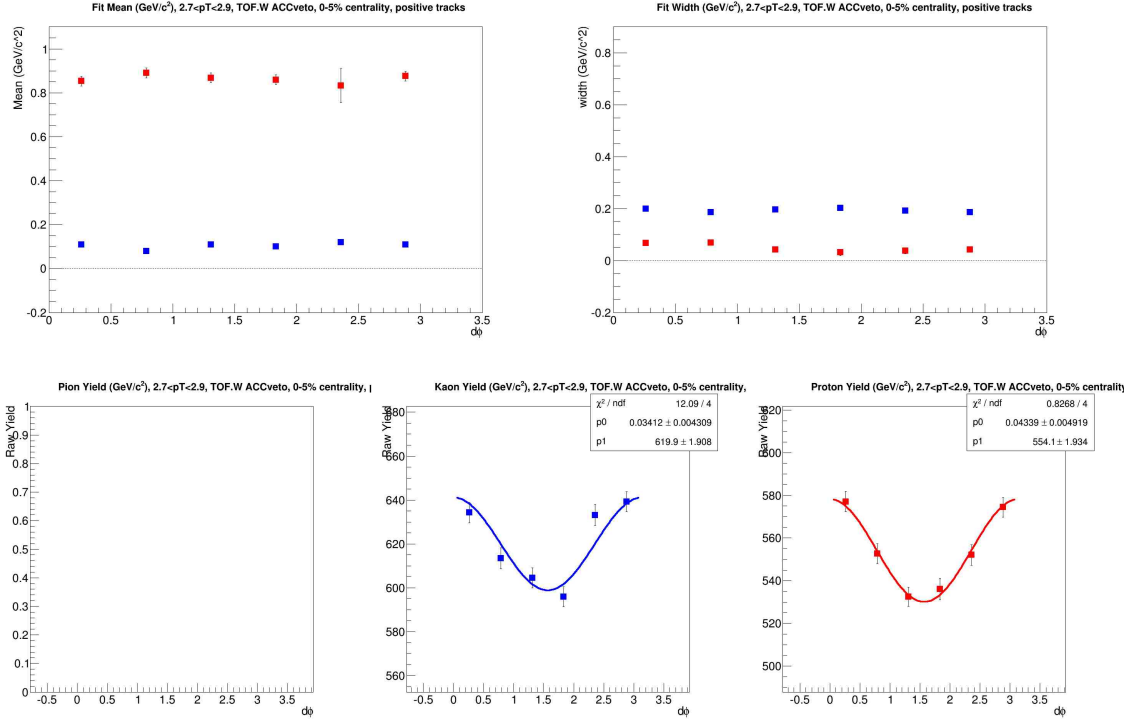
(a) $N_{\text{p.e.}}$ vs m^2



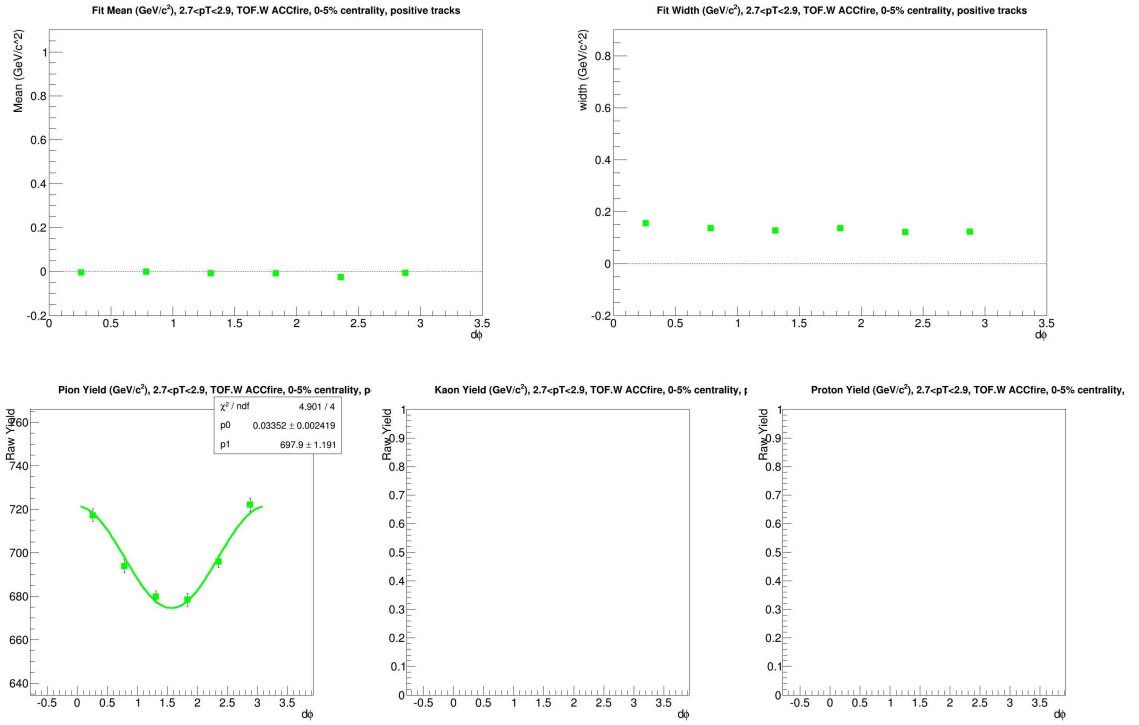
(b) m^2 for ACC vetoed tracks



(c) m^2 for ACC fired tracks

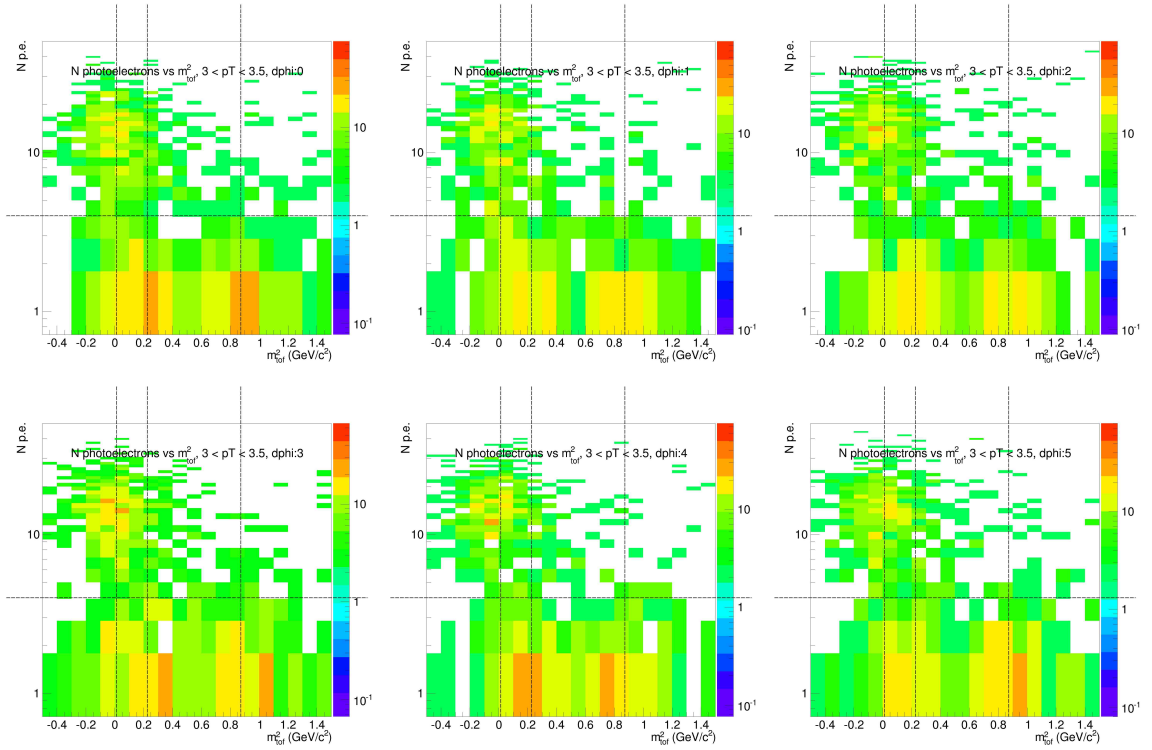


(d) PID parameters and Yields for ACC vetoed tracks

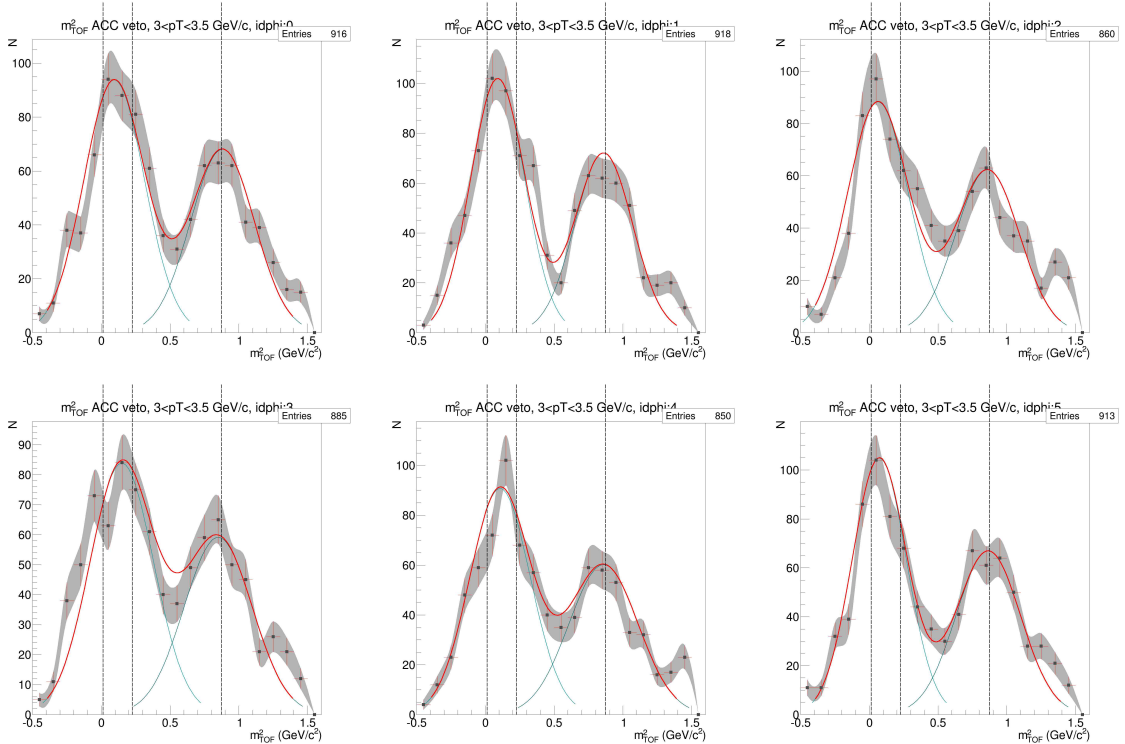


(e) PID parameters and Yields for ACC fired tracks

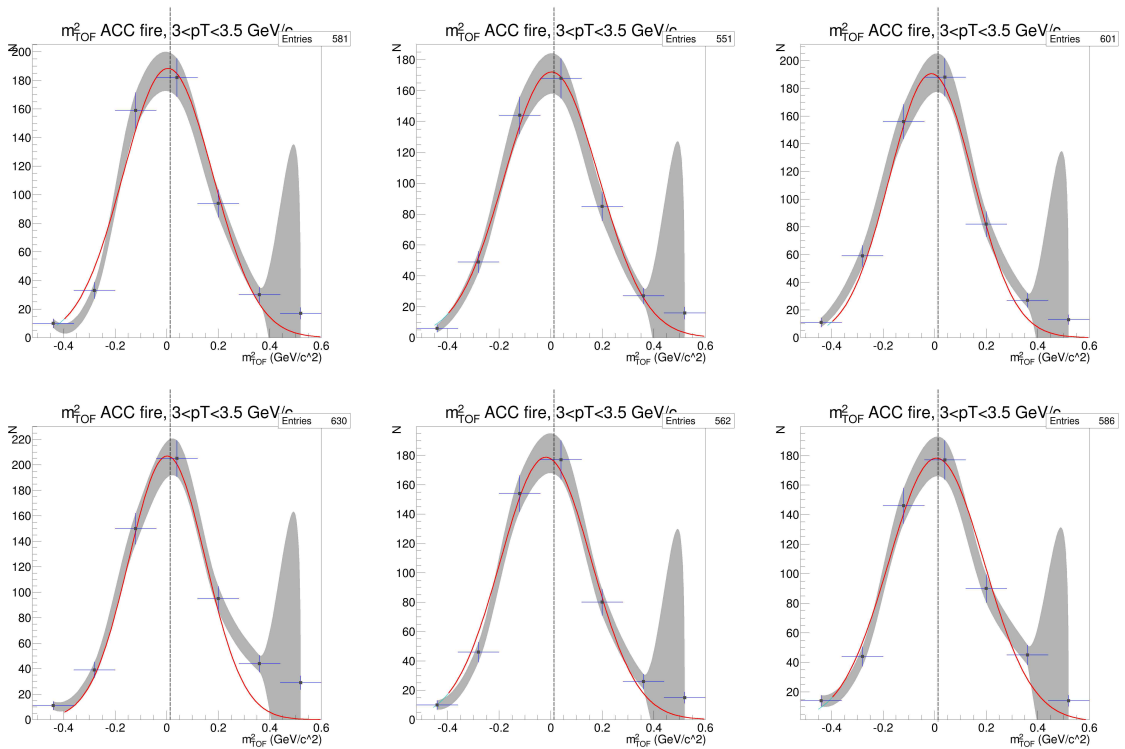
Figure C.27: ACC $N_{p.e.}$ vs m_2 , PID fits, and Yield vs $d\phi$ for $p_T = 2.7-2.9$ GeV/c , TOF.W, positive particles



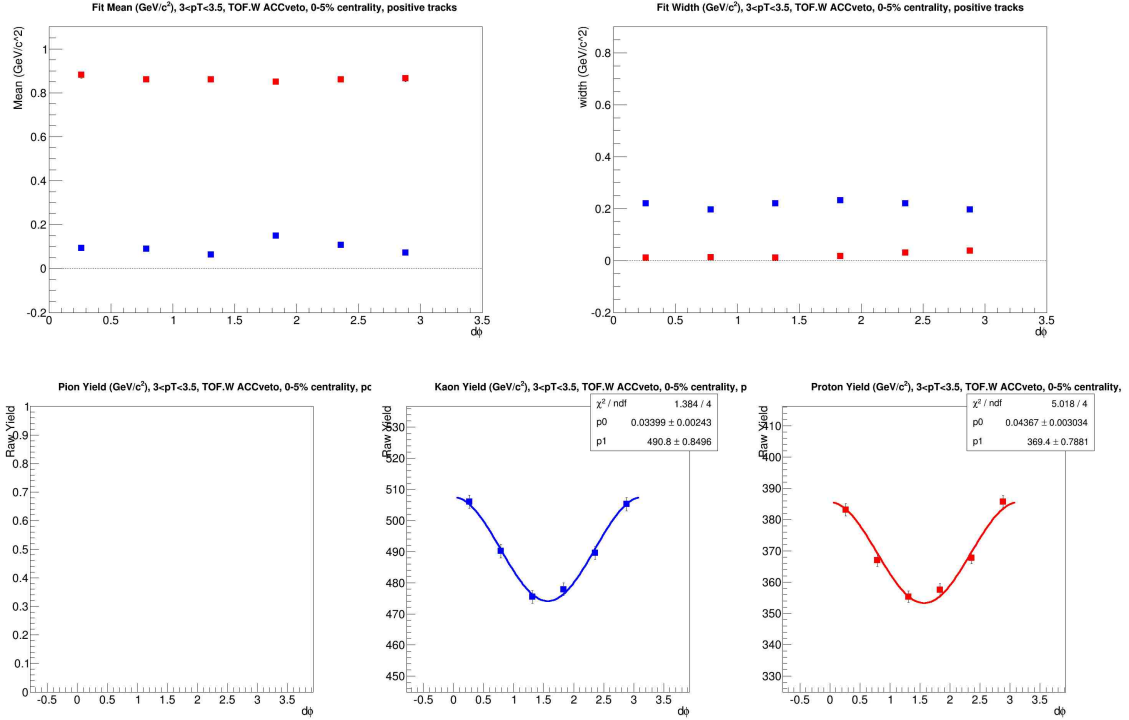
(a) $N_{p.e.}$ vs m^2



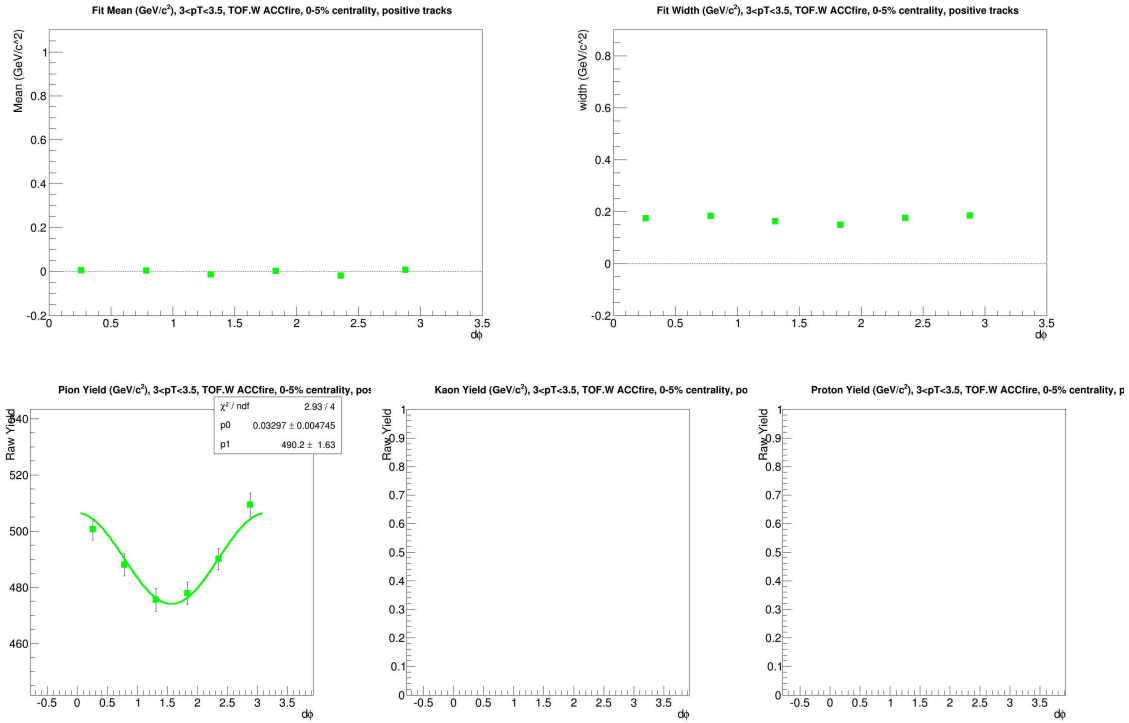
(b) m^2 for ACC vetoed tracks



(c) m^2 for ACC fired tracks

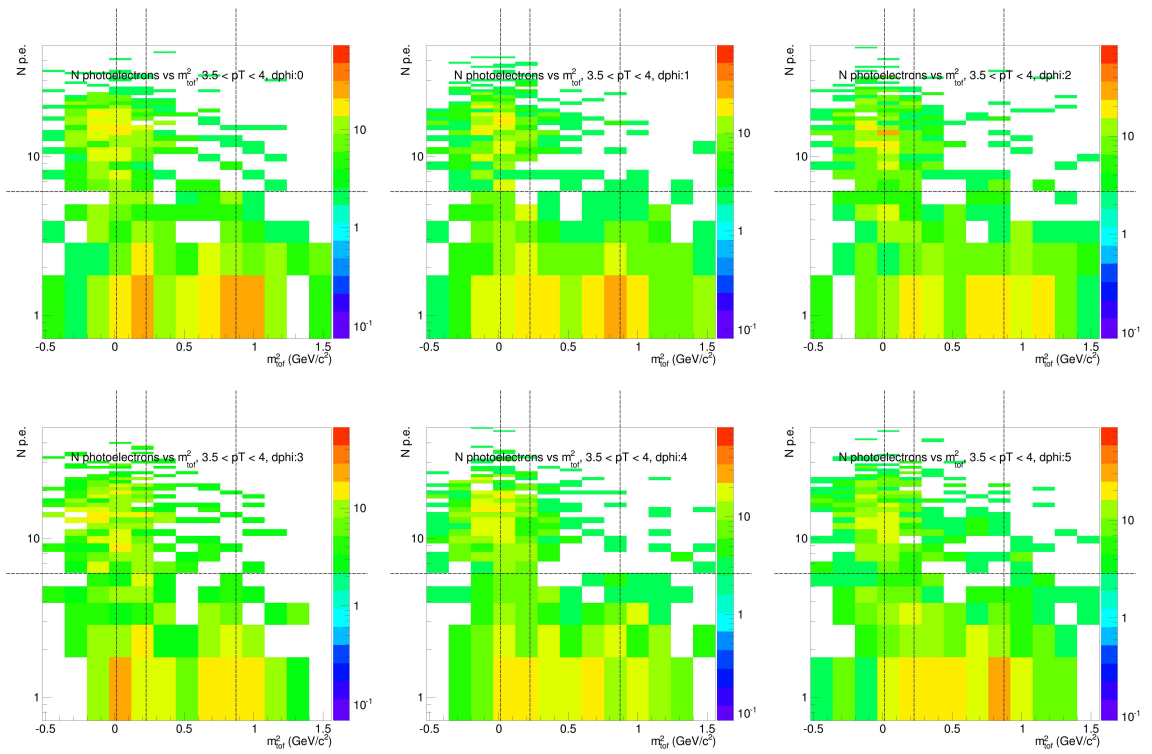


(d) PID parameters and Yields for ACC vetoed tracks

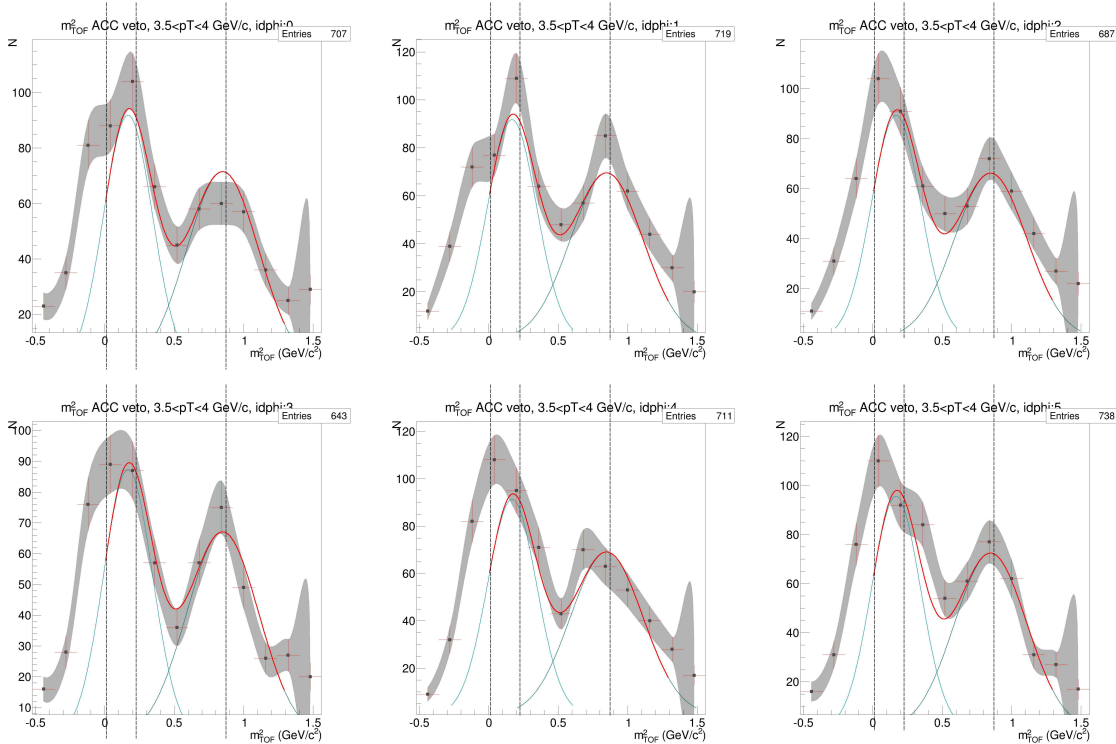


(e) PID parameters and Yields for ACC fired tracks

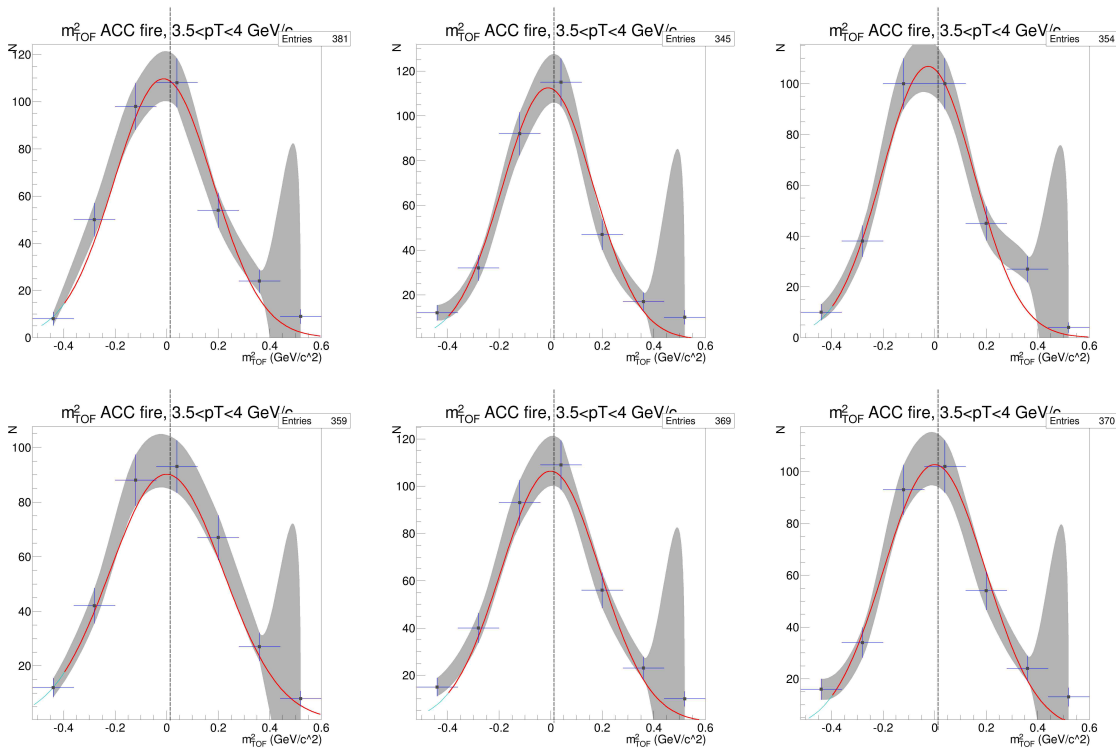
Figure C.28: ACC $N_{p.e.}$ vs m_2 , PID fits, and Yield vs $d\phi$ for $p_T=3.0-3.5$ GeV/c , TOF.W, positive particles



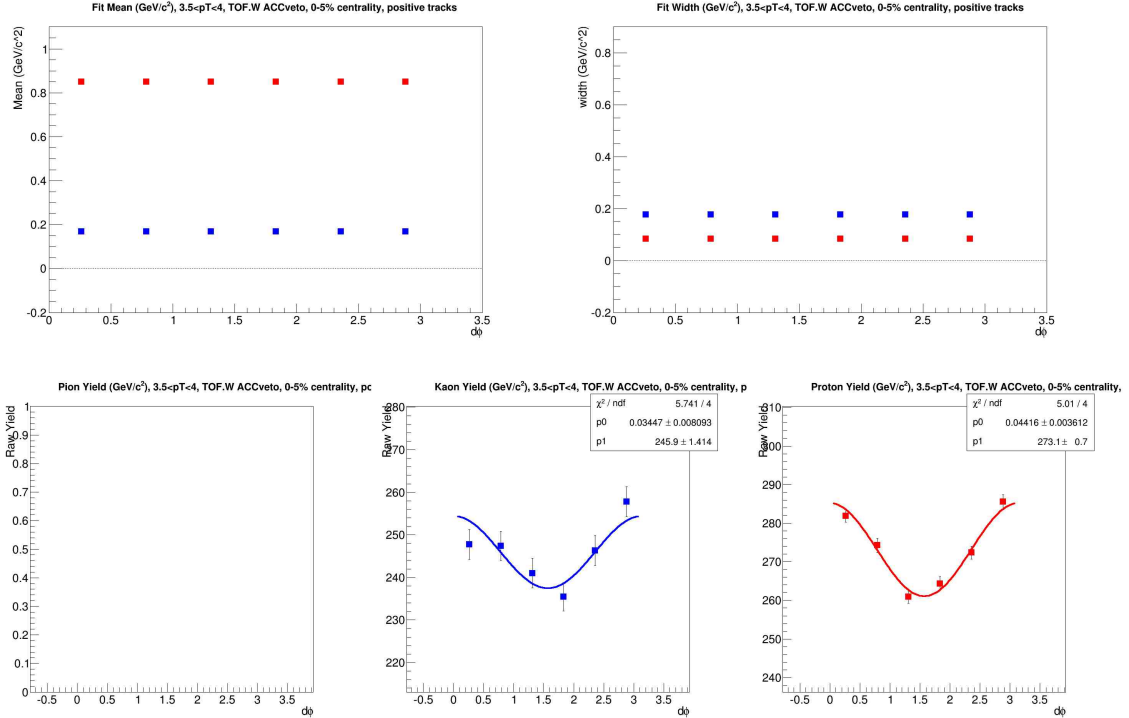
(a) $N_{p.e.}$ vs m^2



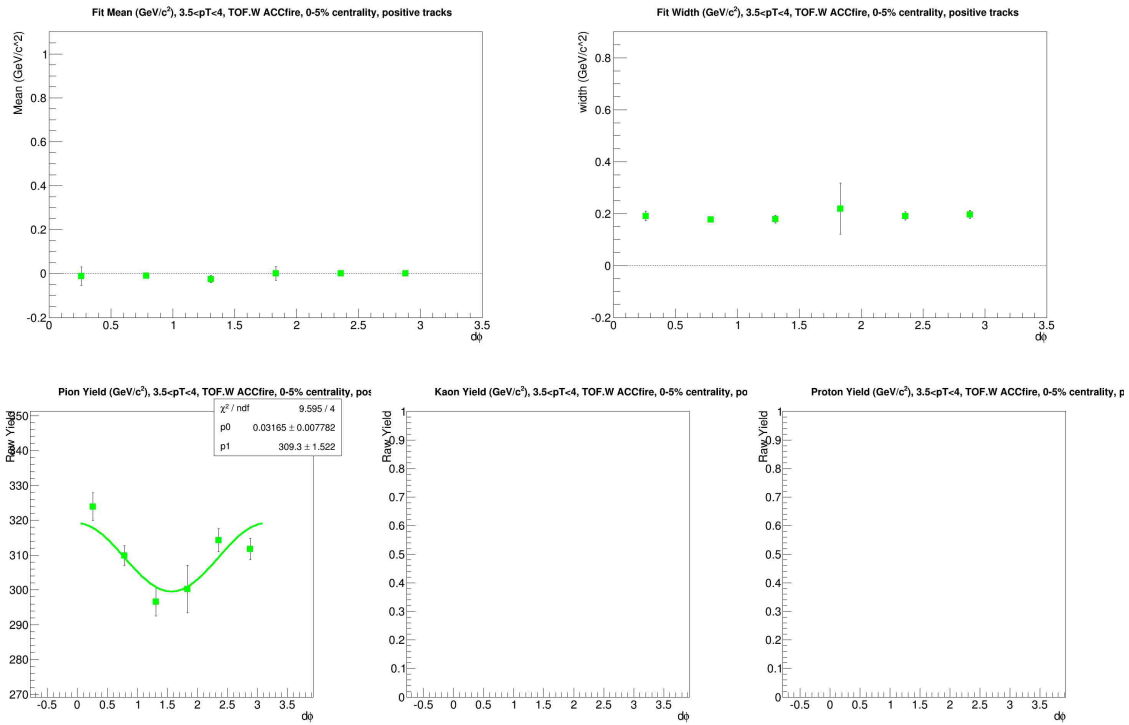
(b) m^2 for ACC vetoed tracks



(c) m^2 for ACC fired tracks

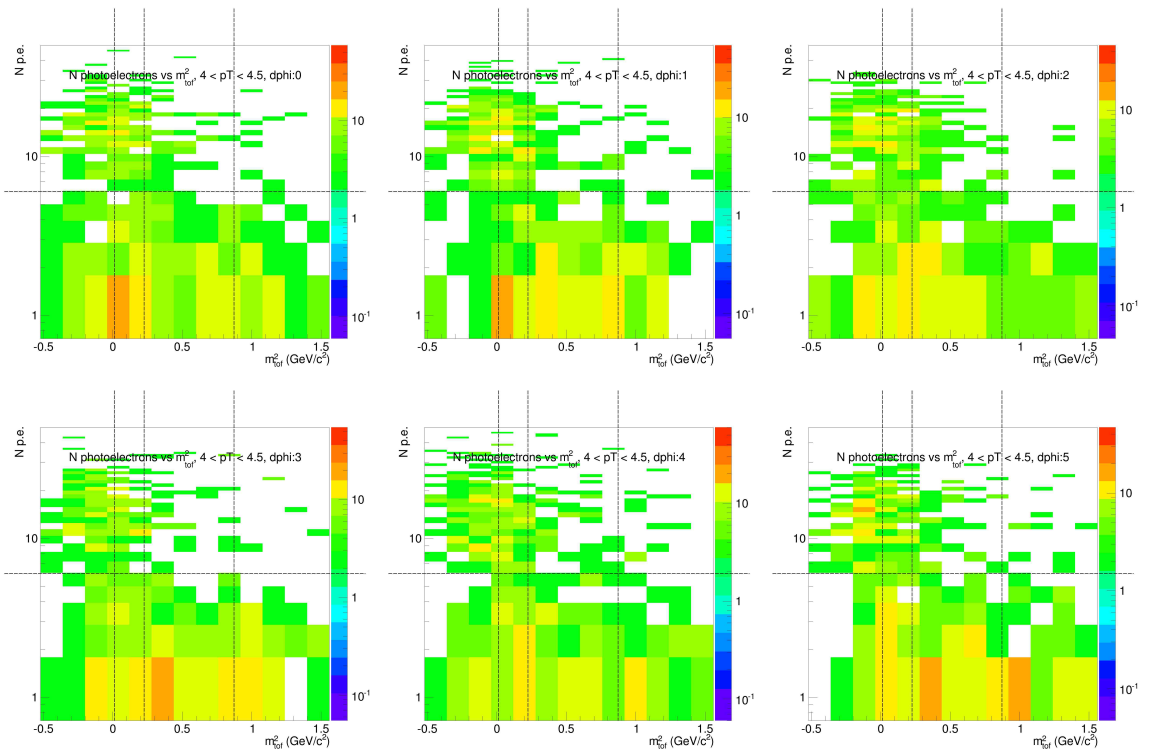


(d) PID parameters and Yields for ACC vetoed tracks

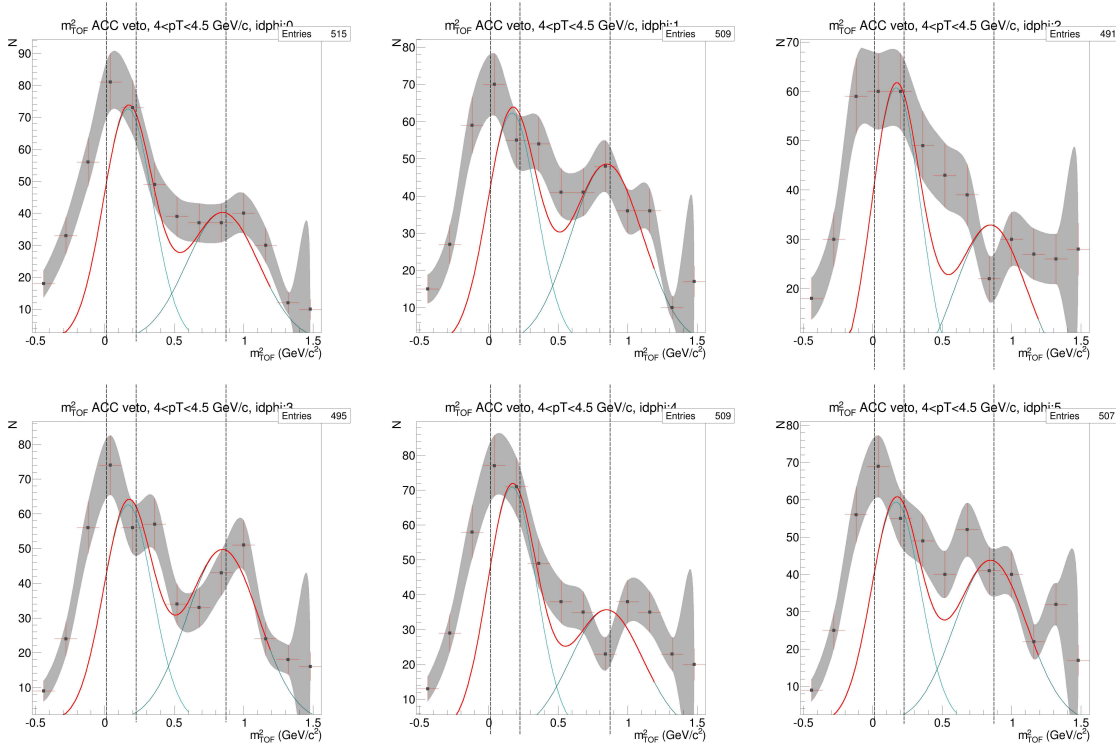


(e) PID parameters and Yields for ACC fired tracks

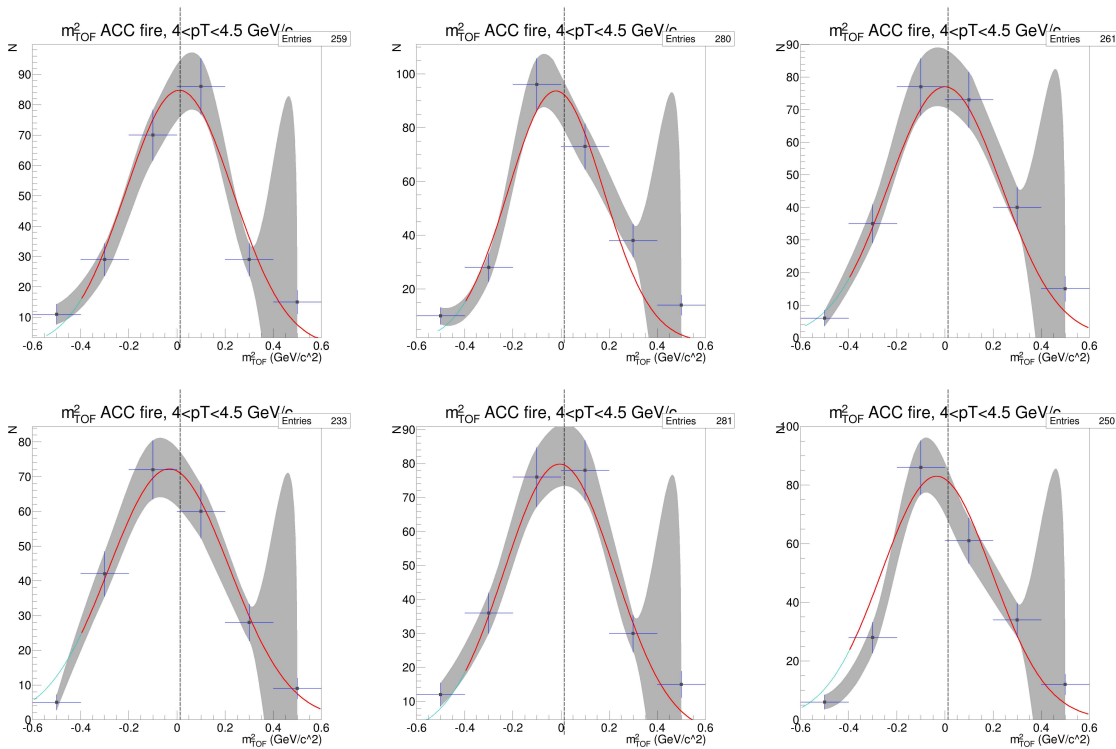
Figure C.29: ACC N_{p.e.} vs m_2 , PID fits, and Yield vs $d\phi$ for $p_T=3.5-4.0$ GeV/c, TOF.W, positive particles



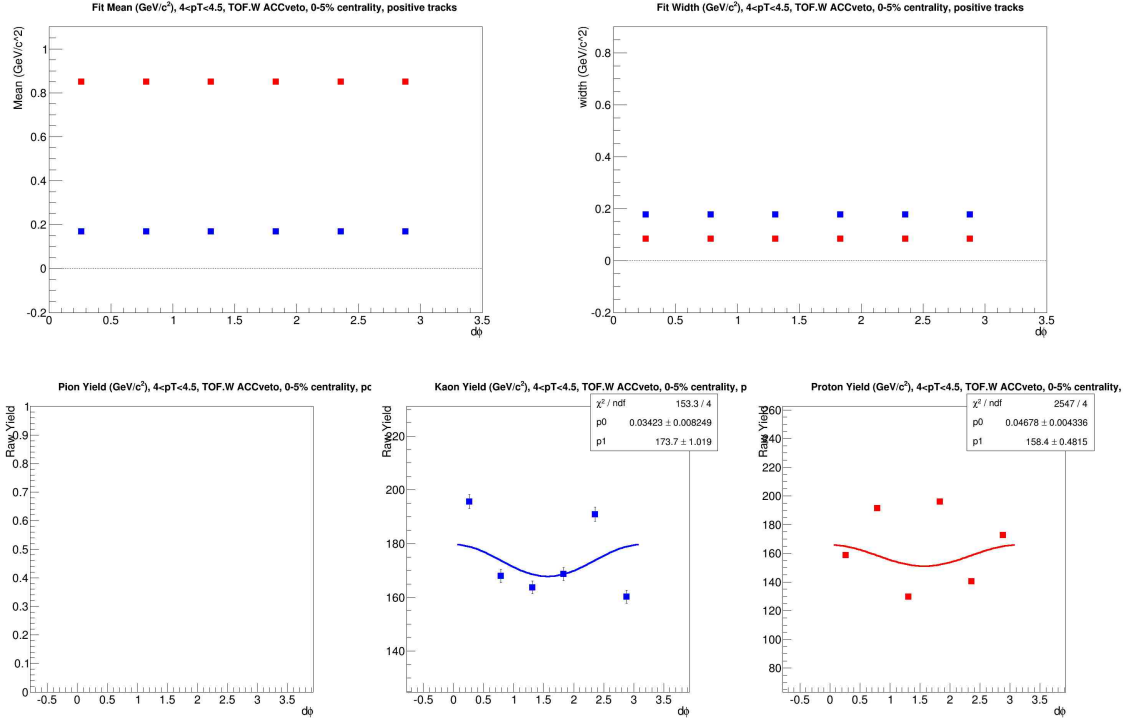
(a) $N_{p.e.}$ vs m^2



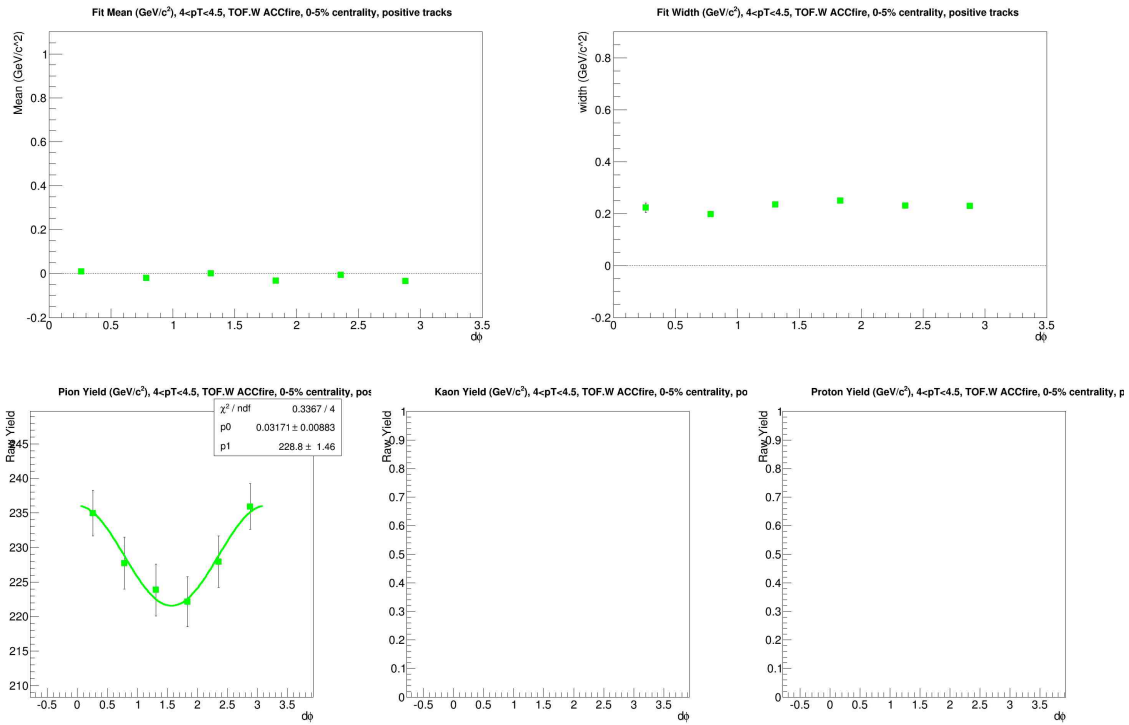
(b) m^2 for ACC vetoed tracks



(c) m^2 for ACC fired tracks



(d) PID parameters and Yields for ACC vetoed tracks



(e) PID parameters and Yields for ACC fired tracks

Figure C.30: ACC N_{p.e.} vs m₂, P_TD³fits, and Yield vs dφ for p_T=4.0-4.5 GeV/c, TOF.W, positive particles

Bibliography

- [1] David J. Gross and Frank Wilczek. Asymptotically free gauge theories. i. *Phys. Rev. D*, 8:3633–3652, Nov 1973.
- [2] H. David Politzer. Reliable perturbative results for strong interactions? *Phys. Rev. Lett.*, 30:1346–1349, Jun 1973.
- [3] John C. Collins and M. J. Perry. Superdense Matter: Neutrons Or Asymptotically Free Quarks? *Phys. Rev. Lett.*, 34:1353, 1975.
- [4] Edward V. Shuryak. Quantum Chromodynamics and the Theory of Superdense Matter. *Phys. Rept.*, 61:71–158, 1980.
- [5] R. J. Fries, J. I. Kapusta, and Y. Li. Near-fields and initial energy density in the color glass condensate model. 2006.
- [6] Judy Goldhaber. Bevalac had 40-year record of historic discoveries. *Berkeley Lab Science Articles Archive*, October 1992.
- [7] ARTHUR L. ROBINSON. Nuclear squeeze at lawrence berkeley lab. *Science*, 224(4651):857–858, 1984.
- [8] H. A. Gustafsson, H. H. Gutbrod, B. Kolb, H. Löhner, B. Ludewigt, A. M. Poskanzer, T. Renner, H. Riedesel, H. G. Ritter, A. Warwick, F. Weik, and H. Wieman. Collective flow observed in relativistic nuclear collisions. *Phys. Rev. Lett.*, 52:1590–1593, Apr 1984.
- [9] F. Wojciech. *Phenomenology of Ultra-relativistic Heavy-ion Collisions*. World Scientific, 2010.
- [10] Jean Barrette. Anisotropic azimuthal distributions of identified particles in Au + Au collisions at 11.5/A-GeV/c. *Nucl. Phys.*, A661:329–332, 1999.
- [11] T. Abbott, Y. Akiba, D. Alburger, D. Beavis, R. R. Betts, L. Birstein, M. A. Bloomer, P. D. Bond, C. Chasman, Y. Y. Chu, B. A. Cole, J. B. Costales, H. J. Crawford, J. B. Cumming, R. Debbe, E. Duek, J. Engelage, S. Y. Fung, L. Grodzins, S. Gushue, H. Hamagaki, O. Hansen, S. Hayashi, S. Homma, H. Z. Huang, Y. Ikeda, S. Katcoff, S. Kaufman, K. Kimura, K. Kitamura, K. Kurita, R. J. Ledoux, M. J. Levine, Y. Mi-ake, R. J. Morse, S. Nagamiya, J. Olness, C. G. Parsons, L. P. Remsberg, M. Sarabura,

- A. Shor, P. Stankus, S. G. Steadman, G. S. F. Stephanos, T. Sugitate, M. J. Tannenbaum, M. Torikoshi, J. H. van Dijk, F. Videbaek, M. Vient, P. Vincent, E. Vulgaris, V. Vutsadakis, W. A. Watson, H. E. Wegner, D. S. Woodruff, Y. D. Wu, and W. A. Zajc. Kaon and pion production in central si+au collisions at 14.6 A gev/ c . *Phys. Rev. Lett.*, 64:847–850, Feb 1990.
- [12] C. Hohne. Strangeness production in nuclear collisions: Recent results from experiment NA49. *Nucl. Phys.*, A661:485–488, 1999.
- [13] M. C. Abreu et al. Evidence for deconfinement of quarks and gluons from the J/ψ suppression pattern measured in Pb + Pb collisions at the CERN SPS. *Phys. Lett.*, B477:28–36, 2000.
- [14] Ulrich W. Heinz and Barbara V. Jacak. Two particle correlations in relativistic heavy ion collisions. *Ann. Rev. Nucl. Part. Sci.*, 49:529–579, 1999.
- [15] Peter Braun-Munzinger and Johanna Stachel. Dynamics of ultrarelativistic nuclear collisions with heavy beams: An Experimental overview. *Nucl. Phys.*, A638:3–18, 1998.
- [16] J. W. Cronin, H. J. Frisch, M. J. Shochet, J. P. Boymond, P. A. Piroué, and R. L. Sumner. Production of hadrons at large transverse momentum at 200, 300, and 400 gev. *Phys. Rev. D*, 11:3105–3123, Jun 1975.
- [17] J. H. Kühn. Nucleon-number dependence of large-transverse-momentum reactions and multiple scattering. *Phys. Rev. D*, 13:2948–2953, Jun 1976.
- [18] D. M. Alde, H. W. Baer, T. A. Carey, G. T. Garvey, A. Klein, C. Lee, M. J. Leitch, J. W. Lillberg, P. L. McGaughey, C. S. Mishra, J. M. Moss, J. C. Peng, C. N. Brown, W. E. Cooper, Y. B. Hsiung, M. R. Adams, R. Guo, D. M. Kaplan, R. L. McCarthy, G. Danner, M. J. Wang, M. L. Barlett, and G. W. Hoffmann. Nuclear dependence of the production of Υ resonances at 800 gev. *Phys. Rev. Lett.*, 66:2285–2288, May 1991.
- [19] Flip Tanedo. When feynman diagrams fail, 2010.
- [20] Flip Tanedo. When youre a jet, youre a jet all the way, 2011.
- [21] M. D. Corcoran et al. Evidence for multiple scattering of high-energy partons in nuclei. *Phys. Lett.*, B259:209–215, 1991.
- [22] T. Fields and M. D. Corcoran. Nuclear rescattering effects in massive dihadron production. *Phys. Rev. Lett.*, 70:143–145, Jan 1993.
- [23] S. S. Adler et al. Elliptic flow of identified hadrons in Au+Au collisions at $s(NN)^{**}(1/2) = 200\text{-GeV}$. *Phys. Rev. Lett.*, 91:182301, 2003.

- [24] B. I. Abelev, M. M. Aggarwal, Z. Ahammed, B. D. Anderson, M. Anderson, D. Arkhipkin, G. S. Averichev, Y. Bai, J. Balewski, O. Barannikova, L. S. Barnby, J. Baudot, S. Bekele, V. V. Belaga, A. Bellingeri-Laurikainen, R. Bellwied, F. Benedosso, S. Bhardwaj, A. Bhasin, A. K. Bhati, H. Bichsel, J. Bielcik, J. Bielcikova, L. C. Bland, S-L. Blyth, B. E. Bonner, M. Botje, J. Bouchet, A. V. Brandin, A. Bravar, T. P. Burton, M. Bystersky, R. V. Cadman, X. Z. Cai, H. Caines, M. Calderón de la Barca Sánchez, J. Castillo, O. Catu, D. Cebra, Z. Chajecki, P. Chaloupka, S. Chattopadhyay, H. F. Chen, J. H. Chen, J. Cheng, M. Cherney, A. Chikanian, W. Christie, J. P. Coffin, T. M. Cormier, M. R. Cosentino, J. G. Cramer, H. J. Crawford, D. Das, S. Das, S. Dash, M. Daugherty, M. M. de Moura, T. G. Dedovich, M. DePhillips, A. A. Derevschikov, L. Didenko, T. Dietel, P. Djawotho, S. M. Dogra, W. J. Dong, X. Dong, J. E. Draper, F. Du, V. B. Dunin, J. C. Dunlop, M. R. Dutta Mazumdar, V. Eckardt, W. R. Edwards, L. G. Efimov, V. Emelianov, J. Engelage, G. Eppley, B. Erazmus, M. Estienne, P. Fachini, R. Fatemi, J. Fedorisin, P. Filip, E. Finch, V. Fine, Y. Fisyak, J. Fu, C. A. Gagliardi, L. Gaillard, M. S. Ganti, V. Ghazikhanian, P. Ghosh, J. E. Gonzalez, Y. G. Gorbunov, H. Gos, O. Grebenyuk, D. Grosnick, S. M. Guertin, K. S. F. F. Guimaraes, N. Gupta, T. D. Gutierrez, B. Haag, T. J. Hallman, A. Hamed, J. W. Harris, W. He, M. Heinz, T. W. Henry, S. Hepplemnann, B. Hippolyte, A. Hirsch, E. Hjort, A. M. Hoffman, G. W. Hoffmann, M. J. Horner, H. Z. Huang, S. L. Huang, E. W. Hughes, T. J. Humanic, G. Igo, P. Jacobs, W. W. Jacobs, P. Jakl, F. Jia, H. Jiang, P. G. Jones, E. G. Judd, S. Kabana, K. Kang, J. Kapitan, M. Kaplan, D. Keane, A. Kechechyan, V. Yu. Khodyrev, B. C. Kim, J. Kiryluk, A. Kisiel, E. M. Kislov, S. R. Klein, A. Kocoloski, D. D. Koetke, T. Kollegger, M. Kopytine, L. Kotchenda, V. Kouchpil, K. L. Kowalik, M. Kramer, P. Kravtsov, V. I. Kravtsov, K. Krueger, C. Kuhn, A. I. Kulikov, A. Kumar, A. A. Kuznetsov, M. A. C. Lamont, J. M. Landgraf, S. Lange, S. LaPointe, F. Laue, J. Lauret, A. Lebedev, R. Lednicky, C-H. Lee, S. Lehocka, M. J. LeVine, C. Li, Q. Li, Y. Li, G. Lin, X. Lin, S. J. Lindenbaum, M. A. Lisa, F. Liu, H. Liu, J. Liu, L. Liu, Z. Liu, T. Ljubicic, W. J. Llope, H. Long, R. S. Longacre, W. A. Love, Y. Lu, T. Ludlam, D. Lynn, G. L. Ma, J. G. Ma, Y. G. Ma, D. Magestro, D. P. Mahapatra, R. Majka, L. K. Mangotra, R. Manweiler, S. Margetis, C. Markert, L. Martin, H. S. Matis, Yu. A. Matulenko, C. J. McClain, T. S. McShane, Yu. Melnick, A. Meschanin, J. Millane, M. L. Miller, N. G. Minaev, S. Mioduszewski, C. Mironov, A. Mischke, D. K. Mishra, J. Mitchell, B. Mohanty, L. Molnar, C. F. Moore, D. A. Morozov, M. G. Munhoz, B. K. Nandi, C. Natrass, T. K. Nayak, J. M. Nelson, N. S. Nepali, P. K. Netrakanti, L. V. Nogach, S. B. Nurushev, G. Odyniec, A. Ogawa, V. Okorokov, M. Oldenburg, D. Olson, M. Pachr, S. K. Pal, Y. Paneratsev, S. Y. Panitkin, A. I. Pavlinov, T. Pawlak, T. Peitzmann, V. Perevoztchikov, C. Perkins, W. Peryt, S. C. Phatak, R. Picha, M. Planinic, J. Pluta, N. Poljak, N. Porile, J. Porter, A. M. Poskanzer, M. Potekhin, E. Potrebenikova, B. V. K. S. Potukuchi, D. Prindle, C. Pruneau, J. Putschke, G. Rakness, R. Raniwala, S. Raniwala, R. L. Ray, S. V. Razin, J. Reinnarth, D. Relyea, A. Ridiger, H. G. Ritter, J. B. Roberts, O. V. Rogachevskiy, J. L. Romero, A. Rose, C. Roy, L. Ruan, M. J. Russcher, R. Sahoo,

- T. Sakuma, S. Salur, J. Sandweiss, M. Sarsour, P. S. Sazhin, J. Schambach, R. P. Scharenberg, N. Schmitz, J. Seger, I. Selyuzhenkov, P. Seyboth, A. Shabetai, E. Shahaliev, M. Shao, M. Sharma, W. Q. Shen, S. S. Shimanskiy, E. P. Sichtermann, F. Simon, R. N. Singaraju, N. Smirnov, R. Snellings, G. Sood, P. Sorensen, J. Sowinski, J. Speltz, H. M. Spinka, B. Srivastava, A. Stadnik, T. D. S. Stanislaus, R. Stock, A. Stolpovsky, M. Strikhanov, B. Stringfellow, A. A. P. Suaide, N. L. Subba, E. Sugarbaker, M. Sumbera, Z. Sun, B. Surrow, M. Swanger, T. J. M. Symons, A. Szanto de Toledo, A. Tai, J. Takahashi, A. H. Tang, T. Tarnowsky, D. Thein, J. H. Thomas, A. R. Timmins, S. Timoshenko, M. Tokarev, T. A. Trainor, S. Trentalange, R. E. Tribble, O. D. Tsai, J. Ulery, T. Ullrich, D. G. Underwood, G. Van Buren, N. van der Kolk, M. van Leeuwen, A. M. Vander Molen, R. Varma, I. M. Vasilevski, A. N. Vasiliev, R. Vernet, S. E. Vigdor, Y. P. Viyogi, S. Vokal, S. A. Voloshin, W. T. Waggoner, F. Wang, G. Wang, J. S. Wang, X. L. Wang, Y. Wang, J. W. Watson, J. C. Webb, G. D. Westfall, A. Wetzler, C. Whitten, H. Wieman, S. W. Wissink, R. Witt, J. Wood, J. Wu, N. Xu, Q. H. Xu, Z. Xu, P. Yepes, I-K. Yoo, V. I. Yurevich, W. Zhan, H. Zhang, W. M. Zhang, Y. Zhang, Z. P. Zhang, Y. Zhao, C. Zhong, R. Zoukarneev, Y. Zoukarneeva, A. N. Zubarev, and J. X. Zuo. Identified baryon and meson distributions at large transverse momenta from Au + Au collisions at $\sqrt{s_{NN}} = 200$ GeV. *Phys. Rev. Lett.*, 97:152301, Oct 2006.
- [25] Matthew Luzum and Paul Romatschke. Conformal relativistic viscous hydrodynamics: Applications to rhic results at $\sqrt{s_{NN}} = 200$ gev. *Phys. Rev. C*, 78:034915, Sep 2008.
- [26] Julia Velkovska. Lecture 12: Hydrodynamics in heavy ion collisons, elliptic flow.
- [27] Rudolph C. Hwa and C. B. Yang. Recombination of shower partons at high p_T in heavy-ion collisions. *Phys. Rev. C*, 70:024905, Aug 2004.
- [28] Vardan Khachatryan et al. Evidence for Collective Multiparticle Correlations in p-Pb Collisions. *Phys. Rev. Lett.*, 115(1):012301, 2015.
- [29] A. Adare, S. Afanasiev, C. Aidala, N. N. Ajitanand, Y. Akiba, H. Al-Bataineh, J. Alexander, A. Angerami, K. Aoki, N. Apadula, Y. Aramaki, E. T. Atomssa, R. Averbeck, T. C. Awes, B. Azmoun, V. Babintsev, M. Bai, G. Baksay, L. Baksay, K. N. Barish, B. Bassalleck, A. T. Basye, S. Bathe, V. Baublis, C. Baumann, A. Bazilevsky, S. Belikov, R. Belmont, R. Bennett, A. Berdnikov, Y. Berdnikov, J. H. Bhom, A. A. Bickley, D. S. Blau, J. S. Bok, K. Boyle, M. L. Brooks, H. Buesching, V. Bumazhnov, G. Bunce, S. Butsyk, C. M. Camacho, S. Campbell, A. Caringi, C.-H. Chen, C. Y. Chi, M. Chiu, I. J. Choi, J. B. Choi, R. K. Choudhury, P. Christiansen, T. Chujo, P. Chung, O. Chvala, V. Cianciolo, Z. Citron, B. A. Cole, Z. Conesa del Valle, M. Connors, P. Constantin, M. Csanad, T. Csorgo, T. Dahms, S. Dairaku, I. Danchev, K. Das, A. Datta, G. David, M. K. Dayananda, A. Denisov, A. Deshpande, E. J. Desmond, K. V. Dharmawardane, O. Dietzsch, A. Dion, M. Donadelli, O. Drapier, A. Drees, K. A. Drees, J. M. Durham, A. Durum, D. Dutta, L. D’Orazio, S. Edwards, Y. V.

Efremenko, F. Ellinghaus, T. Engelmore, A. Enokizono, H. En'yo, S. Esumi, B. Fadem, D. E. Fields, M. Finger, M. Finger, F. Fleuret, S. L. Fokin, Z. Fraenkel, J. E. Frantz, A. Franz, A. D. Frawley, K. Fujiwara, Y. Fukao, T. Fusayasu, I. Garishvili, A. Glenn, H. Gong, M. Gonin, Y. Goto, R. Granier de Cassagnac, N. Grau, S. V. Greene, G. Grim, M. Grosse Perdekamp, T. Gunji, H.-Å. Gustafsson, J. S. Haggerty, K. I. Hahn, H. Hamagaki, J. Hamblen, R. Han, J. Hanks, E. P. Hartouni, E. Haslum, R. Hayano, X. He, M. Heffner, T. K. Hemmick, T. Hester, J. C. Hill, M. Hohlmann, W. Holzmann, K. Homma, B. Hong, T. Horaguchi, D. Hornback, S. Huang, T. Ichihara, R. Ichimiya, J. Ide, Y. Ikeda, K. Imai, M. Inaba, D. Isenhower, M. Ishihara, T. Isobe, M. Issah, A. Isupov, D. Ivanischev, Y. Iwanaga, B. V. Jacak, J. Jia, X. Jiang, J. Jin, B. M. Johnson, T. Jones, K. S. Joo, D. Jouan, D. S. Jumper, F. Kajihara, S. Kametani, N. Kamihara, J. Kamin, J. H. Kang, J. Kapustinsky, K. Karatsu, M. Kasai, D. Kawall, M. Kawashima, A. V. Kazantsev, T. Kempel, A. Khanzadeev, K. M. Kijima, J. Kikuchi, A. Kim, B. I. Kim, D. H. Kim, D. J. Kim, E. Kim, E.-J. Kim, S. H. Kim, Y.-J. Kim, E. Kinney, K. Kiriluk, Á. Kiss, E. Kistenev, D. Kleinjan, L. Kochenda, B. Komkov, M. Konno, J. Koster, D. Kotchetkov, A. Kozlov, A. Král, A. Kravitz, G. J. Kunde, K. Kurita, M. Kurosawa, Y. Kwon, G. S. Kyle, R. Lacey, Y. S. Lai, J. G. Lajoie, A. Lebedev, D. M. Lee, J. Lee, K. Lee, K. B. Lee, K. S. Lee, M. J. Leitch, M. A. L. Leite, E. Leitner, B. Lenzi, X. Li, P. Lichtenwalner, P. Liebing, L. A. Linden Levy, T. Liška, A. Litvinenko, H. Liu, M. X. Liu, B. Love, R. Luechtenborg, D. Lynch, C. F. Maguire, Y. I. Makdisi, A. Malakhov, M. D. Malik, V. I. Manko, E. Mannel, Y. Mao, H. Masui, F. Matathias, M. McCumber, P. L. McGaughey, D. McGlinchey, N. Means, B. Meredith, Y. Miake, T. Mibe, A. C. Mignerey, P. Mikeš, K. Miki, A. Milov, M. Mishra, J. T. Mitchell, A. K. Mohanty, H. J. Moon, Y. Morino, A. Morreale, D. P. Morrison, T. V. Moukhanova, T. Murakami, J. Murata, S. Nagamiya, J. L. Nagle, M. Naglis, M. I. Nagy, I. Nakagawa, Y. Nakamiya, K. R. Nakamura, T. Nakamura, K. Nakano, S. Nam, J. Newby, M. Nguyen, M. Nihashi, R. Nouicer, A. S. Nyanin, C. Oakley, E. O'Brien, S. X. Oda, C. A. Ogilvie, M. Oka, K. Okada, Y. Onuki, A. Oskarsson, M. Ouchida, K. Ozawa, R. Pak, V. Pantuev, V. Papavassiliou, I. H. Park, J. Park, S. K. Park, W. J. Park, S. F. Pate, H. Pei, J.-C. Peng, H. Pereira, V. Peresedov, D. Yu. Peressounko, R. Petti, C. Pinkenburg, R. P. Pisani, M. Proissl, M. L. Purschke, A. K. Purwar, H. Qu, J. Rak, A. Rakotozafindrabe, I. Ravinovich, K. F. Read, S. Rembeczki, K. Reygers, V. Riabov, Y. Riabov, E. Richardson, D. Roach, G. Roche, S. D. Rolnick, M. Rosati, C. A. Rosen, S. S. E. Rosendahl, P. Rosnet, P. Rukoyatkin, P. Ružička, B. Sahlmueller, N. Saito, T. Sakaguchi, K. Sakashita, V. Samsonov, S. Sano, T. Sato, S. Sawada, K. Sedgwick, J. Seele, R. Seidl, A. Yu. Semenov, R. Seto, D. Sharma, I. Shein, T.-A. Shibata, K. Shigaki, M. Shimomura, K. Shoji, P. Shukla, A. Sickles, C. L. Silva, D. Silvermyr, C. Silvestre, K. S. Sim, B. K. Singh, C. P. Singh, V. Singh, M. Slunečka, R. A. Soltz, W. E. Sondheim, S. P. Sorensen, I. V. Sourikova, N. A. Sparks, P. W. Stankus, E. Stenlund, S. P. Stoll, T. Sugitate, A. Sukhanov, J. Sziklai, E. M. Tagagui, A. Taketani, R. Tanabe, Y. Tanaka, S. Taneja, K. Tanida, M. J. Tannenbaum, S. Tarafdar, A. Taranenko, P. Tarján, H. Themann, D. Thomas, T. L. Thomas, M. To-

- gawa, A. Toia, L. Tomášek, H. Torii, R. S. Towell, I. Tserruya, Y. Tsuchimoto, C. Vale, H. Valle, H. W. van Hecke, E. Vazquez-Zambrano, A. Veicht, J. Velkovska, R. Vértesi, A. A. Vinogradov, M. Virius, V. Spectra and ratios of identified particles in au+au and $d+au$ collisions at $\sqrt{s_{NN}} = 200$ gev. *Phys. Rev. C*, 88:024906, Aug 2013.
- [30] Rudolph C. Hwa and C. B. Yang. Final-state interaction as the origin of the cronin effect. *Phys. Rev. Lett.*, 93:082302, Aug 2004.
- [31] Michael L. Miller, Klaus Reygers, Stephen J. Sanders, and Peter Steinberg. Glauber modeling in high energy nuclear collisions. *Ann. Rev. Nucl. Part. Sci.*, 57:205–243, 2007.
- [32] Jamie Nagle. The physics of relativistic heavy ion collisions. *18th National Nuclear Physics Summer School*, July 2006.
- [33] A. De Rújula, S. L. Glashow, H. D. Politzer, S. B. Treiman, F. Wilczek, and A. Zee. Possible non-regge behavior of electroproduction structure functions. *Phys. Rev. D*, 10:1649–1652, Sep 1974.
- [34] H. Abramowicz, I. Abt, L. Adamczyk, M. Adamus, V. Andreev, S. Antonelli, B. Antunović, V. Aushev, Y. Aushev, A. Baghdasaryan, K. Begzsuren, O. Behnke, A. Behrendt Dubak, U. Behrens, A. Belousov, P. Belov, A. Bertolin, I. Bloch, E. G. Boos, K. Borras, V. Boudry, G. Brandt, V. Brisson, D. Britzger, I. Brock, N. H. Brook, R. Brugnera, A. Bruni, A. Buniatyan, P. J. Bussey, A. Bylinkin, L. Bystritskaya, A. Caldwell, A. J. Campbell, K. B. Cantun Avila, M. Capua, C. D. Catterall, F. Ceccopieri, K. Cerny, V. Chekelian, J. Chwastowski, J. Ciborowski, R. Ciesielski, J. G. Contreras, A. M. Cooper-Sarkar, M. Corradi, F. Corriveau, J. Cvach, J. B. Dainton, K. Daum, R. K. Dementiev, R. C. E. Devenish, C. Diaconu, M. Dobre, V. Dodonov, G. Dolinska, S. Dusini, G. Eckerlin, S. Egli, E. Elsen, L. Favart, A. Fedotov, J. Feltesse, J. Ferencei, J. Figiel, M. Fleischer, A. Fomenko, B. Foster, E. Gabathuler, G. Gach, E. Gallo, A. Garfagnini, J. Gayler, A. Geiser, S. Ghazaryan, A. Gzhko, L. K. Gladilin, L. Goerlich, N. Gogitidze, Yu. A. Golubkov, M. Gouzevitch, C. Grab, A. Grebenyuk, J. Grebenyuk, T. Greenshaw, I. Gregor, G. Grindhammer, G. Grzelak, O. Gueta, M. Guzik, C. Gwenlan, D. Haidt, W. Hain, R. C. W. Henderson, P. Henkenjohann, J. Hladk, D. Hochman, D. Hoffmann, R. Hori, R. Horisberger, T. Hreus, F. Huber, Z. A. Ibrahim, Y. Iga, M. Ishitsuka, A. Iudin, M. Jacquet, X. Janssen, F. Januschek, N. Z. Jomhari, H. Jung, I. Kadenko, S. Kananov, M. Kapichine, U. Karshon, J. Katzy, M. Kaur, P. Kaur, C. Kiesling, D. Kisielewska, R. Klanner, M. Klein, U. Klein, C. Kleinwort, R. Kogler, N. Kondrashova, O. Kononenko, Ie. Korol, I. A. Korzhavina, P. Kostka, A. Kotański, U. Kötz, N. Kovalchuk, H. Kowalski, J. Kretzschmar, D. Krücker, K. Krüger, B. Krupa, O. Kuprash, M. Kuze, M. P. J. Landon, W. Lange, P. Laycock, A. Lebedev, B. B. Levchenko, S. Levonian, A. Levy, V. Libov, S. Limentani, K. Lipka, M. Lisovyi, B. List, J. List, E. Lobodzinska, B. Lobodzinski, B. Löhr,

E. Lohrmann, A. Longhin, D. Lontkovskyi, O. Yu. Lukina, I. Makarenko, E. Malinovski, J. Malka, H.-U. Martyn, S. J. Maxfield, A. Mehta, S. Mergelmeyer, A. B. Meyer, H. Meyer, J. Meyer, S. Mikocki, F. Mohamad Idris, A. Morozov, N. Muhammad Nasir, K. Müller, V. Myronenko, K. Nagano, Th. Naumann, P. R. Newman, C. Niebuhr, A. Nikiforov, T. Nobe, D. Notz, G. Nowak, R. J. Nowak, J. E. Olsson, Yu. Onishchuk, D. Ozerov, P. Pahl, C. Pascaud, G. D. Patel, E. Paul, E. Perez, W. Perlański, A. Petrukhin, I. Picuric, H. Pirumov, D. Pitzl, B. Pokorny, N. S. Pokrovskiy, R. Polifka, M. Przybycień, V. Radescu, N. Raicevic, T. Ravdandorj, P. Reimer, E. Rizvi, P. Robmann, P. Roloff, R. Roosen, A. Rostovtsev, M. Rotaru, I. Rubinsky, S. Rusakov, M. Ruspa, D. Šálek, D. P. C. Sankey, M. Sauter, E. Sauvan, D. H. Saxon, M. Schioppa, W. B. Schmidke, S. Schmitt, U. Schneekloth, L. Schoeffel, A. Schöning, T. Schörner-Sadenius, F. Sefkow, L. M. Shcheglova, R. Shevchenko, O. Shkola, S. Shushkevich, Yu. Shyrma, I. Singh, I. O. Skillicorn, W. Słomiński, A. Solano, Y. Soloviev, P. Sopicki, D. South, V. Spaskov, A. Specka, L. Stanco, M. Steder, N. Stefaniuk, B. Stella, A. Stern, P. Stopa, U. Straumann, T. Sykora, J. Sztuk-Dambietz, D. Szuba, J. Szuba, E. Tassi, P. D. Thompson, K. Tokushuku, J. Tomaszewska, D. Traynor, A. Trofymov, P. Truöl, I. Tsakov, B. Tseepeldorj, T. Tsurugai, M. Turcato, O. Turkot, J. Turnau, T. Tymieniecka, A. Valkárová, C. Vallée, P. Van Mechelen, Y. Vazdik, A. Verbytskyi, O. Viazlo, R. Walczak, W. A. T. Wan Abdullah, D. Wegener, K. Wichmann, M. Wing, G. Wolf, E. Wünsch, S. Yamada, Y. Yamazaki, J. Žáček, N. Zakharchuk, A. F. Żarnecki, L. Zawiejski, O. Zenaiev, Z. Zhang, B. O. Zhautykov, N. Zhmak, R. Žlebčík, H. Zohrabyan, F. Zomer, and D. S. Zotkin. Combination of measurements of inclusive deep inelastic $e^\pm p$ scattering cross sections and qcd analysis of hera data. *The European Physical Journal C*, 75(12):1–98, 2015.

- [35] K.A. Olive et al. (Particle Data Group). Data files and plots of cross-sections and related quantities in the 2014 review of particle physics. *Chin. Phys. C*, 38(090001), 2014.
- [36] Kazu Itakura. Introduction to the color glass condensate. October 2012.
- [37] Larry D. McLerran. The Color glass condensate and small x physics: Four lectures. *Lect. Notes Phys.*, 583:291–334, 2002.
- [38] Thomas K Hemmick. A pederstrian’s guide to rhic and its experiments. *CERN-Fermilab HCP Summer School*, June 2011.
- [39] Larry McLerran. A Brief Introduction to the Color Glass Condensate and the Glasma. In *Proceedings, 38th International Symposium on Multiparticle Dynamics (ISMD08): Hamburg, Germany, September 15-20, 2008*, pages 3–18, 2008.
- [40] Hirotsugu Fujii and Kazunori Itakura. Expanding color flux tubes and instabilities. *Nucl. Phys.*, A809:88–109, 2008.

- [41] Hagedorn R. and Rafelski J. Statistical mechanics of quarks and hadrons. page 237, 1981.
- [42] Berndt Muller. Strangeness and the Quark-Gluon Plasma: Thirty Years of Discovery. *Acta Phys. Polon.*, B43:761, 2012.
- [43] Johann Rafelski and Berndt Müller. Strangeness production in the quark-gluon plasma. *Phys. Rev. Lett.*, 48:1066–1069, Apr 1982.
- [44] CAD @ BNL. Rhic accelerators. *BNL website*, July 2016.
- [45] A. Pikin et al. Rhic ebis: basics of design and status of commissioning. *Journal of Instrumentation*, 5(C09003), September 2010.
- [46] J. M. Brennan M. Blaskiewicz and K. Mernick. Three-dimensional stochastic cooling in the relativistic heavy ion collider. *Phys. Rev. Lett.*, 105(094801), August 2010.
- [47] K.F. Read for PHENIX collab. *15th Winter Workshop on Nuclear Dynamics*, Park City, Utah, January 1999.
- [48] Sky Deva Rolnick. *Measurement of Dielectron Continuum in p + p at sqrt(s) = 200 GeV as a Baseline study for Chiral Symmetry Restoration*. PhD thesis, University of California, Riverside, 2015.
- [49] Henner Buesching. The electromagnetic calorimeter. *FOCUS Talk*, February 2003.
- [50] Sergey Butsyk. Phenix drift chamber operation principles. *FOCUS Talk*, January 2003.
- [51] Anders Oskarsson. The pad chambers. *FOCUS Talk*, January 2003.
- [52] Hiroshi Masui. Phenix focus: Time of flight. *FOCUS Talk*, February 2004.
- [53] Lucas Taylor. Resistive plate chambers. *CMS Detectors Web Page*, November 2011.
- [54] A. Akindinov et al. The multigap resistive plate chamber as a time-of-flight detector. *Nucl. Instrum. Meth.*, A456:16–22, 2000.
- [55] Tomoaki Nakamura. Introduction to phenix beam beam counter (bbc). *FOCUS Talk*, December 2002.
- [56] Mickey Chiu. Phenix focus: Zero degree calorimeter. *FOCUS Talk*, December 2003.
- [57] Sebastian White. RHIC/PHENIX hosted group page, 2003.
- [58] Tarun Kanti Ghosh, K. Adcox, S. S. Adler, N. Ajitanand, Y. Akiba, J. Alexander, L. Aphecetche, Y. Arai, S. H. Aronson, R. Averbeck, T. C. Awes, K. N. Barish, P. D. Barnes, J. Barrette, B. Bassalleck, S. Bathe, V. Baublis, A. Bazilevsky, S. Belikov, F. G. Bellaiche, S. T. Belyaev, M. J. Bennett, Y. Berdnikov, S. Botelho, M. L.

Brooks, D. S. Brown, N. Bruner, D. Bucher, H. Buesching, V. Bumazhnov, G. Bunce, J. Burward-Hoy, S. Butsyk, T. A. Carey, P. Chand, J. Chang, W. C. Chang, L. L. Chavez, S. Chernichenko, C. Y. Chi, J. Chiba, M. Chiu, R. K. Choudhury, T. Christ, T. Chujo, M. S. Chung, P. Chung, V. Cianciolo, B. A. Cole, D. G. D'Enterria, G. David, H. Delagrange, A. Denisov, A. Deshpande, E. J. Desmond, O. Dietzsch, B. V. Dinesh, A. Drees, A. Durum, D. Dutta, K. Ebisu, Y. V. Efremenko, K. El Chenawi, H. En'yo, S. Esumi, L. Ewell, T. Ferdousi, D. E. Fields, S. L. Fokin, Z. Fraenkel, A. Franz, A. D. Frawley, S-Y Fung, S. Garpman, T. K. Ghosh, A. Glenn, A. L. Godoi, Y. Goto, S. V. Greene, M. Grosse Perdekamp, S. K. Gupta, W. Guryn, H-Å Gustafsson, J. S. Haggerty, H. Hamagaki, A. G. Hansen, H. Hara, E. P. Hartouni, R. Hayano, N. Hayashi, X. He, T. K. Hemmick, J. Heuser, J. C. Hill, D. S. Ho, K. Homma, B. Hong, A. Hoover, T. Ichihara, K. Imai, M. S. Ippolitov, M. Ishihara, B. V. Jacak, W. Y. Jang, J. Jia, B. M. Johnson, S. C. Johnson, K. S. Joo, S. Kametani, J. H. Kang, M. Kann, S. S. Kapoor, S. Kelly, B. Khachaturov, A. Khanzadeev, J. Kikuchi, D. J. Kim, H. J. Kim, S. Y. Kim, Y. G. Kim, W. W. Kinnison, E. Kistenev, A. Kiyomichi, C. Klein-Boesing, S. Klinksiek, L. Kochenda, D. Kochetkov, V. Kochetkov, D. Koehler, T. Kohama, A. Kozlov, P. J. Kroon, K. Kurita, M. J. Kweon, Y. Kwon, G. S. Kyle, R. Lacey, J. G. Lajoie, J. Lauret, A. Lebedev, D. M. Lee, M. J. Leitch, X. H. Li, Z. Li, D. J. Lim, M. X. Liu, X. Liu, Z. Liu, C. F. Maguire, J. Mahon, Y. I. Makdisi, V. I. Manko, Y. Mao, S. K. Mark, S. Markacs, G. Martinez, M. D. Marx, A. Masaike, F. Matathias, T. Matsumoto, P. L. McGaughey, E. Melnikov, M. Merschmeier, F. Messer, M. Messer, Y. Miake, T. E. Miller, A. Milov, S. Mioduszewski, R. E. Mischke, G. C. Mishra, J. T. Mitchell, A. K. Mohanty, D. P. Morrison, J. M. Moss, F. Mühlbacher, M. Muniruzzaman, J. Murata, S. Nagamiya, Y. Nagasaka, J. L. Nagle, Y. Nakada, B. K. Nandi, J. Newby, L. Nikkinen, P. Nilsson, S. Nishimura, A. S. Nyanin, J. Nystrand, E. O'Brien, C. A. Ogilvie, H. Ohnishi, I. D. Ojha, M. Ono, V. Onuchin, A. Oskarsson, L. Österman, I. Otterlund, K. Oyama, L. Paffrath, A. P. T. Palounek, V. S. Pantuev, V. Papavassiliou, S. F. Pate, T. Peitzmann, A. N. Petridis, C. Pinkenburg, R. P. Pisani, P. Pitukhin, F. Plasil, M. Pollack, K. Pope, M. L. Purschke, I. Ravinovich, K. F. Read, K. Reygers, V. Riabov, Y. Riabov, M. Rosati, A. A. Rose, S. S. Ryu, N. Saito, A. Sakaguchi, T. Sakaguchi, H. Sako, T. Sakuma, V. Samsonov, T. C. Sangster, R. Santo, H. D. Sato, S. Sato, S. Sawada, B. R. Schlei, Y. Schutz, V. Semenov, R. Seto, T. K. Shea, I. Shein, T-A Shibata, K. Shigaki, T. Shiina, Y. H. Shin, I. G. Sibiriak, D. Silvermyr, K. S. Sim, J. Simon-Gillo, C. P. Singh, V. Singh, M. Sivertz, A. Soldatov, R. A. Soltz, S. Sorensen, P. W. Stankus, N. Starinsky, P. Steinberg, E. Stenlund, A. Ster, S. P. Stoll, M. Sugioka, T. Sugitate, J. P. Sullivan, Y. Sumi, Z. Sun, M. Suzuki, E. M. Takagui, A. Taketani, M. Tamai, K. H. Tanaka, Y. Tanaka, E. Taniguchi, M. J. Tannenbaum, J. Thomas, J. H. Thomas, T. L. Thomas, W. Tian, J. Tojo, H. Torii, R. S. Towell, I. Tserruya, H. Tsuruoka, A. A. Tsvetkov, S. K. Tuli, H. Tydesjö, N. Tyurin, T. Ushiroda, H. W. van Hecke, C. Velissaris, J. Velkovska, M. Velkovsky, A. A. Vinogradov, M. A. Volkov, A. Vorobyov, E. Vznuzdaev, H. Wang, Y. Watanabe, S. N. White, C. Witzig, F. K. Wohn, C. L. Woody, W. Xie, and et al. First results from rhic-phenix.

Pramana, 57(2):355–369, 2001.

- [59] David William Kleinjan. *Measurement of the Transverse Single Spin Asymmetry and the Invariant Cross Section of Inclusive Eta Mesons Produced from Transversely Polarized Proton-Proton Collisions at Center of Mass Energy of 200 GeV*. PhD thesis, University of California, Riverside, 2014.
- [60] Abby Bickley. The physics of the reaction plane detector. *FOCUS Talk*, February 2007.
- [61] Eric Richardson. The reaction plane detector. *FOCUS Talk*, January 2007.
- [62] Eric Richardson. The phenix trigger system. *FOCUS Talk*, April 2004.
- [63] Alberica Toia. Participants and spectators at the heavy-ion fireball. *CERN Courier*, April 2013.
- [64] J. T. Mitchell et al. Event reconstruction in the PHENIX central arm spectrometers. *Nucl. Instrum. Meth.*, A482:491–512, 2002.
- [65] Mattias Ohlsson, Carsten Peterson, and Alan L. Yuille. Track finding with deformable templates the elastic arms approach. *Computer Physics Communications*, 71(1):77 – 98, 1992.
- [66] Brennan C. Schaefer. *Measurements of directed, elliptic, and triangular flow of charged hadrons from Cu+Au collisions at $\sqrt{s} = 200$ GeV with PHENIX at RHIC*. PhD thesis, Vanderbilt University, 2016.
- [67] Akio Kiyomichi. Identified charged hadron spectra and particle ratios at $\sqrt{s}=200$ gev for qm2002. *PHENIX internal analysis notes*, AN148, 2002.
- [68] B. Alver and G. Roland. Collision geometry fluctuations and triangular flow in heavy-ion collisions. *Phys. Rev.*, C81:054905, 2010. [Erratum: *Phys. Rev.* C82,039903(2010)].
- [69] A. M. Poskanzer and S. A. Voloshin. Methods for analyzing anisotropic flow in relativistic nuclear collisions. *Phys. Rev. C*, 58:1671–1678, Sep 1998.
- [70] Jamie Nagle, Shawn Beckman, Javier Orjuela-Koop, and Anne Sickles. Phenix run-08 dau a 200 gev centrality categorization: Addendum. *PHENIX internal analysis notes*, AN1087, February 2013.
- [71] A. Taranenko and Roy A. Lacey. Systematic study of azimuthal anisotropy of charged hadrons in au+au collisions. *PHENIX internal analysis notes*, AN957, January 2011.
- [72] Shengli Huang. Phenix results on collectivity in 3he+au collisions. September 2015.
- [73] A. Adare, S. Afanasiev, C. Aidala, N. N. Ajitanand, Y. Akiba, H. Al-Bataineh, A. Al-Jamel, J. Alexander, K. Aoki, L. Aphecetche, R. Armendariz, S. H. Aronson, J. Asai,

E. T. Atomssa, R. Averbeck, T. C. Awes, B. Azmoun, V. Babintsev, G. Baksay, L. Baksay, A. Baldisseri, K. N. Barish, P. D. Barnes, B. Bassalleck, S. Bathe, S. Batsouli, V. Baublis, F. Bauer, A. Bazilevsky, S. Belikov, R. Bennett, Y. Berdnikov, A. A. Bickley, M. T. Bjorndal, J. G. Boissevain, H. Borel, K. Boyle, M. L. Brooks, D. S. Brown, D. Bucher, H. Buesching, V. Bumazhnov, G. Bunce, J. M. Burward-Hoy, S. Butsyk, S. Campbell, J.-S. Chai, B. S. Chang, J.-L. Charvet, S. Chernichenko, C. Y. Chi, J. Chiba, M. Chiu, I. J. Choi, T. Chujo, P. Chung, A. Churyn, V. Cianciolo, C. R. Cleven, Y. Cobigo, B. A. Cole, M. P. Comets, P. Constantin, M. Csanad, T. Csorgo, T. Dahms, K. Das, G. David, M. B. Deaton, K. Dehmelt, H. Delagrange, A. Denisov, D. d'Enterria, A. Deshpande, E. J. Desmond, O. Dietzsch, A. Dion, M. Donadelli, J. L. Drachenberg, O. Drapier, A. Drees, A. K. Dubey, A. Durum, V. Dzhordzhadze, Y. V. Efremenko, J. Egdemir, F. Ellinghaus, W. S. Emam, A. Enokizono, H. En'yo, B. Espagnon, S. Esumi, K. O. Eyser, D. E. Fields, M. Finger, M. Finger, F. Fleuret, S. L. Fokin, B. Forestier, Z. Fraenkel, J. E. Frantz, A. Franz, A. D. Frawley, K. Fujiwara, Y. Fukao, S.-Y. Fung, T. Fusayasu, S. Gadrat, I. Garishvili, F. Gastineau, M. Germain, A. Glenn, H. Gong, M. Gonin, J. Gosset, Y. Goto, R. Granier de Cassagnac, N. Grau, S. V. Greene, M. Grosse Perdekamp, T. Gunji, H.-Å. Gustafsson, T. Hachiya, A. Hadj Henni, C. Haegemann, J. S. Haggerty, M. N. Hagiwara, H. Hamagaki, R. Han, H. Harada, E. P. Hartouni, K. Haruna, M. Harvey, E. Haslum, K. Hasuko, R. Hayano, X. He, M. Heffner, T. K. Hemmick, T. Hester, J. M. Heuser, H. Hiejima, J. C. Hill, R. Hobbs, M. Hohlmann, M. Holmes, W. Holzmann, K. Homma, B. Hong, T. Horaguchi, D. Hornback, S. Huang, M. G. Hur, T. Ichihara, H. Iiuma, K. Imai, M. Inaba, Y. Inoue, D. Isenhower, L. Isenhower, M. Ishihara, T. Isobe, M. Issah, A. Isupov, B. V. Jacak, J. Jia, J. Jin, O. Jinnouchi, B. M. Johnson, K. S. Joo, D. Jouan, F. Kajihara, S. Kametani, N. Kamihara, J. Kamin, M. Kaneta, J. H. Kang, H. Kanou, T. Kawagishi, D. Kawall, A. V. Kazantsev, S. Kelly, A. Khanzadeev, J. Kikuchi, D. H. Kim, D. J. Kim, E. Kim, Y.-S. Kim, E. Kinney, . Kiss, E. Kistenev, A. Kiyomichi, J. Klay, C. Klein-Boesing, L. Kochenda, V. Kochetkov, B. Komkov, M. Konno, D. Kotchetkov, A. Kozlov, A. Kral, A. Kravitz, P. J. Kroon, J. Kubart, G. J. Kunde, N. Kurihara, K. Kurita, M. J. Kweon, Y. Kwon, G. S. Kyle, R. Lacey, Y. S. Lai, J. G. Lajoie, A. Lebedev, Y. Le Borne, S. Leckey, D. M. Lee, M. K. Lee, T. Lee, M. J. Leitch, M. A. L. Leite, B. Lenzi, X. Li, X. H. Li, H. Lim, T. Lika, A. Litvinenko, M. X. Liu, B. Love, D. Lynch, C. F. Maguire, Y. I. Makdisi, A. Malakhov, M. D. Malik, V. I. Manko, Y. Mao, L. Maek, H. Masui, F. Matathias, M. C. McCain, M. McCumber, P. L. McGaughey, Y. Miake, P. Mike, K. Miki, T. E. Miller, A. Milov, S. Mioduszewski, G. C. Mishra, M. Mishra, J. T. Mitchell, M. Mitrovski, A. Morreale, D. P. Morrison, J. M. Moss, T. V. Moukhanova, D. Mukhopadhyay, J. Murata, S. Nagamiya, Y. Nagata, J. L. Nagle, M. Naglis, I. Nakagawa, Y. Nakamiya, T. Nakamura, K. Nakano, J. Newby, M. Nguyen, B. E. Norman, R. Nouicer, A. S. Nyanin, J. Nystrand, E. O'Brien, S. X. Oda, C. A. Ogilvie, H. Ohnishi, I. D. Ojha, M. Oka, K. Okada, O. O. Omiwade, A. Oskarsson, I. Otterlund, M. Ouchida, K. Ozawa, R. Pak, D. Pal, A. P. T. Palounek, V. Pantuev, V. Papavassiliou, J. Park, W. J. Park, S. F. Pate, H. Pei, J.-C. Peng,

- H. Pereira, V. Peresedov, D. Yu. Peressounko, C. Pinkenburg, R. P. Pisani, M. L. Purschke, A. K. Purwar, H. Qu, J. Rak, A. Rakotozafindrabe, I. Ravinovich, K. F. Read, S. Rembeczki, M. Reuter, K. Reygers, V. Riabov, Y. Riabov, G. Roche, A. Romana, M. Rosati, S. S. E. Rosendahl, P. Rosnet, P. Rukoyatkin, V. L. Rykov, S. S. Ryu, B. Sahlmueller, N. Saito, T. Sakaguchi, S. Sakai, H. Sakata, V. Samsonov, H. D. Sato, S. Sato, S. Sawada, J. Seele, R. Seidl, V. Semenov, R. Seto, D. Sharma, T. K. Shea, I. Shein, A. Shevel, T.-A. Shibata, K. Shigaki, M. Shimomura, T. Shohjoh, K. Shoji, A. Sickles, C. L. Silva, D. Silvermyr, C. Silvestre, K. S. Sim, C. P. Singh, V. Singh, S. Skutnik, M. Slunečka, W. C. Smith, A. Soldatov, R. A. Soltz, W. E. Sondheim, S. P. Sorensen, I. V. Sourikova, F. Staley, P. W. Stankus, E. Stenlund, M. Stepanov, A. Ster, S. P. Stoll, T. Sugitate, C. Suire, J. P. Sullivan, J. Sziklai, T. Tabaru, S. Takagi, E. M. Takagui, A. Taketani, K. H. Tanaka, Y. Tanaka, K. Tanida, M. J. Tannenbaum, A. Taranenko, P. Tarján, T. L. Thomas, T. Todoroki, M. Togawa, A. Toia, J. Tojo, L. Tomášek, H. Torii, R. S. Towell, V-N. Tram, I. Tserruya, Y. Systematic study of azimuthal anisotropy in cu + cu and au + au collisions at $\sqrt{s_{NN}} = 62.4$ and 200 gev. *Phys. Rev. C*, 92:034913, Sep 2015.
- [74] Francesco Noferini. Anisotropic flow of identified particles in Pb-Pb collisions at $\sqrt{s_{NN}} = 2.76$ TeV measured with ALICE at the LHC. *Nucl. Phys.*, A904-905:483c–486c, 2013.
- [75] J. L. Nagle, A. Adare, S. Beckman, T. Koblesky, J. Orjuela Koop, D. McGlinchey, P. Romatschke, J. Carlson, J. E. Lynn, and M. McCumber. Exploiting Intrinsic Triangular Geometry in Relativistic He3+Au Collisions to Disentangle Medium Properties. *Phys. Rev. Lett.*, 113(11):112301, 2014.
- [76] Bjrn Schenke and Raju Venugopalan. Collective effects in lightheavy ion collisions. *Nucl. Phys.*, A931:1039–1044, 2014.
- [77] P. Romatschke. Light-heavy-ion collisions: a window into pre-equilibrium qcd dynamics? *The European Physical Journal C*, 75(7):1–15, 2015.
- [78] A. Adare et al. Measurement of long-range angular correlation and quadrupole anisotropy of pions and (anti)protons in central d+Au collisions at $\sqrt{s_{NN}}=200$ GeV. *Phys. Rev. Lett.*, 114(19):192301, 2015.
- [79] Alex Krasnitz, Yasushi Nara, and Raju Venugopalan. Elliptic flow of colored glass in high energy heavy ion collisions. *Physics Letters B*, 554(12):21 – 27, 2003.
- [80] E E Zabrodin, L V Bravina, B H Brusheim Johansson, J Crkovska, G Kh Eyyubova, V L Korotkikh, I P Lokhtin, L V Malinina, S V Petrushanko, and A M Snigirev. Features of triangular flow of strange and non-strange hadrons at lhc. *Journal of Physics: Conference Series*, 668(1):012099, 2016.
- [81] Betty Bezverkhny Abelev et al. Long-range angular correlations of π , K and p in p-Pb collisions at $\sqrt{s_{NN}} = 5.02$ TeV. *Phys. Lett.*, B726:164–177, 2013.

- [82] A. Adare et al. Cold Nuclear Matter Effects on J/ψ Yields as a Function of Rapidity and Nuclear Geometry in Deuteron-Gold Collisions at $\sqrt{s_{NN}} = 200$ GeV. *Phys. Rev. Lett.*, 107:142301, 2011.
- [83] Chin-Hao Chen, Gabor David, Shengli Huang, and Takao Sakaguchi. Measurement of second-order fourier coefficients of the emission angle dependent pi0 yields in run8 d+au collisions. *PHENIX Internal Analysis Note*, AN1164, April 2014.
- [84] Arianna Batista Camejo. Charmonium production in pp, ppb and pbpb collisions at forward rapidity with alice at the lhc. *Journal of Physics: Conference Series*, 668(1):012049, 2016.
- [85] M. J. Leitch, W. M. Lee, M. E. Beddo, C. N. Brown, T. A. Carey, T. H. Chang, W. E. Cooper, C. A. Gagliardi, G. T. Garvey, D. F. Geesaman, E. A. Hawker, X. C. He, L. D. Isenhower, D. M. Kaplan, S. B. Kaufman, D. D. Koetke, P. L. McGaughey, J. M. Moss, B. A. Mueller, V. Papavassiliou, J. C. Peng, G. Petitt, P. E. Reimer, M. E. Sadler, W. E. Sondheim, P. W. Stankus, R. S. Towell, R. E. Tribble, M. A. Vasiliev, J. C. Webb, J. L. Willis, and G. R. Young. Measurement of differences between J/ψ and ψ' suppression in $p - A$ collisions. *Phys. Rev. Lett.*, 84:3256–3260, Apr 2000.
- [86] Christopher Powell. J/ψ production in d+Au collisions at $\sqrt{s_{NN}} = 200$ GeV at the STAR Experiment. Master's thesis, Cape Town U., 2010.
- [87] Ehab Abbas et al. J/Psi Elliptic Flow in Pb-Pb Collisions at $\sqrt{s_{NN}} = 2.76$ TeV. *Phys. Rev. Lett.*, 111:162301, 2013.
- [88] K. Adcox et al. Formation of dense partonic matter in relativistic nucleus-nucleus collisions at RHIC: Experimental evaluation by the PHENIX collaboration. *Nucl. Phys.*, A757:184–283, 2005.
- [89] F. Antinori et al. Production of strange and multistrange hadrons in nucleus nucleus collisions at the SPS. *Nucl. Phys.*, A661:130–139, 1999.
- [90] Sidney D. Drell and Tung-Mow Yan. Massive lepton-pair production in hadron-hadron collisions at high energies. *Phys. Rev. Lett.*, 25:316–320, Aug 1970.